SELF-AGGREGATED ORGANIC MATERIALS IN BIOCATALYSIS AND BIOMEDICINE

Thesis Submitted for the Degree of

Doctor of Philosophy (Science)

to

Jadavpur University

September 2023

by

ANUP KUMAR GHOSH

School of Biological Sciences

Indian Association for the Cultivation of Science

Jadavpur, Kolkata 700 032

India

इंडियन एसोसियेशन फर दि कल्टिवेशन आफ साइंस
ইণ্ডিয়ান এ্যাসোসিয়েশন ফর দি কালটিভেশন অব সায়েন্স
Indian Association for the Cultivation of Science
2A & B Raja S. C. Mullick Road, Jadavpur,
Kolkata - 700032, India

Dr. Prasanta Kumar Das
Senior Professor
School of Biological Sciences

Phone : +91-33-2473-4971
Fax : +91-33-2473-2805
Email : bcpkd@iacs.res.in

To Whom It May Concern

This is to certify that the thesis entitled "**SELF-AGGREGATED ORGANIC MATERIALS IN BIOCATALYSIS AND BIOMEDICINE**" submitted by Sri Anup Kumar Ghosh who got his name registered on 10.09.2018 for the award of Ph.D. (Science) degree of Jadavpur University, is absolutely based upon his own work under the supervision of Prof. Prasanta Kumar Das and that neither this thesis nor any part of it has been submitted for either any degree/diploma or any other academic award anywhere before.

Prasanta Kr. Das 07/09/23
(PRASANTA KUMAR DAS)

Signature of the supervisor
and date with official seal

Dr. Prasanta K. Das
Senior Professor
Chair-School of Biological Sciences
Indian Association for the Cultivation of Science
Jadavpur, Kolkata - 700032

Dedicated to My Beloved

Maa and Baba

DECLARATION

The research work embodied in this thesis entitled "**SELF-AGGREGATED ORGANIC MATERIALS IN BIOCATALYSIS AND BIOMEDICINE**" being submitted to Jadavpur University, Kolkata has been carried out at Indian Association for the Cultivation of Science, Jadavpur, under the supervision of Prof. Prasanta Kumar Das, Senior Professor, School of Biological Sciences, Indian Association for the Cultivation of Science. This work is original and has not been submitted in part or in full, for any degree or diploma to this or any other university.

Anup Kumar Ghosh
07/09/2023

ANUP KUMAR GHOSH

September 2023

CONTENTS

CONTENTS

Self-Aggregated Organic Materials in Biocatalysis and Biomedicine

Architecting and Analyzing Naphthalimide-Centered Fluorescent Organic Nanoparticles: A Comprehensive Study in Design, Development, and Characterization

PREFACE

The research work documented in the current thesis entitled "**SELF-AGGREGATED ORGANIC MATERIALS IN BIOCATALYSIS AND BIOMEDICINE**" demonstrates the creation and utilization of functional soft materials developed through rationally designed amphiphiles. The focus is on development of luminescent supramolecular self-assemblies, coined as fluorescent organic nanoparticles (FONPs), that are used in responsive mediated biomedicinal applications. The thesis explores self-aggregation of light-emitting amphiphiles with distinct photoluminescence in aggregate states, valuable for sensing and bioimaging. The thesis further illustrates the fusion of carbon dots and self-assembled organic nanoparticles to craft soft-nanoconjugates, which find purpose in cancer theranostics. Ultimately, the research holds potential to make significant contributions in various interdisciplinary scientific applications.

The present investigations have been carried out by the author in the School of Biological Sciences, Indian Association for the Cultivation of Science, Jadavpur, Kolkata 700 032, India during the period 2017-2013 under the supervision of Prof. Prasanta Kumar Das.

The thesis contains four chapters in addition to general introduction.

The **Introduction** primarily emphasizes the elegance of self-assemblies. It offers a succinct overview of how nature's ingenuity has spurred scientists to create bio-inspired soft materials and mimic their functionality. Additionally, it briefly showcases familiar self-assembled supramolecular systems, highlighting their interactions and diverse applications, with a specific focus on their responsive attributes in theranostic applications. The introduction also spotlights a novel concept: crafting self-assembled photoluminescent materials with distinct optical properties, specifically for biosensing and biomedical purposes. The discussion touches upon the potentials of nanomaterials. The introduction concludes by describing the fusion of nanomaterials with self-assembled soft materials and accentuates the promising future of these soft-nanoconjugates.

Chapter 1 highlights the dominance of fluorometric detection as a sensing technique due to its rapid response, high selectivity, sensitivity, and operational ease. The study focuses on creating a fluorescent organic nanoparticle-protamine (FONP-Pro) conjugate for precise

heparin detection through the aggregation-induced emission (AIE) property of FONPs. Naphthalene diimide-based amphiphilic molecules (NDI-**1**), featuring naphthyl and aminopyridyl units, form AIE-active organic nanoparticles that emit orange light (λ_{em} = 594 nm) via intramolecular charge transfer. Aminopyridine residues induce a negative surface charge on NDI-**1** FONPs, facilitating interaction with positively charged protamine to form FONP-Pro conjugates. This interaction quenches AIE-gen's orange emission. The addition of heparin to the conjugate restores FONPs' fluorescence by unwinding protamine due to strong binding affinity between heparin & protamine. The developed FONP-Pro effectively senses heparin with high selectivity against other biomolecules. The resulting heparin sensor achieves a detection limit of 12 nM, utilizing NDI-**1** FONP's fluorescence 'turn-off/on' mechanism.

Chapter 2 demonstrates targeted cellular imaging of GABA (γ-aminobutyric acid) receptor ($GABA_AR$) enriched cells (SH-SY5Y and A549) using naphthalene diimide (NDI) derived FONPs with therapeutic potential. Through self-assembly, nipecotic acid tethered L-aspartic acid appended NDI derivative (**NDI-nip**) forms spherical organic particles in DMSO-water through *J*-type aggregation. **NDI-nip**, featuring naphthyl residue and nipecotic acid at both terminals, exhibits AIE at and above 60 % water content in DMSO, emitting orange light (λ_{em} = 579 nm) through excimer formation. These **NDI-nip** FONPs (1:99 v/v DMSO-water) show excellent cell viability and photostability, enabling selective bioimaging and targeted delivery of anticancer drug curcumin to $GABA_AR$ overexpressed cancer cells. This subsequently leads to fluorescence quenching of **NDI-nip** FONPs in $GABA_AR$ enriched neuroblastoma and cancer cells. In the presence of GABA, **NDI-nip** FONPs regain their native fluorescence in the same cell lines and the same effect was not observed in non-cancerous $NIH3T3$ cells. Curcumin-loaded **NDI-nip** FONPs ([curcumin] = 100 μM and [**NDI-nip** FONPs] = 50 μM) exhibit higher killing efficiency in SH-SY5Y (88 ± 3%) and A549 (72 ± 2%) cells compared to $NIH3T3$ (37 ± 2%). The presence of nipecotic acid aids selective cellular internalization of **NDI-nip** FONPs into $GABA_AR$ overexpressing cells. This orange-emitting **NDI-nip** FONPs hold promise for targeted diagnostics and drug delivery in $GABA_AR$ enriched cancer cells.

Chapter 3 illustrates the emerging prominence of AIE-based FONPs as advanced sensors, owing to their easy fabrication, high signal-to-noise ratio, and biocompatibility. The study explores the detection and analysis of protein disulfide isomerase (PDI) enzyme's redox

behaviour using AIE properties of innovative naphthalimide (NI) derivatives containing thiol (-SH) and disulfide (-S-S-) groups. Spherical self-aggregated organic nanoparticles were crafted using synthesized NI-based amphiphiles (**NISH**, **NISS**, **NINSS**, and **TNINSH**) through *J*-type aggregation in DMSO-water (f_w = 99 vol%). Naphthyl-residue-containing NI-derived amphiphiles (**NINSS** and **TNINSH**) exhibited AIE behaviours (blue and yellow emissions) at 470 and 550 nm, respectively, in DMSO-water (f_w = 99 vol%). These **NINSS** and **TNINSH** FONPs were effectively employed for sensing PDI, leveraging its thiol-disulfide exchange redox nature. Fluorescence quenching of **NINSS** FONPs resulted from PDI-mediated disulfide reduction to thiol, while **TNINSH** emission progressively shifted and intensified ("Dual-AIE") due to PDI-driven thiol-to-disulfide oxidation. Both **NINSS** and **TNINSH** FONPs demonstrated highly efficient PDI sensing through an AIE-based "fluorescence off/on" mechanism, achieving detection limits of approximately 12.6-17.7 ng/mL and 11.7-16.5 ng/mL, respectively. In vitro cell imaging using **NINSS** and **TNINSH** FONPs with NIH3T3 (non-cancer) and B16F10 (melanoma) cells revealed accurate eukaryotic cell diagnosis upon interaction with native PDI. Importantly, these FONPs exhibited enhanced sensitivity for cancer cell detection due to PDI overexpression within cancer cells.

Chapter 4 outlines the creation of a **NIONP-CaCD** conjugate by covalently linking a self-assembled organic nanoparticle (**NIONP**) and Ca^{2+}-doped carbon dots (**CaCD**) through a boronic acid-diol linkage. A naphthalimide based lysosome targeting unit appended boronic acid tailed amphiphile was synthesized, forming **NIONP** via *J*-aggregation in a DMSO-water system, while **CaCD** was synthesized through hydrothermal methods. These nanomaterials were connected using a boronic acid-diol interaction between the phenylboronic acid in **NIONP** and hydroxyl groups on **CaCD**, aided by Lewis acid-base chemistry. The formation of **NIONP**, **CaCD**, and the **NIONP-CaCD** conjugate was characterized using microscopic and spectroscopic techniques. The resulting blue-emitting **NIONP-CaCD** conjugate was then employed in bioimaging and pro-drug-free drug combination therapy for cancer treatment. Hydroxychloroquine (HCQ) was encapsulated within the conjugate, exhibiting higher loading capacity than individual carriers (**NIONP** or **CaCD**). Importantly, the conjugate disintegrated into separate components upon exposure to lysosomal pH (4.5-5.0), liberating HCQ and **CaCD** inside the cells. This cytocompatible **NIONP-CaCD-HCQ** formulation led to about 1.5-fold

increased cancer cell death compared to standalone therapy, attributed to Ca^{2+} overload-induced apoptosis (calcicoptosis) and HCQ-triggered lysosomal membrane permeabilization (LMP) induced cell death. Due to its potential for Ca^{2+} overload-based oncotherapy and HCQ-induced lysosomal cell death, the **NIONP-CaCD** conjugate holds promise as a potential candidate for cancer theranostics.

Each chapter (**Chapter 1** to **4**) begins with a short Introduction followed by Results and Discussion, Conclusion, Experimental section, Characterization Data along with the Spectra (^{1}H- and ^{13}C-NMR and MALDI-TOF Mass) of the synthesized amphiphilic molecules and finally the References.

ACKNOWLEDGEMENT

As I reach the culmination of my doctoral journey, I wish to express my heartfelt gratitude and profound acknowledgment to the multitude of individuals who have consistently been my pillars of strength and provide unwavering support in ways beyond my imagination. This journey would have remained incomplete without the dedication and assistance of my colleagues, friends, and supporters, all of whom have been indispensable companions throughout this adventure. It brings me great satisfaction to bring this voyage to a close by extending my heartfelt gratitude to each and every one of them as well as those whose names might have inadvertently escaped mention.

First and the foremost, I extend my deepest respect and heartfelt gratitude to my supervisor, Prof. Prasanta Kumar Das, for his unwavering support, guidance, and consistent encouragement during the various phases of my doctoral research. His dynamic leadership, visionary outlook, and sincere dedication have been a tremendous source of inspiration. He remained a steadfast presence throughout all the projects, providing motivation even in the face of setbacks and steering me toward the right path. Without his guidance, achieving this goal would have been an insurmountable challenge. It was an immense privilege and honor to have the opportunity to work under his tutelage, and I couldn't have asked for a more exceptional mentor for my doctoral studies.

I am delighted to express my appreciation to my research institution, Indian Association for the Cultivation of Science (IACS), for affording me the opportunity to pursue my doctoral research and to the Council of Scientific and Industrial Research (CSIR) for the fellowship that supported my journey.

I am forever indebted to my teachers who nurtured my knowledge from my earliest years in primary school to my Master's in Chemistry. To all the dedicated teachers at Katwa Kashiram Das Insitution, I owe the shaping of my character, and I must mention Kanchan Sir, who ignited my passion for chemistry during my

ACKNOWLEDGEMENT

school days. My stepping into the arena of research remains incomplete without acknowledging the pivotal role played by my college and university teachers whose inspiration and guidance propelled me into the world of academia today. Additionally, I extend my heartfelt appreciation to all the faculty members of our department at IACS for their support.

It brings me great joy to extend my heartfelt gratitude to the staff at IACS, with special mention to Supriyo da, Champa di, Gopal da, Suman da, Sumit da, Goutam da, Banik da, Sanjib da and Sujit da. Their invaluable assistance was instrumental in the success of my experimental work throughout my entire Ph.D. journey. I would also like to express my appreciation to Ashoke da and Chanchal da, whose constant assistance and support always helped me during this voyage.

Speaking of my lab, it is an absolute pleasure to be part of this close-knit family. The lab itself feels like a cozy household, brimming with its unique and enjoyable camaraderie. Expressing my gratitude to my senior and junior lab mates is a task that words alone cannot do justice to. I would like to express my heartfelt appreciation to my seniors, namely Moumita Di, Krishnendu da, Deep da, Saheli di, Soumik da, Pritam da, Debayan da, Deblina Di, Monalisa Di and Aparajita di, for their advice and constant support. To my junior lab mates, Sudeshna, Aftab, Kathakoli, Afreen, Debolina, Rajarshi and Ambalika, I owe my sincere thanks for their uplifting company. I wish to extend a special thanks to Pritam da for his endless cooperation and mentorship during my initial research period and finally I reserve special gratitude to my co-lab mate Monalisa di with whom I shared most of my lab hours, for her constant encouragement and support. They provided me with immense support in every conceivable manner. I will forever hold dear their role in creating beautiful memories and vibrant days at IACS, both within and beyond the laboratory. I also convey my thanks to my other senior and junior lab mates with whom I may not have shared a lab but whose presence has contributed to the positive atmosphere of our workplace.

I also extend my heartfelt gratitude to some of my friends, including Deba, Sohail, Bumba, Pran, Amit, Sanu, Anirban, Koushik, Paromita, Chandrani,

Arunima, Oisharya, Pujita, Aditi, Riya, Sarbani, Kakoli, Esha for enriching my journey with delightful memories and vibrant experiences at various phases.

I want to express my heartfelt gratitude to Rimi (Ms. Sudeshna Bhowmick), whose generous care, love and encouragement brightened my journey and helped me overcome its challenges. Words alone cannot adequately convey the depth of my appreciation for her constant support.

I also pay my homage and express my deepest respect to all my family members, my late thakuma, dida, bhalomama, natunmama, mami, mejda, mejdi, all my pisis and my beloved cousins for their throughout unconditional love and care for me. I owe my deepest gratitude especially to chotomama (Sri Souvikendu Ghosh) for his immense support, care and encouragement since my childhood.

Last but certainly not least, I must express my heartfelt gratitude to my beloved Maa (Smt. Aloka Ghosh) and Baba (Sri Asoke Kumar Ghosh) for granting me the freedom to pursue my dreams. Words seem inadequate to express the depth of my feelings for them for their sacrifices and the efforts they put into nurturing me to my current stage. They are my unwavering pillars of support, and I cannot overstate their importance in my life. I owe everything to them - every past achievement and every future endeavor. Thank you for believing in me, for being there during my toughest moments, and for your unconditional love and care, even in the face of my quirks. I am forever indebted to you for shaping me into the person I have become.

Above all, I am grateful to the Almighty, the merciful and compassionate, for bestowing upon me blessings, opportunities, and the capability to navigate my journey successfully.

Anup Kumar Ghosh

September 2023

LIST OF ABBREVIATIONS

ACQ	:	Aggregation caused quenching
AFM	:	Atomic force microscopy
AG	:	Ambidextrous gelator
AIE	:	Aggregation induced emission
Boc	:	*tert*-Butoxycarbonyl
BSA	:	Bovine serum albumin
Cbz	:	Carboxybenzyl
CD	:	Circular dichroism
CDs	:	Carbon dots
Cur	:	Curcumin
CytC	:	Cytochrome C
DAPI	:	4',6-diamidino-2-phenylindole
DCC	:	*N, N'*-dicyclohexylcarbodiimide
DCM	:	Dichloromethane
DHB	:	2,5-Dihydroxybenzoic acid
DLS	:	Dynamics light scattering
DMAP	:	4-*N, N*-(dimethylamino)pyridine
DMEM	:	Dulbecco's modified eagle's medium
DMF	:	*N, N*-Dimethylformamide
DMSO	:	Dimethyl sulfoxide

DNA	:	Deoxyribonucleic acid
DPH	:	1,6-diphenyl-1,3,5-hexatriene
EDTA	:	Ethylenediaminetetraacetic acid
EtOAc	:	Ethyl acetate
EtOH	:	Ethanol
FBS	:	Fetal bovine serum
FEG-TEM	:	Field-emission gun transmission electron microscopy
FE-SEM	:	Field-emission scanning electron microscopy
FITC	:	Fluorescein isothiocyanate
FONPs	:	Fluorescent organic nanoparticles
FTIR	:	Fourier transform infrared
GABA	:	γ-aminobutyric acid
GOx	:	Glucose oxidase
Hb	:	Hemoglobin
HCQ	:	Hydroxychloroquine
Hep	:	Heparin
HOBt	:	Hydroxybenzotriazole
HRMS	:	High resolution mass spectrometry
HRP	:	Horseradish peroxidase
ICT	:	Intramolecular charge transfer
KBr	:	Potassium bromide
LMHG	:	Low-molecular-weight hydrogel

LMOG	:	Low-molecular-weight organogel
LMWG	:	Low-molecular-weight gel
Lys	:	Lysozyme
MALDI	:	Matrix-assisted laser desorption/ionization
MeOH	:	Methanol
MTT	:	(3-(4,5-Dimethylthiazol-2-yl)-2,5-diphenyltetrazolium bromide
NDI	:	Naphthalene diimide
NHS	:	N-hydroxy succinimide
NI	:	Naphthalimide
NMR	:	Nuclear magnetic resonance
PBS	:	Phosphate-buffered saline
PDI	:	Protein disulfide-isomerase
PEG	:	Polyethylene glycol
Pep	:	Pepsin
PHDFDA	:	poly(heptadecafluorodecylacrylate)
PL	:	Photoluminescnce
Pro	:	Protamine
RESS	:	Rapid Expansion of Supercritical Solution
RIR	:	Restricted intramolecular rotation
SAFIN	:	Self-assembled fibrillar network
SOD	:	Superoxide dismutase
SSI	:	Suspension stability index

TCSPC	:	Time-correlated single photon count
TEM	:	Transmission electron microscopy
TFA	:	Trifluoroacetic acid
THF	:	Tetrahydrofuran
TOF	:	Time of flight
Tryp	:	Trypsin
UV	:	Ultra-violet
XPS	:	X-ray photoelectron spectroscopy
XRD	:	X-ray diffraction

SYNOPSIS

Mother Nature operates its own precision-driven factory, crafting intricate nanoscale devices and materials at the nanoscale with precision, adaptability, and error-correction capabilities. Humanity has long benefitted from drawing inspiration from these natural processes. One such emulation is the meticulous construction of materials atom by atom or molecule by molecule, resulting in innovative supramolecular architectures akin to "molecular lego" building blocks. Such supramolecular entities arise from diverse non-covalent interactions, including hydrogen bonding, π-π stacking, van der Waals forces, electrostatic interactions, and hydrophobic forces. The diverse structural nature of these amphiphilic molecules and their interactions in different environments result in a plethora of morphologies, including micelles, reverse micelles, vesicles, microemulsions, and gel fibers. Customized soft materials, endowed with unique traits, hold vast potential across electronics, photonics, and biotechnology fields. Tailoring the amphiphiles' structures and enhancing physicochemical attributes of self-aggregates is pivotal for specific applications. Additionally, the field of biosensing and biomedicine has been transformed by organic nanoparticles with unique luminescent properties coined as aggregation-induced emission (AIE). Nanotechnology's emergence has revolutionized research, particularly across material science and biomedicine. The fusion of self-assembled species with carbon dots, produces novel soft-nanoconjugates with enhanced physicochemical and optical characteristics, rendering them suitable for diverse applications. This thesis provides an overview of diverse self-assembled systems derived from amphiphiles, tailored for specific applications, featuring distinct properties of soft materials. It encompasses the creation of fluorescent organic nanoparticles (FONPs) with unique physicochemical and photoluminescent attributes, harnessing for biosensing, bioimaging and target-specific transporting cargo within mammalian cells. Furthermore, the thesis demonstrates the fabrication of CD-ONP conjugate with promising implications for cancer treatment. Altogether, the focus is on "smart" supramolecular systems applicable in bioimaging, the sensing of biologically important entities within mammalian cells, and advanced drug delivery.

Chapter 1 demonstrates the fabrication of a bola-type amphiphilic molecule, designated as NDI-**1**, by tagging L-aspartic acid to naphthalene diimide (NDI) with 3-aminopyridyl and naphthyl residues at both terminals. NDI-**1** underwent *J*-type aggregation in

a DMSO-water binary solvent mixture, forming spherical organic nanoparticles (Figure 1). Initially, the molecularly dissolved state in DMSO exhibited faint blue emission, but upon aggregation at 30 vol% water content, these molecules displayed aggregation-induced emission (AIE) in orange through excimer formation. As water content increased to 99 vol%, the excimer band intensity progressively heightened, with a maximum emission at 594 nm upon excitation at 350 nm (Figure 1). The presence of a π-electron-rich naphthyl residue promoted intramolecular charge transfer (ICT), resulting in longer wavelength (orange) emitting fluorescent organic nanoparticles (FONPs).

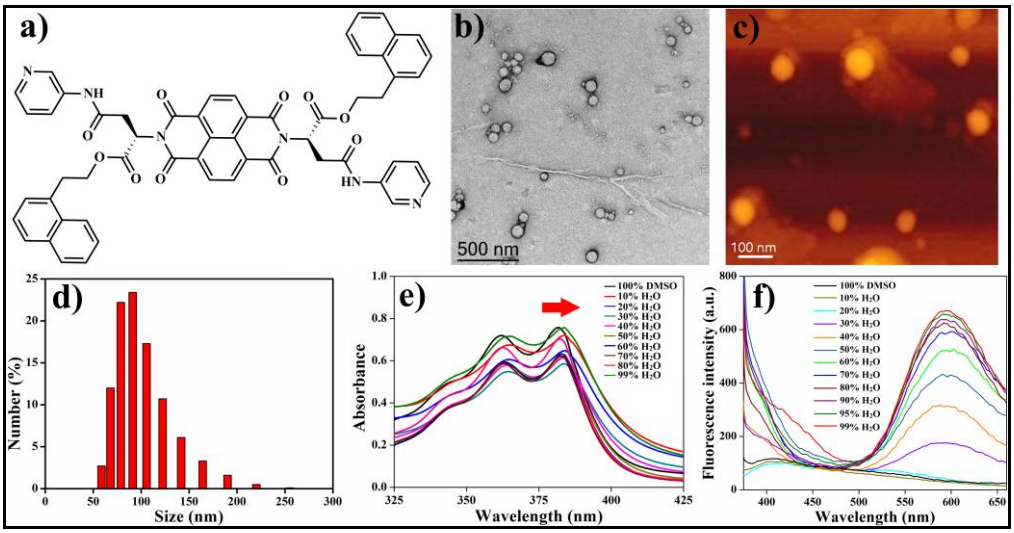

Figure 1. (a) Structure of NDI-**1** molecule, (b) negatively stained TEM image, (c) AFM image, (d) DLS plot of particles size distribution of NDI-**1** in (1:99, v/v) DMSO-water binary solvent mixture ([NDI-**1**] = 50 μM), (e) UV–visible and (f) fluorescence of spectra NDI-**1** (50 μM) in varying DMSO–water solvent mixtures.

This unique FONP variant carried a negative surface charge due to the 3-aminopyridyl unit, forming conjugates with positively charged protamine and thereby quenching the fluorescence of NDI-**1** FONPs. This stable FONP-Pro conjugate, enveloped by protamine, could function as a "fluorescence turn-on" sensor by restoring the excimer band intensity, enabling selective detection of heparin amidst other negatively charged biomolecules. Leveraging this approach, the fluorometric sensor exhibited remarkable sensitivity, detecting heparin levels as low as 180 ng/mL (equivalent to 12 nM) (Figure 2). This straightforward fluorescence off/on strategy capitalizing on AIE principles holds significant promise for the wide-ranging detection of trace heparin levels in clinical samples.

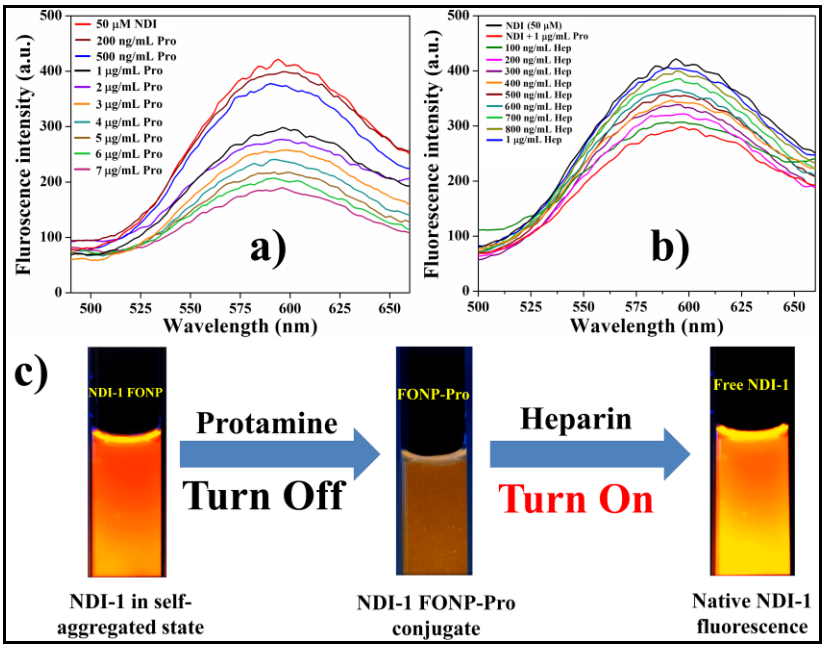

Figure 2. Fluorescence spectra of NDI-**1** in the absence and presence of varying concentrations of (a) protamine (Pro), (b) heparin in (1:99, v/v) DMSO-phosphate buffer saline (pH = 7.4, 10 mM) solution of FONP-Pro conjugate, (c) photograph for heparin sensing by fluorescence off/on of NDI-**1** FONPs through formation of FONP-protamine conjugate. (λ_{ex} = 365 nm).

In a nutshell, we designed NDI-**1**, an amphiphilic molecule, that forms orange-emitting FONPs through AIE in a DMSO-water mixture. These FONPs, wrapped with protamine, act as a fluorescence 'turn-on' sensor, detecting heparin selectively at low levels (12 nM). This simple technique holds promise for sensitive and selective heparin detection in clinical samples (Figure 3).

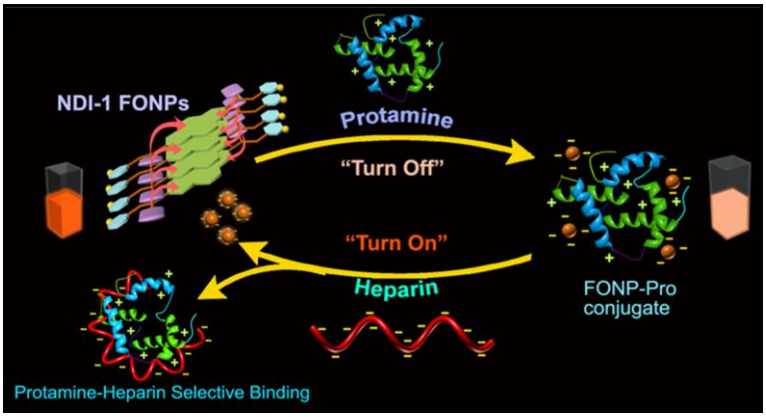

Figure 3. Schematic Representation of Heparin-Sensing by Quenching and Restoration of AIE of NDI-**1** FONPs through Formation of the FONP–Pro Conjugate.

Chapter 2 delineates the designing of L-aspartic acid-tagged naphthalene diimide (NDI) amphiphilic compound, **NDI-nip** (Figure 4a), featuring naphthyl and nipecotic acid moieties. **NDI-nip** self-assembled into spherical organic nanoparticles (50-70 nm) through *J*-type aggregation in a DMSO-water binary system (Figure 4b,c,d). It exhibited weak blue emission in DMSO and induced orange emission above 60 vol% water content through excimer formation. The excimer fluorescence progressively intensified with increasing water content, peaking at 579 nm (λ_{ex} = 350 nm) at 99 vol% (Figure 4g).

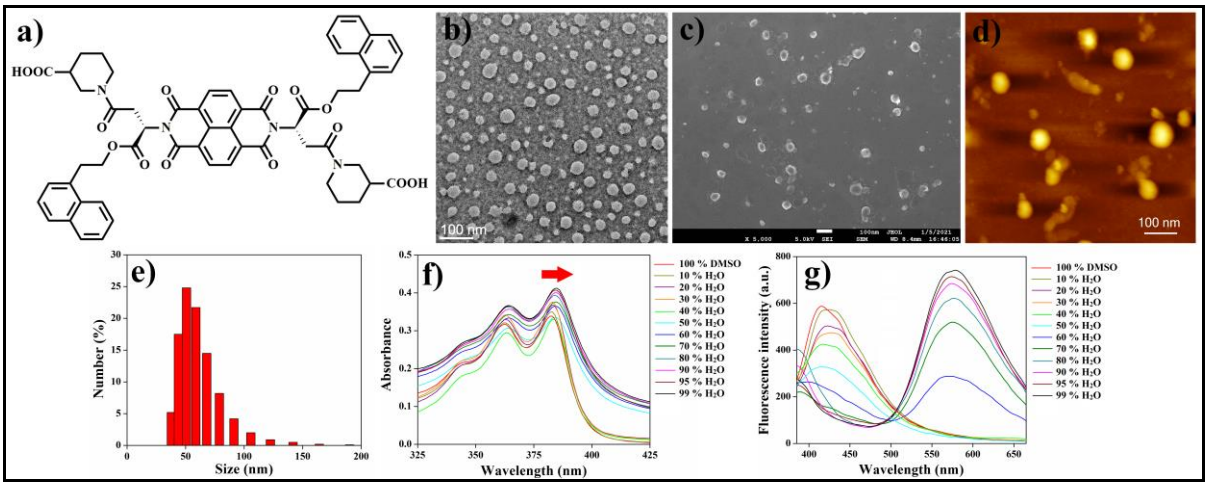

Figure 4. (a) Structure of **NDI-nip** molecule, (b) negatively stained TEM image, (c) FESEM image, (d) AFM image, (e) DLS plot of particles size distribution of **NDI-nip** in (1:99, v/v) DMSO-water binary solvent mixture ([**NDI-nip**] = 10 μM), (f) UV-visible and (g) fluorescence of spectra **NDI-nip** (10 μM) in varying DMSO–water solvent mixtures.

These cytocompatible orange FONPs were successfully utilized for targeted cellular imaging and drug delivery. **NDI-nip** FONPs, containing nipecotic acid units, were employed for targeted imaging of $GABA_A$ receptor-enriched cells (SH-SY5Y and A549), displaying fluorescence quenching in these cells but not in the presence of native GABA (Figure 5a-d). Moreover, these FONPs efficiently encapsulated the anti-cancer drug curcumin, demonstrating selective cancer cell killing (SH-SY5Y and A549) over non-cancerous NIH3T3 cells. The cytotoxicity of curcumin-loaded **NDI-nip** FONPs ([curcumin] = 100 μM and [**NDI-nip** FONPs] = 50 μM) demonstrated notably greater effectiveness against SH-SY5Y (88 ± 3%) and A549 (72 ± 2%) cells compared to NIH3T3 (37 ± 2%) (Figure 5e). Thus, these target-specific **NDI-nip** FONPs hold promise as potent cancer-targeting diagnostic agents with specialized cargo transport for $GABA_A$R-enriched cancer cells.

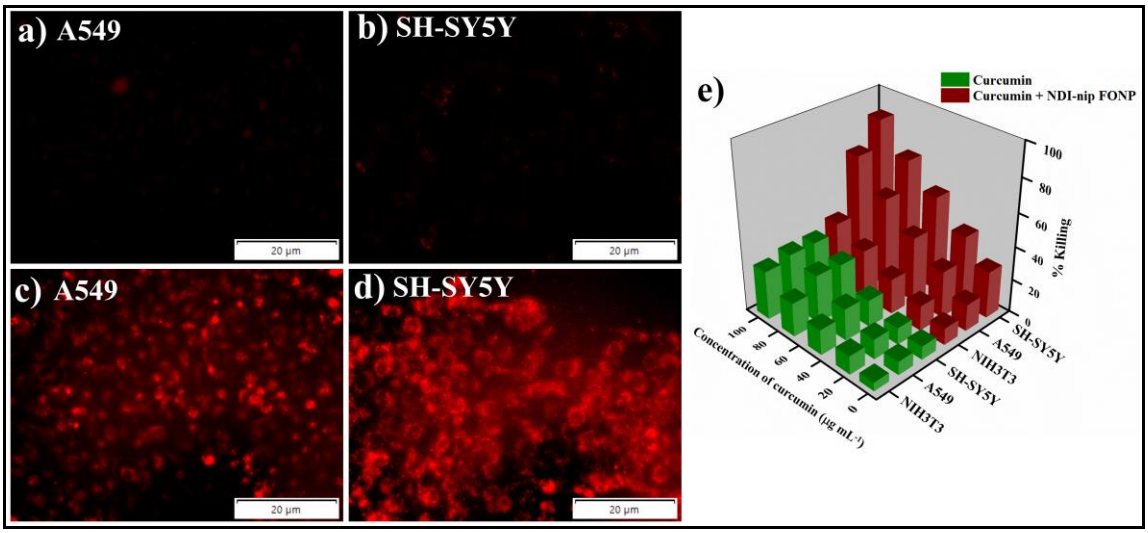

Figure 5. Fluorescence microscopic images of cells after 24 h incubation with only **NDI-nip** (100 μM) and with (**NDI-nip** + GABA) where [**NDI-nip**] = 100 μM, [GABA] = 200 μg/mL for (a,c) A549 and (b,d,) SH-SY5Y cells, respectively, (e) Killing efficiency (determined by MTT assay) of curcumin loaded **NDI-nip** FONPs and free curcumin toward NIH3T3, A549 and SH-SY5Y cells for 24 h. Percent experimental errors are within ±~3% in triplicate experiments.

In summary, we developed **NDI-nip**, an amphiphilic compound with naphthyl and nipecotic acid moieties, forming orange-emitting FONPs through aggregation. These FONPs showed selective internalization in $GABA_A$ receptor-enriched cells, serving as effective diagnostic and drug delivery agents for cancer cells (Figure 6). The study highlights their potential for targeted cancer therapies and imaging.

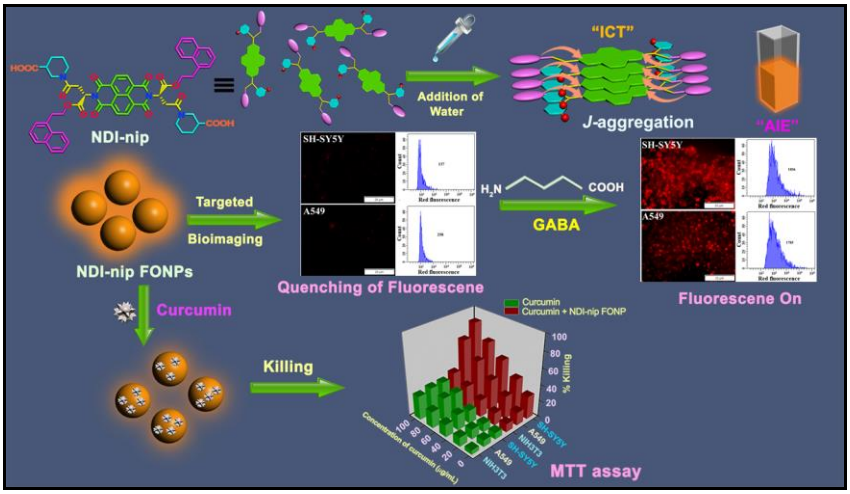

Figure 6. Schematic Representation of Targeted Diagnostic and Delivery by Orange-Emitting **NDI-nip** Nanoparticles for $GABA_A$ Receptor-Enriched Cancer Cells.

Chapter 3 illustrates the design of naphthalimide (NI) based amphiphiles incorporating thiol (**NISH** and **TNINSH**) and disulfide moieties (**NISS** and **NINSS**) within their molecular structure (Figure 7). Utilizing *J*-type aggregation in a 1:99 (v/v) DMSO-H_2O mixture, these NI-derived amphiphiles formed self-assembled spherical organic nanoparticles (50-120 nm) (Figure 8a-f). **NINSS** and **TNINSH**, containing naphthyl groups, exhibited aggregation-induced emission (AIE) at $f_w \geq 30$ vol%, generating excimer formation. Emission intensity of **NINSS** and **TNINSH** excimer peaks increased with rising water content up to f_w = 99 vol% (λ_{em} at 470 nm and 550 nm, respectively, λ_{ex} = 350 nm) (Figure 8g,h).

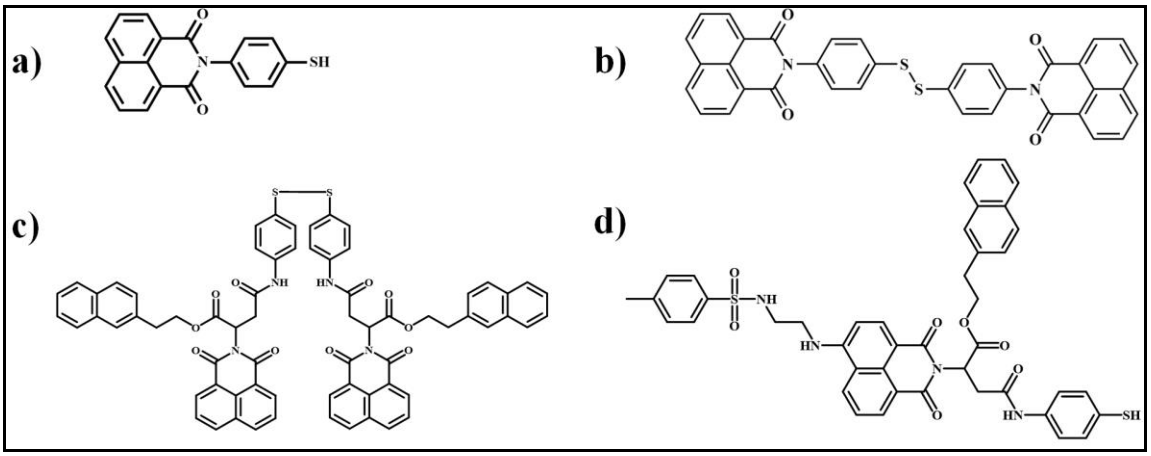

Figure 7. Molecular structure of NI-based amphiphiles (a) **NISH**, (b) **NISS**, (c) **NINSS** and (d) **TNINSH**.

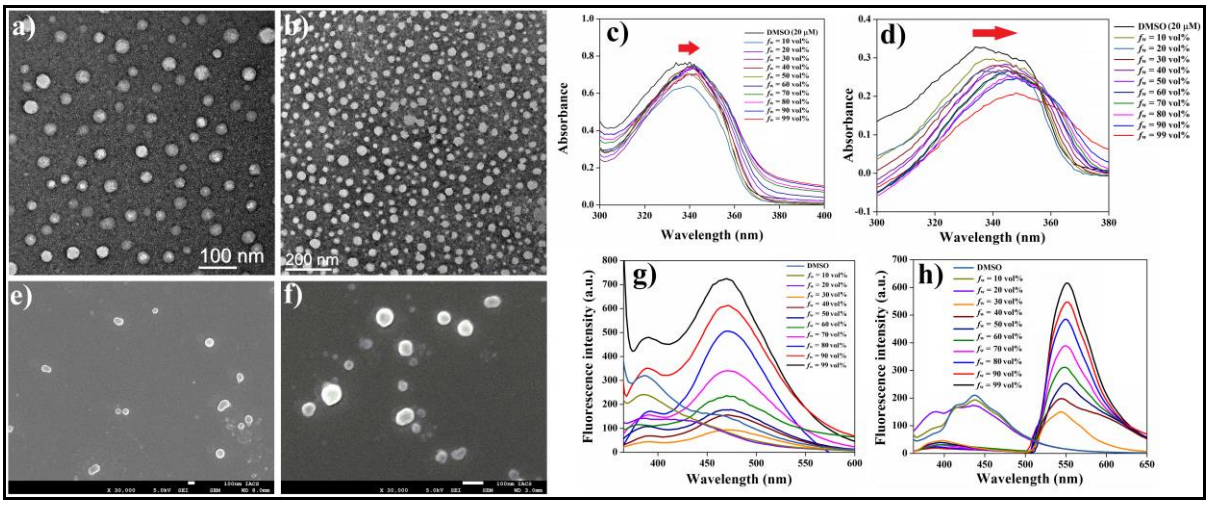

Figure 8. (a,c) Negatively stained TEM images, (b,f) FESEM images, (c,g) UV-vis spectra and (d,h) fluorescence spectra of **NINSS** and **TNINSH**, respectively.

Derived FONPs from **NINSS** and **TNINSH** demonstrated biocompatibility and stability, enabling efficient PDI sensing by exploiting AIE-driven fluorescence changes both in vitro and within cells. **NINSS** FONPs at λ_{em} = 470 nm exhibited fluorescence quenching upon PDI addition, resulting from disulfide (-S-S-) reduction to thiol (-SH) by PDI (Figure 9a). Similarly, **TNINSH** FONPs showed "dual-AIE" behavior, with yellow emission shifting to reddish emission upon PDI addition due to disulfide dimer generation via thiol oxidation (Figure 9b). As highly sensitive probes, **NINSS** and **TNINSH** FONPs analyzed PDI's redox behavior with LODs of ~12.6-17.7 ng/mL and ~11.7-16.5 ng/mL, respectively. These FONPs successfully diagnosed cancer (B16F10) and non-cancer (NIH3T3) cells, demonstrating superior sensitivity in cancer cell detection due to PDI overexpression. In conclusion, **NINSS** and **TNINSH** FONPs can serve as diagnostic probes for selective and sensitive PDI analysis, capitalizing on their AIE-driven fluorescence off/on mechanism.

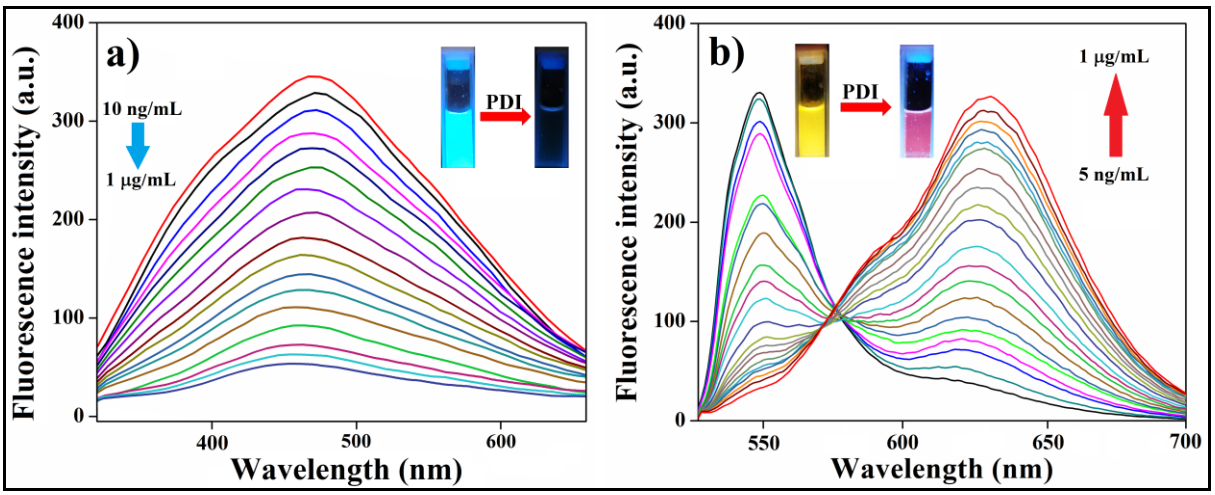

Figure 9. Fluorescence spectra of (a) **NINSS** FONPs (2.5 μM), (d) **TNINSH** FONPs (5 μM) in presence of PDI in (1:99, v/v) DMSO-PBS (pH = 7.4, 10 mM), [GSH] and [GSSG] = 10 μM

In essence, we designed amphiphiles based on naphthalimide (NI) with thiol and disulfide groups, forming self-assembled nanoparticles. These aggregates emitted light when aggregated, with enhanced signals in water-rich environments. These fluorescent nanoparticles were adept at sensing PDI enzyme activity both in cuvette and within cells, showing potential for diagnostics (Figure 10). The system's sensitivity allowed for accurate detection of cancer cells due to their higher PDI levels. This suggests promising applications for diagnosing and studying cellular behavior.

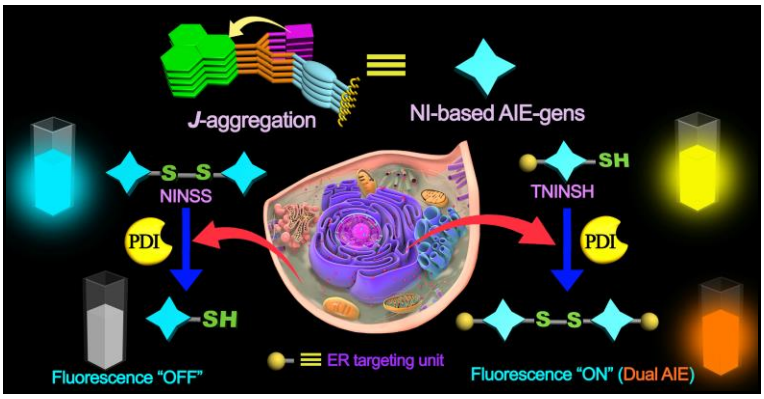

Figure 10. Schematic representation of analyzing PDI redox state by exploitation of AIE of **NINSS** and **TNINSH** FONPs. NI: naphthalimide, AIE: aggregation induced emission.

Chapter 4 describes the design and development of **NIONP-CaCD** conjugate through boronic acid-diol covalent linkage between self-assembled organic nanoparticle (**NIONP**) and Ca^{2+}-doped carbon dots (**CaCD**) (Figure 11). A naphthalimide-based lysosome targeting unit-appended boronic acid tailed amphiphile, **NIONP** was synthesized, which underwent *J*-aggregation in a DMSO-water system, resulting in the formation of spherical shaped organic nanoparticle (ONP). On the other hand, Ca^{2+}-doped carbon dot (**CaCD**), surface functionalized with hydroxyl (-OH) moiety was synthesized via the hydrothermal method.

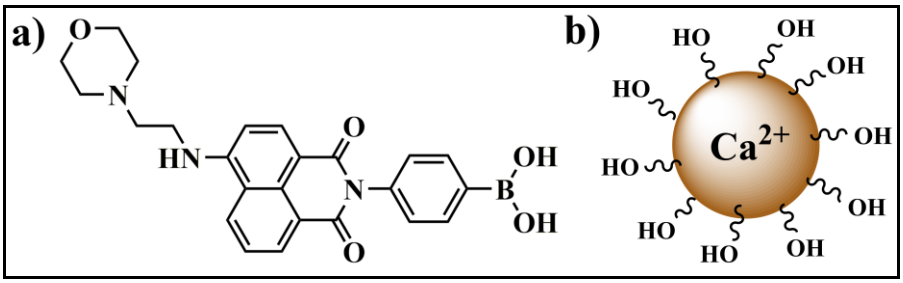

Figure 11. Molecular structure of (a) **NIONP** and (b) **CaCD**.

These two nanomaterials were connected through a covalent bond using a boronic acid-diol interaction (Lewis acid-base chemistry). This interaction occurred between the phenylboronic acid-based **NIONP** and the hydroxyl group-functionalized **CaCD**, enabling the development of the **NIONP-CaCD** conjugate. The formation of **NIONP**, **CaCD**, and **NIONP-CaCD** conjugate was characterized by different microscopic and spectroscopic techniques (Figure 12). The newly fabricated **NIONP-CaCD** conjugate was then utilized for bioimaging purposes, capitalizing on the inherent fluorescence of **CaCD** (Figure 12). Additionally, it was

employed in pro-drug-free drug combination therapy for the treatment of cancer. As we envisaged pro-drug-free drug combination chemotherapy, we utilized Ca^{2+} overload as a prodrug and Ca^{2+} doped carbon dot as a pro-drug activator and also introduced hydroxychloroquine (HCQ) as the free frug.

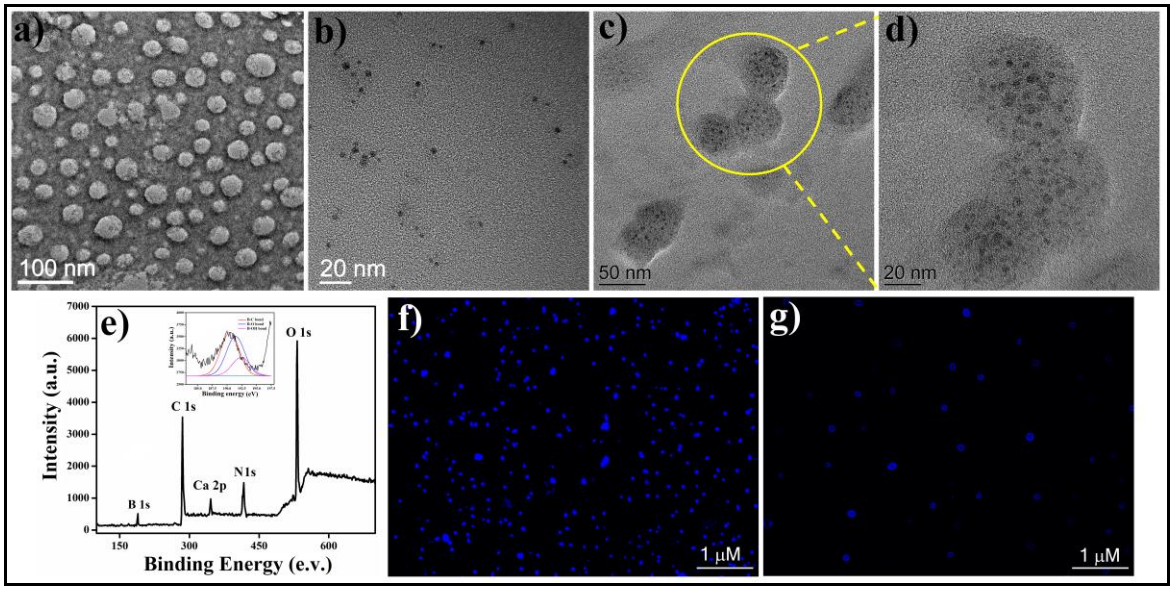

Figure 12. TEM images of (a) **NIONP**, (b) **CaCD** and (c,d) **NIONP-CaCD** conjugate; (e) XPS spectra (deconvoluted spectra, inset) of **NIONP-CaCD** conjugate; fluorescence microscopic images of (f) **CaCD** and (g) **NIONP- CaCD** conjugate.

The **NIONP-CaCD** conjugate was found to be stable in biological milieu and also exhibited excellent ability of uploading HCQ (**NIONP-CaCD-HCQ**) with compared to its individual components. Moreover, the luminescent characteristics exhibited by both **CaCD** and the **NIONP-CaCD** conjugate confirmed their internalization ability inside A549 and HepG2 cells, suggesting their potential utility as bioprobes for diagnostic applications. Interestingly, the disintegration of the **NIONP-CaCD** conjugate into its individual components occurred via the cleavage of the boronate-diol bond within the lysosomal pH range (4.5-5.0), leading to the release of both **HCQ** and **CaCD** (Figure 13). Following this, this subsequent liberation of pro drug (Ca^{2+}) and free drug (HCQ) could instigate cell death triggered by the lysosomal membrane permeabilization (LMP) induced by HCQ in association with Ca^{2+} overload mediated apoptosis (calcicoptosis) (Figure 13). This biocompatible pro-drug-free formulation, **NIONP-CaCD-HCQ**, led to an approximate 1.5-fold rise in cancer cell mortality compared to using the individual cargo carriers separately in standalone therapy.

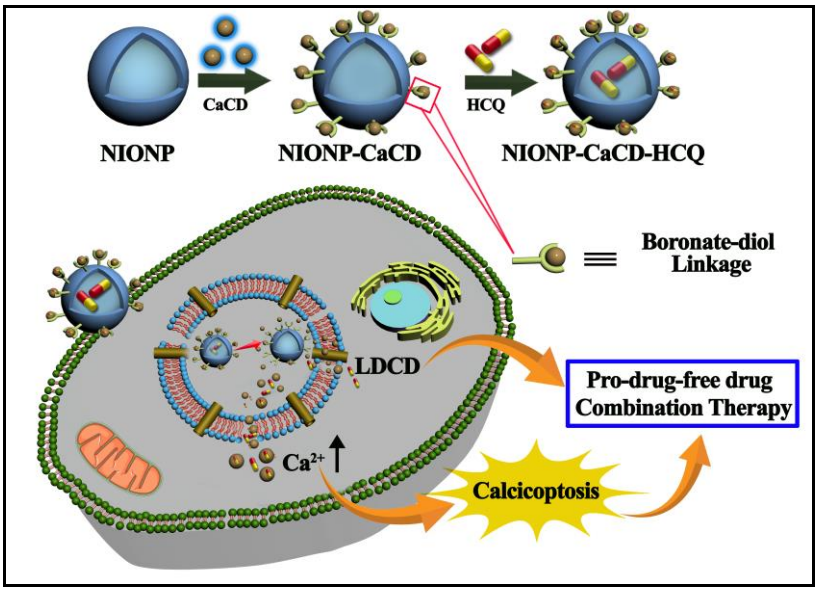

Figure 13. Schematic representation of fabrication of **NIONP-CaCD** conjugate through boronate-diol linkage and its application in cancer theranostic by exploiting pro-drug-free drug combination therapy.

In summary, we synthesized a cytocompatible **NIONP-CaCD** conjugate by covalently linking self-assembled organic nanoparticles (**NIONP**) and Ca^{2+}-doped carbon dots (**CaCD**) through a boronic acid-diol interaction and this nanoconjugate exhibited improved drug (HCQ) loading efficiency with compare to its constituents. Significantly, the potent synergy between Ca^{2+} overload-mediated calcicoptosis and HCQ-triggered lysosomal cell death, enabled by this **NIONP-CaCD** conjugate, holds promising theranostic potential in the domain of combination therapy for cancer treatment.

Introduction

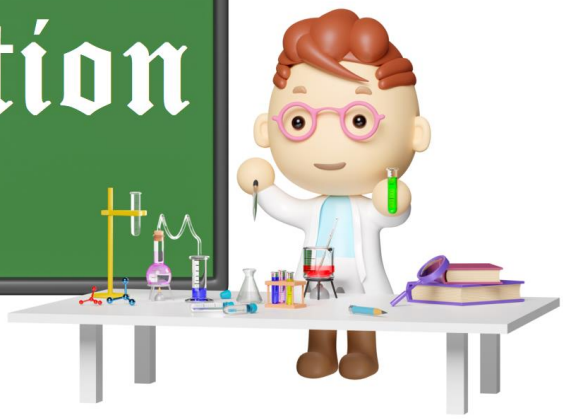

"If we knew what it was, we were doing, it would not be called research, would it?"

~Albert Einstein

INTRODUCTION

"Nature is our kindest friend and best critic in experimental science if we only allow her intimations to fall unperceived."

~ Michael Faraday

Science is a systematic and organized body of knowledge that is derived from the study of the natural world through observation, experimentation, and analysis. It seeks to understand the fundamental principles, laws, and mechanisms that govern the behavior of the universe and all its components. The relationship between nature and science is deeply intertwined and symbiotic. Science is the systematic study and exploration of the natural world, while nature serves as the source of the phenomena, materials, and processes that science seeks to understand. Nature and science are two fundamental pillars that shape our understanding of the world. Science serving as a powerful tool to unravel the mysteries of nature, and nature providing the canvas upon which science paints its intricate theories and discoveries. This symbiotic relationship between nature and science has led to profound insights, technological advancements, and a deeper appreciation for the wonders of the natural world (Figure 1).[1,2]

THE PROFOUND INTERDEPENDENCE OF NATURE AND SCIENCE: EXPLORING ORIGINS AND DEPENDENCY

The interplay between nature and science is a symphony of discovery and understanding, where each element harmoniously complements the other, leading to a deeper comprehension of the universe and our place within it. This intricate relationship is characterized by origins rooted in human curiosity, an interconnection that fuels exploration, and a mutual dependency that drives progress and conservation.

❖ **Origins: A Curious Gaze at the Natural World**

The origins of the relationship between nature and science trace back to the dawn of human curiosity. From ancient civilizations gazing at the stars to modern laboratories probing the subatomic realm, humans have sought to unravel the mysteries of the natural world. Nature, with its myriad forms, behaviors, and patterns, ignited the spark of curiosity that led to the birth of science. The innate human desire to understand the world around us has driven us to observe, question, and seek explanations for the natural phenomena that unfold in our environment.

❖ **Dependency: A Reciprocal Relationship of Progress and Conservation**

The relationship between nature and science is one of mutual dependency. Science relies on nature as its wellspring of inspiration and raw material. The diverse array of life forms, ecosystems in nature provide the rich tapestry from which scientific inquiry draws its questions. In turn, science's discoveries and innovations have a profound impact on nature. Technological advancements, born from scientific insights, allow us to explore natural process for practical purposes, from harnessing energy to treating diseases. This very dependency highlights a responsibility – as science advances, it also uncovers the consequences of human actions on nature, underscoring the need for conservation, sustainable practices, and ethical stewardship.

Figure 1. The nexus of nature, mankind, and science: an enchanting tale. (Taken from Reference 1,2)

The importance of nature in science is manifold. It serves as the muse that sparks scientific curiosity, the subject of investigation that reveals universal truths, and the source of raw materials for innovation. Science, in turn, enriches our understanding of nature, empowering us to appreciate its intricate beauty, address its challenges, and seek harmonious coexistence. This reciprocal relationship guides us toward a more profound connection with the natural world, reminding us of our role as both explorers and caretakers. Originating from our innate desire to understand, this relationship has evolved into a dynamic interconnection where each element depends on the other for progress and preservation. As we continue to explore the depths of nature through the lens of science, we cultivate a deeper appreciation for the wonders of the universe and a heightened awareness of our collective responsibility to nurture and protect the delicate balance of our planet.

NATURE'S INGENIOUS SYMPHONY: THE SCIENCE OF SELF-ASSEMBLY

Nature's vast and intricate tapestry hold the secrets of a remarkable phenomenon known as self-assembly. From the microscopic world of cells to the grandeur of ecosystems, self-assembly is at the heart of nature's ability to create complex and ordered structures without external guidance (Figure 2).[3-7] This fascinating process, deeply rooted in the evolution of living systems, serves as an origin for the exploration of self-assembly in science and inspires innovative applications in materials design and nanotechnology.

Figure 2. The dance of symmetry: exploring order in nature's elegance. (Taken from Reference 3-7)

Self-assembly dates back to 400 BC, when Democritus, a Greek philosopher, envisioned that the earth and solar system might have evolved from organization of atomistic components. Later, Descartes, a French philosopher, postulated that the universe has self-structured out of chaos via organization of small components to large assemblages according to natural laws of physics. In 1935, Langmuir and Blodgett developed a method to form a closely packed monolayer of amphiphilic molecules on solid and liquid surfaces. Although these studies did not use the term “self-assembly”, they were indirectly explaining the self-assembly process. The self-assembly was initially used in Self-assembled monolayers (SAMs), which were discovered in 1983 by Nuzzo et al.[8]

Nature's profound mastery of self-assembly has captivated scientists across disciplines. Materials science and nanotechnology draw inspiration from the design principles encoded in nature's self-assembling structures (Figure 3).[9] Researchers seek to mimic biological self-

assembly to fabricate materials with unique properties, such as self-healing polymers, responsive nanomaterials, and smart coatings. These endeavors have the potential to revolutionize drug delivery, sensors, and other fields, offering solutions inspired by nature's age-old wisdom.

Figure 3. Nature's masterpiece: the intricate symphony of self-assembly. (Taken from Reference 9)

Origin of self-assembly has fueled the exploration of this captivating phenomenon in science and engineering. From the elegance of molecular interactions to the complexity of biological structures, self-assembly stands as a testament to nature's ingenuity as an architect of order from chaos. As we delve deeper into the mysteries of self-assembly in nature, we not only gain a deeper appreciation of life's intricacies but also unlock the potential for transformative applications that benefit society and the natural world.

HARMONY UNVEILED: THE ENIGMATIC SELF-ASSEMBLY OF AMPHIPHILES IN NATURE AND SCIENCE

"Nature's Architect: The Origin of Self-Assembly" evokes the notion of nature's creative prowess in orchestrating the intricate and harmonious dance of self-assembly, unraveling the

underlying principles that govern this captivating phenomenon. Karl Lothar Wolf's coinage of the term "Übermoleküle" in 1937 marked the birth of the concept of supramolecular chemistry, signifying the study of larger, organized structures formed through non-covalent interactions, such as hydrogen-bonded acetic acid dimers.[10]

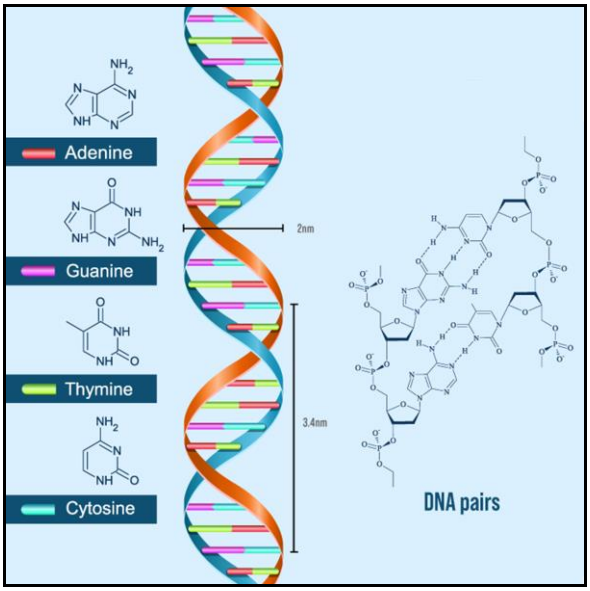

Figure 4. Chemical structure of DNA. (Taken from Reference 14)

At the molecular level, self-assembly finds its genesis in the inherent properties of atoms and molecules. Non-covalent interactions, such as hydrogen bonding, van der Waals forces, and hydrophobic interactions, orchestrate the spontaneous organization of molecules into intricate arrangements.[11-13] Nature's biomolecules, from proteins and DNA to lipids and carbohydrates, are prime examples of the exquisite self-assembly at work. The folding of proteins into specific functional conformations or the precise base pairing in DNA are proof to the elegance of nature's self-assembling capabilities (Figure 4).[14]

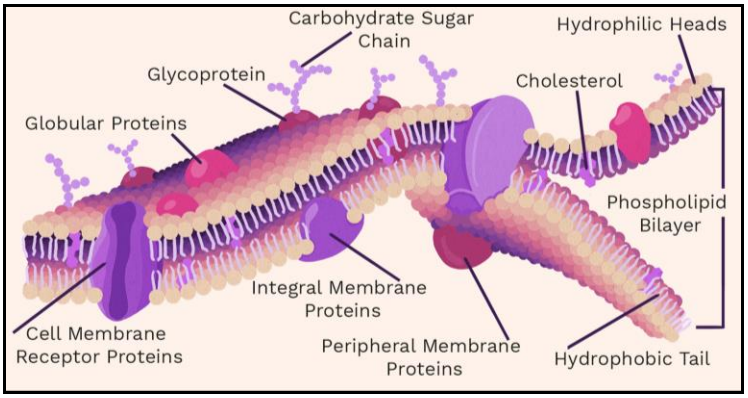

Figure 5. Cross-section of cell-membrane. (Taken from Reference 15)

In living organisms, self-assembly is a guiding principle in shaping the structure and function of cells. Cell membranes, composed of self-assembled phospholipids, create selectively permeable barriers essential for life's processes (Figure 5).[15] The cytoskeleton, built upon self-assembly of proteins like actin and tubulin, enables cellular movement and maintains cellular shape. From the assembly of viruses' protective capsids to the formation of intricate shells by marine organisms, nature showcases diverse and complex self-organizing systems.

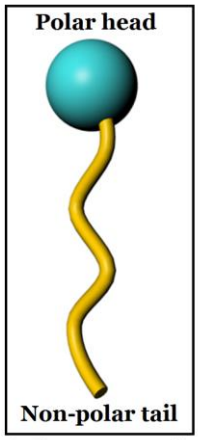

Figure 6. Structure of amphiphile.

Now, when we focus on the fundamental units of self-assembled structures in the vast realm of self-assembly, we arrive at "amphiphiles" or "surfactants." The term "amphiphile" derives from the *Greek* words "*amphi*," meaning "both," and "*philos*," meaning "loving." True to their name, amphiphiles possess a dual nature, displaying an affinity for both aqueous and non-aqueous environments. This unique characteristic drives them to orchestrate some of nature's most remarkable self-assembly processes. At the heart of amphiphiles' captivating behavior lies their molecular structure, which consists of two distinct regions: a hydrophilic (water-attracting) "head" and a hydrophobic (water-repelling) "tail".[16,17] This unique property allows them to spontaneously organize into complex structures due to the desire to minimize unfavorable interactions between the hydrophobic part of the molecule and water.[18,19]

Amphiphiles are classified into four main categories based on their head group charge: anionic, with negatively charged head groups; cationic, with positively charged head groups; zwitterionic, featuring both positive and negative charges in their backbone; and nonionic, lacking any charge (Figure 7).[20] Anionic amphiphiles serve as detergents, while cationic ones like cetyltrimethylammonium bromide (CTAB) has positive head group.[17,20] Zwitterionic amphiphiles, exemplified by phospholipids like phosphatidylcholine, exhibit both positive and negative charges, responding to pH changes. Nonionic surfactants lack charges, with polar heads comprising polyether or polyhydroxyl functionalities.[17] In addition, macromolecular amphiphiles include gemini types with two hydrophilic heads and hydrophobic chains, and bola-amphiphiles have polar head groups on both ends of alkyl chains.[17,20,21]

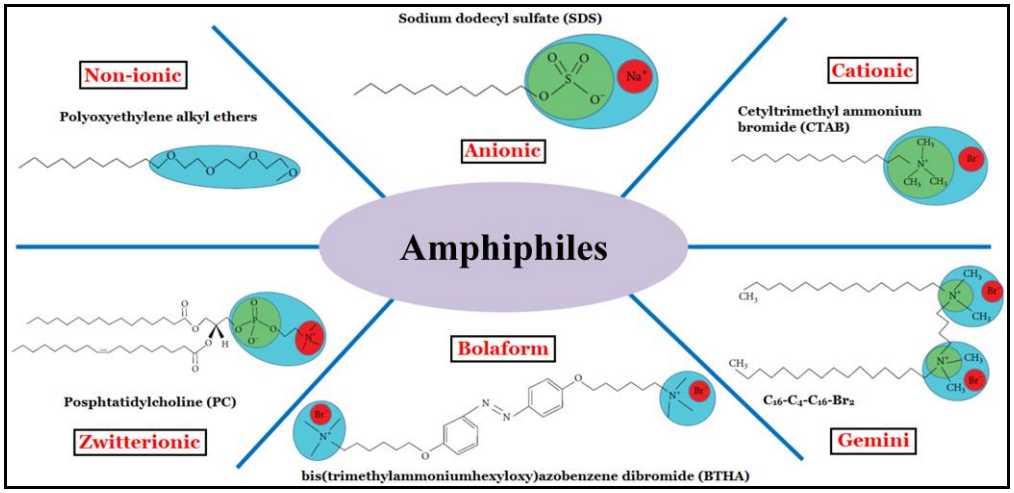

Figure 7. Classification and examples of amphiphiles. (Taken from Reference 20)

Amphiphiles' captivating self-assembly properties have garnered immense attention across scientific disciplines. In the realm of medicine, they serve as critical components in drug delivery, enabling the controlled release of therapeutic compounds.[20] In nanotechnology, amphiphiles inspire the creation of nanoscale structures with applications ranging from sensors to catalysis.[22,23] Furthermore, their role in the formation of cellular membranes highlights their significance in biology, influencing processes such as cell signaling and membrane transport.[23] Amphiphiles illuminate the appealing interplay between molecular forces and the natural world's propensity for organization. Their dual nature, harnessed through intricate self-assembly, has bestowed upon them the title of molecular architects, shaping both understanding of fundamental scientific principles and the boundaries of technological innovation.

UNLOCKING THE MAGIC OF NON-COVALENT INTERACTIONS: FOSTERING AMPHIPHILE ASSEMBLY

In the intricate realm of molecular interactions, where forces shape the fundamental behaviors of matter, non-covalent interactions stand as attractive orchestrators of assembly and arrangement. Amphiphile self-assembly is manifested by a range of non-covalent interactions that delicately balance hydrophilic and hydrophobic components. These include hydrogen bonding, van der Waals forces, electrostatic interactions, the hydrophobic effect, π-π interactions, ion-dipole interactions, and solvent effects (Figure 8).[24-29] While the assembly forces at play may be weak individually, their cumulative effect yields a sturdy cohesion among various amphiphiles.[20]

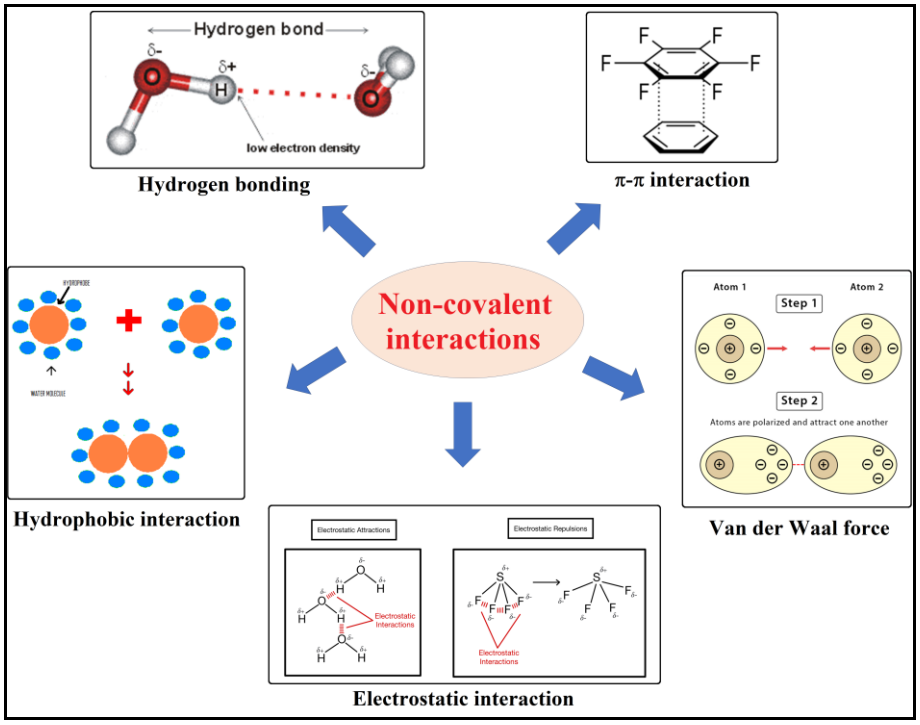

Figure 8. Different types of non-covalent interactions. (Taken from Reference 24-28)

This amalgamation of weak interactions offers both the resilience necessary for flexibility and the strength to withstand slight disruptions. Comparatively frail when juxtaposed with covalent bonds, these interactions stand in stark contrast to the robustness exhibited by metal-ligand interactions, a notable exception (Table 1).[20] Of these interactions, hydrogen bonding emerges as a linchpin in many biological processes within cells. It both forges and severs bonds among biomolecules, adapting to their exigencies. Virtually all biomolecules possess hydrogen bond acceptors and donors within their structures. Consider the case of water molecules (H_2O), where non-bonding electrons act as acceptors and hydrogen atoms as donors. Consequently, hydrogen bonding significantly shapes water's properties and its vital roles in biological systems.[30,31] Concurrently, the hydrophobic effect stands as another primary impetus behind self-assembly. This force unites nonpolar (hydrophobic) molecules, culminating in supramolecular self-aggregation.[32,33] Alongside hydrogen bonding, the van der Waals interaction exerts its influence-weak in nature and attenuating with distance.[34] It amalgamates London forces engendered by transient dipoles and Debye forces arising from dipoles and induced dipoles. An illustration lies within biological membranes, where closely packed hydrocarbon chains of phospholipids arise due to van der Waals interactions.[35]

Table 1. Strength of the primary noncovalent interaction driving amphiphile self-assembly.

Bonding and interaction type	Energy in (kJ/mol)
Covalent bond	100–400
Ion-ion/ion-dipole/dipole-dipole	200–300/50–200/5–50
Hydrogen bond	4-120
Cation-n(π) interaction	5-80
π-π interaction	0–50
Van der Waal's interaction	<5
Metal-ligand	0-400

The array of self-assembled nanostructures, ranging from micelles and reverse micelles to vesicles and supramolecular gels, embodies the outcomes of these subtle interactions.[38] Thus, the marriage of these forces, although individually feeble, orchestrates the intricate symphony of self-assembly.[39]

ASSORTED SELF-AGGREGATED SYSTEMS

The fabrication of nanoscale materials adorned with specialized functionalities tailored for precise applications has been revolutionized by the advent of supramolecular self-assemblies, particularly within the realm of the bottom-up approach.[40] From the perspective of a chemist, supramolecular aggregates represent intricately assembled forms of molecular constituents. Their chemical and physical pathways often guided by a combination of interaction observations and environmental contexts.[40] Mastering the geometry of these self-aggregates hinges on meticulous molecular design and solvent system adjustments. Molecular recognition comes into play through the incorporation of precise units into the amphiphilic framework, effectively fine-tuning it for specific tasks. These self-assembled structures, deftly constructed through non-covalent interactions, not only showcase the intrinsic beauty of molecular organization but also serve as a cornerstone for advancing fields spanning from nanotechnology to biomimetic engineering.[41-44]

MICELLES

Let's embark on an exploration of one of the most fundamental forms of self-assembly: micelles. Micelles, fascinating manifestations of self-assembly in the nanoscale realm, unveil a

profound interplay between molecular forces. Comprising amphiphilic molecules, these spherical entities arise when hydrophobic tails huddle at the core, ensconced away from the aqueous environment, while hydrophilic head groups flourish at the surface, harmonizing with water.[45]

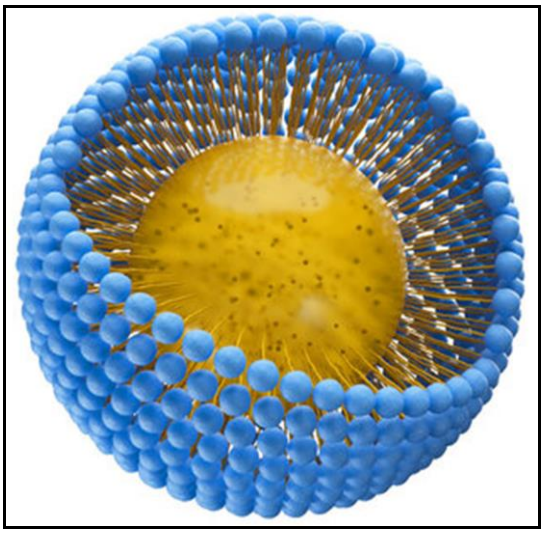

Figure 9. Structure of micelle. (Taken from reference 47)

This intriguing transformation occurs once a certain concentration threshold, termed the 'Critical Micellar Concentration' (CMC), is attained.[16,46] The CMC, a characteristic intrinsic to each surfactant, dictates the size and shape of the micelle, influenced by factors like temperature, pH, and ionic strength. Below the CMC, surfactants linger as solitary molecules enveloped by water, while above this threshold, they metamorphose into the micellar state, tucking their hydrophobic portions away from the aqueous milieu (Figure 9).[13,47] This intricate transition not only underpins their role as effective detergents but also transforms the micellar core into a vessel for multistep chemical reactions, providing an innovative platform for "green chemistry" practices.[48] As entities bridging molecular design and functional utility, micelles continue to inspire innovations at the intersection of chemistry, biology, and materials science.

REVERSE MICELLES

Navigating the realm of self-assembly, we encounter the intriguing concept of reverse micelles, a counterintuitive yet attractive phenomenon. Emerging in non-polar solvents instead of water, reverse micelles challenge our conventional notions.[30-32] Amphiphilic molecules, often with polar heads and hydrophobic tails, cluster together in these unique nanostructures. In this hydrophobic environment, the polar head groups huddle at the core, crafting a secluded

"water pocket" at their core, while the hydrophobic tails extend outward, forming a protective shield (Figure 10).[49-51]

Figure 10. Structure of reverse micelles. (Taken from Reference 51)

Parallels can be drawn between reverse micelles and biological membranes due to their adeptness at compartmentalization, lending them substantial utility in biomimetic applications.[52-54] This distinctive architecture finds applications in various fields, including nanotechnology and catalysis, where they act as nanoreactors, facilitating controlled chemical reactions within their hydrophilic cores. Reverse micelles serve as a remarkable evidence to the versatility of self-assembly, bending the rules to craft functional nano environments in unexpected settings.

VESICLES

Vesicles, intricate entities arising from the organization of amphiphilic molecules, capture the essence of self-assembly's creative prowess. These versatile structures, akin to microscopic bubbles, form bilayers with hydrophilic heads in the aqueous environment and hydrophobic tails secluded within (Figure 11).[50,55-57] This dual-layered arrangement engenders a unique interior space, offering a haven for encapsulating compounds of diverse polarities. Beyond their resemblance to cellular membranes, vesicles exhibit remarkable potential for drug delivery, allowing for the controlled release of therapeutic agents.[19,58-60] Their characteristics allows them to adapt to changes in their environment, making them valuable candidates for mimicking cellular functions and developing synthetic cell models. As a testament to the multifaceted interplay of non-covalent forces, vesicles stand as a canvas for scientific

exploration, providing insights into natural processes while paving the way for innovative applications across biomedicine and materials sciences.

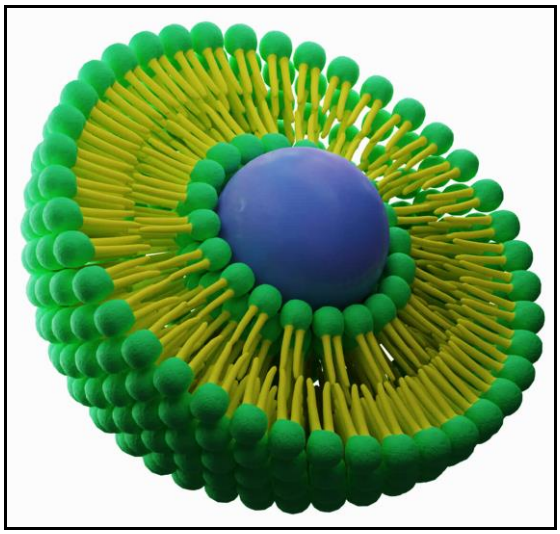

Figure 11. Structure of vesicle. (Taken from Reference 57)

SUPRAMOLECULAR GELS

Supramolecular gels illuminate the remarkable artistry of self-assembly, boasting a vast array of applications across interdisciplinary sciences (Figure 12).[61] By strategically arranging molecules with complementary shapes and charges, these gels form three-dimensional frameworks that encapsulate solvents, resulting in a gel-like consistency.[62-64] Within this enigmatic state, a sparse number of gelator molecules skillfully entrap a multitude of solvent molecules. This intermediate phase, perched between solubilization and crystallization, embraces both chemical cross-linking and physical interactions for gelation. This malleable architecture not only presents mechanical strength but also a remarkable responsiveness to external stimuli like temperature, pH, or light.[65] A self-assembled fibrillar network (SAFIN) materializes through the harmonious synergy of hydrogen bonding, π-π stacking, donor-acceptor interactions, metal chelation, van der Waals forces, and other subtle interactions.[66] Supramolecular gels, with their dynamic and adaptable nature, find applications in diverse fields, including drug delivery, tissue engineering, and sensors.[67-71] Low molecular weight gelators (LMWGs) gracefully cluster into three primary categories: hydrogelators, [72-75] which immobilize water; organogelators,[76-80] versed in organic solvent gelation; and ambidextrous gelators,[81-85] capably immobilizing both aqueous and organic solvents' gravitational flow. The

intricacy of these self-assembled networks evokes awe, offering fertile ground for innovation and application across various scientific horizons.

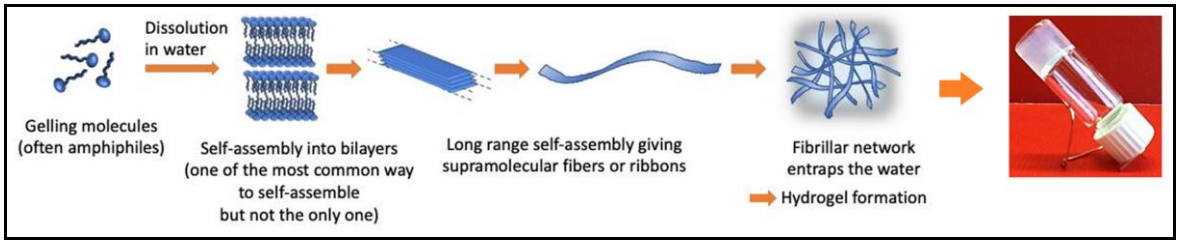

Figure 12. Schematic representation of the formation of self-assembled fibrillar network (SAFIN) and gel. (Taken from the Reference 61)

ORGANIC NANOPARTICLES

Organic nanoparticles represent a dynamic frontier in nanotechnology, showcasing the marvels of self-assembly at a miniature scale. Comprising small organic molecules or polymers (diameters ranging from 10 nm to 1 μm), these nanoparticles form through intricate interactions, including van der Waals forces, hydrogen bonding, and π-π stacking.[86-88] Their tunable properties and controllable size make them promising candidates for a plethora of applications spanning electronics, photonics, sensors, biotechnology, and more.[89-95] By manipulating the molecular structure and assembly conditions, organic nanoparticles can be tailored to exhibit specific functions, responding to environmental cues or encapsulating therapeutic agents.[91-95] Organic nanoparticles fall into two primary categories: nanospheres and nanocapsules (Figure 13).[90] Nanospheres represent matrix particles with solid interiors, while nanocapsules consist of a liquid or empty core enclosed by an organic solid shell. Although typically spherical, these entities can also assume non-spherical forms, highlighting their diverse nature and applications.

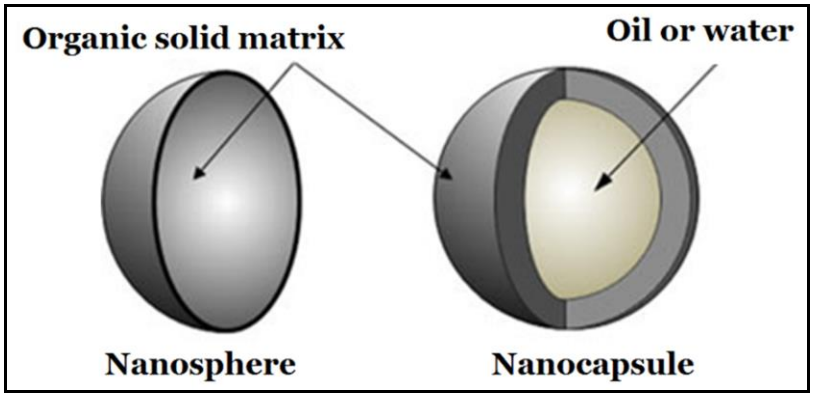

Figure 13. Structure of organic nanoparticles. (Taken from Reference 90)

ILLUMINATING ASSEMBLY: DECODING THE BIRTH OF FLUORESCENT ORGANIC NANOPARTICLES THROUGH AGGREGATION INDUCED EMISSION

"Together We Shine, United We Soar!"

. . . .[96]

From the inception of life, light has remained an indispensable force for survival. Luminophores serve as the bearers of light, and to fathom the intricacies of this phenomenon, numerous groundbreaking innovations in light-emitting processes have transpired. Traditional explorations of organic luminescence have primarily unfolded in solution states, treating luminophoric molecules as isolated entities that remain largely unaffected by chromophoric interactions.[97-100] However, a challenge emerges when examining emission properties at elevated concentrations, leading to what is termed the "concentration quenching" phenomenon.[101,102] This reduction in fluorescence is attributed to the formation of aggregates, a phenomenon aptly known as "Aggregation-Caused Quenching" (ACQ) (Figure 14).[101-105] Remarkably, many conventional fluorophores comprise multiple planar aromatic rings, fostering potent π-π interactions that ultimately quench emission. Traditional fluorophores often suffer from the "Kasha's rule," where nonradiative decay processes dominate upon aggregation, resulting in reduced fluorescence.[106,107] Regrettably, the ACQ effect has generally been perceived as detrimental in terms of real-world applications.

In response to the limitations posed by conventional fluorophores afflicted by ACQ, numerous endeavors were undertaken to surmount these challenges. In the year 2001, an intriguing concept was first introduced by Tang and co-workers in their study of silole derivatives.[108] They discovered that these molecules exhibited weak fluorescence when dissolved in solvents, but their luminescence dramatically increased upon aggregation in the solid state or in concentrated solutions. This phenomenon was coined "Aggregation Induced Emission (AIE)," challenging the conventional wisdom (ACQ) and showcasing a counterintuitive behavior where certain molecules exhibit enhanced luminescence as they aggregate.[96,101,105,109] Subsequent to these initial discoveries, extensive refinements in molecular

design have been embraced to harness efficient AIE during self-assembly.[110,111] Coined as Fluorescent Organic Nanoparticles (FONPs), these aggregates marked a significant advancement.[112-115] The design involved non-planar or propeller-shaped π-conjugated molecules adept at evading robust π-π interactions in their assembled state.[116]

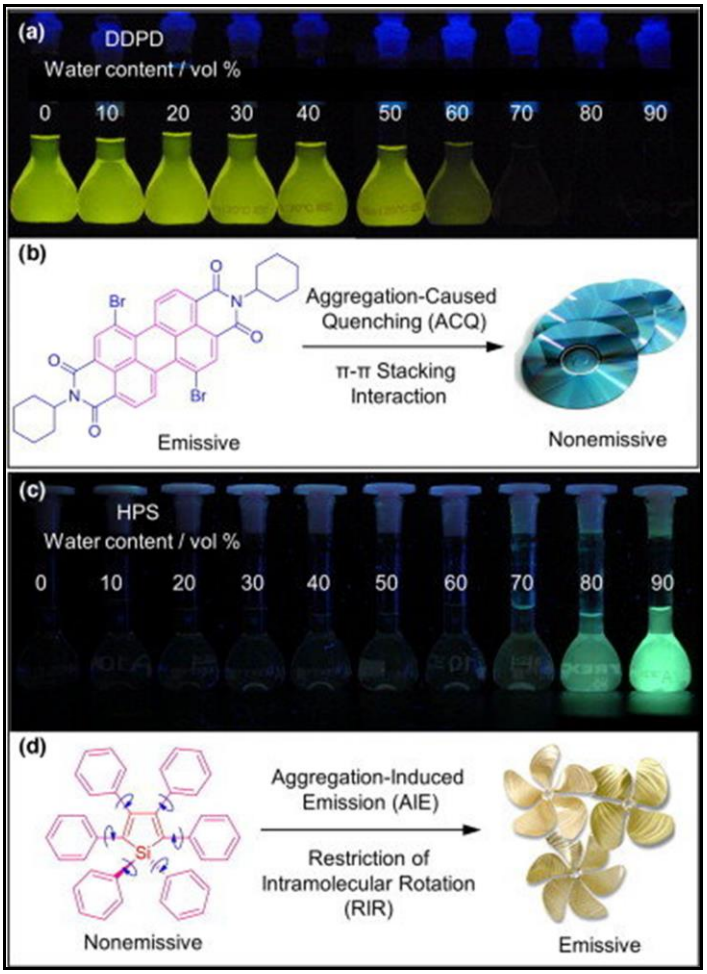

Figure 14. Examples of aggregation-caused quenching and aggregation-induced emission. (Taken from Reference 103)

This strategic maneuver curtailed intramolecular rotation, thereby minimizing non-radiative pathways and amplifying emission intensity during self-assembly (Figure 15).[101,117] Moreover, pre-associated excimer formation, *J*-aggregation, E-Z isomerization, twisted intramolecular charge transfer (TICT), and excited-state intramolecular proton transfer (ESIPT) collectively govern the emergence of AIE, countering the effects of ACQ.[96,109,117-119] In contemporary times, the significance of FONPs has surged remarkably due to their facile synthesis, biodegradability, cytocompatibility, and non-toxic nature. This has propelled their

application in optoelectronic device development, chemical and biosensors, and biological probes.[120-125] A diverse array of AIE dyes, such as tetraphenylethene, siloles, cyano-substituted diarylethene, triphenylethene, distyrylanthracene, naphthalene diimide, and naphthalimide derivatives, have been synthesized and harnessed to construct AIE-based FONPs, fostering diverse applications in the aforesaid domains.[126-134]

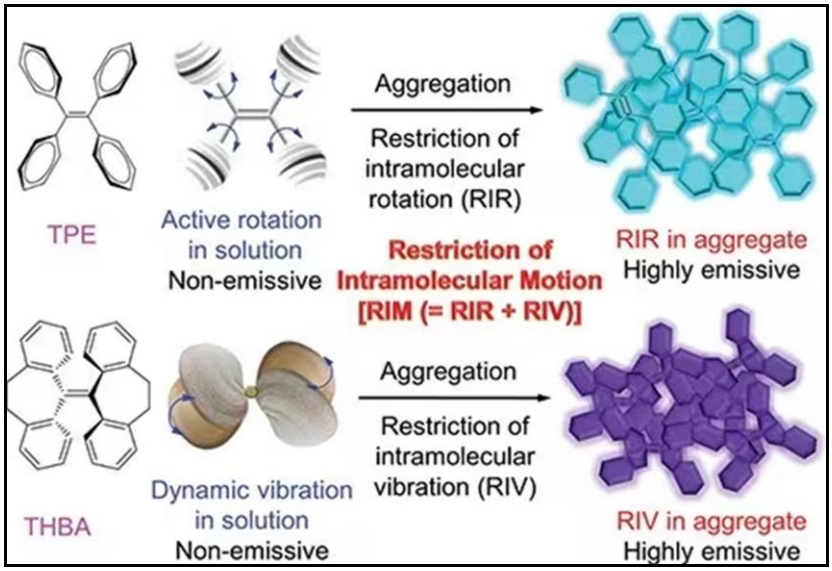

Figure 15. Schematic representation of both ACQ and AIE. (Taken from Reference 101)

ENGINEERING FLUORESCENT ORGANIC NANOPARTICLES: CRAFTING LUMINESCENT NANOSTRUCTURES

Organic nanoparticles' features are tailored based on their constituent building blocks, strategically optimized for specific application requirements. This drives the development of various synthesis strategies. Two primary approaches are employed in organic nanoparticle generation: "bottom-up" and "top-down."[90,135,136] The bottom-up method involves assembling distinct organic molecules into nanoparticles, often through self-assembly, enabling precise functionalization.[135] Conversely, top-down techniques involve reducing bulk materials to nano size via grinding or milling, yet these methods have drawbacks like high energy usage, costly equipment, and contamination risks.[136,138] The selection of organic nanoparticle types hinges on synthesis methods, including self-assembly, polymerization, emulsion techniques, nanoprecipitation, and more.[90,137] Factors like method choice, amphiphilicity of building blocks, and encapsulation matrix molecular weight influence particle size.

SELF-ASSEMBLY METHOD

Self-assembly is a practical method for generating organic nanoparticles, involving the accumulation of amphiphilic block copolymers, host-guest complexes, or small amphiphilic molecules.[90,137] These weak interactions make the nanoparticles responsive to external stimuli, useful in temperature or pH-sensitive systems. Assembly mechanisms include coordination, thin film hydration, and templates.[137] Mixing these polymers and organic emitters in a solvent, then rapidly introducing a poor solvent, aggregates hydrophobic parts around emitters, while hydrophilic chains stabilize the outer surface. Alternatively, emitter conjugation with polymer hydrophobic chains creates FONPs, embedding emitters in the self-assembled matrix (Figure 16).[137] Targeting moieties can be added for diverse biological functions.

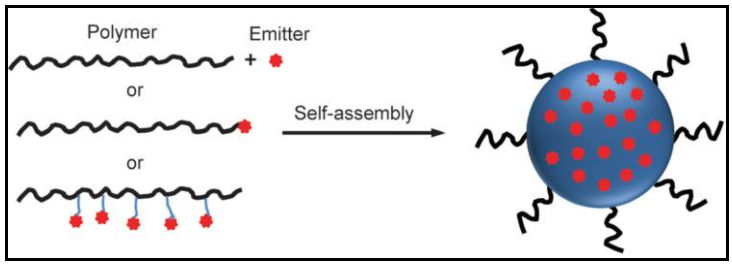

Figure 16. Schematic illustration of polymer-encapsulated organic nanoparticle preparation from self-assembly. (Taken from Reference 137)

POLYMERIZATION METHOD

In a conventional polymerization process, an organic solvent containing monomers and organic emitters is evenly dispersed as small, stable oil droplets within an aqueous solution, facilitated by an emulsifier and ultrasonication. Polymerization of the monomers within these oil droplets begins upon introducing initiators into the emulsion, resulting in the formation of dispersed organic nanoparticle suspensions. As solvent continues to evaporate, finely dispersed polymeric nanoparticles are obtained (Figure 17)[137]. Notably, the emitters employed can be either reactive or non-reactive towards the monomers throughout the polymerization process.

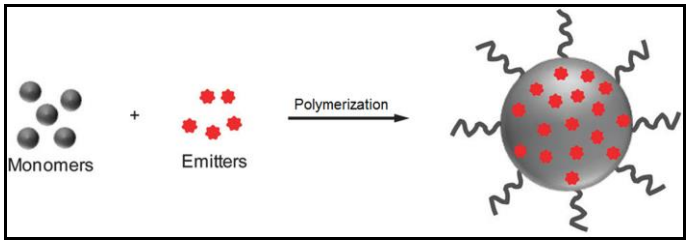

Figure 17. Schematic illustration of polymer-encapsulated organic nanoparticle preparation from *in situ* polymerization. (Taken from Reference 137)

EMULSION METHOD

Emulsification provides a cost-effective method for creating ONPs, eliminating the need for expensive equipment. In the emulsion process, emitters and the polymer matrix are dissolved in an organic solvent, forming a uniform solution.[90] This organic solvent (e.g., dichloromethane) does not mix with water. Upon introducing the solvent into an aqueous solution containing emulsifiers and subjecting it to ultrasonication or vigorous stirring, emulsifiers stabilize small organic droplets, forming a homogeneous 'oil-in-water' emulsion.

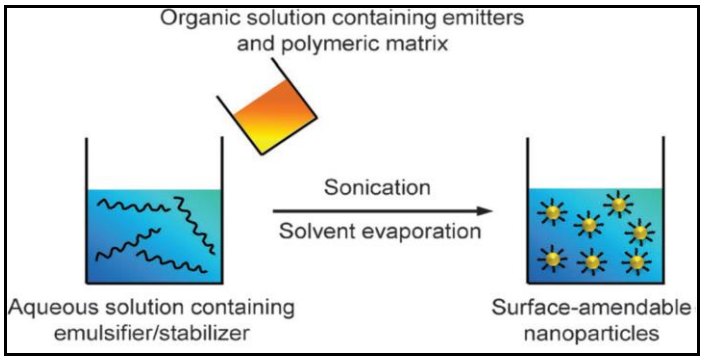

Figure 18. Schematic illustration of polymer-encapsulated organic nanoparticle preparation from emulsion. (Taken from Reference 137)

After solvent evaporation, a stable suspension of polymer-encapsulated nanoparticles in water is achieved (Figure 18)[88,90,137]. Emulsions are categorized into three types based on droplet sizes: macroemulsion, miniemulsion, and microemulsion. Macroemulsion yields ONPs larger than 1 μm, while mini and microemulsions create nanoparticles under 500 nm in size. The surface of these nanoparticles can be further functionalized for specific applications.

NANOPRECIPITATION METHOD

Nanoprecipitation and emulsion techniques diverge in their choice of organic solvents for nanoparticle creation. Unlike emulsion, nanoprecipitation necessitates an organic solvent that is miscible with water, without the inclusion of an emulsifier in the aqueous component. In a standard nanoprecipitation procedure, an organic solvent solution containing emitters and the encapsulation matrix (e.g., THF) swiftly combines with an excess of water while undergoing ultrasonication.[90,137] This rapid interaction reduces the solvent's hydrophobicity, prompting emitters and the hydrophobic portions of the encapsulation matrix to aggregate into nanoparticles. The hydrophilic segments of the polymeric matrix align within the aqueous phase, enabling subsequent functionalization (Figure 19).[137]

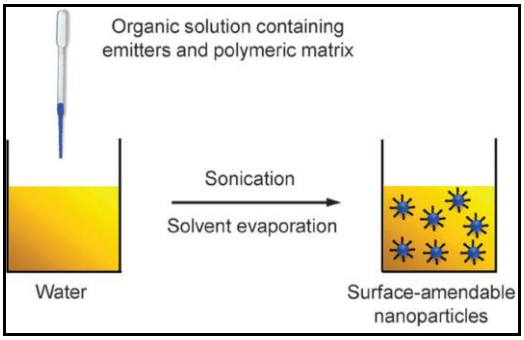

Figure 19. Schematic illustration of polymer-encapsulated organic nanoparticle preparation from nanoprecipitation. (Taken from Reference 137)

REPRECIPITATION METHOD

The conventional reprecipitation technique involves dissolving a target compound (typically within the mM concentration range) in an organic solvent (like THF, DMF, DMSO, acetone, or alcohol) (Figure 20).[137,139,140] Subsequently, a small volume of this diluted solution is rapidly introduced into a vigorously stirred poor solvent (typically water) at a constant temperature, using a microsyringe. These organic solvents can be mixed with water in various ratios. This process triggers the reprecipitation and nano crystallization of the target compound within the poor solvent, resulting in the dispersion of π-conjugated organic nanocrystals within medium.

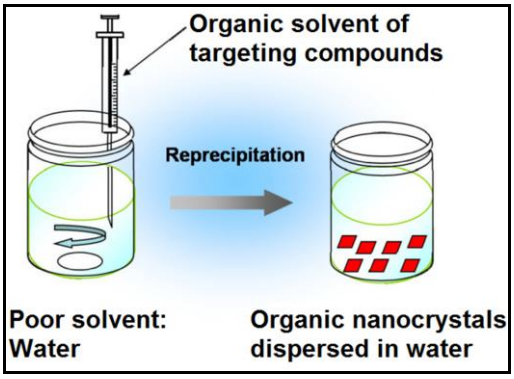

Figure 20. Schematic illustration of polymer-encapsulated organic nanoparticle preparation from reprecipitation. (Taken from Reference 137)

PARTICLE REPLICATION IN NONWETTING TEMPLATES (PRINT)

In 2005, DeSimone's team introduced PRINT technology, a "top-down" method crafting precise microparticles and nanoparticles (20 nm-100 μm) (Figure 21).[137] Using nonwetting PFPE-based elastomer, this soft lithography technique enables size, geometry, and composition control. PRINT has evolved as a versatile tool for diverse nanoparticle production, like PEG

hydrogels, PLGA, and biologics. PRINT-made nanoparticles efficiently load chemotherapeutics, siRNA, proteins, and contrast agents with notable capacities. Surface attributes of PRINT particles can be adjusted for enhanced tumor accumulation or prolonged circulation.

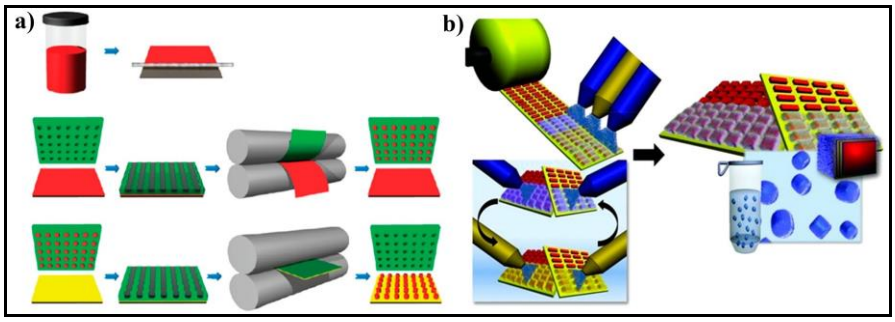

Figure 21. Schematic illustration of (a) the preparation of organic nanoparticles from PRINT method and (b) The spray-LbL on PRINT nanoparticles. (Taken from Reference 137)

LAYER-BY-LAYER (LBL) ASSEMBLY

Layer-by-Layer (LbL) assembly stands as a versatile and universally applicable method to create multifunctional nanoparticles, involving the coating of nanoparticle cores with polymers, biomolecules, colloids, and more (Figure 22).[137] The assembly process harnesses diverse interaction forces, including electrostatic interactions, biological recognition, hydrogen bonding, and host-guest interactions. Through this technique, different layers can be meticulously stacked, each contributing distinct functionalities, such as stimuli-responsiveness, targeting capabilities, and prolonged systemic circulation times. LbL assembly's adaptability renders it a tailored solution to address a spectrum of biomedical applications, seamlessly integrating multiple functions within a single nanoarchitecture.[90,137]

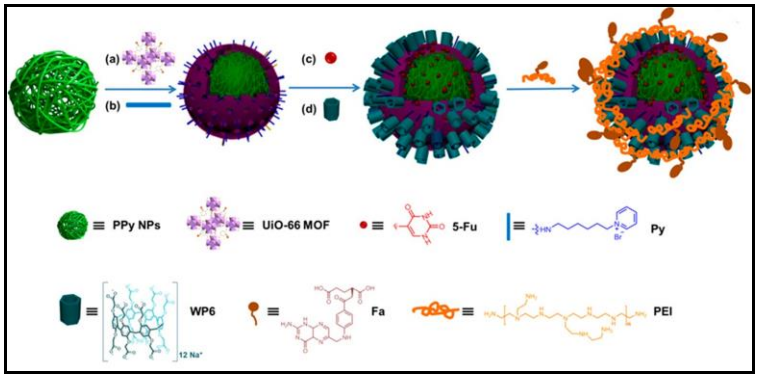

Figure 22. Schematic illustration of the preparation of organic nanoparticles from layer-by-layer assembly. (Taken from Reference 137)

ELECTROSPRAYING

Electrospraying is a versatile and cost-effective approach for crafting relatively small organic nanoparticles, encompassing various techniques like single-needle electrospraying, coaxial electrospraying, multiaxial electrospraying, and both single and multiplexed electrospray methods (Figure 23).[137] This method operates on the principle of expelling material solution from a syringe as nanoparticles under the influence of high voltage. These resulting organic nanoparticles are often employed as carriers for controlled delivery of drugs, proteins, vitamins, and growth factors, exhibiting precise encapsulation, controlled morphology, and dependable reproducibility. Co-electrospraying and coaxial electrospraying stand out as potent techniques for generating nanoparticles loaded with drugs.[137]

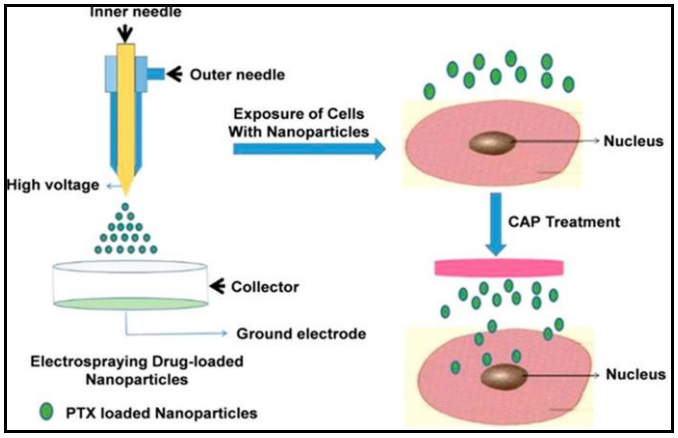

Figure 23. Schematic illustration of the preparation of organic nanoparticles from electronspraying method. (Taken from Reference 137)

MICROFLUIDICS

Microfluidic technology (Figure 24) has rapidly evolved since the early 1980s, offering precise handling of fluids, including single-phase and multi-phase substances, within microchannels of small volumes (microliters to picoliters).[137] Viscous forces predominantly affect flow in microchannels, while their larger surface area enables rapid and uniform heat and mass transfer. Microfluidic devices are constructed from materials like glass, silicon, polydimethylsiloxane (PDMS), and paper.[137] These systems can be categorized as single-phase flow, multiphase flow (gas-liquid and liquid-liquid), and integrated microfluidic systems.

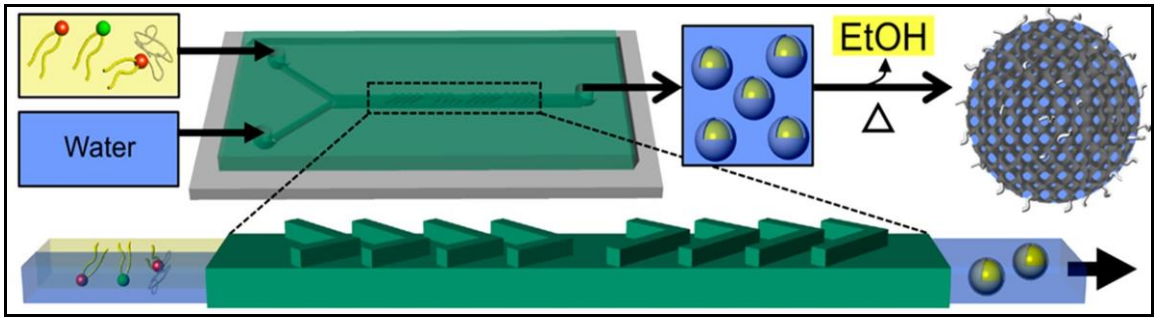

Figure 24. Schematic illustration of the preparation of organic nanoparticles from microfluidics method. (Taken from Reference 137)

SUPERCRITICAL DRYING

Supercritical Drying involves two procedures for nanoparticle production using supercritical fluid: one utilizes rapid expansion of a supercritical solution into ambient air, resulting in well-dispersed particles due to high supersaturation and quick pressure reduction, often employing CO_2; the other involves expansion into a liquid solvent, preventing primary nanoparticles from growing in the jet due to solvent presence (Figure 25).[140,141] An example employs water as a solvent for supercritical expansion, producing (PHDFDA) particles.

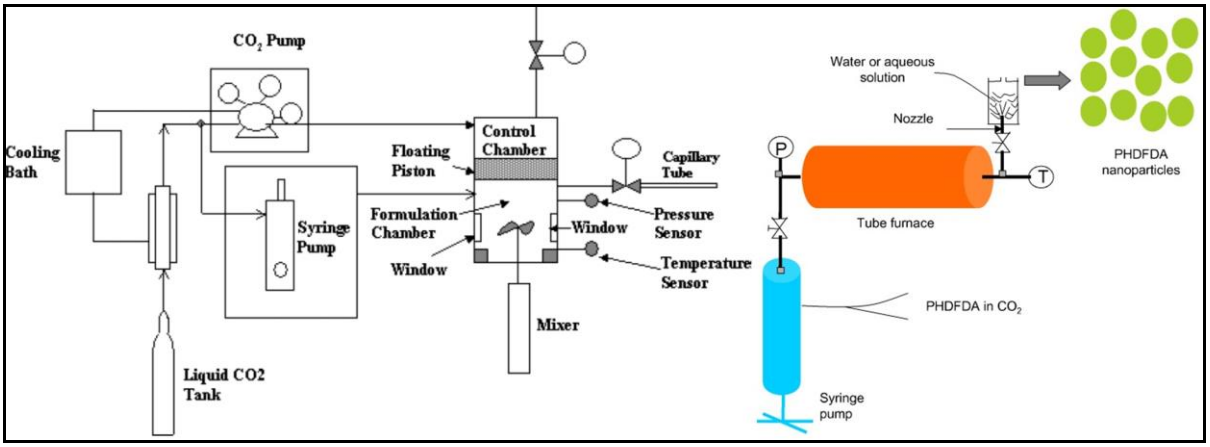

Figure 25. Schematic illustration of the preparation of organic nanoparticles from supercritical drying method (REES). (Taken from Reference 140, 141)

SPRAY DRYING

Spray-drying process has been used in the past few years for the production of microsized organic particles or to convert nanoparticle suspensions in dry powder mainly for biomedical and pharmaceutical applications especially in drug delivery. A typical spray-drying process consists in the atomization of a liquid into a spray of fine droplets brought

subsequently in contact with a hot drying gas to evaporate the moisture and to form the solid product which is finally recovered via generally a cyclone unit (Figure 26).[142]

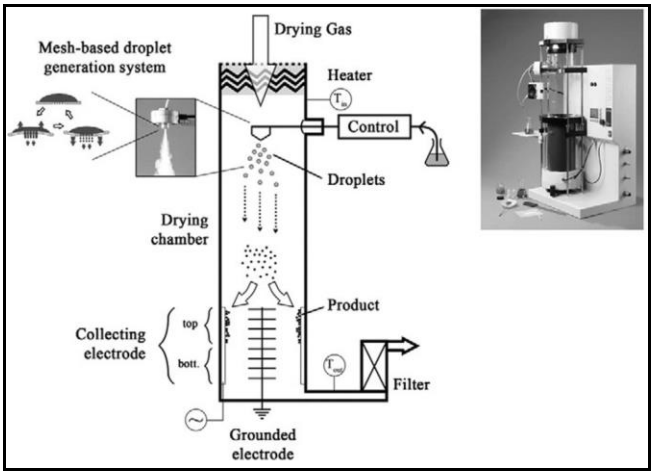

Figure 26. Schematic illustration of the preparation of organic nanoparticles from spray drying method. (Taken from Reference 142)

EXPLORING THE ROLE OF ORGANIC NANOPARTICLES IN CELL BIOLOGY: APPLICATIONS AND INSIGHTS

HARNESSING ORGANIC NANOPARTICLES FOR BIOSENSING AND BIOIMAGING

Organic nanoparticles, specifically "Fluorescent Organic Nanoparticles (FONPs)", derived from small molecules hold immense potential in sensing biomolecules and biohazardous agents.[112-115] FONP-based probes offer distinct advantages over traditional fluorophores, thanks to their structural flexibility, straightforward synthesis, favorable water solubility, cytocompatibility, and high photostability. Notably, their aggregation-induced emission circumvents concentration quenching, eliminating the need for organic solvents (unlike conventional fluorophores) to exhibit sensing capabilities.[120-124,143] Unlike many organic dyes that experience photobleaching within cells at low concentrations, FONPs resist this issue. Moreover, intracellular dyes often diffuse back into the extracellular medium due to concentration gradients during cell division, leading to diminished emission and unspecific staining in cell co-culture systems. Consequently, FONPs have gained prominence, particularly in biological labeling as marker (Figure 27) and the extended in vivo monitoring of tumor growth.[144-148] This transformative technology promises breakthroughs in sensitive and specific biosensing, illuminating cellular intricacies and advancing diagnostics and drug development.

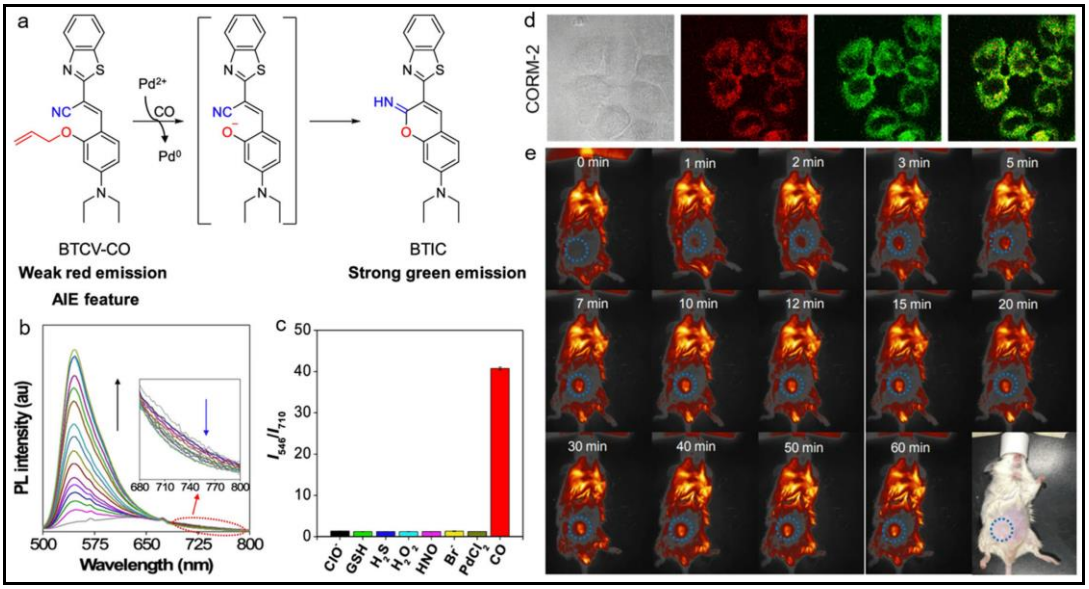

Figure 27. AIE based probe for CO detection and *in-vivo* fluorescence imaging. (Taken from Reference 146)

FONP: SHAPING THE LANDSCAPE OF DELIVERY VEHICLES FOR THERAPEUTICS

The realm of research aimed at pioneering drug-delivery systems, capable of simultaneously enhancing drug bioavailability and efficacy while mitigating toxicity, has experienced a pronounced resurgence. In the quest for cutting-edge delivery modalities, achieving specific cargo delivery with minimal side effects, intelligent drug release for maximal impact, and other ambitious objectives remains a challenge. Additionally, these drug delivery systems are required to exhibit prolonged circulation times, heightened permeability, and resilience against metabolic pre-systemic degradation. AIE based FONPs have emerged as promising and versatile delivery vectors, offering a sophisticated platform for transporting a wide array of therapeutic agents (Figure 28).[125,149-156] Leveraging their unique attributes, including tunable surface functionalization, biocompatibility, and controllable size, AIE-gens enable precise encapsulation and controlled release of drugs, nucleic acids, and other bioactive molecules. Their fluorescence properties facilitate real-time tracking and imaging, enhancing the understanding of drug distribution and cellular interactions. [149-156] With the potential to bypass biological barriers, target specific tissues, and respond to external stimuli, FONPs hold considerable potential for revolutionizing targeted drug delivery and advancing personalized medicine strategies.

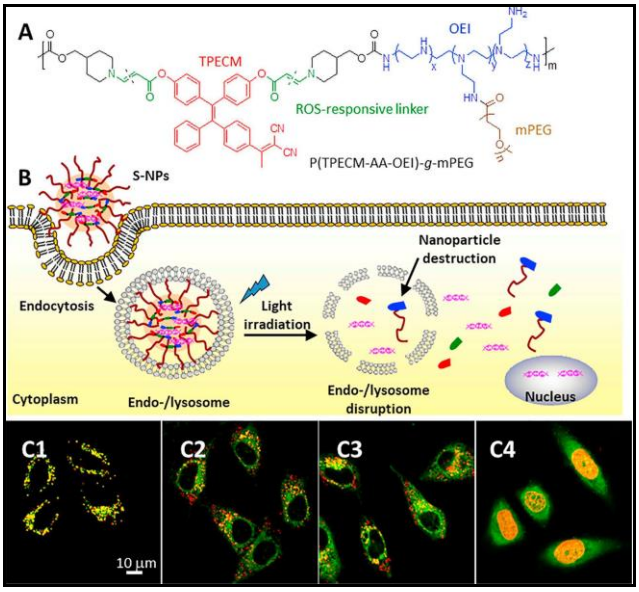

Figure 28. AIE-gen as a photoactive polymeric gene delivery vector. (Taken from reference 152)

EXPLORING THE FRONTIER: NANOSCIENCE AND NANOTECHNOLOGY UNVEILED

Nanoscience and nanotechnology encompass a frontier of scientific exploration that delves into the extraordinary world of matter at the nanoscale, where dimensions reach as small as one billionth of a meter (10^{-9} meter). At the heart of nature's architecture lie atoms and molecules, dwelling within the nanometer realm-the nanoscale. These molecular constituents, possessing nanoscale dimensions, orchestrate intricate assemblies through self-organization, dictating pivotal material attributes like optical, electrical, and mechanical traits. This orchestration echoes nature's adeptness in forging the complex molecular machinery that sustains life. In essence, mastery over structures at ~1-100 nm scale holds the key to engineering novel materials with tailored properties. Nanoscience, by probing and understanding phenomena within this scale, unveils insights into the fundamental building blocks of nature. Nanotechnology, on the other hand, harnesses this knowledge to engineer, manipulate, and fabricate structures and systems at the nanoscale, birthing transformative applications across diverse fields such as materials science, electronics, medicine, and energy (Figure 29).[157] This interdisciplinary realm of discovery continues to unlock unprecedented opportunities, offering the potential to revolutionize industries, reshape technologies, and advance our understanding of the very fabric of the universe.[157-160]

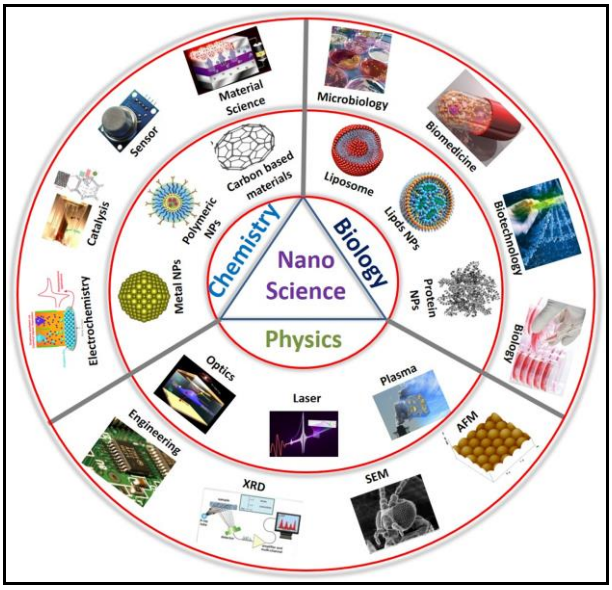

Figure 29. Nanoscience and nanotechnology: unveiling the microscopic marvels. (Taken from reference 157)

CARBON DOTS: A BRIGHT FUTURE IN NANOMATERIAL SCIENCE

Carbon dots, a fascinating class of carbon-based nanomaterials, have garnered significant attention for their unique properties and versatile applications. These nanoscale structures, often less than 10 nanometers in size, are composed of carbon atoms arranged in various configurations, resulting in intriguing optical, electronic, and surface properties. Carbon dots exhibit exceptional photoluminescence that can be tuned by controlling their size, surface chemistry, and synthesis methods.[161-164] This tunable fluorescence, coupled with their biocompatibility and low toxicity, makes carbon dots promising candidates in diverse fields such as bioimaging, sensing, cargo delivery, and optoelectronics.[165-168] In contrast to toxic heavy-metal-based quantum dots such as CdS, CdSe, and PbSe, which often grapple with cytotoxicity and poor aqueous stability, fluorescent CDs emerge as spherical light-emitting nanoparticles of choice (Figure 30). Their ease of functionalization and compatibility with various matrices further enhance their utility in designing advanced nanomaterials for cutting-edge applications. As research into carbon dots continues to evolve, their potential to revolutionize technology and impact multiple industries remains an exciting and rapidly expanding area of exploration.

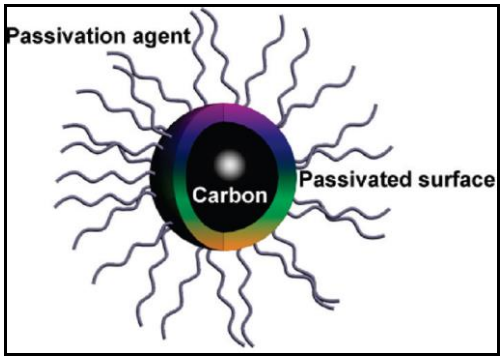

Figure 30. Schematic representation of a carbon dot structure.

NANOSCIENCE MEETS SOFT MATTER: EXPLORING SYNERGISTIC SOFT-NANOCONJUGATES

Self-assembled systems and nanomaterials have converged to spark the intriguing inquiry: Can their amalgamation yield a superior hybrid material? Chemists sought to unlock this possibility, often blending these materials with others to create composites with enhanced attributes. The quest for such hybrids led to the synthesis of nanoparticles in situ or the incorporation of nanomaterials into self-assembled systems.[29] These hybrid entities, arising from the strategic integration of nanoscale components with soft matter matrices, offer a dynamic platform for designing advanced materials with tailored functionalities.[169-172] By harmonizing the unique attributes of both realms, soft-nanoconjugates combine the flexibility, adaptability, and biocompatibility inherent to soft materials with the precision, tunability, and enhanced properties offered by nanomaterials. This synergy opens avenues for innovation across fields such as drug delivery, tissue engineering, sensing, and catalysis.[169-175] Soft-nanoconjugates hold the promise of revolutionizing our ability to engineer multifunctional materials that address complex challenges, paving the way for transformative breakthroughs in various scientific and technological domains (Figure 31).[173-175]

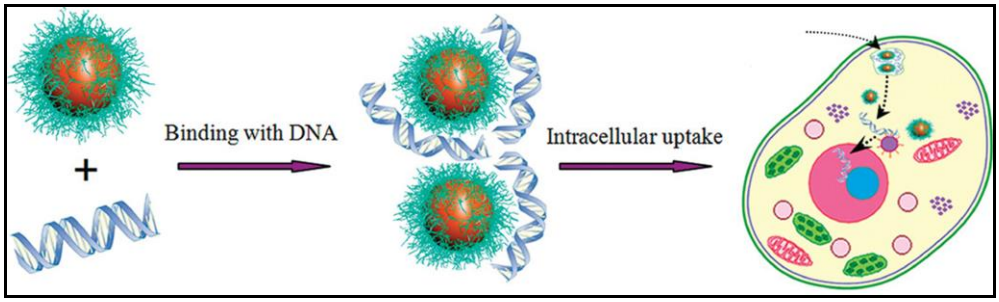

Figure 31. Schematic illustration of positively charged polypeptide-conjugated AuNPs binding with DNA for intercellular delivery. (Taken from reference 174)

The nanoconjugate between carbon dots (CDs) and fluorescent organic nanoparticles (FONPs) represents a fascinating hybrid entity at the nexus of nanotechnology and fluorescence. This innovative amalgamation harnesses the unique optical properties and tunable fluorescence of both CDs and FONPs, offering a versatile platform for advanced applications in biomedicine, sensing, and imaging. The integration of CDs and FONPs into a single nanoconjugate holds the potential to synergistically enhance signal brightness, resistance to photobleaching, and multiplexed fluorescence emissions, enabling cutting-edge advancements in biomarker development, cellular imaging, and diagnostic technologies. This collaborative alliance between CDs and FONPs promises to unveil new frontiers in nanomaterial design and functional versatility.

SOFT-NANOCONJUGATE IN CANCER THERANOSTIC

The application of soft-nanoconjugates in cancer theranostics showcases a remarkable synergy between soft materials and nanotechnology. Carbon dot-organic nanoparticle nanoconjugates represent a compelling frontier in cancer theranostics, unifying the distinct attributes of carbon dots and organic nanoparticles for multifaceted advancements. Leveraging carbon dots' remarkable optical properties and organic nanoparticles' therapeutic potential, these nanoconjugates exemplify a promising paradigm shift towards more efficient and targeted approaches in oncology. The synergistic integration of these two components enables targeted drug delivery, real-time imaging of treatment responses, and the potential for combining multiple therapeutic strategies. Moreover, for enhanced cancer treatment outcomes, combination therapy embodies a cutting-edge approach that capitalizes on the synergy between soft materials and nanotechnology. By ingeniously integrating multiple therapeutic modalities into a single platform, these innovative hybrids offer a potent arsenal against cancer cells. This convergence of capabilities holds the promise of enhanced cancer diagnosis, treatment monitoring, and therapy, positioning CDs-FONPs nanoconjugates as a promising avenue towards more effective and personalized cancer theranostics.

To this end the present thesis highlights the design and development of smart AIE based fluorescent organic nanomaterials (FONPs) for sensing, bioimaging and therapeutic applications and also fabrication of ONP-CD nanoconjugate and its application in cancer theranostics.

PRESENT THESIS

FABRICATION OF ORANGE EMITTING ORGANIC NANOPARTICLE-PROTAMINE CONJUGATE: FLUOROMETRIC SENSOR OF HEPARIN

Fluorescent bioprobes, such as fluorescent inorganic nanoparticles (FINs) and organic dyes, have been extensively studied for sensing applications. However, FINs can be hazardous due to non-biodegradability and presence of heavy metals, while organic dyes suffer from aggregation-caused quenching (ACQ). Fluorescent organic nanoparticles (FONPs) with aggregation-induced emission (AIE) properties are emerging as a safer alternative. These FONPs are easily synthesized and exhibit non-toxic, biodegradable characteristics. Self-assembled π-conjugated molecules can form task-specific FONPs with tunable AIE behavior, making them useful for smart sensors. Heparin, a polysaccharide used as an anticoagulant, requires precise quantification. Fluorometric assays are favored for their simplicity and sensitivity, but many probes lack binding affinity for heparin. To address this, biomolecules like protamine can be incorporated to enhance binding affinity. However, there's limited research on protamine-doped biosensors, particularly using FONPs, to exploit the AIE phenomenon for heparin detection.

To this end in Chapter 1, I developed a novel naphthalene diimide (NDI) based fluorescent organic nanoparticle (FONP). The NDI-**1** amphiphiles, incorporating 3-amino pyridine tags, self-assembled into organic nanoparticles in a DMSO-water solvent mixture. These NDI-**1** FONPs exhibited an aggregation-induced emission (AIE) at 594 nm, exhibiting an orange light due to a combination of excimer formation and intramolecular charge transfer (ICT). The NDI-**1** FONPs carried a negative surface charge, facilitated by the amino pyridine residues at both terminals, enabling interaction with positively charged protamine to form the FONP-Pro conjugate. Therefore, NDI-**1** FONP was non-covalently combined with protamine, resulting in a FONP-Pro conjugate designed for heparin detection (Figure 32). Upon the addition of protamine, the fluorescence intensity of the FONPs got quenched. Notably, introducing heparin to the FONP-Pro conjugate led to the restoration of fluorescence signal (Figure 32). This restoration was attributed to the detachment of protamine from the FONP surface, driven by the strong binding affinity between heparin and protamine. Consequently, the presence of heparin could be easily detected by observing the fluorescence quenching (off) and subsequent restoration (on) of the NDI-**1** FONP, achieving a limit of detection (LOD) of 12 nM.

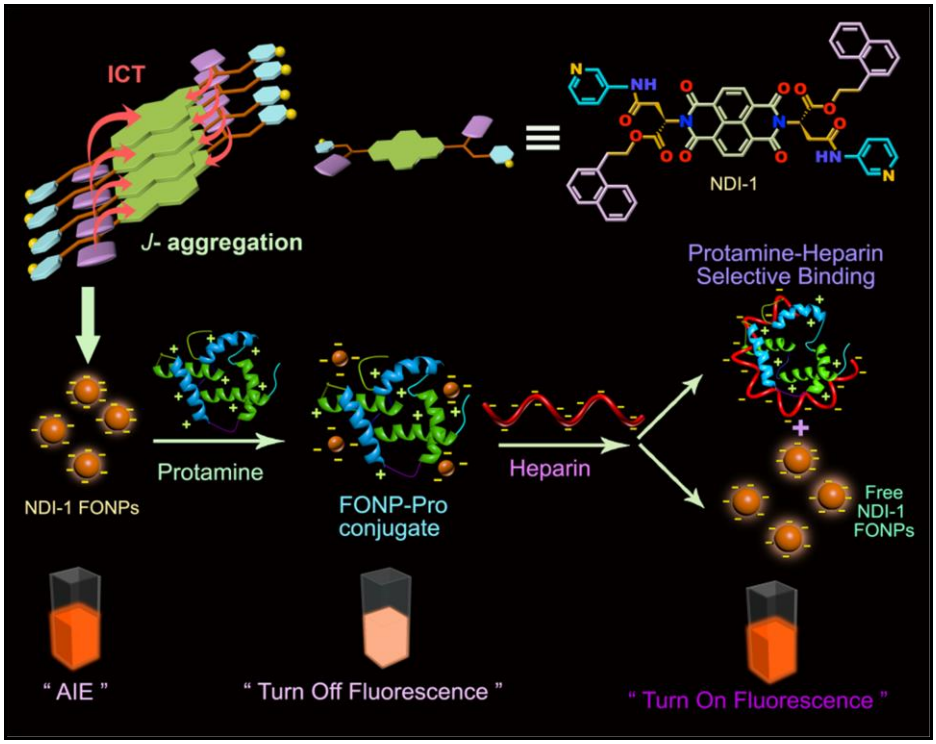

Figure 32. Schematic representation of heparin sensing by quenching and restoration of AIE of NDI-1 FONPs through formation of FONP-protamine conjugate. AIE: aggregation-induced emission, ICT: intramolecular charge transfer.

NIPECOTIC ACID TETHERED NAPHTHALENE DIIMIDE BASED ORANGE EMITTING ORGANIC NANOPARTICLES AS TARGETED DELIVERY VEHICLE AND DIAGNOSTIC PROBE TOWARDS GABA$_A$ RECEPTOR ENRICHED CANCER CELLS

Luminescent nanoparticles are valued for sensing and imaging, yet toxicity concerns remain. Fluorescent organic nanoparticles (FONPs) overcome limitations of traditional fluorescent materials, such as toxicity and aggregation-caused quenching (ACQ). FONPs, with aggregation-induced emission (AIE), offer safe and sensitive diagnostic potential, derived from π-conjugated molecules with target-specific motifs. In neuroscience, the GABA$_A$R is vital for inhibitory neurotransmission and its dysfunction leads to neurological disorders. Existing GABA detection methods lack resolution, sensitivity, and spatiotemporal capabilities. FONPs offer promise for bio-imaging and intracellular cargo transport, prompting the need for target-specific fluorescent diagnostic probes. Nipecotic acid, chosen for FONP design, inhibits [^{3}H]GABA uptake and is enhanced with a lipophilic anchor for blood-brain barrier penetration, facilitating GABA$_A$R-related studies.

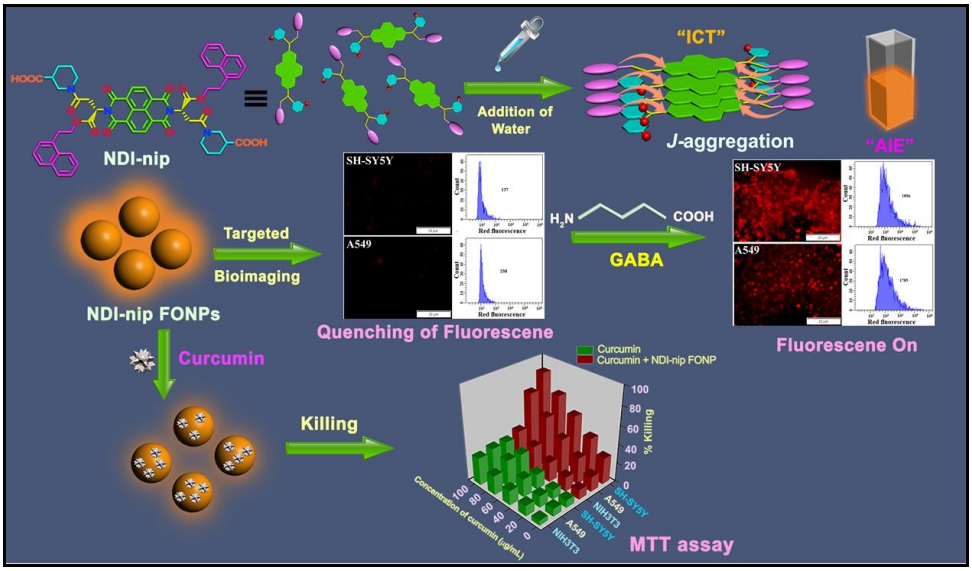

Figure 33. Schematic representation of fabrication of **NDI-nip** FONPs as the targeted diagnostic probe and delivery vehicle towards $GABA_AR$ enriched cancer cells. AIE: aggregation-induced emission, ICT: intramolecular charge transfer.

The newly developed amphiphilic molecule, **NDI-nip** (Figure 33), self-aggregated in a DMSO-water (f_w = 99 vol%) solvent mixture, exhibiting aggregation-induced emission (AIE) at 579 nm (orange emission). The luminescence of **NDI-nip** FONPs was exploited for bioimaging and targeted delivery of anticancer drug for selective neuroblastoma cell (SH-SY5Y) and cancer cell (A549) killing. **NDI-nip** FONP fluorescence diminished in $GABA_AR$-enriched cell lines (SH-SY5Y and A549), but presence of GABA prevented the emission quenching (Figure 33). Curcumin-loaded **NDI-nip** FONPs effectively targeted and killed $GABA_AR$-enriched cells (SH-SY5Y and A549) while sparing normal cells (NIH3T3).

NAPHTHALIMIDE BASED AIEGENS FOR SENSING PROTEIN DISULFIDE ISOMERASE THROUGH THIOL-DISULFIDE REDOX EXCHANGE

Fluorescent probes are widely applied in sensing, bioimaging, and diagnosis due to their sensitivity, versatility, and non-invasiveness. Among luminescent probes, fluorescent organic nanoparticles (FONPs) offer stability, tunability, and biocompatibility. The discovery of aggregation-induced emission (AIE) in 2001 showed strong emission upon aggregation. Over two decades, diverse AIE-based FONPs have emerged, crucial for target-specific applications. Protein disulfide isomerase (PDI), a member of the thioredoxin superfamily, is a 57-kDa dithiol-disulfide oxidoreductase with molecular chaperone functions crucial for cellular

homeostasis. Overexpressed in the endoplasmic reticulum (ER), PDI catalyzes protein folding by mediating disulfide formation, cleavage, and rearrangement. In cancer, PDI's roles extend to proliferation, survival, and metastasis, making selective detection of its varying redox state crucial. However, there is severe scarcity of reports on in-vitro or intracellular PDI sensing using diagnostic probes.

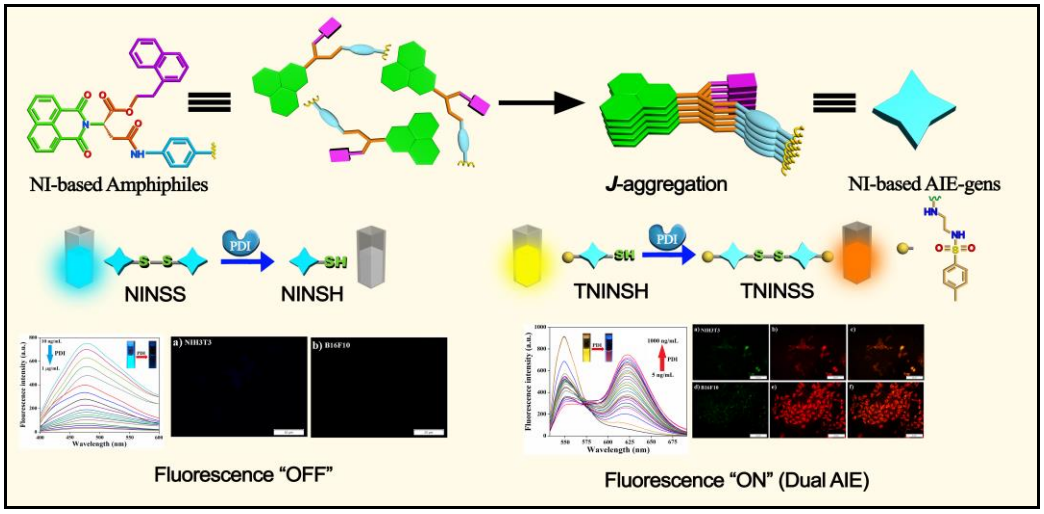

Figure 34. Schematic representation of analyzing PDI redox state by exploitation of AIE of **NINSS** and **TNINSH** FONPs. NI: Naphthalimide, AIE: aggregation induced emission.

On this account, in Chapter 3, we developed amphiphiles based on 1,8-naphthalimide (NI) with thiol (-SH) and disulfide (-S-S-) groups (Figure 34) to study PDI's redox behavior. These amphiphiles, **NISH** & **TNINSH** (thiol-containing), and **NISS** & **NINSS** (disulfide-containing), self-assembled into organic nanoparticles in DMSO-H_2O (f_w = 99 vol%) through *J*-type aggregation. **NINSS** and **TNINSH** exhibited AIE (blue and yellow) at 470 and 550 nm in 1:99 (v/v) DMSO-H_2O. **NINSS** FONPs fluorescence decreased with PDI, reducing disulfide bonds to thiols. **TNINSH** (with ER-targeting N-tosylethylenediamine) displayed enhanced AIE with a fluorescence shift due to disulfide formation upon thiol oxidation by PDI (Figure 34). **NINSS** and **TNINSH** FONPs were highly effective in AIE-based fluorometric PDI sensing with detection limits of ~12.6-17.7 ng/mL and ~11.7-16.5 ng/mL, respectively. These biocompatible FONPs selectively diagnosed cancer (B16F10) cells over non-cancerous (NIH3T3) cells due to overexpressed PDI. Both FONPs offer sensitive and selective PDI redox state analysis through their AIE property.

ORGANIC NANOPARTICLE-CARBON DOT CONJUGATES IN SYNERGISTIC COMBINATION THERAPY FOR CANCER TREATMENT

Nanotechnology's impact on therapeutics is significant, with various nanoparticles developed for encapsulating agents. Organic nanoparticles (ONPs) and carbon dots (CDs) offer promise in therapeutic delivery and diagnostics due to their capabilities, though limitations exist such as biocompatibility, stability issues, and manufacturing complexity. Combining ONPs and CDs could overcome these hurdles, resulting in a soft ONP-CD conjugate with enhanced drug loading and diagnostic properties. While a few attempts exist with other nanoconjugates, the potential of ONP-CD conjugates remains largely unexplored. Novel strategies are essential to enhance cancer treatment efficacy. Combination therapy, a recent advancement, merges therapeutic modalities or diverse agents with varying mechanisms of action to optimize outcomes while minimizing adverse effects.

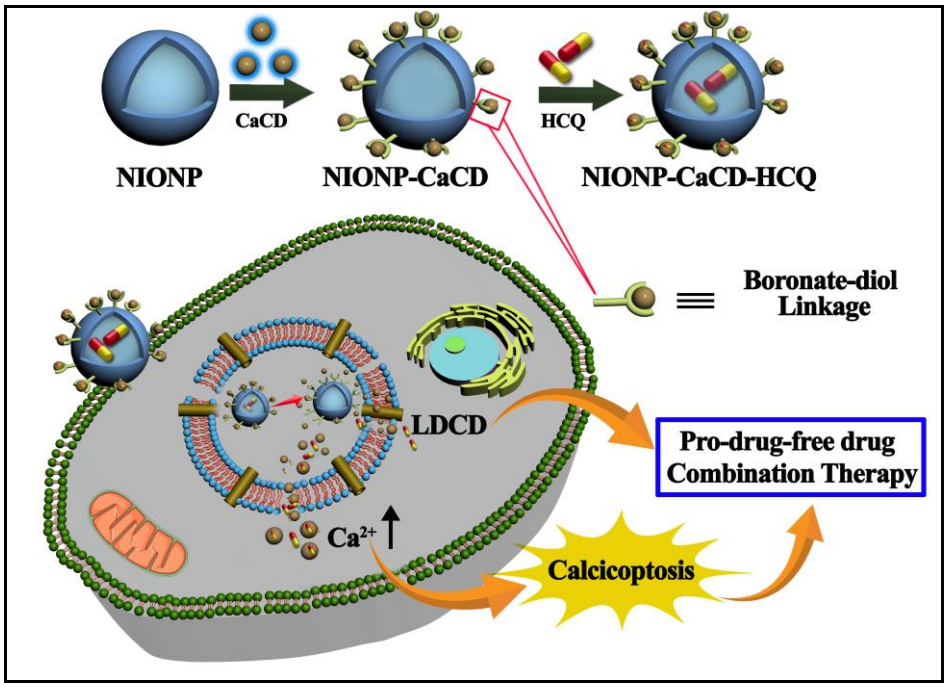

Figure 35. Schematic representation of fabrication of the **NIONP-CaCD** conjugate through boronate-diol linkage between **NIONP** and **CaCD** and its utilization in cancer theranostics through pro-drug-free drug combination therapy. HCQ: hydroxychloroquine.

To this end, Chapter 4 demonstrates the fabrication of **NIONP-CaCD** conjugate between self-assembled organic nanoparticles (**NIONP**) and Ca^{2+} doped carbon dots (**CaCD**) via boronate-diol interaction (Figure 35). This recently developed **NIONP-CaCD** conjugate was utilized for bioimaging by exploiting the inherent fluorescence of **CaCD** and also for pro-drug-

free drug combination therapy in cancer treatment. This **NIONP-CaCD** conjugate exhibited stability in biological conditions. Notably, the **NIONP-CaCD** conjugate demonstrated enhanced drug delivery efficiency into A549 and HepG2 cells compared to drug-loaded **NIONP** or **CaCD** alone, leading to increased cancer cell eradication by the conjugate. Interestingly, the breakdown of this **NIONP-CaCD** conjugate into its individual components have transpired through the cleavage of the boronate-diol bond within the lysosomal pH range (4.5-5.0). Subsequent liberation of **CaCD** and **HCQ** could lead to cell death initiated by lysosomal membrane permeabilization (LMP), possibly intertwined with Ca^{2+} overload mediated apoptosis (calcicoptosis). Hence, within this study, we present the **NIONP-CaCD** conjugate as an innovation for Ca^{2+} overload-based oncotherapy, in synergism with HCQ-induced lysosomal cell death.

REFERENCES

[1] Google image, https://www.opendemocracy.net/en/

[2] Google image, https://www.freepik.com/

[3] Google image, https://www.madagascandirect.com/

[4] Google image, https://martin-grolms.de/

[5] Google image, https://www.freepik.com/

[6] Google image, https://commons.wikimedia.org/

[7] Google image, https://www.flickr.com/

[8] Mehraeen, S. Self-Assembly of Nanostructures and Patchy Nanoparticles. *IntechOpen* **2020**.

[9] Chen, X.; Yin, J. Mechanical Self-Assembly in Nature. *Springer* **2001**, New York.

[10] Wolf, K. L.; Frahm, H.; Harms, H. Z. Über den Ordnungszustand der Moleküle in Flüssigkeiten *Phys. Chem. Abt. B* **1937**, *36*, 237.

[11] Lehn, J. M. Supramolecular chemistry. *Science* **1993**, *260*, 1762-1763.

[12] Menger, F. M. Remembrances of self-assemblies past. *Langmuir* **2011**, *27*, 5176-5183.

[13] Sarkar, S.; Choudhury, P.; Dinda, S.; Das, P. K. Tailor-made self-assemblies from functionalized amphiphiles: diversity and applications. *Langmuir* **2018**, *36*, 10449-10468.

[14] Google image, https://www.geeksforgeeks.org/

[15] Google image, https://www.thoughtco.com/

[16] Zana, R.; Lang, J.; Mittal, K. L.; Fendler, E. J. *Solution Behavior of Surfactants (Vol. 2)*, Plenum, New York, **1984**.

[17] Israelachvili, J. N.; Mitchell, D. J.; Ninham, B. W. Theory of self-assembly of hydrocarbon amphiphiles into micelles and bilayers. *J. Chem. Soc., Faraday trans. 2* **1976**, *72*, 1525-1568.

[18] Esch, J. H. V. More than the sum of its parts. *Nature* **2010**, *466*, 193-194.

[19] Blanazs, A.; Armes, S. P.; Ryan, A. J. Self-Assembled Block Copolymer Aggregates: From Micelles to Vesicles and their Biological Applications. *Macromol. Rapid Commun.* **2009**, *30*, 267-277.

[20] Lombardo, D.; Kiselev, M. A.; Magazù, S.; Calandra, P. Amphiphiles Self-Assembly: Basic Concepts and Future Perspectives of Supramolecular Approaches. *Adv. Condens. Matter. Phys.* **2015**, *11*, 1-22.

[21] Fuhrhop, J. H.; Wang, T. Bolaamphiphiles. *Chem. Rev.* **2004**, *104*, 2901-2938.

[22] Zhang, X; Wang, C. Supramolecular amphiphiles. *Chem. Soc. Rev.* **2011**, *40*, 94-101.

[23] Kashapov, R.; Gaynanova, G.; Gabdrakhmanov, D.; Kuznetsov, D.; Pavlov, R.; Petrov, K.; Zakharova, L.; Sinyashin, O. Self-Assembly of Amphiphilic Compounds as a Versatile Tool for Construction of Nanoscale Drug Carriers. *Int. J. Mol. Sci.* **2020**, *21*, 6961.

[24] Google image, https://www.chemistrylearner.com/

[25] Google image, https://www.expii.com/

[26] Google image, https://water.lsbu.ac.uk/

[27] Google image, https://en.wikipedia.org/

[28] Google image, https://chem.libretexts.org/

[29] Choudhury, P.; Dinda, S.; Das, P. K. Fabrication of soft-nanocomposites from functional molecules with diversified applications. *Soft Matter* **2020**, *16*, 27-53.

[30] Angell, C. A.; Poole, P. H.; Shao, J. Glass-forming liquids, anomalous liquids, and polyamorphism in liquids and biopolymers. *Il Nuovo Cimento D* **1994**, *16*, 993-1025.

[31] Magazu, S.; Migliardo, F.; Benedetto, A. Puzzle of Protein *Dynamical Transition*. *J. Phys. Chem. B* **2011**, *115*, 7736-7743.

[32] Clarke, S. The hydrophobic effect: Formation of micelles and biological membranes, 2nd edition (Tanford, Charles). *J. Chem. Educ.* **1981**, *58*, A246.

[33] Iglesias, A. S.; Grzelczak, M.; Altantzis, T.; Goris, B.; Juste, J. P.; Bals, S.; Tendeloo, G. V.; Donaldson, Jr. S. H.; Chmelka, B. F.; Israelachvili, J. N.; Marzán, L. M. L. Hydrophobic Interactions Modulate Self-Assembly of Nanoparticles. *ACS Nano* **2012**, *6*, 11059–11065.

[34] Gao, H. Y.; Wagner, H.; Held, P. A.; Du, S.; Gao, H. J.; Studer, A.; Fuchs, H. In-plane Van der Waals interactions of molecular self-assembly monolayer. *Appl. Phys. Lett.* **2015**, *106*, 081606.

[35] Lipowsky, R.; Sackmann, E. Structure and Dynamics of Membranes. *Elsevier*, The Netherlands, **1995**.

[36] Wang, B. Y.; Xu, H.; Zhang, X. Tuning the Amphiphilicity of Building Blocks: Controlled Self-Assembly and Disassembly for Functional Supramolecular Materials. *Adv. Mater.* **2009**, *21*, 2849-2864.

[37] Marguet, M.; Bonduelle, C.; Lecommandoux, S. Multicompartmentalized polymeric systems: towards biomimetic cellular structure and function. *Chem. Soc. Rev.* **2013**, *42*, 512-529.

[38] Samanta, S.; Raval, P.; Reddy, G. N. M.; Chaudhuri, D. Cooperative Self-Assembly Driven by Multiple Noncovalent Interactions: Investigating Molecular Origin and Reassessing Characterization. *ACS Cent. Sci.* **2021**, *7*, 1391-1399.

[39] Zhao, Y.; Sakai, F.; Su, L.; Liu, Y.; Wei, K.; Chen, G.; Jiang, M. Progressive Macromolecular Self-Assembly: From Biomimetic Chemistry to Bio-Inspired Materials. *Adv. Mater.* **2013**, *25*, 5215-5256.

[40] Lehn, J. M. From supramolecular chemistry towards constitutional dynamic chemistry and adaptive chemistry. *Chem. Soc. Rev.* **2007**, *36*, 151-160.

[41] Grieser, F.; Drummond, C. The Physicochemical Properties of Self-Assembled Surfactant Aggregates As Determined by Some Molecular Spectroscopic Probe Techniques *J. Phys. Chem.* **1988**, *92*, 5580-5593.

[42] Gazit, E. Self-assembled peptide nanostructures: the design of molecular building blocks and their technological utilization. *Chem. Soc. Rev.* **2007**, *36*, 1263-1269.

[43] Santis, E. D.; Ryadnov, M. G. Peptide self-assembly for nanomaterials: the old new kid on the block. *Chem. Soc. Rev.* **2015**, *44*, 8288-8300.

[44] Levin, A.; Hakala, T. A.; Schnaider, L.; Bernardes, G. J. L.; Gazit, E.; Knowles, T. P. J. Biomimetic peptide self-assembly for functional materials. *Nat. Rev. Chem.* **2020**, *4*, 615-634.

[45] McLntire, G. L.; Dorsey, J. G. Micelles in Analytical Chemistry. *Crit. Rev. Anal. Chem.* **1990**, *21*, 257-278.

[46] Dominguez, A.; Fernanadez, A.; Gonzalez, N.; Iglesius, E.; Montenegro, L. Determination of Critical Micelle Concentration of Some Surfactants by Three Techniques. *J. Chem. Educ.* **1997**, *74*, 1227.

[47] Google image, https://www.sciencephoto.com/

[48] Macquarrie, D. J. Organically modified micelle templated silicas in green chemistry. *Top. Catal.* **2009**, *52*, 1640-1650.

[49] Paul, B. K.; Moulik, S. P. MICROEMULSIONS: AN OVERVIEW *J. Disper. Sci. Technol.* **1997**, *18*, 301-307.

[50] Luisi, P. L.; Straub, B. E. Reverse Micelles: Biological and Technological Relevance of Amphiphilic Structures in Apolar Media. *Springer*, New York, NY **1984**.

[51] Google image, https://pixels.com/

[52] Sankaran, R.; Bong, J. H.; Chow, Y. H.; Wong, F.; Ling, T. C.; Show, P. L. Reverse Micellar System in Protein Recovery - A Review of the Latest Developments. *Curr. Protein. Pept. Sci.* **2019**, *20*, 1012-1026.

[53] Arsene, M. L.; Răut, I.; Călin, M.; Jecu, M. L.; Doni, M.; Gurban, A. M. Versatility of Reverse Micelles: From Biomimetic Models to Nano (Bio)Sensor Design. *Processes* **2021**, *9*, 345.

[54] Chatzidaki, M. D.; Papavasileiou, K. D.; Papadopoulos, M. G.; Xenakis, A. Reverse Micelles As Antioxidant Carriers: An Experimental and Molecular Dynamics Study. *Langmuir* **2017**, *33*, 5077-5085.

[55] Fendler, J. H. Membrane Mimetic Chemistry. *Wiley*, New York, **1982**.

[56] Sapala, A. R.; Dhawana, S.; Haridas, V. Vesicles: self-assembly beyond biological lipids. *RSC Adv.* **2017**, *7*, 26608-26624.

[57] Google image, https://www.renderhub.com/

[58] Somjen, G. J.; Gilat, T. Contribution of vesicular and micellar carriers to cholesterol transport in human bile. *J. Lipid Res.* **1985**, *26*, 699-704.

[59] Palivan, C. G.; Goers, R.; Najer, A.; Zhang, X.; Cara, A.; Meier, W. Bioinspired polymer vesicles and membranes for biological and medical applications. *Chem. Soc. Rev.* **2016**, *45*, 377-411.

[60] Shaha, S.; Dhawan, V.; Holma, R.; Nagarsenker, M. S.; Perrie, Y. When liposomes met antibodies: Drug delivery and beyond. *Adv. Drug Deliv. Rev.* **2020**, *154*, 151-162.

[61] Google image, https://assemblingsugars.fr/

[62] Sangeetha, N. M.; Maitra, U. Supramolecular gels: Functions and uses. *Chem. Soc. Rev.* **2005**, *34*, 821-836.

[63] Yu, G.; Yan, X.; Han, C.; Huang, F. Characterization of supramolecular gels. *Chem. Soc. Rev.* **2013**, *42*, 6697-6722.

[64] Chivers, P. R. A.; Smith, D. K. Shaping and structuring supramolecular gels. *Nat. Rev. Mater.* **2019**, *4*, 463–478.

[65] Panja, S.; Adams, D. J. Stimuli responsive dynamic transformations in supramolecular gels. *Chem. Soc. Rev.* **2021**, *50*, 5165-5200.

[66] Estroff, L. A.; Hamilton, A. D. Water gelation by small organic molecules. *Chem. Rev.* **2004**, *104*, 1201-1218.

[67] Banerjee, S.; Das, R. K.; Maitra, U. Supramolecular gels 'in action'. *J. Mater. Chem.* **2009**, *19*, 6649-6687

[68] Cao, X.; Gao, A.; Hou, J.; Yi, T. Fluorescent supramolecular self-assembly gels and their application as sensors: A review. **2021**, *434*, 213792.

[69] Lim, J. Y. C.; Lin, Q.; Xue, K.; Loh, X. J. Recent advances in supramolecular hydrogels for biomedical applications. **2019**, *3*, 100021.

[70] Lee, K. Y.; Mooney, D. J. Hydrogels for tissue engineering. *Chem. Rev.* **2001**, *101*, 1869-1879.

[71] Sato, K.; Hendricks, M. P.; Palmer, L. C.; Stupp, S. I. Peptide supramolecular materials for therapeutics. *Chem. Soc. Rev.* **2018**, *47*, 7539-7551.

[72] Ma, D.; Tu, K.; Zhang, L. M. Bioactive Supramolecular Hydrogel with Controlled Dual Drug Release Characteristics. *Biomacromolecules* **2010**, *11*, 2204-2212.

[73] Kalafatovic, D.; Nobis, M.; Javid, N.; Frederix, P. W. J. M.; Anderson, K. I.; Saunders, B. R.; Ulijn, R. V. MMP-9 triggered micelle-to-fibre transitions for slow release of doxorubicin. *Biomater. Sci.* **2015**, *3*, 246-249.

[74] Moitra, P.; Kumar, K.; Kondaiah, P.; Bhattacharya, S. Efficacious Anticancer Drug Delivery Mediated by a pH-Sensitive Self-Assembly of a Conserved Tripeptide Derived from Tyrosine Kinase NGF Receptor. *Angew. Chem. Int. Ed.* **2014**, *53*, 1113-1117.

[75] Rajamalli, P.; Prasad, E. Tunable morphology and mesophase formation by naphthalene-containing poly (aryl ether) dendron-based low-molecular-weight fluorescent gels. *Langmuir* **2013**, *29*, 1609-1617.

[76] Suzuki, M.; Hanabusa, K. L-Lysine-based low-molecular-weight gelators. *Chem. Soc. Rev.* **2009**, *38*, 967-975.

[77] Suzuki, M.; Hanabusa, K. Polymer organogelators that make supramolecular organogels through physical cross-linking and self-assembly. *Chem. Soc. Rev.* **2010**, *39*, 455-463.

[78] Zeng, L.; Lin, X.; Li, P.; Liu, F. Q.; Guo, H.; Li, W. H. Recent advances of organogels: from fabrications and functions to applications. *Prog. Org. Coat.* **2021**, *159*, 106417.

[79] Vintiloiu, A.; Leroux, J. C. Organogels and their use in drug delivery-a review. *J. Control Release* **2008**, *125*, 179-192.

[80] Skilling, K. J.; Citossi, F.; Bradshaw, T. D.; Ashford, M.; Kellam, B.; Marlow, M. Insights into low molecular mass organic gelators: a focus on drug delivery and tissue engineering applications. *Soft Matter*, **2014**, *10*, 237-256.

[81] Miravet, J. F.; Escuder, B. Pyridine-functionalised ambidextrous gelators: towards catalytic gels. *Chem. Commun.* **2005**, 5796-5798.

[82] Yan, N.; Xu, Z.; Diehn, K. K.; Raghavan, S. R.; Fang, Y.; Weiss, R. G. Pyrenyl-Linker-Glucono Gelators. Correlations of Gel Properties with Gelator Structures and Characterization of Solvent Effects. *Langmuir* **2013**, *29*, 793-805.

[83] Tsuge, A.; Matsumoto, S. Hashimura, D.; Araki, K. Development of novel aromatic ambidextrous gelators based on molecular design. *Tetrahedron Lett.* **2020**, *61*, 151501.

[84] Imura, Y.; Matsue, K.; Sugimoto, H.; Ito, R.; Kondo, T.; Kawai, T. Ambidextrous gel property and pH-responsive sol–gel transition of low molecular mass gelator based on a long-chain amide derivative. *Chem. Lett.* **2009**, *38*, 778-779.

[85] Liu, K.; Yan, N.; Peng, J.; Liu, J.; Zhang, Q.; Fang, Y. Supramolecular gels based on organic diacid monoamides of cholesteryl glycinate. *J. Colloid Interface Sci.* **2008**, *327*, 233-242.

[86] Horn, D.; Rieger, J. Organic Nanoparticles in the Aqueous Phase-Theory, Experiment, and Use. *Angew. Chem. Int. Ed* **2001**, *40*, 4330-4361.

[87] Ealia, S. A. M.; Saravanakumar, M. P. A review on the classification, characterisation, synthesis of nanoparticles and their application. *IOP Conf. Ser.: Mater. Sci. Eng.* **2017**, *263*, 032019.

[88] Goshen, K. M.; Magdassi, S. Organic nanoparticles from microemulsions: Formation and applications. *Curr. Opin. Colloid Interface Sci.* **2012**, *17*, 290-296.

[89] Li, K.; Liu, B. Polymer-encapsulated organic nanoparticles for fluorescence and photoacoustic imaging. *Chem. Soc. Rev.* **2014**, *43*, 6570-6597.

[90] Allouche, J. Synthesis of Organic and Bioorganic Nanoparticles: An Overview of the Preparation Methods. *Springer*, London, **2013**.

[91] Wani, W. A.; Shahid, M.; Hussain, A.; AlAjmi, M. F. Fluorescent Organic Nanoparticles: New Generation Materials with Diverse Analytical and Biomedical Applications. *Springer*, Singapore, **2018**.

[92] Ashoka, A. H.; Aparin, I. O.; Reischa, A.; Klymchenko, A. S. Brightness of fluorescent organic nanomaterials. *Chem. Soc. Rev.* **2023**, 52, 4525-4548.

[93] Choudhury, P.; Das, P. K. Progress and trends in self-assembly driven fluorescent organic nanoparticles: A brief overview. *J. Indian Chem. Soc.* **2021**, *98*, 100123.

[94] Montaseri, H.; Kruger, C. A.; Abrahamse, H. Review: Organic nanoparticle based active targeting for photodynamic therapy treatment of breast cancer cells. *Oncotarget*. **2020**, *11*, 2120-2136.

[95] Nadal, G. V.; Köber, M.; Nsamela, A.; Terenziani, F.; Sissa, C.; Pescina, S.; Sonvico, F.; Gazzali, A. M.; Wahab, H. A.; Grisanti, L.; Olivera, M. E.; Palena, M. C.; Guzman, M. L.; Giacobbe, L. C. L.; Kairuz, A. J.; Ventosa, N.; Ratera, I.; Belfield, K. D.; Maoz, B. M. Fluorescent Multifunctional Organic Nanoparticles for Drug Delivery and Bioimaging: A Tutorial Review. *Pharmaceutics* **2022**, *14*, 2498.

[96] Mei, J.; Leung, N. L. C.; Kwok, R. T. K.; Lam, J. W. Y.; Tang, B. Z. Aggregation-Induced Emission: Together We Shine, United We Soar! *Chem. Rev.* **2015**, *115*, 11718-11940.

[97] Thomas, S. W.; Joly, G. D.; Swager, T. M. Chemical Sensors Based on Amplifying Fluorescent Conjugated Polymers. *Chem. Rev.* **2007**, *107*, 1339-1386.

[98] Hide, F.; Garcia, M. A. D.; Schwartz, B. J.; Heeger, A. J. New Developments in the Photonic Applications of Conjugated Polymers. *Acc. Chem. Res.* **1997**, *30*, 430-436.

[99] Liu, J.; Yang, Z.; Ye, B.; Zhao, Z.; Ruan, Y.; Guo, T.; Yu, X.; Chena, G.; Xua, S. A review of stability-enhanced luminescent materials: fabrication and optoelectronic applications. *J. Mater. Chem. C* **2019**, *7*, 4934-4955.

[100] Peng, H. S.; Chiu, D. T. Soft fluorescent nanomaterials for biological and biomedical imaging. *Chem. Soc. Rev.* **2015**, *44*, 4699-4722.

[101] J. Mei, Y. Hong, J. W. Y. Lama, A. Quin, Y. Tang, B. Z. Tang, Aggregation-Induced Emission: The Whole Is More Brilliant than the Parts. *Adv. Mater.* **2014**, *26*, 5429-5479.

[102] Zhang, K.; Liu, J.; Zhang, Y.; Fan, J.; Wang, C. K.; Lin, L. Theoretical Study of the Mechanism of Aggregation-Caused Quenching in Near-Infrared Thermally Activated Delayed Fluorescence Molecules: Hydrogen-Bond Effect. *J. Phys. Chem. C* **2019**, *123*, 40, 24705-24713.

[103] Wang, H.; Zhao, E.; Lam, J. W. Y.; Tang, B. Z. AIE luminogens: emission brightened by aggregation. *Mater. Today* **2015**, *18*, 365-377.

[104] Birks, J. B. Photophysics of Aromatic Molecules, *Wiley-Interscience*, London, **1970**.

[105] Hong, Y.; Lam, J. W. Y.; Tang, B. Z. Aggregation-induced emission: phenomenon, mechanism and applications. *Chem. Commun.* **2009**, 4332-4353.

[106] Kasha, M. Characterization of electronic transitions in complex molecules. *Discuss. Faraday Soc.* **1950**, *9*, 14-19.

[107] Valle, J. C.; Catalán, J. Kasha's rule: a reappraisal. *Phys. Chem. Chem. Phys.* **2019**, *21*, 10061-10069.

[108] Luo, J.; Xie, Z.; Lam, J. W. Y.; Cheng, L.; Chen, H.; Qiu, C.; Kwok, H. S.; Zhan, X.; Liu, Y.; Zhu, D.; Tang, B. Z.; Aggregation-induced emission of 1-methyl-1,2,3,4,5-pentaphenylsilole. *Chem. Commun.* **2001**, 1740-1741.

[109] Hong, Y.; Lama, J. W. Y.; Tang, B. Z. Aggregation-induced emission. *Chem. Soc. Rev.* **2011**, *40*, 5361-5388.

[110] Feng, H. T.; Lam, J. W. Y.; Tang, B. Z. Self-assembly of AIEgens. *Coord. Chem. Rev.* **2020**, *406*, 213142.

[111] Wu, T.; Huang, J.; Yan, Y. Self-Assembly of Aggregation-Induced-Emission Molecules. *Chem. Asian J.* **2019**, *14*, 730-750.

[112] Zhang, X.; Zhang, X.; Tao, L.; Chi, Z.; Xu, J.; Wei, Y. Aggregation induced emission-based fluorescent nanoparticles: fabrication methodologies and biomedical applications. *J. Mater. Chem. B* **2014**, *2*, 4398-4414.

[113] Yang, B.; Zhang, X.; Zhang, X.; Huang, Z.; Wei, Y.; Tao, L. Fabrication of aggregation-induced emission based fluorescent nanoparticles and their biological imaging application: recent progress and perspectives. *Mater. Today* **2016**, *19*, 284-291.

[114] Yan, L.; Zhang, Y.; Xu, B.; Tian, W. Fluorescent nanoparticles based on AIE fluorogens for bioimaging. *Nanoscale* **2016**, *8*, 2471-2487.

[115] Gao, H.; Zhao, X.; Chen, S. AIEgen-Based Fluorescent Nanomaterials: Fabrication and Biological Applications. *Molecules* **2018**, *23*, 419.

[116] Kaeser, A.; Schenning, A. P. H. J. Fluorescent Nanoparticles Based on Self-Assembled π-Conjugated Systems. *Adv. Mater.* **2010**, *22*, 2985-2997.

[117] Leung, N. L. C.; Xie, N.; Yuan, W.; Liu, Y.; Wu, Q.; Peng, Q.; Miao, Q.; Lam, J. W. Y.; Tang, B. Z. Restriction of Intramolecular Motions: The General Mechanism behind Aggregation-Induced Emission. **2014**, *20*, 15349-15353.

[118] Guan, J.; Shen, C.; Peng, J.; Zheng, J. What Leads to Aggregation-Induced Emission? *J. Phys. Chem. Lett.* **2021**, *12*, 4218-4226.

[119] Peng, Q.; Shuai, Z. Molecular mechanism of aggregation-induced emission. **2021**, *2*, e91.

[120] Li, J.; Wang, J.; Li, H.; Song, N.; Wang, D.; Tang, B. Z. Supramolecular materials based on AIE luminogens (AIEgens): construction and applications. *Chem. Soc. Rev.* **2020**, *49*, 1144-1172.

[121] Chen, Y.; Lam, J. W. Y.; Kwok, R. T. K.; Liu, B.; Tang, B. Z. Aggregation-induced emission: fundamental understanding and future developments. *Mater. Horiz.* **2019**, *6*, 428-433.

[122] Cai, X.; Liu, B. Aggregation-Induced Emission: Recent Advances in Materials and Biomedical Applications. *Angew. Chem. Int. Ed* **2020**, *59*, 9868-9886.

[123] Mei, J.; Huang, Y.; Tian, H. Progress and Trends in AIE-Based Bioprobes: A Brief Overview. *ACS Appl. Mater. Interfaces* **2018**, *10*, 15, 12217-12261.

[124] Wang, Y.; Nie, J.; Fang, W.; Yang, L.; Hu, Q.; Wang, Z.; Sun, J. Z.; Tang, B. Z. Sugar-Based Aggregation-Induced Emission Luminogens: Design, Structures, and Applications. *Chem. Rev.* **2020**, *120*, 4534-4577.

[125] Wang, D.; Lee, M. M. S.; Xu, W.; Kwok, R. T. K.; Lam, J. W. Y.; Tang, B. Z. Theranostics based on AIEgens. *Theranostics* **2018**, *8*, 4925-4956.

[126] Chen, M.; Li, L.; Nie, H.; Tong, J.; Yan, L.; Xu, B.; Sun, J. Z.; Tian, W.; Zhao, Z.; Qin, A.; Tang, B. Z. Tetraphenylpyrazine-based AIEgens: facile preparation and tunable light emission. *Chem. Sci.* **2015**, *6*, 1932-1937.

[127] La, D. D.; Bhosale, S. V.; Jones, L. A.; Bhosale, S. V. Tetraphenylethylene-Based AIE-Active Probes for Sensing Applications. *ACS Appl. Mater. Interfaces* **2018**, *10*, 12189-12216.

[128] Lyu, G.; Southern, T. J. F.; Charles, B. L.; Roger, M.; Gerbier, P.; Clément, S.; Evans, R. C. Aggregation-induced emission from silole-based lumophores embedded in organic–inorganic hybrid hosts. *J. Mater. Chem. C Mater.* **2021**, *9*, 13914-13925.

[129] Cheng, H. B.; Zhang, S.; Bai, E.; Cao, X.; Wang, J.; Qi, J.; Liu, J.; Zhao, J.; Zhang, L.; Yoon, J. Future-Oriented Advanced Diarylethene Photoswitches: From Molecular Design to Spontaneous Assembly Systems. *Adv. Mater.* **2022**, *34*, 2108289.

[130] Jimenez, E. R.; Rodríguez, H. Aggregation-induced emission: a review of promising cyano-functionalized AIEgens. *J. Mater. Sci.* **2020**, *55*, 1366-1387.

[131] Kobaisi, M. A.; Bhosale, S. V.; Latham, K.; Raynor, A. M.; Bhosale, S. V. Functional Naphthalene Diimides: Synthesis, Properties, and Applications. *Chem. Rev.* **2016**, *116*, 11685-11796.

[132] Bhosale, S. V.; Kobaisi, M. A.; Jadhav, R. W.; Morajkar, P. P.; Jones, L. A.; George, S. Naphthalene diimides: perspectives and promise. *Chem. Soc. Rev.* **2021**, *50*, 9845-9998.

[133] Dong, H. Q.; Wei, T. B.; Ma, X. Q.; Yang, Q. Y.; Zhang, Y. F.; Sun, Y. J.; Shi, B. B.; Yao, H.; Zhang, Y. M.; Lin, Q. 1,8-Naphthalimide-based fluorescent chemosensors: recent advances and perspectives. *J. Mater. Chem. C* **2020**, *8*, 13501-13529.

[134] Gopikrishna, P.; Meher, N.; Iyer, P. K. Functional 1,8-Naphthalimide AIE/AIEEgens: Recent Advances and Prospects. *ACS Appl. Mater. Interfaces* **2018**, *10*, 12081-12111.

[135] Lombardo, D.; Calandra, P.; Pasqua, L.; Magazù, S. Self-Assembly of Organic Nanomaterials and Biomaterials: The Bottom-Up Approach for Functional Nanostructures Formation and Advanced Applications. *Materials* **2020**, *13*, 1048.

[136] Baig, N.; Kammakakam, I.; Falath, W. Nanomaterials: a review of synthesis methods, properties, recent progress, and challenges. *Mater. Adv.* **2021**, *2*, 1821-1871.

[137] Fang, F.; Li, M.; Zhang, J.; Lee, C. S. Different Strategies for Organic Nanoparticle Preparation in Biomedicine. *ACS Mater. Lett.* **2020**, *2*, 531-549.

[138] Ahmed, M.; Faisal, M.; Ihsan, A.; Naseer, M. M. Fluorescent organic nanoparticles (FONs) as convenient probes for metal ion detection in aqueous medium. *Analyst* **2019**, *144*, 2480-2497.

[139] Xia, Q.; Chen, Z.; Yu, Z.; Wang, L.; Qu, J.; Liu, R. Aggregation-Induced Emission-Active Near-Infrared Fluorescent Organic Nanoparticles for Noninvasive Long-Term Monitoring of Tumor Growth. *ACS Appl. Mater. Interfaces* **2018**, *10*, 17081-17088.

[140] Jagannathan, R.; Irvin, G.; Blanton, T.; Jagannathan, S. Organic Nanoparticles: Preparation, Self-Assembly, and Properties. *Adv. Funct. Mater.* **2006**, *16*, 747-753.

[141] Meziani, M. J.; Pathak, P.; Hurezeanu, R.; Thies, M. C.; Enick, R. M.; Sun, Y. P. Supercritical-fluid processing technique for nanoscale polymer particles. *Angew. Chem. Int. Ed* **2004**, *43*, 704-707.

[142] Li, X.; Anton, N.; Arpagaus, C.; Belleteix, F.; Vandamme, T. F. Nanoparticles by spray drying using innovative new technology: The Büchi Nano Spray Dryer B-90. *J. Control. Release* **2010**, *147*, 304-310.

[143] Granchak, V. M.; Sakhno, T. V.; Korotkova, I. V.; Sakhno, Y. E.; Kuchmy, S. Y. Aggregation-Induced Emission in Organic Nanoparticles: Properties and Applications: a Review. *Theor. Exp. Chem.* **2018**, *54*, 147-177.

[144] Hua, F.; Liu, B. Organelle-specific bioprobes based on fluorogens with aggregation-induced emission (AIE) characteristics. *Org. Biomol. Chem.* **2016**, *14*, 9931-9944.

[145] Ding, D.; Li, K.; Liu, B.; Tang, B. Z. Bioprobes Based on AIE Fluorogens. *Acc. Chem. Res.* **2013**, *46*, 2441-2453.

[146] Wang, J.; Li, C.; Chen, Q.; Li, H.; Zhou, L.; Jiang, X.; Shi, M.; Zhang, P.; Jiang, G.; Tang, B. Z. An Easily Available Ratiometric Reaction-Based AIE Probe for Carbon Monoxide Light-up Imaging. *Anal. Chem.* **2019**, *91*, 9388-9392.

[147] Liang, J.; Tang, B. Z.; Liu, B. Specific light-up bioprobes based on AIEgen conjugates. *Chem. Soc. Rev.* **2015**, *44*, 2798-2811.

[148] Li, Y.; Zhong, H.; Huang, Y.; Zhao, R. Recent Advances in AIEgens for Metal Ion Biosensing and Bioimaging. *Molecules* **2019**, *24*, 4593.

[149] Nadal, G. V.; Köber, M.; Nsamela, A.; Terenziani, F.; Sissa, C.; Pescina, S.; Sonvico, F.; Gazzali, A. M.; Wahab, H. A.; Grisanti, L.; Olivera, M. E.; Palena, M. C.; Guzman, M. L.; Giacobbe, L. C. L.; Kairuz, A. J.; Ventosa, N.; Ratera, I.; Belfield, K. D.; Maoz, B. M. Fluorescent Multifunctional Organic Nanoparticles for Drug Delivery and Bioimaging: A Tutorial Review. *Pharmaceutics* **2022**, *14*, 2498.

[150] Mitragotri, S.; Stayton, P. Organic nanoparticles for drug delivery and imaging. *MRS Bull*. **2014**, *39*, 219-223.

[151] Liu, S.; Feng, G.; Tang, B. Z.; Liu, B. Recent advances of AIE light-up probes for photodynamic therapy. *Chem*. *Sci*. **2021**, *12*, 6488-6506.

[152] Yuan, Y.; Liu, B. Visualization of drug delivery processes using AIEgens. *Chem*. *Sci*. **2017**, *8*, 2537-2546.

[153] Feng, G.; Liu, B. Multifunctional AIEgens for Future Theranostics. *Small* **2016**, *12*, 6528-6535.

[154] Yi, X.; Li, J.; Zhu, Z.; Liu, Q.; Xue, Q.; Ding, D. In vivo cancer research using aggregation-induced emission organic nanoparticles. *Drug Discov*. *Today* **2017**, *22*, 1412-1420.

[155] Dong, Y.; Liu, B.; Yuan, Y. AIEgen based drug delivery systems for cancer therapy. *J Control Release* **2018**, *290*, 129-137.

[156] Qian, J.; Tang, B. Z. AIE Luminogens for Bioimaging and Theranostics: From Organelles to Animals. *Chem* **2017**, *3*, 56-91.

[157] Bayda, S.; Adeel, M.; Tuccinardi, T.; Cordani, M.; Rizzolio, F. The History of Nanoscience and Nanotechnology: From Chemical–Physical Applications to Nanomedicine. *Molecules* **2020**, *25*, 112.

[158] Khan, S.; Mansoor, S.; Rafi, Z.; Kumari, B.; Shoaib, A.; Saeed, M.; Alshehri, S.; Ghoneim, M. M.; Rahamathulla, M.; Hani, U.; Shakeel, F. A review on nanotechnology: Properties, applications, and mechanistic insights of cellular uptake mechanisms. *J. Mol. Liq*. **2022**, *348*, 118008.

[159] Jeevanandam, J.; Barhoum, A.; Chan, Y. S.; Dufresne, A.; Danquah, M. K. Review on nanoparticles and nanostructured materials: history, sources, toxicity and regulations. *Beilstein J. Nanotechnol*. **2018**, *9*, 1050-1074.

[160] Zhu, S.; Meng, H.; Gu, Z.; Zhao, Y. Research trend of nanoscience and nanotechnology – A bibliometric analysis of *Nano Today*. *Nano Today* 2021, *39*, 101233.

[161] Liu, H.; Ye, T.; Mao, C. Fluorescent Carbon Nanoparticles Derived from Candle Soot. *Angew. Chem. Int. Ed.* **2007**, *46*, 6473-6475.

[162] Liu, J.; Li, R.; Yang, B. Carbon Dots: A New Type of Carbon-Based Nanomaterial with Wide Applications. *ACS Cent. Sci.* **2020**, *6*, 2179-2195.

[163] Baker, S. N.; Baker, G. A. Luminescent carbon nanodots: emergent nanolights. *Angew. Chem. Int. Ed.* **2010**, *49*, 6726-6744.

[164] Sun, Y. P.; Zhou, B.; Lin, Y.; Wang, W.; Fernando, K. A. S.; Pathak, P.; Meziani, M. J.; Harruff, B. A.; Wang, X.; Wang, H.; Luo, P. G.; Yang, H.; Kose, M. E.; Chen, B.; Veca, L. M.; Xie, S. Y. Quantum-sized carbon dots for bright and colorful photoluminescence. *J. Am. Chem. Soc.* **2006**, *128*, 7756-4457.

[165] Zhu, S.; Meng, Q.; Wang, L.; Zhang, J.; Song, Y.; Jin, H.; Zhang, K.; Sun, H.; Wang, H.; Yang, B. Highly photoluminescent carbon dots for multicolor patterning, sensors, and bioimaging. *Angew. Chem. Int. Ed.* **2013**, *52*, 3953-3957.

[166] Yang, S. T.; Cao, L.; Luo, P. G.; Lu, F.; Wang, X.; Wang, H.; Meziani, M. J.; Liu, Y.; Qi, G.; Sun, Y. P. Carbon Dots for Optical Imaging in Vivo. *J. Am. Chem. Soc.* **2009**, *131*, 11308-11309.

[167] Ji, C.; Zhou, Y.; Leblanc, R. M.; Peng, Z. Recent Developments of Carbon Dots in Biosensing: A Review. *ACS Sens.* **2020**, *5*, 2724-2741.

[168] Wang, B.; Cai, H.; Waterhouse, G. I. N.; Qu, X.; Yang, B.; Lu, S. Carbon Dots in Bioimaging, Biosensing and Therapeutics: A Comprehensive Review. *Small* **2022**, *2*, 2200012.

[169] Bogue, R. Nanocomposites: a review of technology and applications. *Assem. Autom.* **2011**, *31*, 106-112.

[170] Mikličanin, E. O.; Badnjević, A.; Kazlagić, A.; Hajlovac, M. Nanocomposites: a brief review. *Health Technol.* **2020**, *10*, 51-59.

[171] Shameem, M. M.; Sasikanth, S. M.; Annamalai, R.; Raman, R. G. A brief review on polymer nanocomposites and its applications. *Mater. Today: Proc.* **2021**, *45*, 2536-2539.

[172] Bhattacharya, S.; Samanta, S. K. Soft-Nanocomposites of Nanoparticles and Nanocarbons with Supramolecular and Polymer Gels and Their Applications. *Chem. Rev.* **2016**, *116*, 11967-12028.

[173] Zhang, W.; Ledari, R. T.; Ganjali, F.; Afruzi, F. H.; Hajizadeh, Z.; Saeidirad, M.; Qazi, F. S.; Kashtiaray, A.; Sehat, S. S.; Hamblin, M. R.; Maleki, A. Nanoscale bioconjugates: A review of the structural attributes of drug-loaded nanocarrier conjugates for selective cancer therapy. *Heliyon* **2022**, *8*, e09577.

[174] Yan, X.; Blacklock, J.; Li, J.; Möhwald, H. One-Pot Synthesis of Polypeptide–Gold Nanoconjugates for in Vitro Gene Transfection. *ACS Nano* **2012**, *6*, 111-117.

[175] Capek, I. Dispersions, novel nanomaterial sensors and nanoconjugates based on carbon nanotubes. *Adv. Colloid Interface Sci.* **2009**, *150*, 63-89.

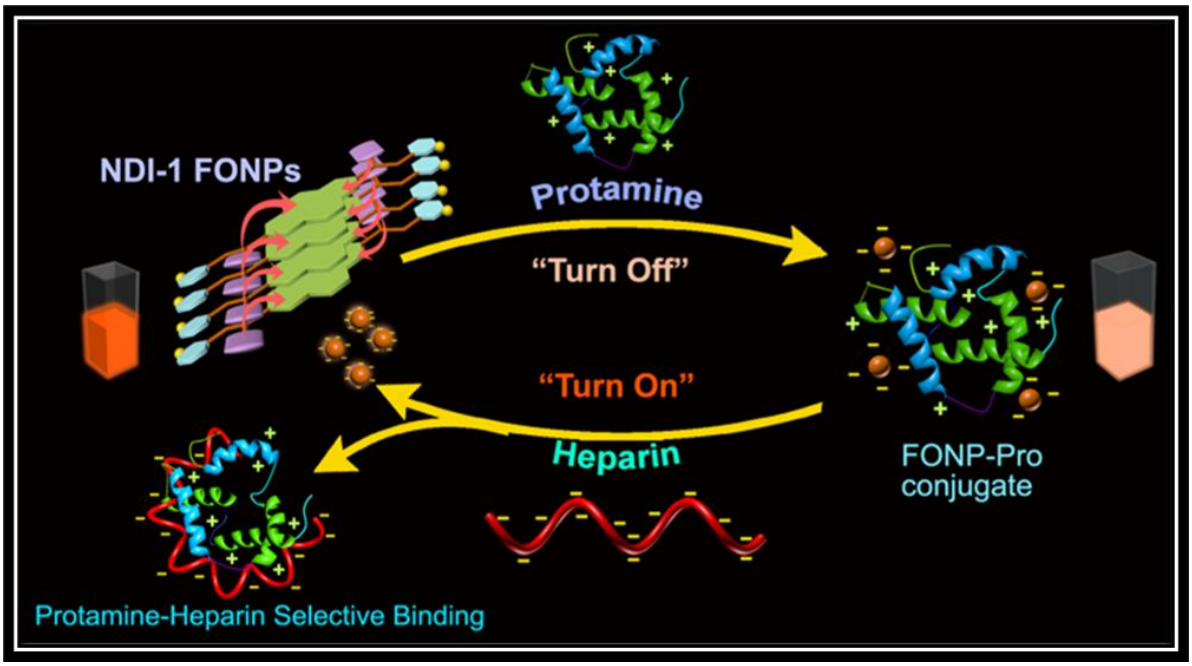

Fabrication of Orange Emitting Organic Nanoparticle-Protamine Conjugate: Fluorometric Sensor of Heparin

1.1 INTRODUCTION

In recent past, fluorescent bioprobes have gained enormous attention across the scientific disciplines primarily in different sensing applications ranging from environmental monitoring to chemo/biosensing, disease diagnosis, and others.[1-7] Numerous fluorescent inorganic nanoparticles (FINs) and organic dyes have been extensively investigated especially for chemo/biosensing purpose owing to their excellent photostability, superior sensitivity and high quantum yield.[7-10] However, most of the FINs are often hazardous to the living organisms due to their non-biodegradability and heavy metal composition.[11] On the other hand, aggregation caused quenching (ACQ) restricts the utility of most organic dyes by reducing the fluorescence intensity in the self-aggregated state or at relatively high molecular concentrations.[12,13] In comparison to FINs and other conventional organic dyes, fluorescent organic nanoparticles (FONPs) with unique aggregation-induced emission (AIE) characteristics are recently gaining interest due to its easy synthesis, potential biodegradability and non-toxic properties.[14-17] Self-assembly of π-conjugated oligomers or chromophoric molecules with multimodal functionality are susceptible to form task specific FONPs. Tuning of intrinsic fluorescence behaviour (i.e., AIE phenomenon) of the FONPs is not only of academic value but also of practical implication as it enables the development of 'light-up' smart sensors for the detection of biologically relevant molecules.[18,19]

Heparin, a negatively charged linear polysaccharide, is often utilized to prevent thrombosis during surgery and treat thrombotic diseases as an anticoagulant drug.[20-24] However, overdose of heparin can cause harmful effects like hemorrhage and heparin-induced thrombocytopenia.[25-27] Hence, quantitative estimation of heparin in plasma is an important task. To date, various techniques like fluorimetry, colorimetry, ion-exchange chromatography, and electrochemical methods have been employed for the estimation of heparin.[28-31] Among them, fluorometric assay has attracted more attention owing to its low-cost, operational simplicity, high sensitivity, and real-time detection. However, in several cases, most of the fluorescent probes could not show efficient fluorometric response toward heparin due to lack of binding affinity.[32] Therefore, inclusion (either covalently or non-covalently) of some analyte specific biomolecules with the fluorescent probes may rapidly interact with heparin so that a

notable fluorometric change takes place. Protamine has the ability to bind strongly with heparin through electrostatic interaction between guanidinium and sulfonate groups. However, reports on development of protamine doped biosensors, especially FONPs are really scarce to detect heparin by exploiting the AIE phenomenon of FONP-protamine conjugates.

In the present study we have developed naphthalene diimide (NDI) based FONP which was non-covalently attached with protamine to form FONP-Pro conjugate for the detection of heparin. 3-Amino pyridine tagged newly developed NDI-**1** bola-type amphiphilic molecules (Figure 1) formed organic nanoparticles in DMSO-water solvent mixture and showed aggregation-induced orange emission. This AIE at 594 nm (orange emission) was exhibited due to excimer formation in combination with intramolecular charge transfer (ICT). Negative surface charge of NDI-**1** FONPs due to the presence of amino pyridine residues at the both terminals favored the interaction with positively charged protamine to form FONP-Pro conjugate. Emission intensity of FONPs got quenched in presence of protamine. Interestingly, the addition of heparin to this FONP-Pro conjugate turned on fluorescence signal of FONPs through unwinding of protamine from FONP surface due to a strong binding affinity between heparin and protamine. Thus, heparin can be easily detected simply by monitoring the fluorescence quenching (off) and restoration (on) of NDI-**1** FONP with limit of detection (LOD) of 12 nM.

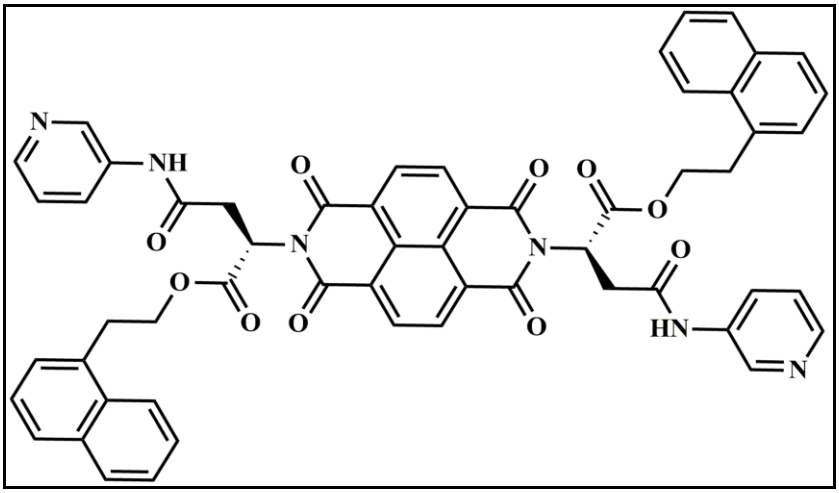

Figure 1. Structure of NDI-**1** molecule.

1.2 RESULTS AND DISCUSSION

1.2.1 DESIGNING OF BOLA-TYPE AMPHIPHILIC MOLECULE NDI-1.

Development of task specific small amphiphilic AIE-active luminogens (AIE-gens) is always challenging and few important parameters need to be considered while designing AIE-gens. For example, distortion in the molecular planarity restricts the intramolecular rotations/motions in the self-assembled state which is one of the prerequisite for the AIE phenomenon.[12] In addition, presence of donor-acceptor (D-A) moiety in the molecular backbone favors the charge transfer process that induces the emission maximum towards the higher wavelength region.[12,13,33,34] Naphthalene diimides (NDIs), one of the versatile and fascinating subclass of the 'rylene' family, are neutral, planar, chemically robust, electron-deficient class of aromatic compounds, which have been utilized in different sensing applications by exploiting its photoluminescence property.[14,16,35-38] Herein, we designed L-aspartic acid tagged NDI-based bola-type amphiphilic molecule (NDI-**1**, Figure 1), where both the terminals were functionalized with pyridyl unit. The synthesized amphiphile NDI-**1** was characterized by ^{1}H-NMR, ^{13}C-NMR, and MALDI-TOF mass spectrometry. Presence of aromatic residues in the molecular backbone may facilitate π-π stacking and hydrophobic interaction during self-assembly. Chirality of the L-aspartic acid residue may also induce the twisted nature in the molecular backbone to restrict intramolecular rotation (RIR) in the self-aggregated state.[12,14,37] Considering the electron-deficient characteristic of the NDI aromatic core, charge transfer from π-electron-donating units (naphthyl residue) in the molecular scaffold is expected to play a key role in its AIE property. Presence of 3-aminopyridine unit at the both terminals may enhance the stability of the bola-type amphiphilic molecules in aqueous medium. Moreover, the presence of lone pair of electrons on the sp^2-hybridized *N*-atom in the pyridyl residue may determine the overall surface charge of the self-assemblies.

1.2.2 SELF-ASSEMBLY OF NDI DERIVATIVE: MICROSCOPIC AND DLS STUDY.

The synthesized NDI derivative (NDI-**1**) was highly soluble in DMSO. Upon addition of water, the transparent solution changed to translucent one at around 40% water content (f_w = 40 vol%) (Figure 2a). This change in the physical appearance indicates the initiation of self-assembly by NDI-**1** bola-type amphiphilic molecules. This translucency got enhanced steadily

(according to the visual appearance) with the increase in water content up to 99 vol% possibly due to the formation of self-assembled structures (Figure 2a). This preliminary observation for self-assembly prompted us to investigate the morphology of the self-aggregated structure.

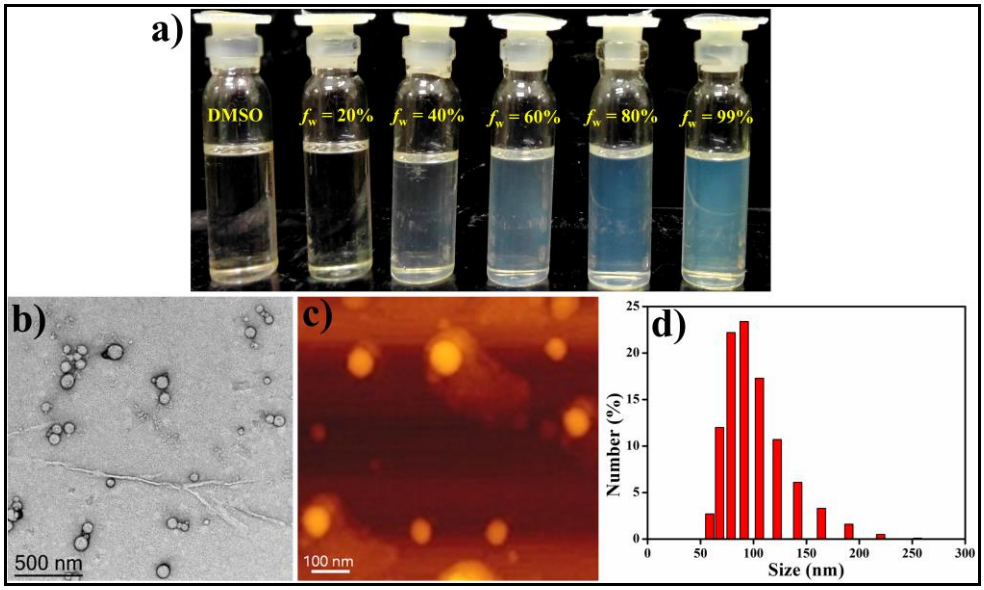

Figure 2. Photograph of (a) formation of translucent solutions with increasing water content in DMSO for NDI-**1** (50 μM); (b) Negatively stained TEM image, (c) AFM image, (d) DLS plot of particles size distribution of NDI-**1** in (1:99, v/v) DMSO–water binary solvent mixture ([NDI-**1**] = 50 μM).

Transmission electron microscopy (TEM) image of NDI-**1** (50 μM) in (1:99, v/v) DMSO-water demonstrated the formation of spherical aggregates having dimension in the range of 80-100 nm (Figure 2b). No clear contrast of the spherical particles indicates the solid nature of these aggregated nanostructures. In concurrence with the TEM image, AFM image of the FONPs produced by the self-aggregation of NDI-**1** (in 1:99, v/v DMSO-water) exhibited spherical shaped nanoparticles with the diameters in the range of 80-100 nm (Figure 2c). The dimension of these spherical aggregates was further confirmed by measuring the mean hydrodynamic diameter (D_h) from dynamic light scattering (DLS) study. D_h of NDI-**1** (50 μM) in (1:99, v/v) DMSO-water was found to be in the range of 80-90 nm (having polydispersity index (PDI) value 0.066) (Figure 2d), which is in concurrence with the microscopic images (Figure 2b,c). This observation suggests that there were no significant changes in morphology as well as the size of the nanoparticles during the formation of NDI-**1** FONP-protamine conjugate in the self-assembled state of NDI-**1**.

1.2.3 SPECTROSCOPIC STUDY FOR SELF-ASSEMBLY OF NDI-1 AMPHIPHILE.

After successful formation of organic nanoparticles, we have monitored the UV-vis spectra to investigate the aggregation pattern of NDI-**1** bola-type amphiphilic molecules during self-assembly. The UV-vis spectra of NDI-**1** (50 μM) in DMSO showed sharp absorption bands in the range of 330-400 nm with absorption maximum (λ_{max}) at 381 (Figure 3a) nm due to π-π* transition polarized along the long axis of NDI-**1** chromophore.[16] Initially, absorbance got dropped immediately upon addition of water to the DMSO solution of NDI-**1**. With increasing water percentage, the optical density further reduced slightly. Alongside, the absorption maximum was gradually red shifted with increase in the water content (above 40% water content, f_w = 40 vol%) and finally the λ_{max} was observed at 385 nm (around 4 nm red shift in comparison to the molecularly dissolved state of NDI-**1** in DMSO) at the highest water percentage (f_w = 99 vol%) (Figure 3a). This characteristic bathochromic shift in the absorption maximum in the presence of water indicates that the formation of self-assembled organic nanoparticles took place through *J*-type aggregation by a stair-like stacking of the NDI chromophore.

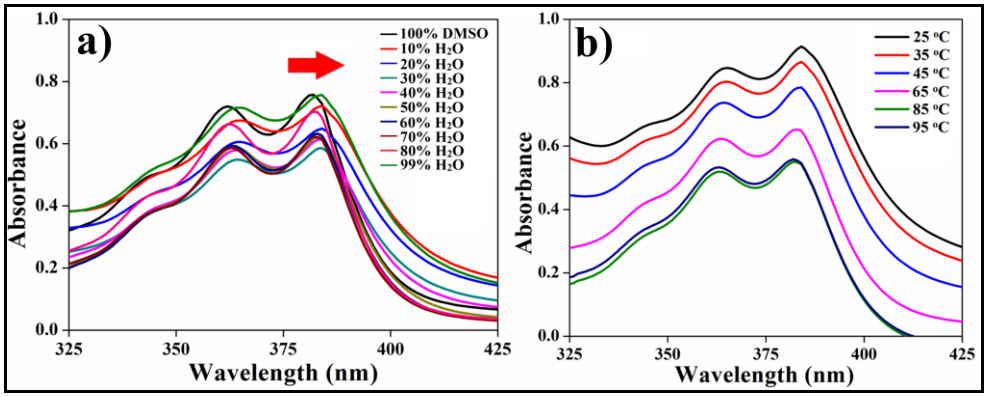

Figure 3. (a) UV–visible spectra of NDI-**1** (50 μM) in varying DMSO–water solvent mixtures. (b) Temperature-dependent UV–visible spectra of NDI-**1** (50 μM) in 1:1 v/v, DMSO–water.

The effect of temperature on the stability of the organic nanoparticles was also studied by UV-vis spectra of the synthesized naphthalene diimide derivatives, NDI-**1** (50 μM), in 1:1 v/v DMSO-water at varying temperatures. With the increase in temperature from 25 °C to 95 °C, the λ_{max} of the respective NDI derivatives got blue shifted ~2-4 nm (Figure 3b). Initially, with elevating temperature (up to 35 °C), no significant change in spectral shift was observed. With

further enhancement in the temperature (at and beyond 45 °C), the λ_{max} got shifted to the lower wavelength. This observation delineates that the aggregated organic nanoparticles formed by NDI derivative was stable at least up to 45 °C.

1.2.4 INVOLVEMENT OF INTERMOLECULAR NONCOVALENT INTERACTIONS IN SELF-ASSEMBLY.

The influence of different non-covalent interactions during self-assembly induced formation of aggregated nanoparticles was monitored by FTIR and solvent-dependent ^{1}H-NMR spectroscopy. The FTIR spectrum of NDI-**1** in $CHCl_3$ (non-aggregated state) showed transmittance peaks at approximately ν = 3174, 1669, and 1538 cm^{-1} (Figure 4a) due to δ_{N-H} (amide A), $\nu_{C=O}$ (amide I, stretching), and ν_{N-H} (amide II, bending). These peaks got shifted to δ_{N-H} (amide A) = 3340-3567cm^{-1} (broad band), $\nu_{C=O}$ (amide I, stretching) = 1627 cm^{-1}, and ν_{N-H} (amide II, bending) = 1565 cm^{-1} in (1:9, v/v) DMSO-d_6-D_2O solvent mixture (Figure 4a). These characteristic shifts in stretching and bending frequencies of the peaks in DMSO-d_6-D_2O solvent mixtures signify the involvement of intermolecular hydrogen bonding between the carbonyl (C=O) and amide N-H (i.e., C=O···H-N) in the process of self-assembly induced formation of organic nanoparticles.

In solvent-dependent ^{1}H-NMR study, the aromatic protons of NDI-**1** exhibited characteristic sharp NMR signals in the region δ = 8.51 ppm (aromatic core of NDI), δ = 8.7-8.8 ppm (pyridyl ring) and δ = 7.0-8.1 ppm (naphthyl ring) in DMSO-d_6, illustrating its non-aggregated state (Figure 4b). With gradual increase in the D_2O content, the characteristic NMR signal got upfield shifted with reduced peak intensity (Figure 4b). At (1:1, v/v) DMSO-d_6-D_2O solvent mixture, ^{1}H-NMR signals of the NDI aromatic core and the naphthyl ring was broadened and shifted to δ = 7.98 ppm, δ = 8.3-8.45 ppm (pyridyl ring) and δ = 6.7-7.8 ppm for the respective protons (Figure 4b). In the non-self-assembled state (DMSO-d_6), no effective π-π stacking as well as hydrophobic interactions was involved. With gradual increase in D_2O content, initiation of self-assembly facilitates the non-covalent interactions (such as π-π stacking, hydrophobic interaction) between the aromatic residues of the molecular framework. These spectroscopic evidences confirmed that non-covalent interactions involved during the formation of self-assembled organic nanoparticles.

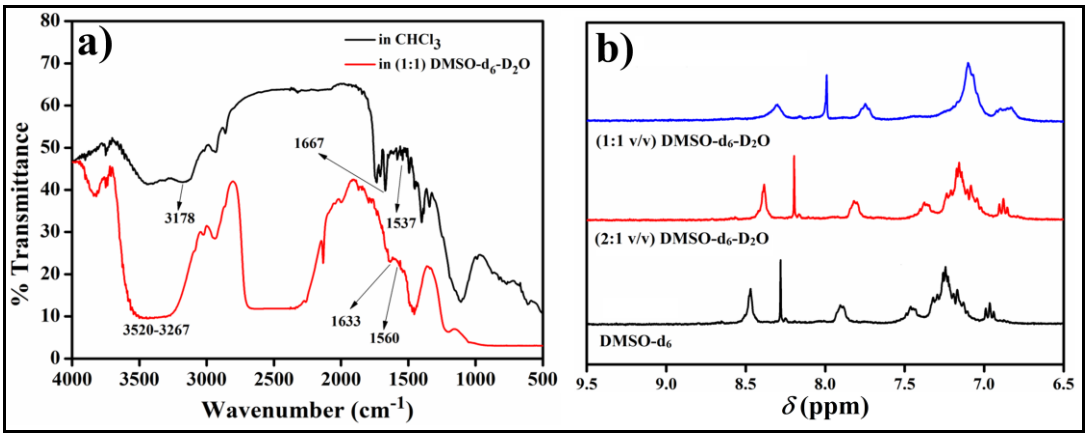

Figure 4. (a) FTIR spectra of NDI-**1** in chloroform (non-self-aggregated form) and in 1:1 (v/v) DMSO-d_6-D2O (self-aggregated form); (b) Solvent dependent ^{1}H-NMR spectra of NDI-**1**.

1.2.5 STUDY OF AIE PHENOMENON OF NDI-1 BOLA-TYPE AMPHIPHILIC MOLECULES.

After successful formation of self-assembled organic nanoparticles, we were curious to study the photophysical properties of this newly developed NDI-**1** bola-type amphiphilic molecules. DMSO solution of NDI-**1** bola-type amphiphilic molecules showed very weak blue fluorescence when irradiated with UV-light excited at 365 nm (Figure 5a).

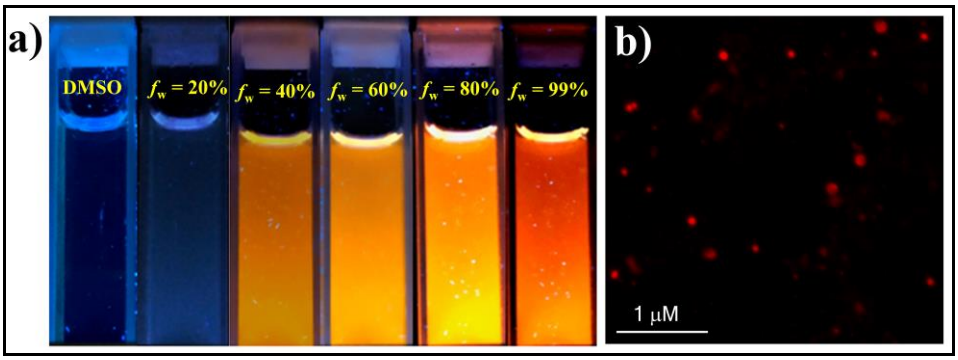

Figure 5. (a) Photograph of change in emission color of NDI-**1** (50 μM) upon UV-light irradiation (λ_{ex} = 365 nm) with increase in water content in DMSO; (b) Fluorescence microscope image of NDI-**1** in (1:99, v/v) DMSO-water mixture.

Initially, the emission colour of the solution did not show any change up to 20 vol% water in DMSO. Beyond 20 vol% water content (f_w = 20 vol%), the emission colour got changed to faint orange and upon gradual increase in the water content, the orange colour intensity was found to be enhanced (Figure 5a). This observation delineates that the NDI-**1** bola-type

amphiphilic molecules exhibited aggregation-induced emission (AIE) in DMSO-water solvent mixture. At 99 vol% water content (f_w = 99 vol%), the NDI-**1** solution showed bright reddish orange emission (Figure 5a) and presence of the red dotted particles in fluorescence microscopic image confirmed the formation of fluorescent organic nanoparticles (FONPs) (Figure 5b).

The observed photophysical change of the self-aggregated organic nanoparticle solution prompted us to investigate the emission behavior of the NDI-**1** bola-type amphiphilic molecules in DMSO-water binary solvent mixture. In photoluminescence study, the emission maximum (λ_{em}) of NDI-**1** (50 μM) in DMSO was observed at 406 nm (excitation wavelength (λ_{ex}) = 350 nm) with very poor fluorescence intensity (Figure 6a). Initially, with increase in water content within the DMSO solution, no significant change in fluorescence intensity (λ_{em} = 406 nm) was observed. Beyond f_w = 20 vol%, this characteristic monomeric peak slowly got disappeared and subsequently a new excimer band with λ_{em} at 588 nm was found to be generated. The intensity of this newly formed excimer band steadily enhanced with increment of the water content in DMSO. At the highest water percentage (f_w = 99 vol%), the emission maximum of the excimer band got shifted to 594 nm and showed ~6-fold higher emission intensity than that was observed for the DMSO solution of NDI-**1** (Figure 6a,b). This observation in the photoluminescence study delineates that NDI-**1** bola-type amphiphilic molecules showed aggregation-induced emission (AIE) through excimer formation. Also, it is in concurrence with the change in emission colour of the amphiphilic solution with varying water content (Figure 5a, 6b).

At this point, we were also curious to know the role of NDI-**1** concentration on its self-assembly (that was so far observed at varying water content using 50 μM of NDI-**1**). To this end, concentration-dependent fluorescence spectra of NDI-**1** in DMSO-water binary solvent mixtures were monitored at 40 vol% water content (Figure 6c). At lower concentration (10 μM) of NDI-**1**, no characteristic excimer band was observed (Figure 6c). With gradual increase in the concentration (from 15 μM onwards) of the bola-type amphiphilic molecules, the characteristic excimer band with λ_{em} = 588 nm was observed. The band intensity gradually enhanced with successive increase in the concentration (up to 75 μM) of NDI-**1** (Figure 6c). This observation clearly depicts that at f_w = 40 vol%, 15 μM of NDI-**1** was sufficient to initiate the self-assembled

aggregation. At higher concentration, a greater number of amphiphilic molecules got self-assembled and showed enhanced AIE even at lower concentration of water (i.e., f_w = 40 vol%).

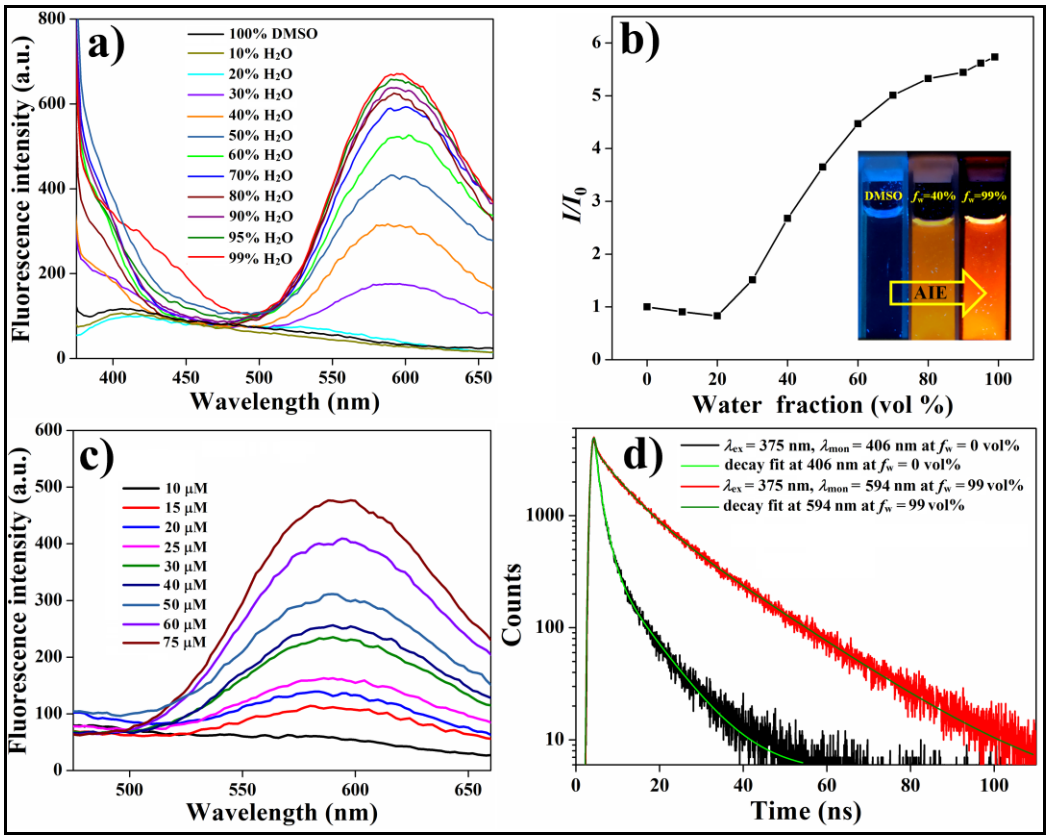

Figure 6. (a) Fluorescence spectra (λ_{ex} = 350 nm) of NDI-**1** (50 μM) in DMSO–water solvent mixture, (b) Plot of relative emission intensity (I/I_o) vs the fraction of water in DMSO of NDI-**1** where I_o = emission intensity in pure DMSO solution, (c) concentration-dependent emission spectra of NDI-**1** at 40% water content in DMSO, (d) TCSPC decay profiles of NDI-**1** monitored at 406 nm (pure DMSO) and 594 nm in (1:99,v/v) DMSO–water mixture upon excitation at 375 nm.

To further explain the emission behavior of NDI-**1** in pure DMSO and DMSO-water mixture, time-correlated single-photon counting (TCSPC) experiment was performed with a picosecond excitation at 375 nm of NDI-**1** (50 μM) in DMSO and DMSO-water mixture (Figure 6d). In each case, the decay curves were fitted by a triexponential function. In DMSO solution of NDI-**1** ($\lambda_{monitored}$ = 406 nm), the components were 1.7 ns (24.8 %), 0.3 ns (72.3 %), 8.32 ns (2.8 %) having short average lifetime ($\langle\tau\rangle$) 0.87 ns (Table 1). With increase in the water content in the DMSO solution of NDI-**1**, the average lifetime ($\lambda_{monitored}$ = 594 nm) was found to increase

and at the highest percentage of water (f_w = 99 vol%), the components were 6.37 ns (16.3 %), 17.63 ns (12.0 %) and 0.27 ns (71.7 %), and the average lifetime of NDI-**1** was 3.35 ns (Table 1). This long decay lifetime arises due to the pre-associated excimer formation by NDI-**1** bola-type amphiphilic molecules in higher content of water. Thus, TCSPC experiment further confirms that the AIE phenomenon of NDI-**1** bola-type amphiphilic molecules took place via excimer formation.

Table 1. Lifetime Values of NDI-**1** in Presence of Different Fractions of Water in DMSO (λ_{ex} = 375 nm).

Fraction of Water (vol%)	$\lambda_{monitored}$ (nm)	τ_1 (ns) (a_1)	τ_2 (ns) (a_2)	τ_3 (ns) (a_3)	Average lifetime (τ) (ns)
0	406	1.7 (0.248)	0.3 (0.723)	8.32 (0.028)	0.87
99	594	6.37 (0.163)	17.63 (0.012)	0.272 (0.717)	3.35

In the pH-dependent photoluminescence study, we have seen that there is no significant change in intensity or in λ_{em} of the characteristic excimer band (Figure 7a). This may conclude that the pH of the medium could not affect the emission and self-assembling ability of NDI-**1**. This observation further suggests that the presence of pyridyl moieties at both terminal end of NDI-**1** did not exhibit any notable effect on the pH sensitivity of the self-aggregates.

Next, we were intrigued to investigate the stability of the NDI-**1** FONPs in the self-aggregated state. To this end, we recorded time-dependent UV-visible and photoluminescence spectra of the organic nanoparticles at f_w = 99 vol % (Figure 7b,c). The relative absorbance (A/A_o at λ_{max} = 381 nm) and relative emission intensity (I/I_o at λ_{em} = 594 nm) were monitored at different timescales (up to 7 days) with 50 μM NDI-**1** in DMSO-water solvent mixture (f_w = 99 vol%). In the case of NDI-**1** FONPs (50 μM), the absorbance and the fluorescence remained same and marginally reduced by 10% after 7 days, which indicates the superior stability of NDI-**1** FONPs at their self-assembled state.

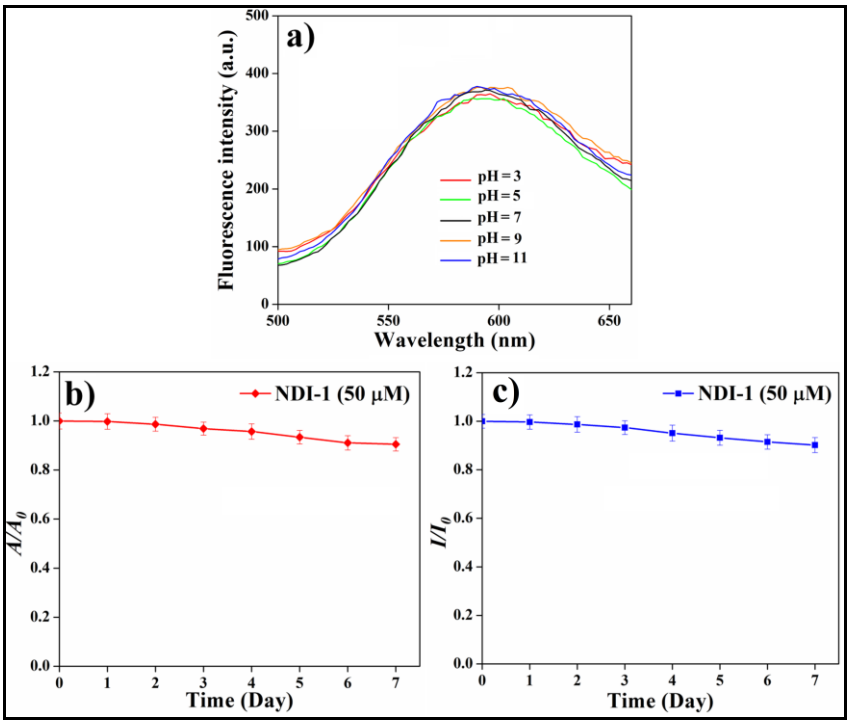

Figure 7. (a) Fluorescence spectra (λ_{ex} = 350 nm) of NDI-**1** (50 μM) in DMSO-water solvent mixture (f_w = 99 vol%) at different pH; Temporal evolution of (b) the absorbance at 381 nm and (c) fluorescence intensity at 594 nm of NDI-**1** (50 μM) in DMSO-water solvent mixture (f_w = 99 vol%).

In order to investigate the role of the charge-transfer process in this AIE mechanism, excitation-dependent emission spectra were recorded for NDI-**1** in f_w = 99 vol% (Figure 8a). The excitation dependent charge-transfer band (λ_{ex} = 360-400 nm) of NDI-**1** showed emission spectra having similar features to that was obtained at λ_{ex} = 350 nm (Figure 8a). The emission maximum (λ_{em} = 594 nm) almost remained unchanged with the increasing excitation wavelength up to 400 nm. Hence, there may be a possibility of charge-transfer (CT) between the donor-acceptor residues.[39] To further elucidate this CT-process (whether intermolecular or intramolecular CT), we have monitored the absorption and emission spectra of NDI-**1** in varying solvents of different polarities. No significant change in absorbance maxima (λ_{max}) was found for NDI-**1** in different solvents (from less polar benzene to moderately polar toluene and finally to chlorobenzene) (Table 2 and Figure 8b). In the photoluminescence study, the emission maxima (λ_{em}) gradually got red-shifted from 588 nm to 604 nm with increasing solvent polarity (Table 2 and Figure 8c).

Table 2. Photophysical property of NDI-**1**[a]

Solvent	Δf	λ_{ab} (nm)	λ_{em} (nm)	$\Delta\nu$ (cm^{-1})
Benzene	0.02	385	588	8968
Toluene	0.013	383	586	9045
o-Xylene	0.027	382	584	9057
m-Xylene	0.012	381	580	9006
Triethylamine	0.048	378	578	9154
Chlorobenzene	0.143	384	604	9486

[a]Abbreviation: Δf = solvent polarity parameters, λ_{ab} = absorption maximum, λ_{em} = emission maximum, $\Delta\nu$ = Stokes shift. Excitation wavelength (λ_{ex} = 350 nm)

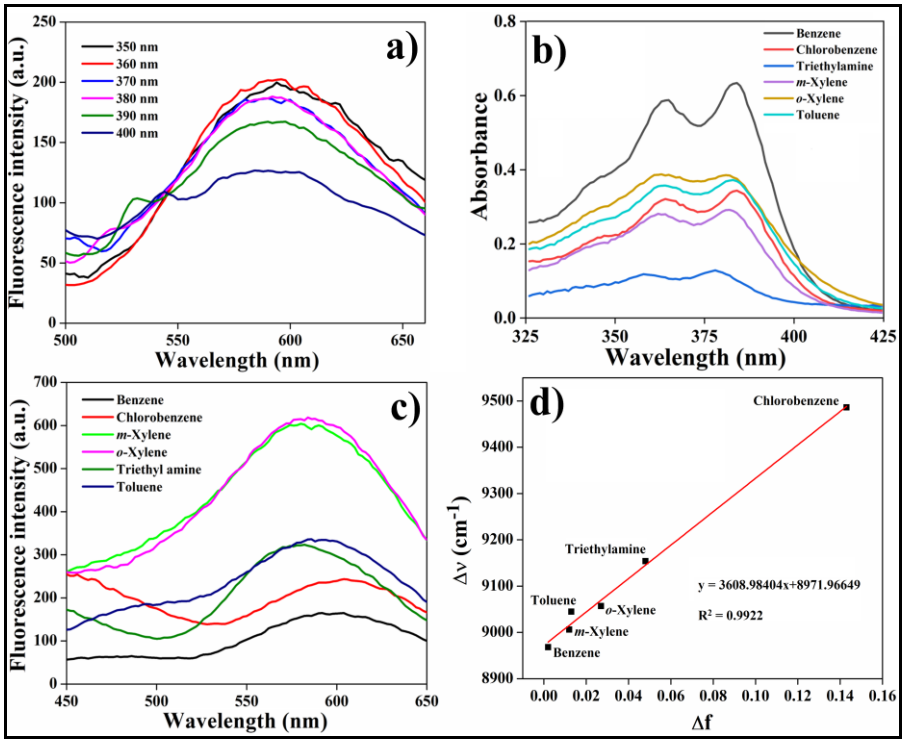

Figure 8. (a) Excitation dependent emission spectra of NDI-**1** (50 µM) in 1:99 v/v, DMSO-water, solvent dependent (b) absorption and (c) emission spectra of NDI-**1** (50 µM), (d) Plot of Stokes shift (Δν) of NDI-1 vs solvent polarity parameter (Δf).

The Stokes shift ($\Delta\nu$) of NDI-**1** in varying solvents was calculated, and their solvatochromic behaviors were quantitatively illustrated by the Lippert-Mataga equation:[40,41]

$$\Delta\nu = \nu_a - \nu_b = \frac{2\Delta f}{hca^3}(\mu_E - \mu_G)^2 + constant \qquad (1)$$

where ν_a and ν_e represent the maximum absorbance and emission wavenumbers, μ_G and μ_E are the dipole moments in the ground and excited states. *h*, *c*, and *a* are the Planck constant, the speed of light, the Onsager solvent cavity radius, respectively. The orientational polarizability or solvent polarity parameter Δf, described in equation 5, is chosen as the measure of polarity.

$$\Delta f = \frac{\varepsilon - 1}{2\varepsilon + 1} - \frac{n^2 - 1}{2n^2 + 1} \qquad (2)$$

where, ε is the static dielectric constant and *n* is the optical refractive index of the solvent. The linear dependence and positive solvatochroism was found for NDI-**1**, suggesting the participation of solvent polarity dependent intramolecular charge transfer (ICT) (Figure 8d and Scheme 1).

1.2.6 FORMATION OF NDI-1 FONP-PROTAMINE CONJUGATE.

After ensuring the formation of orange emitting NDI-**1** AIE-luminogens (AIE-gens), we aim to exploit the emissive property of AIE-gens in sensing biomolecule. To this end, as mentioned in the introduction, quantitative estimation of heparin (negatively charged linear polysaccharide) is very crucial considering its importance in preventing thrombosis during surgery and treating thrombotic diseases as an anticoagulant drug. Herein, we fabricated NDI-**1** based FONP-protamine (FONP-Pro) conjugate for heparin sensing. Protamines are arginine-rich positively charged nuclear proteins. It is well known to bind with heparin primarily through electrostatic interaction. The FONP-Pro conjugate was prepared by mixing varying concentration of protamine ranging from 0.2-7.0 μg mL^{-1} with NDI-**1** FONP (50 μM) solution in (1:99, v/v) DMSO-phosphate buffer saline (pH 7.4, 10 mM).

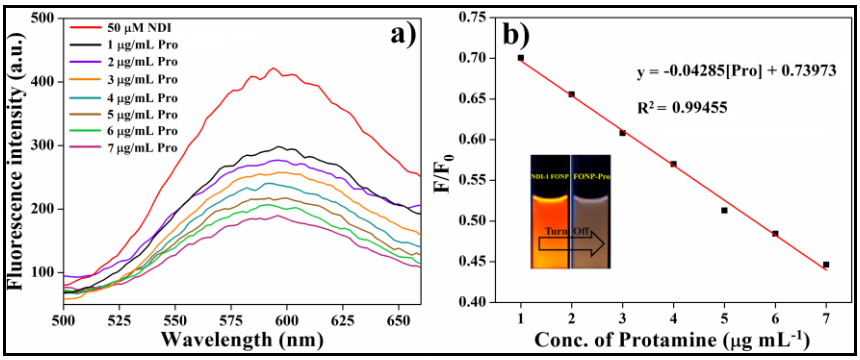

Figure 9. (a) Fluorescence spectra of NDI-**1** in the absence and presence of varying concentrations of protamine (Pro) (excitation wavelength = 350 nm), (b) Stern–Volmer plot of protamine doped in (1:99, v/v) DMSO–PBS (pH = 7.4, 10 mM) solution of NDI-**1** (50 μM).

The formation of FONP-Pro was investigated by monitoring the emission spectra of protamine doped NDI-**1** FONP solution (Figure 9a). Initially in presence of minute amount of protamine (up to 0.5 μg mL^{-1}), marginal decrease in the emission intensity at λ_{em} = 594 nm was observed. Interestingly, the emission intensity of NDI-**1** FONP markedly dropped in presence of 1 μg mL^{-1} protamine (Figure 9a). This emission intensity steadily reduced with increment of protamine concentration (up to 7 μg mL^{-1}, experimentally used highest concentration). The quenching in the orange emission was also evident in the respective solution (in cuvette) upon irradiation with UV-light (λ_{ex} = 365 nm, inset Figure 9b). The observed quenching in the emission of FONPs might have been originated due to feasible electrostatic interactions between positively charged protamine and NDI-**1** having high negative zeta-potential (-29.8 mV).

To quantitatively analyze the quenching of NDI-**1** by protamine, Stern-Volmer equation is applied:

$$\frac{F}{F_0} = 1 + K_{SV}[Q] \qquad (3)$$

In this equation 3, F_o and F are the emission intensities of NDI-**1** in the absence and presence of protamine, respectively; K_{SV} is the Stern-Volmer constant, which characterizes the quenching efficiency of the quencher; and [Q] is the concentration of the quencher. The change in F/F_o of NDI-**1** with protamine concentration is shown in Figure 9b. To this end, the Stern-Volmer plot showed linearity in quenching of NDI-**1** emission by protamine up to 7 μg mL^{-1}, having a Stern-Volmer constant (K_{SV}) of 0.06 mL μg^{-1} (Figure 9b).

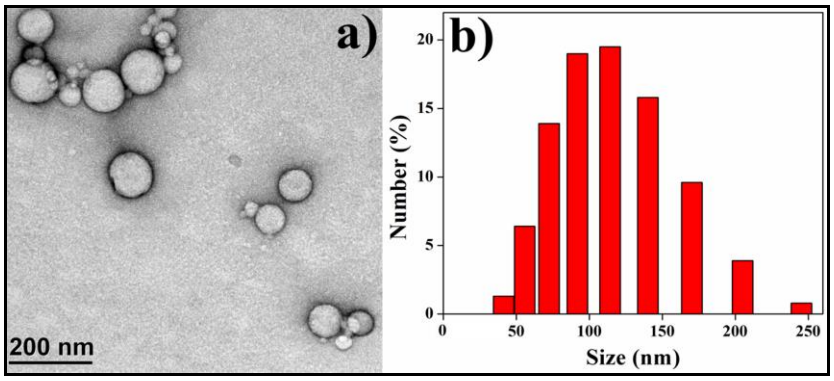

Figure 10. (a) Negatively stained TEM image, (b) DLS plot of particles size distribution of NDI-**1** FONP-Pro conjugate in (1:99, v/v) DMSO-water binary solvent mixture ([NDI-1] = 50 μM, [Protamine] = 1 μg mL^{-1}).

Additionally, TEM image of NDI-**1** FONP-pro conjugate in (1:99, v/v) DMSO-water binary solvent mixture ([NDI-**1**] = 50 μM, [Protamine] = 1 μg mL^{-1}) showed spherical-shaped particles having dimensions of 100-120 nm (Figure 10a). DLS plot of FONP-pro conjugate also confirmed the size of spherical aggregates i.e., 100-120 nm (PDI is 0.156) which was found in the respective TEM image (Figure 10).

Table 3. Zeta (ζ) potential values of NDI-**1** FONP-Protamine conjugate with different Protamine concentration.

Concentration of Protamine in NDI-**1** FONP-pro conjugate (μg mL^{-1})	Zeta (ζ) potential (mV)
1	+29.7
2	+37.4
3	+40.6
4	+48.3
5	+53.1
6	+62.9
7	+69.5

On the other hand, we measured zeta potential of FONP-Pro conjugate using different protamine concentrations from 1 μg mL^{-1} to 7 μg mL^{-1} resulting in the increase in the zeta potential value from +29.7 mV to +69.5 mV (Table 3). FONP-Pro conjugate formation was substantiated from the change in ζ-value from -29.8 mV to +29.7 mV upon the addition of protamine (1 μg mL^{-1}) in NDI-**1** FONP (50 μM) solution. Therefore, this experiment concludes that with increasing the concentrations of protamine, the overall positive charge of the conjugate got enhanced which further confirmed the formation of NDI-**1** FONP-Protamine conjugate.

1.2.7 FLUOROMETRIC SENSING OF HEPARIN.

Successful fabrication of FONP-Pro conjugate prompted us to detect heparin by fluorometric technique. This significant quenching of NDI-**1** FONP emission by protamine provided the advantage of low background signal for heparin sensing. We have also studied the photoluminescence spectra of native NDI-**1** FONPs in presence of heparin to investigate the

effect of heparin on spectral change of FONPs (Figure 11). No remarkable change in emission spectra was observed which indicates that heparin did not bind directly to the NDI-**1** obviously due to the similar negative charges.

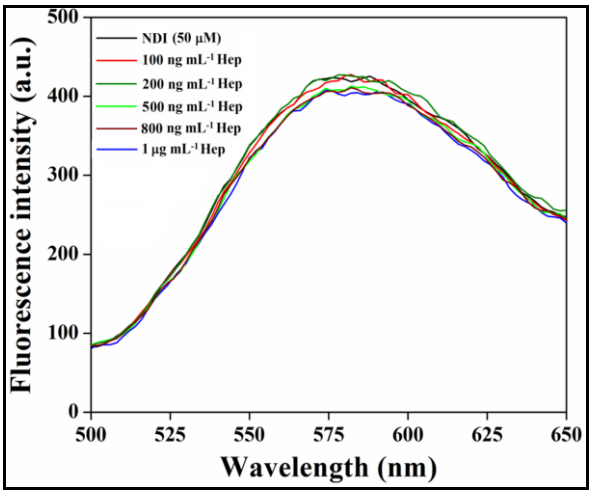

Figure 11. Photoluminescence spectra of NDI-**1** FONPs in presence of heparin in (1:99, v/v) DMSO-phosphate buffer saline (pH = 7.4, 10 mM) solution of NDI-1 FONPs ([NDI-**1**] = 50 μM).

On the other hand, once again FONP-Pro conjugate was prepared using 50 μM of NDI-**1** and 1 μg mL^{-1} of protamine. The fluorescence response of FONP-Pro conjugate towards heparin was monitored in 10 mM PBS solution and the corresponding emission spectra are shown in Figure 12a. Varying amounts of heparin (100-800 ng mL^{-1}) were added in (1:99, v/v) DMSO-phosphate buffer saline (pH 7.4, 10 mM) solution of NDI-**1** FONP-Pro conjugate. A notable increase in emission intensity (λ_{em} = 594 nm) of FONP up to 90% recovery of its (50 μM of NDI-**1**) native emission (in absence of protamine, Figure 9a) was observed upon the addition of 100-800 ng mL^{-1} of heparin (Figure 12a). Thereafter no further change in the fluorescence intensity was noted up to 1 μg mL^{-1} of heparin (Figure 12a). Interestingly, the enhancement in fluorescence intensity was prominent even at a very low concentration of heparin (100 ng mL^{-1}) when added to the conjugate solution. The visual change in the emission quenching of NDI-**1** FONP upon addition of protamine (due to the formation of NDI-**1**-Pro conjugate) and consequently fluorescence recovery in presence of heparin (Figure 12b inset) upon irradiation with UV-light irradiation (λ_{ex} = 365 nm) was shown in Figure 13.

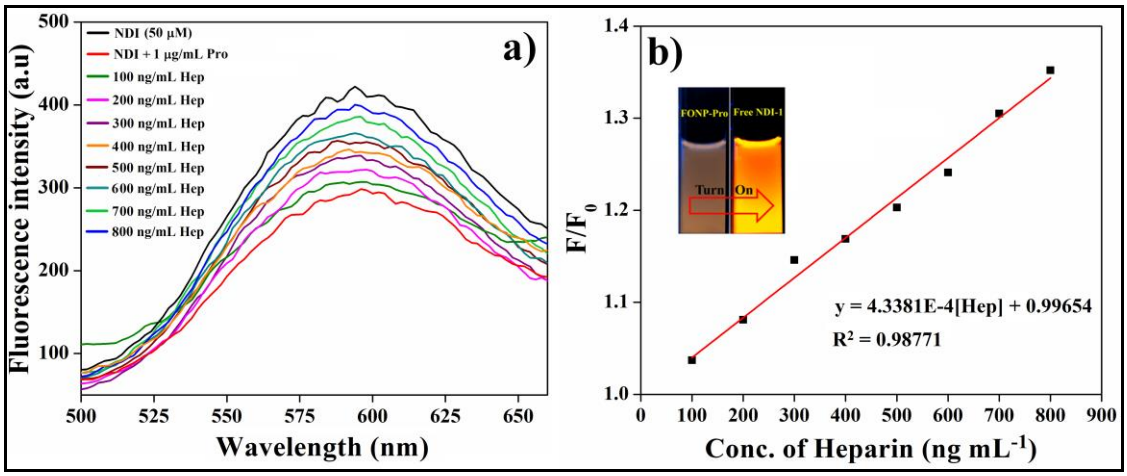

Figure 12. (a) Emission spectra of NDI-1 in absence and presence of varying heparin concentration in (1:99, v/v) DMSO-phosphate buffer saline (pH = 7.4, 10 mM) solution of FONP-Pro conjugate, (d) Stern-Volmer plot of heparin doped in (1:99, v/v) DMSO-phosphate buffer saline (pH = 7.4, 10 mM) solution of FONP-Pro conjugate ([NDI-1] = 50 μM, [Protamine] = 1 μg mL^{-1}).

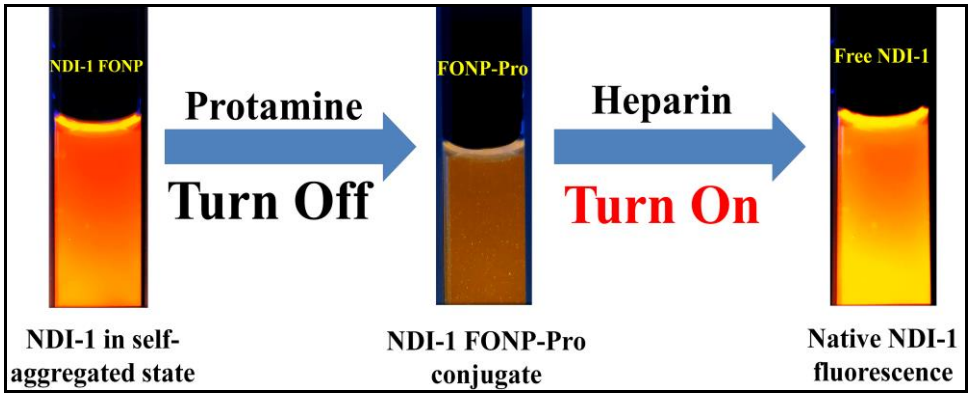

Figure 13. Photograph for heparin sensing by fluorescence off/on of AIE of NDI-**1** FONPs through formation of FONP-protamine conjugate. Excitation wavelength = 365 nm.

In presence of protamine (1 μg mL^{-1}) NDI-**1** (50 μM) FONP solution showed poor orange emission than that of native NDI-**1** FONP solution. This weak emission was due to the NDI-**1**-Pro conjugate formation. However, NDI-**1** FONP regained its fluorescence intensity upon addition of heparin (0.8 μg mL^{-1}) and the resulting solution showed bright orange emission as comparable to that of native FONP solution (Figure 13). This fluorescence 'turn-on' signal of NDI-**1** might be due to the strong binding affinity of negatively charged heparin with the positively charged protamine molecules through electrostatic interaction. In the presence of

heparin, protamine gets unwrapped from the NDI-**1** FONP surface (to form heprain-protamine conjugate), resulting in the restoration of native NDI-**1** FONP fluorescence (Scheme 1). As the fluorescence intensity of NDI-**1** FONP enhanced with increase in the concentration of heparin in the conjugate system, a linear regression curve was obtained from Stern-Volmer equation having $K_{SV} = 4.34\times10^{-4}$ mL ng^{-1} (Figure 12b).

Table 4. Zeta (ζ) potential values of solutions resulting by gradual addition of heparin (of varying concentrations) into NDI-**1** FONP-Protamine conjugate system.

Zeta-potential of NDI-**1** (50 μM) (mV)	Zeta-potential of Protamine in NDI-**1** FONP-pro conjugate ([NDI-**1**] = 50 μM, [Protamine] = 1 μg mL^{-1}). (mV)	Concentration of Heparin adding in NDI-**1** FONP-pro conjugate (ng mL^{-1})	Zeta-potential of the resulting solution (mV)
-29.8	+29.7	100	+26.8
		200	+21.4
		300	+17.7
		400	+12.1
		500	+5.3
		600	-11.6
		700	-18.2
		800	-25.7
		1000	-28.9

Moreover, this fact was also verified by measuring the zeta potential values of the solution resulting from gradual addition of heparin (of varying concentrations) into the NDI-**1** FONP-Protamine conjugate solution. The results showed that with increasing concentration of heparin into the FONP-Pro conjugate solution, zeta potential decreases up to -28.9 mV which validated the unwinding of protamine molecules from NDI-**1** FONP surface and regeneration of native NDI-**1** FONPs (Table 4). After successful detection of heparin by simple fluorescence 'turn-on' technique, we were interested to quantify the limit of detection (LOD) value of heparin molecules in presence of FONP-Pro conjugate. To quantify heparin in solution, the changes in emission intensity shown in Figure 12a were correlated to the heparin concentration using $\phi = (F - F_o)/F_o$, where F_o and F were fluorescence intensities of FONP-Pro conjugate at 594 nm in the absence and presence of heparin, respectively (Figure 14).

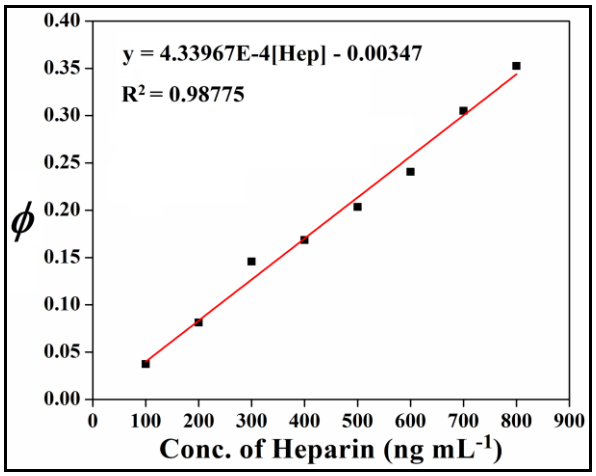

Figure 14. Fluorescence response of the FONP-Pro conjugate towards heparin sensing with varying concentrations of heparin in (1:99, v/v) DMSO-phosphate buffer saline (pH = 7.4, 10 mM) solution of FONP-Pro conjugate ([NDI-**1**] = 50 μM, [Protamine] = 1 μg mL^{-1}).

The calibration parameter (ϕ) is defined to minimize the influence of fluorescence background and to estimate the assay sensitivity. The ϕ was a function of heparin concentration in 10 mM PBS (pH = 7.4) in the presence of 50 μM NDI-**1** and 1 μg mL^{-1} protamine. The linear regression equation was $\phi = (F - F_0)/F_0 = -0.00347 + 4.33967\times10^{-4}$ [Hep], with a correlation coefficient (R^2) of 0.988. Moreover, the limit of detection (LOD) of 180 ng mL^{-1} (12 nM considering the average molecular weight of heparin, ~15 kDa) was calculated based on 3σ/S (σ was the standard deviation and S was the slope of the calibration curve). Considering the recommended therapeutic dosing level of heparin for cardiovascular surgery (17-67 μM) and for post-operative and long-term care (1.7-10 μM), the probe showed remarkable sensitivity for the detection of heparin in samples.[42]

NDI-**1** FONP-Pro conjugate showed good sensitivity for heparin in pure buffer. However, to be more useful in a bioassay, the detection system should be able to tolerate any interference from real biological samples. Therefore, FBS (fetal bovine serum) was used to investigate the feasibility of the method for use with biological samples (Figure 15a). The spectra of the sensor in 10% FBS containing buffered water/ethanol (85/15) solution showed that addition of heparin (0.1 to 1 μg mL^{-1}) to a solution of NDI-**1** FONP-Pro conjugate resulted in a gradual increase in the fluorescence intensity and further addition of heparin does not lead to obvious changes in the emission behavior in diluted solution of bovine serum.

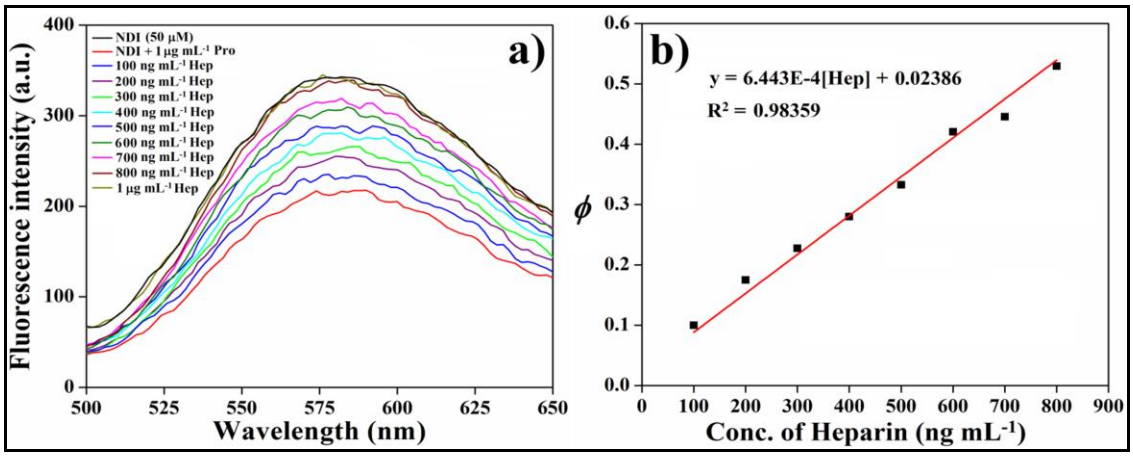

Figure 15. (a) Fluorescence spectra of NDI-**1** FONP-Pro conjugate (([NDI-**1**] = 50 μM, [Protamine] = 1 μg mL^{-1}) in 10% FBS (fetal bovine serum) containing buffered (10 mM, PBS, pH 7.4) water/ethanol (85/15) solution upon addition of varying concentration of heparin, (b) Fluorescence response of the FONP-Pro conjugate towards heparin sensing with varying concentrations of heparin in (1:99, v/v) DMSO-phosphate buffer saline (pH = 7.4, 10 mM) solution of FONP-Pro conjugate ([NDI-**1**] = 50 μM, [Protamine] = 1 μg mL^{-1}).

The heparin saturation concentration in serum is comparatively lower in serum to that of only buffer due to charge pairing between the proteins in serum and NDI-**1** FONP-Pro conjugate, which partially blocks the interaction between NDI-**1** FONP-Pro conjugate and heparin. In order to explore the practical application of NDI-**1** FONP-Pro conjugate in a "turn-on" assay for heparin sensing, the LOD (limit of detection) was calculated in a similar way to the previously mentioned method (Figure 15b). The LOD of this sensing technique in serum solution was found to be 208 ng mL^{-1} (~14 nM considering the average molecular weight of heparin, ~15 kDa) which indicates NDI-**1** FONP-Pro conjugate is a promising fluorescence probe for the detection of heparin in biological systems.

1.2.8 SELECTIVITY OF NDI-1 FOR HEPARIN DETECTION.

Selectivity is one of the important parameters to evaluate the performance of a newly developed fluorescence sensor. The major pre-requisite parameters for a smart fluorometric sensor are high selectivity and sensitivity. Selectivity has been considered to be one of the greatest challenges for heparin detection operating in biological media. To ascertain that the present technique is specific to heparin sensing, a number of other proteins were also examined through fluorescence sensing using NDI-**1** FONP-Pro conjugate. We have used two positively

charged proteins i.e, cytochrome c (Cyt c), trypsin (Tryp), two neutral proteins i.e, horseradish peroxidase (HRP) and hemoglobin (Hb); two acidic proteins, bovine serum albumin (BSA) and pepsin (Pep) and also double stranded-DNA under similar experimental conditions as mentioned in the preceding paragraph.

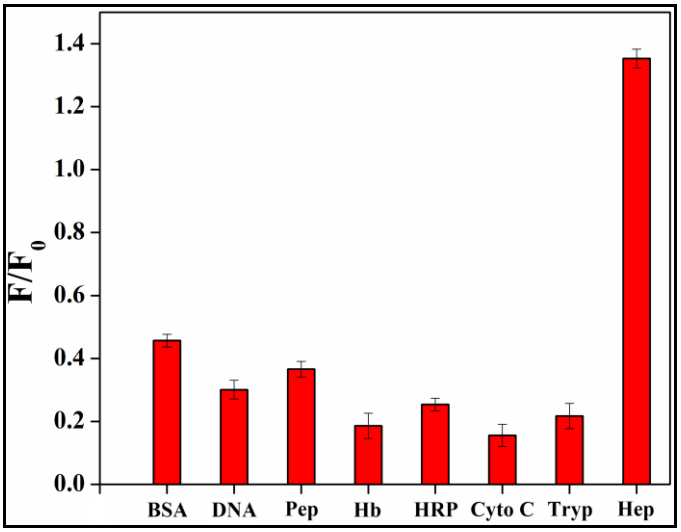

Figure 16. Selectivity of FONP-Pro conjugate ([NDI-**1**] = 50 μM, [protamine] = 1 μg mL^{-1}) to heparin over other biomolecules in (1:99, v/v) DMSO-phosphate buffer saline (pH = 7.4, 10 mM) solution of FONP-Pro conjugate. The error bars represent the standard deviations.

In each case 800 ng mL^{-1} of protein, other biomolecules and heparin was added separately in (1:99, v/v) DMSO-phosphate buffer saline (pH = 7.4, 10 mM) solution of FONP-Pro conjugate. Except heparin no significant change in enhancement of relative fluorescence intensity was observed in presence of the added biomolecules (Figure 16). The selectivity study of NDI-**1** suggested that the selective binding affinity of negatively charged heparin molecules to the positively charged protamine facilitated unwinding of protamine molecules from NDI-**1** FONP surface. Consequently, the NDI-**1** FONPs became free from the NDI-pro conjugate and regained its native emission intensity. In the present study, the direct attachment of protamine on NDI-**1** FONPs surface possibly made this sensing probe more sensitive as well as more selective towards heparin. The simplistic and selective sensing mechanism of heparin by this FONP-Pro conjugate is found to be superior in contrast to some previously reported methods (Table 5).[42-51] Hence, the newly developed NDI-pro conjugate emerges as a selective and efficient heparin sensor.

Table 5. Literature Survey on Reported Heparin Sensing.

Probes	LOD	Response type	References
Cationic polythiophene	0-60 μM	Colorimetric technique	42
Molecular rotor dye, Thioflavin-T	34-90 nM	Fluorescence turn-on sensing	43
Silacyclopentadiene derivative.	23 nM	Fluorescence turn-on sensing	44
Quinine Derivatives	30 nM	Fluorescence turn-on sensing	45
Polycation-induced benzoperylene probe	50 nM	Fluorescence turn-off sensing	46
AuNPs (protamine-coated)	40 nM	Colorimetric technique	47
Long chain associated pyrene derivative	0.157 μM	Ratiometric fluorescence sensing	48
Chromophore-tethered copolymer	Not measured	Fluorescence turn-off sensing	49
Anthracene and tetraphenylethene derivative	20 nM	Ratiometric fluorescence sensing	50
$CuInS_2$ quantum dots	12.46 nM	Fluorescence turn-off sensing	51
FONP-Pro conjugate	**12 nM**	**Fluorescence turn-on sensing by successful formation of FONP-protamine conjugate and exploiting the AIE property of synthesized NDI-1 FONPs for sensing**	**Present Chapter**

1.3 CONCLUSION

In conclusion, we have designed L-aspartic acid tagged naphthalene diimide (NDI) based bola-type amphiphilic molecule (NDI-**1**) having 3-aminopyridyl and naphthyl residues at both the terminals. NDI-**1** bola-type amphiphilic molecules formed spherical organic nanoparticles in DMSO-water binary solvent mixture via *J*-type aggregation. The amphiphilic solution in molecularly dissolved state (in DMSO) showed weak blue emission. However, these weakly emissive bola-type amphiphilic molecules exhibited aggregation-induced orange emission through excimer formation at 30 vol% water content. With gradual increase of water content up to 99 vol%, the excimer band intensity was successively enhanced with emission

maximum 594 nm upon excitation at 350 nm. Presence π-electron rich naphthyl residue at the donor site facilitates the ICT process to exhibit higher wavelength emitting (orange) FONPs. This novel FONPs comprise of negative surface charge (due to presence of 3-aminopyridyl unit) formed conjugates with positively charged protamine leading to the quenching of fluorescence of NDI-**1** FONPs. This stable protamine wrapped FONP conjugate (FONP-Pro) can act as a fluorescence 'turn-on' (restoration of excimer band intensity) sensor for selective detection of heparin over other negatively charged biomolecules. This fluorometric sensor can detect as low as 180 ng/mL (equivalent to 12 nM) of heparin. Hence, this simple fluorescence off/on technique by exploitation of AIE will have wide horizon for the detection of low levels of heparin in clinical samples.

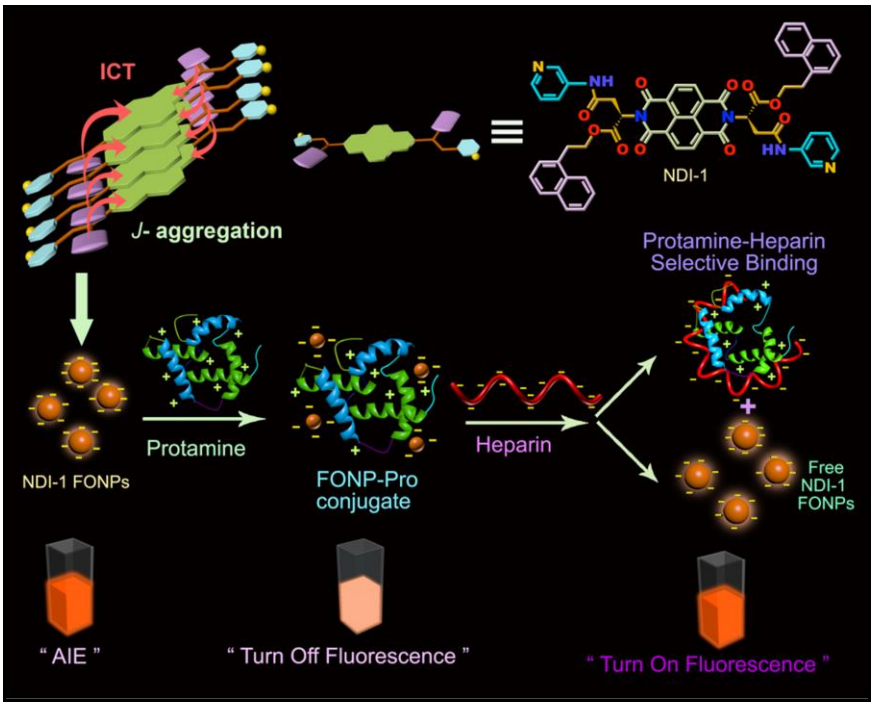

Scheme 1. Schematic Representation of Heparin-Sensing by Quenching and Restoration of AIE of NDI-**1** FONPs through Formation of the FONP–Pro Conjugate. AIE: Aggregation-induced emission, ICT: intramolecular charge transfer.

1.4 EXPERIMENTAL SECTION

1.4.1 MATERIALS.

1,4,5,8-Naphthalenetetracarboxylic dianhydride, 1-naphthaleneethanol, *N*-(tert-Butoxycarbonyl)-L-aspartic acid 4-benzyl ester, 3-aminopyridine, heparin, protamine and all deuteriated solvents were procured from Sigma-Aldrich. *N*,*N*-dicyclohexylcarbodiimide (DCC), 4-*N*,*N*-(dimethylamino) pyridine (DMAP), *N*-hydroxybenzotriazole (HOBT), *N*-hydroxysuccinimide (NHS), trifluoroacetic acid (TFA), triethylamine (Et_3N), pyridine, palladium 10% on activated charcoal, solvents, silica gel (60-120 mesh and 100-200 mesh) for column chromatography, other reagents were acquired from SRL, India. Milli-Q water was used for all experiments. Thin layer chromatography was performed on Merck precoated silica gel 60-F_{254} plates. Protamine and heparin (average MW ~15 kDa) were brought from Sigma-aldrich. Sodium hydroxide (NaOH) pellets and sodium carbonate (Na_2CO_3) were bought from Spectrochem, India. NMR spectroscopy was performed in 300 MHz and 400 MHz AVANCE (Bruker) spectrometer. MALDI-TOF spectra were recorded on Bruker Ultraflex MALDI mass spectrometer with 2,5-dihydroxy benzoic (DHB) acid as matrix.

1.4.2 SYNTHESIS OF NDI-1.

To synthesize NDI-**1**, *N*-(*tert*-butoxycarbonyl)-L-aspartic acid 4-benzyl ester (1.2 eqv) and 1-naphthaleneethanol (1.0 eqv) were coupled together using DCC (1.1 eqv), DMAP (1.1 eqv) and HOBT (1.1 eqv). Dry dichloromethane (DCM) was used as solvent and the reaction was stirred for 12 h under nitrogen atmosphere. 1(N) HCl was used to wash the organic layer and the organic solvent was dried over anhydrous sodium sulfate. After evaporation of the organic part, the coupled product (Scheme 2) was purified by column chromatography using 60-120 mesh silica gel using 1% methanol in chloroform as eluent. TFA (1.5 eqv) was used to deprotect the BOC (*tert*-butoxycarbonyl) group from the coupled product and the reaction was carried out in dry DCM. After 4h of stirring, the organic solvent was removed and the concentrated mass was dried. The obtained mass was solubilized in EtOAc. Aqueous Na_2CO_3 solution (10%) and water was used to wash the organic layer for two times and the organic part was dried over anhydrous Na_2SO_4. The organic part was evaporated to obtain free amine derivative. Finally, 1,4,5,8-naphthalenetetracarboxylic dianhydride (1.0 eqv) and free amine derivative (2.2 eqv) were

heated (90 °C, 12 h) in dry DMF. The reaction mixture was cooled to room temperature and DMF was removed by vacuum distillation. The crude mass was solubilized in DCM and washed with water. The expected product was collected from DCM part. Purification of the condensed product was performed by column chromatography (100-200 mesh silica gel, 3% MeOH/$CHCl_3$ as an eluent) and washed with diethyl ether to obtain the product.

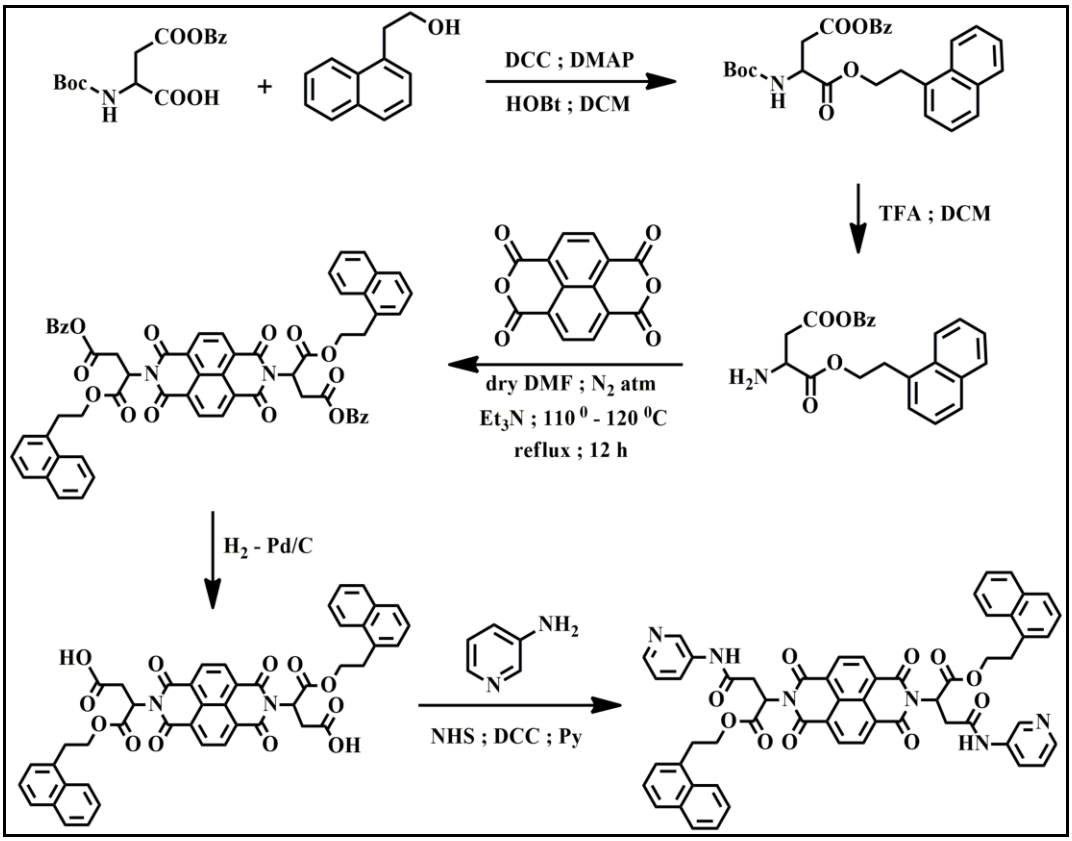

Scheme 2. Synthetic scheme of naphthalene diimide (NDI) based bola-amphiphile NDI-**1**.

The hydrogenation reaction of the obtained product (in the preceding step) was carried out in presence of Pd on activated charcoal in dry THF and the reaction mixture was stirred overnight at room temperature to deprotect the benzyl protection. The whole mixture was filtered in a $celite_{545}$ column where hot THF was used as eluent. The THF was then removed completely with vacuum pump to get the acid. NHS activation of the acid was performed by using the previously formed acid, DCC (2.6 equiv), and NHS (2.3 equiv) in dry DMF and stirred overnight under N_2 atmosphere. To this activated acid, 3-aminopyridine (2 equiv) and dry pyridine (excess) were added. The reaction mixture was stirred overnight and the DMF was distilled out under vacuum. The residue mixture was then purified through column chromatography by using 100–

200 mesh silica gel and 5% MeOH/$CHCl_3$ as the eluent to obtain pure NDI-**1** (Scheme 2). NDI-**1** was characterized by ^{1}H-NMR, ^{13}C-NMR and MALDI-TOF mass spectrometry.

1.4.3 PREPARATION OF SAMPLE.

NDI-**1** is highly soluble in DMSO. So, stock solution of all the NDI derivative (10 mM) was prepared in DMSO. From this stock solution of DMSO, desired amount aliquot was added to the DMSO-water solvent system of different ratios to achieve 50 μM concentration for different experiments.

1.4.4 TRANSMISSION ELECTRON MICROSCOPY (TEM) STUDY.

For transmission electron microscopic investigation, NDI-**1** (50 μM) solution in (1:99 v/v) DMSO-water and NDI-**1** FONP-Pro conjugate in (1:99, v/v) DMSO-water binary solvent mixture ([NDI-**1**] = 50 μM, [Protamine] = 1 μg mL^{-1}) were deposited on a 300-mesh carbon-coated copper grid and dried. The copper grid was negatively stained with freshly prepared uranyl acetate solution (1 μL, 1% w/v), and the excess solution was immediately blotted with a filter paper. The sample was then dried for 4 h in vacuum before taking the image. JEOL JEM 2010 microscope was used to take the TEM images.

1.4.5 ATOMIC FORCE MICROSCOPY (AFM) STUDY.

The AFM image of NDI-**1** was taken on a Veeco, model AP0100 instrument in noncontact mode. 10 μL of solution of NDI-**1** (100 μM) taken in (1:99 v/v) DMSO-water was deposited on freshly cleaved (1 cm × 1 cm) mica and dried overnight before imaging.

1.4.6 DYNAMIC LIGHT SCATTERING (DLS) STUDY AND ZETA (ζ) POTENTIAL MEASUREMENT.

Mean hydrodynamic diameter (D_h) of aggregates of NDI-**1** (50 μM) in (1:99 v/v) DMSO-water mixture and NDI-**1** FONP-Pro conjugate in (1:99, v/v) DMSO-water binary solvent mixture ([NDI-**1**] = 50 μM, [Protamine] = 1 μg mL^{-1}) were determined by DLS using a fixed-angle apparatus (Zen 3690 Zetasizer Nano ZS instrument (Malvern Instrument Ltd.)). The scattering intensity was measured at an angle of 175°. The zeta (ζ) potential measurement was performed with solution of 50 μM concentration of NDI-**1** in (1:99 v/v) DMSO-water mixture as

well as of the FONP-Pro conjugates in (1:99, v/v) DMSO-phosphate buffer saline (pH = 7.4, 10 mM) solution ([NDI-**1**] = 50 μM, [Protamine] = 1-7 μg mL^{-1}) at room temperature and also for the solution resulting from gradual inclusion of heparin into the NDI-**1** FONP-Pro conjugate solution in (1:99, v/v) DMSO-phosphate buffer saline (pH = 7.4, 10 mM) solution ([NDI-**1**] = 50 μM, [Protamine] = 1 μg mL^{-1}) at room temperature.

1.4.7 UV-VISIBLE STUDY.

UV-vis spectra were recorded on a PerkinElmer Lambda 25 spectrophotometer. We have taken the UV-vis spectra of NDI-**1** (50 μM) in different solvent mixtures of DMSO-water varying the volume of DMSO (non-self-aggregated solvent) from 100% to 1%, i.e., (1:99 v/v) DMSO-water (self-aggregated solvent). Temperature-dependent UV-vis spectroscopic study of NDI-**1** was also performed in (1:1 v/v) DMSO-water ([NDI-**1**] = 50 μM) to investigate the self-aggregation behavior of NDI-**1**. UV-vis spectra of NDI-**1** (50 μM) were also recorded in different organic solvents (benzene, chlorobenzene, *o*-xylene, *m*-xylene, toluene, triethylamine) of varying polarities to monitor the intramolecular charge transfer (ICT) process.

1.4.8 FTIR STUDY.

FTIR measurements were performed at the non-self-assembled state in $CHCl_3$ and in the self-aggregated state in (1:9 v/v) DMSO-d_6-D_2O for NDI-**1** at room temperature. All the experiments were performed in Perkin Elmer Spectrum 100 FTIR spectrometer using 1 mm CaF_2 cell (in $CHCl_3$ solution and (1:9 v/v) DMSO-d_6-D_2O)).

1.4.9 SOLVENT-DEPENDENT ^{1}H-NMR STUDY.

Avance 300 MHz (Bruker) spectrometer was used to record solvent dependent ^{1}H-NMR spectra of NDI-**1** (1 mM) in DMSO-d_6 and in various solvent mixture of DMSO-d_6-D_2O (2:1 (v/v) and 1:1 (v/v) DMSO-d_6-D_2O).

1.4.10 FLUORESCENCE MICROSCOPY STUDY.

10 μL solution of NDI-**1** (50 μM) in (1:99 v/v) DMSO-water solvent mixture was drop-cast on a glass slide, dried, and observed under fluorescence microscope (Olympus IX-83) at 40x magnification.

1.4.11 PHOTOLUMINESCENCE STUDY.

We have recorded the emission spectra of the solutions of NDI-**1** (excitation wavelength (λ_{ex}) = 350 nm) in a Varian Cary Eclipse luminescence spectrometer. NDI-**1** stock solution was prepared in DMSO. The required amount of NDI-**1** stock solution was added to different solvent mixtures of DMSO-water so that the final concentration of NDI-**1** was 50 μM. Concentration dependent emission spectra of NDI-**1** were also obtained at 40 vol% water in DMSO. pH dependent fluorescence spectra of NDI-**1** (50 μM) in (1:99 v/v) DMSO-water were also documented in different pH medium (pH = 3 to 11). Excitation dependent emission spectra of NDI-**1** (50 μM) in (1:99 v/v) DMSO-water were recorded with excitation range 350-400 nm. Emission spectra of NDI-**1** (50 μM) were recorded in different organic solvents (benzene, chlorobenzene, *o*-xylene, *m*-xylene, toluene, triethylamine) of varying polarities to monitor the intramolecular charge transfer (ICT) process.

1.4.12 QUANTUM YIELD (QY) MEASUREMENT.

QYs are generally measured relative to an optical dilute standard fluorophore solution that exhibits a well-known quantum yield (ϕ_s). The quantum yields of the unknown fluorophore (ϕ_u) were determined by using the Parker-Rees method.

Equation

$$\emptyset_u = \left(\frac{A_s F_u n_u^2}{A_u F_s n_s^2}\right)\emptyset_s \qquad (4)$$

Here, A_u = the absorbance of unknown sample at the excitation wavelength, A_s = the absorbance of reference sample at the excitation wavelength, F_u = the total area of integrated fluorescence intensity for the unknown sample when excited at the same excitation wavelength, and F_s = the area of the integrated fluorescence intensity for the known sample when excited at the same excitation wavelength. We used a solution with similar absorbance (<0.01) for the determination of quantum yield. The refractive indices of the solvents in which the unknown and the standard samples were prepared are given by n_u and n_s respectively. Here, in our study we have chosen quinine sulfate in 0.1 M sulfuric acid (H_2SO_4) as the standard and its QY (ϕ_s) is known to be 54.0%.

1.4.13 TIME RESOLVED STUDY.

Time correlation single photon count (TCSPC) measurement was performed in a picosecond diode laser IBH-405. A stock solution of NDI-**1** was prepared in DMSO, and requisite amount of water was added to 1 mL of DMSO to make (1:99 v/v) DMSO-water solution having an absorbance value <0.1. All the samples were excited at 375 nm followed by monitoring of the emission at 406 nm for only DMSO and at 594 nm for (1:99 v/v) DMSO-water binary solvent mixtures. The fluorescence decays were analyzed with IBH DAS6 software. Equation 2 was used to analyze the experimental time resolved fluorescence decay $p(t)$.

$$p(t) = b + \sum_{i}^{n} \alpha_i \exp\left(-\frac{t}{\tau_i}\right) \quad (5)$$

where n is the number of discrete emissive species, b is a baseline correction ("dc" offset), and α_i and τ_i are pre-exponential factors and excited state fluorescence lifetimes associated with the i-th component, respectively. For multiexponential decays, the average lifetime was calculated from equation 3.

$$< \tau > = \sum_{i=1}^{n} \alpha_i \tau_i \quad (6)$$

Where $\alpha_i = \frac{\alpha_i}{\sum \alpha_i}$ which indicates the contribution of a decay component.

1.4.14 STABILITY EXPERIMENT OF NDI-1 FONPs.

Stability of NDI-**1** FONPs (50 μM) in f_w = 99 vol % was monitored for a long time period (up to 7 days). The absorbance and emission intensities of this solution were recorded at 381 and 594 nm, respectively, at different time interval for the determination of suspension stability of NDI-**1** FONPs.

1.4.15 HEPARIN SENSING STUDY.

NDI-**1**-Pro conjugate was formed by mixing the NDI-**1** solution (50 μM) and protamine solution (1 μg mL^{-1} from the stock of 2 mg mL^{-1}) in (1:99, v/v) DMSO-phosphate buffer saline (pH = 7.4, 10 mM). Fluorescence spectra were taken by exciting at 350 nm with changing the concentration of protamine. Stern-Volmer constant (K_{SV}) of protamine in presence of NDI-**1**

was determined using the equation: $F_o/F = 1 + K_{SV}[Q]$, where F_o and F are the fluorescence intensities of protamine in conjugate form [NDI-**1** (50 μM) + protamine (1 μg mL^{-1})] and with gradual increase of protamine concentration and [Q] signifies the concentration of the quencher protamine. In order to demonstrate the practical application of the fabricated fluorescence sensor, photoluminescence study of interaction of heparin solution with FONP-Pro conjugate in buffer solution as well as in FBS (fetal bovine serum) solution were recorded by addition of heparin of varying concentration into the solution of NDI-**1** FONP-Pro conjugate. We also evaluated the detection limit of the sensing mechanism and studied the selectivity of the fluorimetric probe against different biomolecules.

1.5 CHARACTERIZATION DATA

NDI-1: ^{1}H-NMR (400 MHz, DMSO-d_6, 25 °C): δ/ppm: 8.83 (m, 1H, C-2 proton of aminopyridine ring), 8.69 (s, 1H, C-4 proton of aminopyridine ring), 8.51 (s, 4H, NDI core), 7.86-8.13(m, 4H, C-4,C-5,C-8 proton of naphthyl ring and C-6 proton of aminopyridine ring), 7.11-7.63 (m, 2H, C-3,C-7 proton of naphthyl ring) 6.94-6.98 (m, 2H, C-2 proton of naphthyl ring), 5.96-6.16 (m, 2H, chiral centre of L-aspartic acid residue), 4.17-4.42 (m, 4H, -O-C$\underline{H}_2$-CH_2-$C_{10}H_7$), 2.69-3.15 (m, 8H, -O-CH_2-C$\underline{H}_2$-$C_{10}H_7$ and methylene protons of L-aspartic acid residue).

^{13}C-NMR (100 MHz, $CDCl_3$): δ/ppm: 170.86, 168.58, 168.51, 162.39, 162.23, 143.67, 142.21, 139.34,138.17, 135.50, 133.49, 131.95, 131.15, 128.52, 128.42, 128.39, 128.35, 127.15, 126.66, 126.60, 126.15, 126.05, 125.99, 125.37, 125.22, 123.29, 67.54, 66.97, 66.07, 66.01, 34.16, 34.11, 33.84, 33.34, 31.47.

MALDI-TOF MS: *m*/*z*: 958.30 $[M]^+$ (calculated); 958.76 (found).

1.6 SPECTRA

1.6.1 ^{1}H-NMR SPECTRUM.

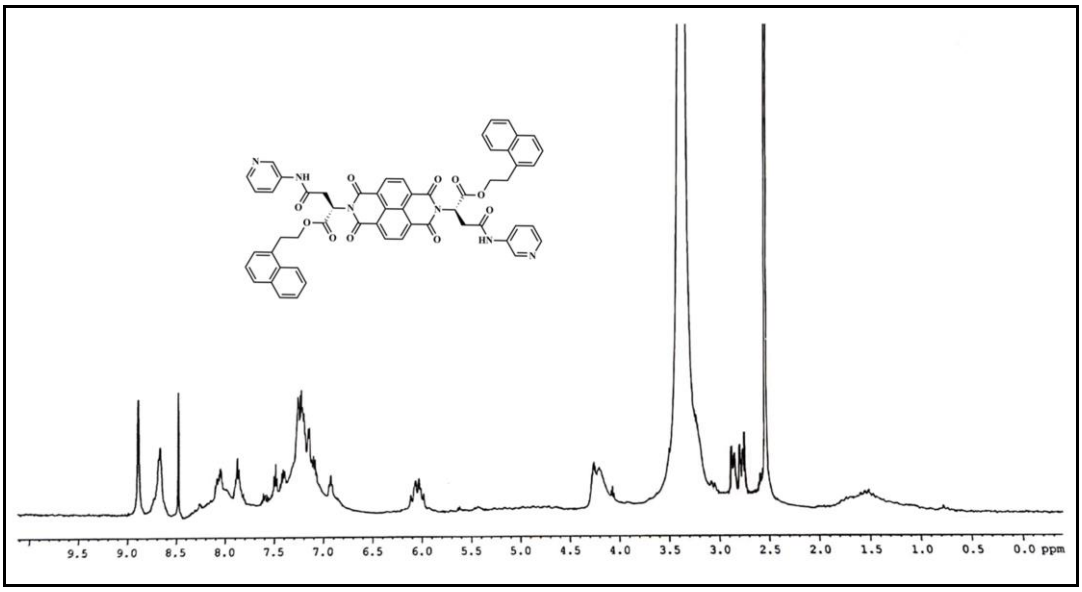

1.6.2 ^{13}C-NMR SPECTRUM.

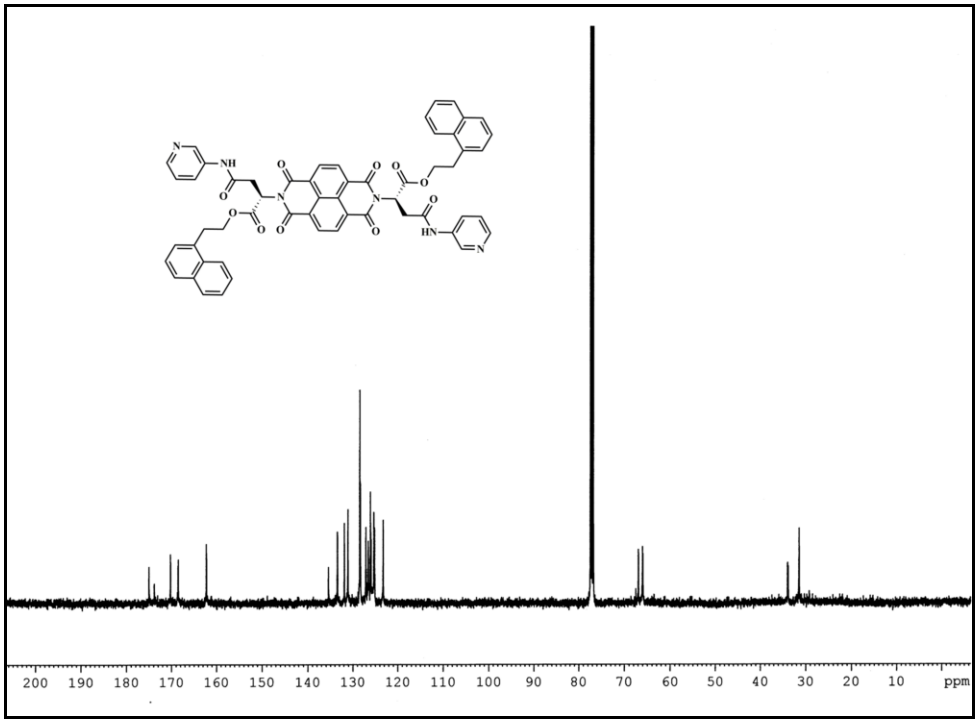

1.6.3 MALDI-TOF MASS SPECTRUM.

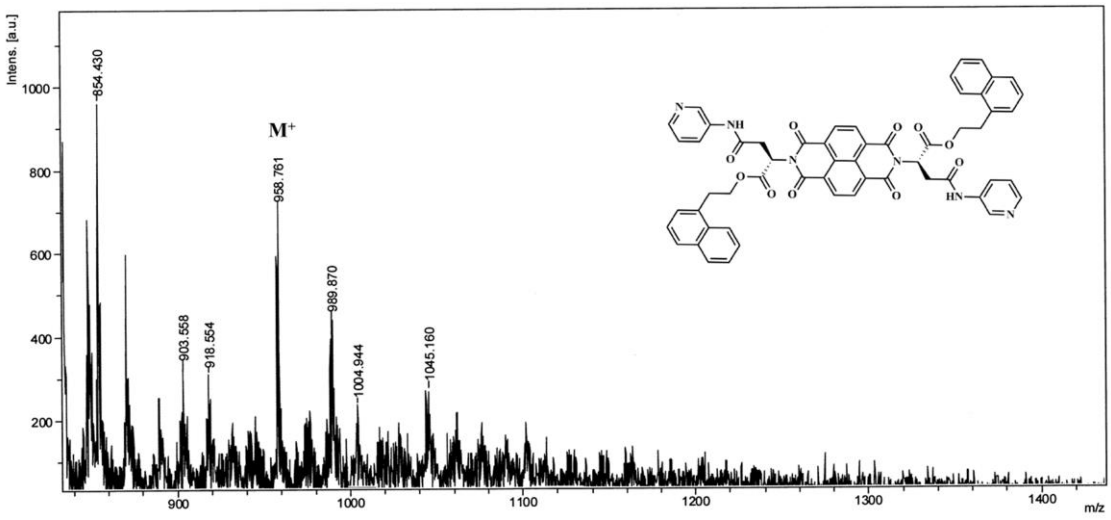

1.7 REFERENCES

[1] Desmonts, L. B.; Reinhoudt, D. N.; Calama, M. C. Design of fluorescent materials for chemical sensing. *Chem. Soc. Rev.* **2007**, *36*, 993-1017.

[2] Kobayashi, H.; Ogawa, M.; Alford, R.; Choyke, P. L.; Urano, Y. New strategies for fluorescent probe design in medical diagnostic imaging. *Chem. Rev.* **2010**, *110*, 2620-2640.

[3] Chan, C. W.; Smith, D. K. Pyrene-based heparin sensors in competitive aqueous media-the role of self-assembled multivalency (SAMul). *Chem. Commun.* **2016**, *52*, 3785-3788.

[4] Bau, L.; Tecilla, P.; Mancin, F. Sensing with fluorescent nanoparticles. *Nanoscale* **2011**, *3*, 121-133.

[5] Yao, J.; Yang, M.; Duan, Y. Chemistry, biology, and medicine of fluorescent nanomaterials and related systems: new insights into biosensing, bioimaging, genomics, diagnostics, and therapy. *Chem. Rev.* **2014**, *114*, 6130-6178.

[6] Li, J.; Zhu, J. Quantum dots for fluorescent biosensing and bio-imaging applications. *Analyst*, **2013**, *138*, 2506-2515.

[7] Wu, J.; Liu, W.; Ge, J.; Zhang, H.; Wang, P. New sensing mechanisms for design of fluorescent chemosensors emerging in recent years. *Chem. Soc. Rev*. **2011**, *40*, 3483-3495.

[8] Das, K.; Sarkar, S.; Das, P. K. Fluorescent indicator displacement assay: ultrasensitive detection of glutathione and selective cancer cell imaging. *ACS Appl. Mater. Interfaces* **2016**, *8*, 25691-25701.

[9] Zhang, X.; Zhang, X.; Wang, S.; Liu, M.; Zhang, Y.; Tao, L.; Wei, Y. Facile incorporation of aggregation-induced emission materials into mesoporous silica nanoparticles for intracellular imaging and cancer therapy. *ACS Appl. Mater. Interfaces* **2013**, 5, 1943-1947.

[10] Bromfield, S. M.; Barnard, A.; Posocco, P.; Fermeglia, M.; Pricl, S.; Smith, D. K. Mallard blue: a high-affinity selective heparin sensor that operates in highly competitive media. *J. Am. Chem. Soc.* **2013**, *135*, 2911-2914.

[11] Peynshaert, K.; Manshian, B. B.; Joris, F.; Braeckmans, K.; De Smedt, S. C.; Demeester, J.; Soenen, S. J. Exploiting intrinsic nanoparticle toxicity: the pros and cons of nanoparticle-induced autophagy in biomedical research. *Chem. Rev*. **2014**, *114*, 7581-7609.

[12] Hong, Y.; Lam, J. W. Y.; Tang, B. Z. Aggregation-induced emission: phenomenon, mechanism and applications. *Chem. Commun*. **2009**, 4332-4353.

[13] Thompson, R. B. *Fluorescence Sensors and Biosensors*, CRC: Boca Raton, 2006.

[14] Choudhury, P.; Das, K.; Das, P. K. L-phenylalanine-tethered, naphthalene diimide-based, aggregation-induced, green-emitting organic nanoparticles. *Langmuir* **2017**, *33*, 4500-4510.

[15] An, B. K.; Kwon, S. K.; Jung, S. D.; Park, S. Y. Enhanced emission and its switching in fluorescent organic nanoparticles. *J. Am. Chem. Soc*. **2002**, *124*, 14410-14415.

[16] Choudhury, P.; Sarkar, S.; Das, P. K. Tunable aggregation-induced multicolor emission of organic nanoparticles by varying the substituent in naphthalene diimide. *Langmuir* **2018**, *34*, 14328-14341.

[17] Hoeben, F. J. M.; Jonkheijm, P.; Meijer, E. W.; Schenning, A. P. H. J. About supramolecular assemblies of π-conjugated systems. *Chem. Rev*. **2005**, *105*, 1491-1546.

[18] La, D. D.; Bhosale, S. V.; Jones, L. A.; Bhosale, S. V. Tetraphenylethylene-based AIE-active probes for sensing application. *ACS Appl. Mater. Interfaces* **2018**, *10*, 12189-12216.

[19] Kwok, R. T. K.; Leung, C. W. T; Lam, J. W. Y.; Tang, B. Z. Biosensing by luminogens with aggregation-induced emission characteristics, *Chem. Soc. Rev.* **2015**, *44*, 4228-4238.

[20] Rabenstein, D. L. Heparin and heparan sulfate: structure and function. *Nat. Prod. Rep*. **2002**, *19*, 312-331.

[21] Capila, I.; Linhardt, R. J. Heparin-protein interactions. *Angew. Chem. Int. Ed*. **2002**, *41*, 390-412.

[22] Triggers, M. N. Targets and treatments for thrombosis. *Nature* **2008**, *451*, 914-918.

[23] Bromfield, S. M.; Wilde, E.; Smith, D. K. Heparin sensing and binding-taking supramolecular chemistry towards clinical applications. *Chem. Soc. Rev*. **2013**, *42*, 9184-9195.

[24] Fareed, J.; Hoppensteadt, D. A.; Bick, R. L. An update on heparins at the beginning of the new millennium. *Semin. Thromb. Hemostasis* **2000**, *26*, 5-21.

[25] Girolami, B.; Girolami, A. Heparin-induced thrombocytopenia: a review. *Semin. Thromb. Hemostasis* **2006**, *32*, 803-809.

[26] Warkentin, T. E.; Levine, M. N.; Hirsh, J.; Horsewood, P.; Roberts, R. S.; Gent, M.; Kelton, J. G. Heparin-induced thrombocytopenia in patients treated with low-molecular-weight heparin or unfractionated heparin. *N. Engl. J. Med*. **1995**, *332*, 1330-1335.

[27] Freedman, M. D. Pharmacodynamics, clinical indications, and adverse effects of heparin. *J. Clin. Pharmacol.* **1992**, *32*, 584-596.

[28] Cai, L.; Zhan, R.; Pu, K. Y.; Qi, X.; Zhang, H.; Huang, W.; Liu, B. Butterfly-shaped conjugated oligoelectrolyte/graphene oxide integrated assay for light-up visual detection of heparin. *Anal. Chem*. **2011**, *83*, 7849-7855.

[29] Zhong, Z.; Anslyn, E. V. A colorimetric sensing ensemble for heparin. *J. Am. Chem. Soc*. **2002**, *124*, 9014-9015.

[30] Beni, S.; Limtiaco, J. F. K.; Larive, C. K. Analysis and characterization of heparin impurities. *Anal. Bioanal. Chem*. **2011**, *399*, 527-539.

[31] Gemene, K. L.; Meyerhoff, M. E. Reversible detection of heparin and other polyanions by pulsed chronopotentiometric polymer membrane electrode. *Anal. Chem*. **2010**, *82*, 1612-1615.

[32] Korir, A. K.; Limtiaco, J. F.; Gutierrez, S. M.; Larive, C. K. Ultraperformance ion-pair liquid chromatography coupled to electrospray time-of-flight mass spectrometry for compositional profiling and quantification of heparin and heparin sulfate. *Anal. Chem*. **2008**, *80*, 1297-1306.

[33] Kokado, K.; Chujo, Y. Multicolor tuning of aggregation-induced emission through substituent variation of diphenyl-*o*-carborane. *J. Org. Chem*. **2011**, *76*, 316-319.

[34] Bai, S.; Debnath, S.; Javid, N.; Frederix, P. W. J. M.; Fleming, S.; Pappas, C.; Ulijn, R. V. Differential self-assembly and tunable emission of aromatic peptide bola-amphiphiles containing perylene bisimide in polar solvents including water. *Langmuir* **2014**, *30*, 7576-7584.

[35] Kobaisi, M. A.; Bhosale, S. V.; Latham, K.; Raynor, A. M.; Bhosale, S. V. Functional naphthalene diimides: synthesis, properties, and applications. *Chem. Rev*. **2016**, *116*, 11685-11796.

[36] Kumar, M.; George, S. J. Green fluorescent organic nanoparticles by self-assembly induced enhanced emission of a naphthalene diimide bola amphiphile. *Nanoscale* **2011**, *3*, 2130-2133.

[37] Kulkarni, C.; George, S. J. Carbonate linkage bearing naphthalenediimides: self-assembly and photophysical properties. *Chem. Eur. J.* **2014**, *20*, 4537-4541.

[38] Bell, T. D. M.; Bhosale, S. V.; Forsyth, C. M.; Hayne, D.; Ghiggino, K. P.; Hutchison, J. A.; Jani, C. H.; Langford, S. J.; Lee, M. A. P.; Woodward, C. P. Melt-induced fluorescent signature in a simple naphthalenediimide. *Chem. Commun.* **2010**, *46*, 4881-4883.

[39] Kulkarni, C.; Periyasamy, G.; Balasubramanian, S.; George, S. J. Charge-transfer complexation between naphthalene diimides and aromatic solvents. *Phys. Chem. Chem. Phys*. **2014**, *16*, 14661-14664.

[40] Lippert, V. E. Dipolmoment und elektronenstruktur von angeregten molekülen. *Z. Naturforschg.* **1955**, *10a*, 541-545.

[41] Mataga, N.; Kaifu, Y.; Koizumi, M. Solvent effects upon fluorescence spectra and the dipole moments of excited molecules. *Bull. Chem. Soc. Jpn.* **1956**, *29*, 465-470.

[42] Zhan, R.; Fang, Z.; Liu, B. Naked-eye detection and quantification of heparin in serum with a cationic polythiophene. *Anal. Chem*. **2010**, *82*, 1326-1333.

[43] Mudliar, N. H.; Singh, P. K. Emissive H-aggregates of an ultrafast molecular rotor: a promising platform for sensing heparin. *ACS Appl. Mater. Interfaces* **2016**, *8*, 31505-31509.

[44] Wang, M.; Zhang, D.; Zhang, G.; Zhu, D. The convenient fluorescence turn-on detection of heparin with a silole derivative featuring an ammonium group. *Chem. Commun.* **2008**, *37*, 4469-4471.

[45] Zeng, L.; Wang, P.; Zhang, H.; Zhuang, X.; Dai, Q.; Liu, W. Highly selective and sensitive heparin probing from supramolecular assembly of pyrene derivatives. *Org. Lett*. **2009,** *11*, 4294-4297.

[46] Yanga, Y.; Chena, J.; Zhoua, H.; Lia, W.; Wanga, Y.; Lia, J.; Zhanga, C.; Zhoua, C.; Yu, C. Polycation-induced benzoperylene probe excimer formation and the ratiometric detection of heparin and heparinase. *Biosens. Bioelectron.* **2016,** *75*, 404-410.

[47] Jena, B. K.; Raj, C. R. Optical sensing of biomedically important polyionic drugs using nano-sized gold particles. *Biosens. Bioelectron.* **2008,** *23*, 1285-1290.

[48] Dai, Q.; Liu, W.; Zhuang, X.; Wu, J.; Zhang, H.; Wang, P. Ratiometric fluorescence sensor based on a pyrene derivative and quantification detection of heparin in aqueous solution and serum. *Anal. Chem*. **2011**, *83*, 6559-6564.

[49] Sun, W.; Bandmann, H.; Schrader, T. Fluorescent polymeric heparin sensor. *Chem. Eur. J*. **2007**, *13*, 7701-7707.

[50] Ding, Y.; Shi, L.; We, H. A "turn on" fluorescent probe for heparin and its oversulfated chondroitin sulfate contaminant. *Chem. Sci.* **2015**, *6*, 6361-6366.

[51] Liu, Z.; Ma, Q.; Wang, X.; Lin, Z.; Zhang, H.; Liu, L.; Su, X. A novel fluorescent nanosensor for detection of heparin and heparinase based on $CuInS_2$ quantum dots. *Biosens. Bioelectron.* **2014,** *54*, 617-622.

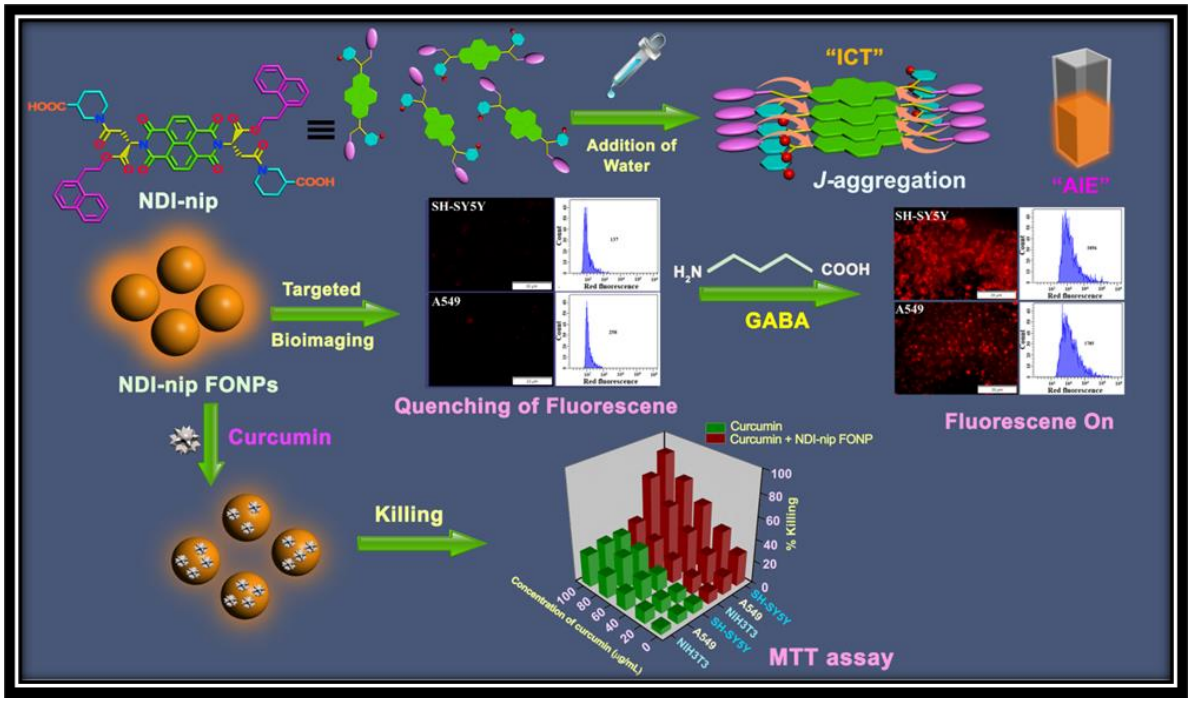

Nipecotic Acid Tethered Naphthalene Diimide based Orange Emitting Organic Nanoparticles as Targeted Delivery Vehicle and Diagnostic Probe towards $GABA_A$ Receptor Enriched Cancer Cells

2.1 INTRODUCTION

Over the past few decades luminescent nanoparticles have drawn enormous interest in chemical, biological, and diagnostic fields primarily as a sensing and imaging tool because of its synthetic ease, cost-effectiveness, high sensitivity and others.[1-5] To this end, various fluorescent materials, including inorganic nanoparticles (e.g., silica/carbon dot, semiconductor quantum dots (QDs), lanthanide ions doped nanomaterials) and organic nanoparticles, have been extensively developed.[6-8] However, most of the fluorescent inorganic nanoparticles (FINs) suffers from potential toxicity and non-biodegradability.[9] Similarly, typical organic dyes and fluorescent molecules encounter challenges in imaging on account of the aggregation caused quenching (ACQ) effect either in the self-assembled state or at its higher concentration.[10-12] Aggregation-induced emission (AIE) is the reverse phenomena of ACQ where the emission gets enhanced upon aggregation as well as in solid state.[10,13] To this end, fluorescent organic nanoparticles (FONPs) with inimitable aggregation-induced emission (AIE) property have emerged as potential theranostic agents displaying biodegradability and non-toxic features.[14-18] FONPs derived from π-conjugated oligomers or chromophoric molecules associated with amplified fluorescence (i.e., AIE) and multimodal functionality including target specific motif will have both academic significance and practical implications as target specific diagnostic probe.[19-22]

Fast inhibitory neurotransmission in the mammalian central nervous system (CNS) is principally mediated by the ubiquitous neurotransmitter GABA (γ-aminobutyric acid) and its synaptic target, the type A GABA receptor ($GABA_AR$).[23-26] The $GABA_AR$ is a channel-forming protein which decreases the neuronal excitability by allowing the passage of chloride ions into the cells.[25-28] A dysfunction in $GABA_AR$ signaling triggers various hyperactive neurological disorders and mental illnesses including Alzheimer's disease, epilepsy, anxiety and insomnia.[29-31] The $GABA_AR$ is a prolific target in therapeutics for diverse array of drugs, including benzodiazepines, barbiturates, anesthetics and ethanol that act through distinct binding sites.[32-34] Variety of methods have been developed for the detection of GABA, based on in vivo magnetic resonance spectroscopy (MRS), micro dialysis, electrochemical and piezoelectric

methods, genetically encoded sensor, nanomaterials-based sensor etc.[35-38] However, $GABA_AR$ targeted diagnostic methods are still lacking due to their poor spatiotemporal resolution, time-consuming, and low sensitivity.[39,40] Nonetheless, reported methods for cellular transporting of GABAergic drugs along with cellular imaging/labelling technique are really scarce. To this end, FONPs can serve as an emerging probe for bio-imaging as well as cellular transportation of cargos. Hence, development of FONPs based target specific fluorescent theranostic probe with high sensitivity and selectivity for $GABA_AR$ containing cellular system is highly warranted. In this regard, nipecotic acid, a cyclic amino acid was chosen as a functionalizing moiety for the basic building block of FONPs. Nipecotic acid is conformationally restricted β-alanine analog which shows in vitro activity as inhibitor of [^{3}H]GABA uptake.[41] Nipecotic acid does not readily penetrate the blood brain barrier (BBB); however, replacement of the nitrogen atom with a lipophilic anchor through *N*-alkylation is reported to exhibit BBB penetration.[41,42]

Herein, we have synthesized naphthalene diimide (NDI) based FONPs, which was covalently tagged with nipecotic acid in both terminal ends as targeting unit for $GABA_AR$ enriched cell lines. This newly developed amphiphilic molecule, **NDI-nip** (Figure 1) took participation in self-aggregation to produce FONPs in DMSO-water (f_w = 99 vol%) solvent mixture and displayed AIE (orange) at 579 nm. The luminescence property of **NDI-nip** FONPs was suitably utilized in bioimaging and target specific delivery of anticancer drug for selective killing of neuroblastoma cell (SH-SY5Y) and cancerous cell (A549). Fluorescence intensity of **NDI-nip** FONPs got quenched in $GABA_AR$ enriched cell lines (SH-SY5Y and A549), while in presence of GABA, no notable quenching of **NDI-nip** FONPs was observed in the same cell lines. The anticancer drug, curcumin loaded **NDI-nip** FONPs were used for selective killing of $GABA_AR$ enriched cell lines (SH-SY5Y and A549) in contrast to normal cell (NIH3T3).

2.2 RESULTS AND DISCUSSION

2.2.1 DESIGNING OF THE AIE-GEN, NDI-NIP.

Aggregation-induced emission (AIE) is a photophysical phenomenon which is being primarily governed by the molecular design of basic building block. Therefore, molecular designing of AIE-active luminogens (AIE-gens) plays a significant role in order to build up

target specific small amphiphilic AIE-gens. Restricted intramolecular rotation (RIR), generating from distortion in the molecular planarity in the self-aggregated state is one of the essential factors to expedite AIE phenomenon by reducing non-radiative decay.[10,13] Additionally, the charge transfer process is facilitated by the inclusion of donor-acceptor (D-A) moiety in the molecular scaffold which engenders modulation in wavelength emission.[10,13,43,44] Naphthalene diimides (NDIs), being a resourceful subclass of the 'rylene' family are electron-deficient n-type semiconductor, which have been exploited as a potential candidate for AIE-gen.[44-47] Motivated by the prominent advantages such as high wavelength associated emission, large Stokes shift, excellent photostability and good biocompatibility, NDI-based AIE-gens have been widely explored in diverse field.[44-46] Considering the electron deficient nature of NDI-core, we have designed **NDI-nip** that was tethered with π-electron rich naphthyl residue (electron-donor) linked through L-aspartic acid (Figure 1).

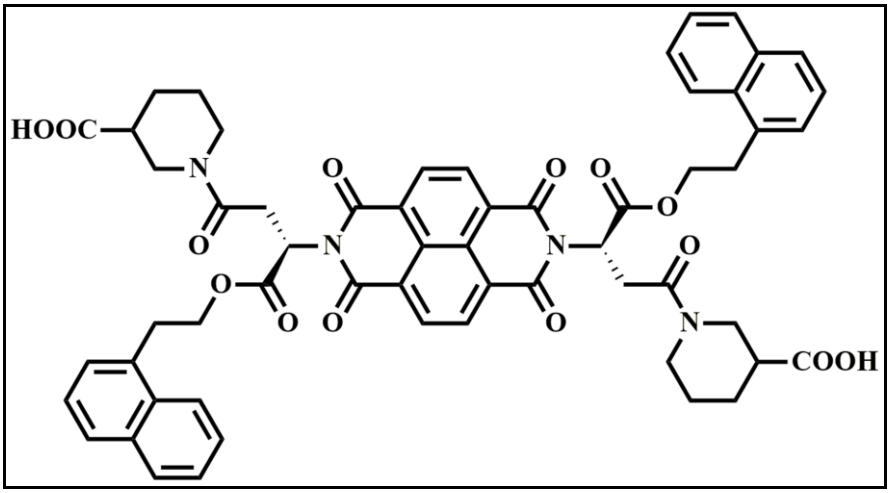

Figure 1. Structure of **NDI-nip** molecule.

This L-aspartic acid tagged **NDI-nip** was further functionalized with nipecotic acid unit at both the terminals (Figure 1). The π-π stacking and hydrophobic interaction may get facilitated during self-assembly by the insertion of aromatic π-moieties (naphthyl residues at both sides) in the molecular backbone. Moreover, electron-deficient NDI core may facilitate charge transfer from naphthyl moieties (electron donating group, EDG) in the molecular skeleton that is anticipated to initiate AIE during self-assembly. In addition, chirality of the L-

aspartic acid may persuade non-planarity, which can promote the RIR in the self-assembled state due to twisted characteristics in the molecular framework. Nipecotic acid, a conformationally restricted β-alanine analog is known to mimic the role of GABA.[41,42] Hence, it was included at the both terminals of the amphiphilic molecule to target the active site of $GABA_A$ receptor in different $GABA_AR$ enriched cell lines (SH-SY5Y and A549).[48,49] ^{1}H-NMR, ^{13}C-NMR, and MALDI-TOF mass spectrometry data of the prepared amphiphile **NDI-nip** along with the different spectroscopic and microscopic data of the self-aggregated **NDI-nip** in varying compositions of DMSO-water were given in experimental section.

2.2.2 MICROSCOPIC AND DLS STUDY OF NDI-NIP.

The newly formed NDI based amphiphilic compound (**NDI-nip**) was freely dissolved in DMSO. The transparent solution of **NDI-nip** in DMSO got transformed into translucent solution upon gradual addition of water (at and above 60% water content (f_w = 60 vol%)) without precipitation indicating the self-aggregation by **NDI-nip** in DMSO-H_2O binary solvent mixture (Figure 2). The macroscopic translucency of the solution was unwavering up to 99% water content (f_w = 99 vol%) owing to the construction of self-aggregated structure. Driven by this introductory finding, the morphology of the self-assembled structure was further examined.

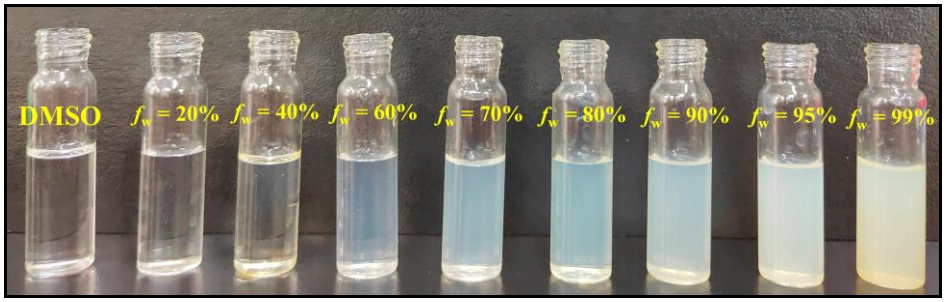

Figure 2. Photograph of formation of translucent solutions with increasing water content in DMSO for **NDI-nip** (10 μM).

Different microscopic studies (TEM, FESEM, AFM) were used to study the self-aggregated structure of **NDI-nip** in 99% water content (f_w = 99 vol%). The spherical aggregate formation of **NDI-nip** (10 μM) in f_w = 99 vol% was evidenced from TEM image and the diameter was observed to be in the range of 50-70 nm (Figure 3a). The solid physical

appearance of the aggregated nanoparticles was confirmed from no clear contrast of the spherical particles. FESEM and AFM images of the organic nanoparticles formed through the self-assembly of **NDI-nip** in f_w = 99 vol% also displayed spherical shaped particles having dimension of 50-70 nm (Figure 3b,c). In concurrence with the microscopic images, the mean hydrodynamic diameter (D_h) of **NDI-nip** in its self-assembled state was found to be around 50-70 nm in dynamic light scattering (DLS) spectroscopy (Figure 3d).

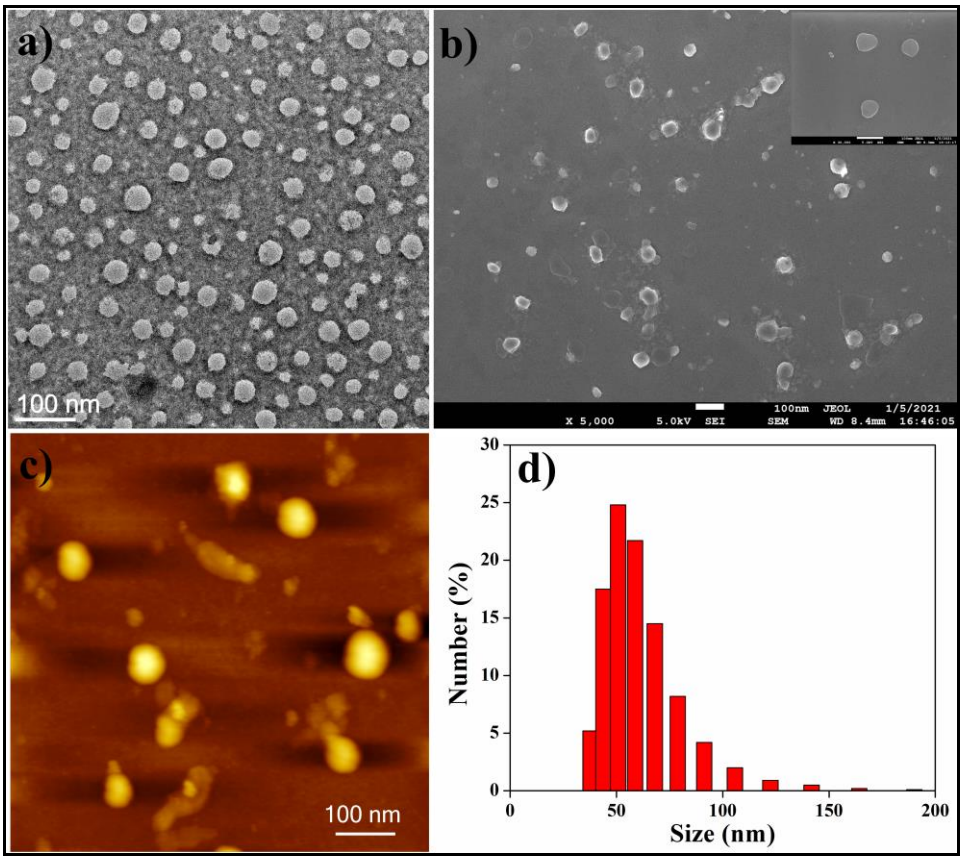

Figure 3. (a) Negatively stained TEM image, (b) FESEM image, (c) AFM image, (d) DLS plot of particles size distribution of NDI-**1** in (1:99, v/v) DMSO–water binary solvent mixture ([**NDI-nip**] = 10 μM).

To check the aggregation properties of **NDI-nip** in different compositions of the DMSO-water mixture, we investigated the mean hydrodynamic diameter (D_h) and the size distribution of the self-aggregates of **NDI-nip**. According to the mean diameter profiles (expressed in number percentage), the average size of the self-aggregates in f_w = 50 vol % was found to be ~450 nm possibly due to the presence of larger spherical aggregates, which was

further evidenced by the TEM image (Figure 4). In the DLS study of **NDI-nip** in varying solvent compositions of DMSO-water, D_h of self-aggregates was observed to be gradually decreased with enhancement in the amount of water in DMSO and finally the D_h of self-aggregates reduced to ~50–70 nm in 1:99 v/v DMSO-water suggesting the formation of organic nanoparticles (Figure 3,4). The higher value of average hydrodynamic diameter at lower f_w may be attributed to the presence of larger aggregates (more like vesicular morphology), which decreased with increasing water content because of the generation of spherical organic nanoparticles at the highest water percentage in a DMSO solution of **NDI-nip** (f_w = 99 vol %).

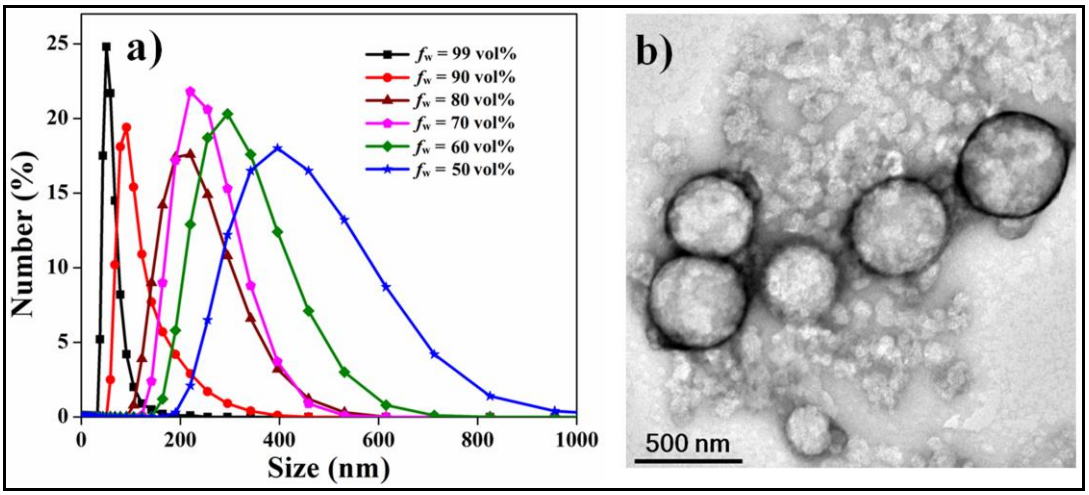

Figure 4. (a) DLS measurement of **NDI-nip** in different compositions of DMSO-water binary solvent mixtures ([**NDI-nip**] = 10 μM), (b) Negatively stained TEM image of **NDI-nip** in (50:50, v/v) DMSO-water binary solvent mixture.

2.2.3 UV-VIS STUDY OF NDI-NIP AMPHIPHILE.

Microscopic observations prompted us to perform spectroscopic investigations to understand the self-aggregation mechanism. We have carried out the UV-vis study of **NDI-nip** (10 μM) in various solvent system of DMSO-H_2O by changing the water content from 0% to 99% (i.e., f_w = 0 to 99 vol%). UV-vis spectra of **NDI-nip** (10 μM) in pure DMSO (non-self-aggregated solvent) showed a characteristics sharp absorption band in the range of 330-400 nm with absorption maxima (λ_{max}) at 381 nm originating from π-π* transition polarized along the long axis of **NDI-nip** chromophore (Figure 5).[21,21,44] The absorption maxima, λ_{max} gradually got red shifted (around 4-5 nm shift for **NDI-nip**) ranging from 381-385 nm with increasing water

content from 0-99% (Figure 5). These characteristic bathochromic shifts in the λ_{max} upon gradual addition of water illustrate the possible participation of *J*-type aggregation during the formation of self-assembled organic nanoparticles by **NDI-nip**.

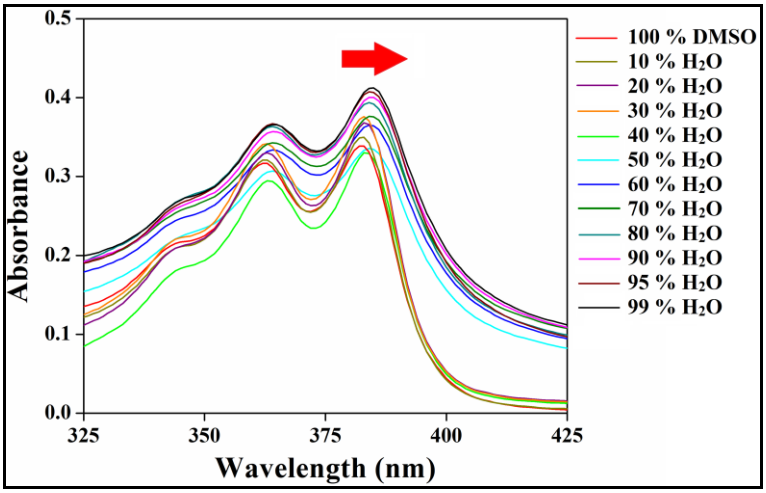

Figure 5. UV–visible spectra of **NDI-nip** (10 μM) in varying DMSO-water solvent mixtures.

2.2.4 INTERMOLECULAR NONCOVALENT INTERACTIONS IN SELF-AGGREGATION OF NDI-NIP.

Fourier transform infrared (FTIR) and solvent-dependent ^{1}H-NMR spectroscopy were utilized to study the role of various non-covalent interactions involved in the development of self-assembled organic nanoparticle by **NDI-nip**.

In the FTIR spectrum, transmittance peaks of **NDI-nip** in non-aggregated state (in $CHCl_3$) displayed at ν = 3174 cm^{-1} for ν_{N-H} (amide A), 1670 cm^{-1} for to $\nu_{C=O}$ (amide I, stretching) and 1502 cm^{-1} for ν_{N-H} (amide II, bending) (Figure 6a). Shifting of these respective peaks to ν = 3273-3564 cm^{-1} (broad band) for ν_{N-H} (amide A), 1615 cm^{-1} for $\nu_{C=O}$ (amide I, stretching) and 1537 cm^{-1} for ν_{N-H} (amide II, bending) was observed in self-aggregated state (1:1, v/v) DMSO-d_6-D_2O solvent mixture (self-aggregated state) (Figure 6a). These shifting in the stretching and bending frequencies of the peaks in DMSO-d_6-D_2O solvent systems demonstrates the participation of intermolecular hydrogen bonding between the amide N–H and carbonyl (C=O) (i.e., N–H···O=C) during self-assembly of **NDI-nip**.

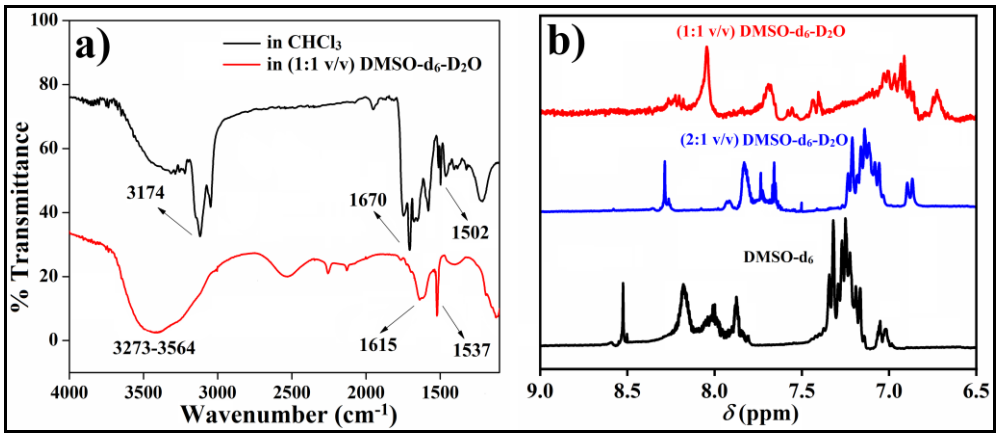

Figure 6. (a) FTIR spectra of **NDI-nip** in $CHCl_3$ (non-self-aggregated form) and in 1:1 (v/v) DMSO-d6-D2O (self-aggregated form), (b) solvent-dependent ^{1}H NMR spectra of **NDI-nip**.

The solvent-dependent ^{1}H-NMR spectrum of **NDI-nip** in non-self-aggregated state (DMSO-d_6) displayed different characteristic aromatic ^{1}H-NMR signals in the region δ = 8.5 ppm (aromatic core of NDI), δ = 7.7-8.2 ppm (C4, C5, C8 proton of naphthyl ring), δ = 7.2-7.4 ppm (C3, C6, C7 proton of naphthyl ring) and δ = 7.0-7.2 ppm (C2 proton of naphthyl ring) (Figure 6b). Upfield shifting of the characteristics NMR signals with diminished peak intensity was witnessed upon gradual addition of D_2O content in DMSO-d_6 (Figure 4c). Various ^{1}H-NMR signals for aromatic protons of the **NDI-nip** got broadened and shifted to δ = 8.18 ppm (NDI-core), δ = 7.4-7.7 ppm, δ = 6.7-7.8 ppm and δ = 6.71-6.76 ppm for the respective protons at (1:1, v/v) DMSO-d_6-D_2O (Figure 6b). These upfield shifting and broadening of ^{1}H-NMR peaks for aromatic protons of **NDI-nip** upon increase in D_2O content established the participation of π-π stacking between the aromatic moieties during self-aggregation of **NDI-nip** amphiphile.

2.2.5 STUDY ON EMISSIVE NATURE OF NDI-NIP FONPs.

Upon development of self-aggregated organic nanoparticles, we investigated emissive behavior of this newly developed π-conjugated moieties containing **NDI-nip** amphiphile. Blue fluorescence of **NDI-nip** in DMSO was observed upon irradiation with UV-light at 365 nm (Figure 7a). Gradual enhancement of H_2O concentration into the stock solution (**NDI-nip** dissolved in DMSO) reduced the blue emission intensity up to <60% water content. The emission color got changed to faint orange at 60% H_2O percentage (f_w = 60 vol%) and the intensity of orange emission got significantly augmented upon gradual inclusion of water

content. At 1:99 v/v DMSO-water, the **NDI-nip** exhibited brightest orange emission (Figure 7a). This finding suggests that the **NDI-nip** amphiphile showed AIE in altering concentrations of DMSO-water solvent system owing to the formation of self-aggregated organic nanoparticles. The presence of the red/orange dotted fluorescent organic nanoparticles (FONPs) in the corresponding fluorescence microscopic image of **NDI-nip** (f_w = 99 vol%) further confirmed the AIE at the self-aggregated state (Figure 7b).

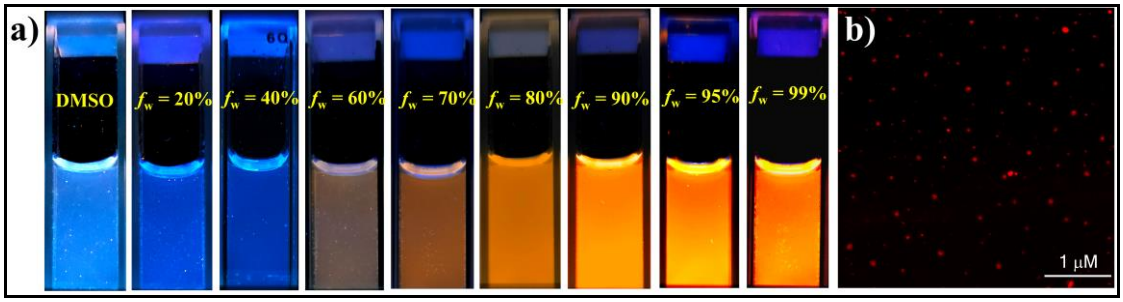

Figure 7. (a) Photograph of change in emission color of **NDI-nip** (10 μM) upon UV-light irradiation (λ_{ex} = 365 nm) with an increase in water content in DMSO, (b) Fluorescence microscope image of **NDI-nip** FONPs in (1:99, v/v) DMSO-water mixture.

The observed macroscopic changes in the fluorescence color of **NDI-nip** FONPs in varying composition of DMSO-H_2O intrigued us to examine the luminescence property through photoluminescence study. **NDI-nip** (10 μM) in DMSO displayed a fluorescence band signal having emission maxima (λ_{em}) at 415 nm that refers the monomeric peak of **NDI-nip** in non-self-assembled state (Figure 8a). The fluorescence intensity of this monomeric peak of **NDI-nip** decreased upon successive addition of water into the system, and a new fluorescent excimer peak with λ_{em} at 568 nm was appeared at 60% water content (f_w = 60 vol%) upon excitation at λ_{ex} = 350 nm. A steady enhancement of the fluorescence signal intensity of this excimer peak was noted with increasing in the amount of H_2O in DMSO solution. **NDI-nip** at f_w = 99 vol% displayed the maximum emission intensity at 579 nm having a bathochromic shift of 164 nm in comparison to the molecularly dissolved monomeric peak of **NDI-nip** in non-self-aggregated state (Figure 8a). The spectral shift in the absorption spectroscopy during self-assembly of **NDI-nip** in the presence of higher amount of water in DMSO can also be correlated with its excimer formation and bathochromic shift in the emission spectra. It is evident from the above spectroscopic studies that **NDI-nip** showed AIE with varying water

composition in DMSO through the excimer formation in its self-aggregated state. It also confirmed the formation of self-aggregated FONP with variation in the emission color upon UV irradiation (Figure 7a, 8b inset).

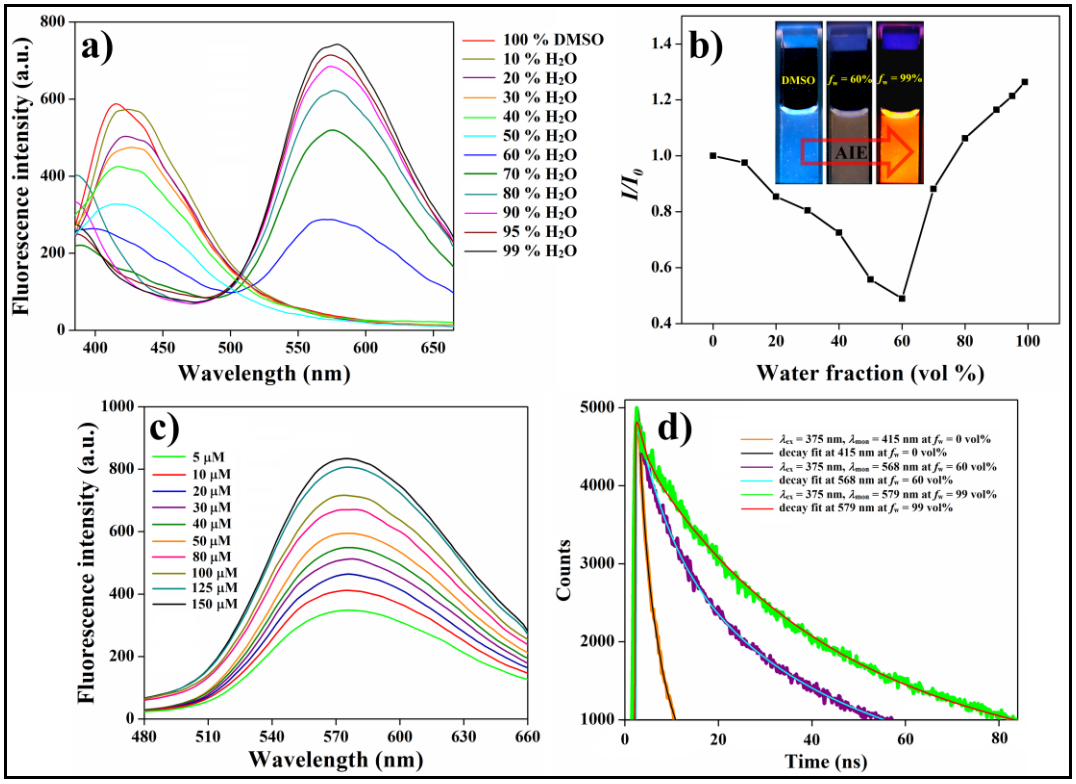

Figure 8. (a) Fluorescence spectra (λ_{ex} = 350 nm) of **NDI-nip** (10 μM) in DMSO-water solvent mixture. (b) Plot of relative emission intensity (I/I_o) vs the fraction of water in DMSO of **NDI-nip** (inset: UV light (λ_{ex} = 365 nm) irradiated image) (c) concentration-dependent emission spectra of **NDI-nip** at 60% water content in DMSO, (d) TCSPC decay profiles of **NDI-nip** monitored at 415 nm (pure DMSO), 568 nm (f_w = 60 vol%) and 579 nm in (1:99, v/v) DMSO-water mixture upon excitation at 375 nm.

Next, concentration-dependent photoluminescence study of **NDI-nip** in DMSO-water was performed at 60 vol% water content to examine the effect of **NDI-nip** concentration on its self-aggregation behavior (Figure 8c). As expected, the characteristic excimer band was observed (λ_{em} = 575 nm) at a lower concentration (5 μM) of **NDI-nip** in f_w = 60 vol% (Figure 8c). The fluorescence intensity of the excimer peak gradually increased with successive increment in the concentration of the **NDI-nip** AIE-gen up to 150 μM (experimentally used highest concentration). A larger number of **NDI-nip** molecules got self-assembled at higher

concentration which resulted in the enhancement of AIE intensity. This observation illustrates that 5 μM of **NDI-nip** at f_w = 60 vol% was sufficient to initiate the AIE and that became saturated at and above 150 μM.

In the pH-dependent photoluminescence study, we have seen that there is no significant change in fluorescence intensity or in emission maxima (λ_{em}) of the characteristic excimer band (Figure 9). This may conclude that the pH of the medium could not affect the emission and aggregation property of **NDI-nip**. This observation further suggests that **NDI-nip** can be used in cancer cell lines (which is in acidic condition) as **NDI-nip** did not exhibit any notable effect on the pH of the medium.

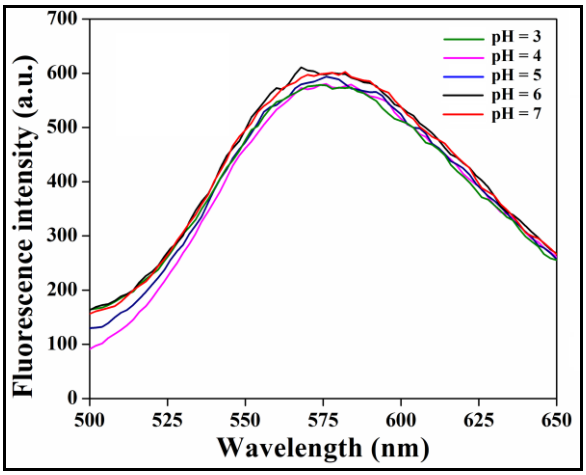

Figure 9. Fluorescence spectra (λ_{ex} = 350 nm) of **NDI-nip** (10 μM) in different pH medium.

Furthermore, the emission nature of **NDI-nip** (10 μM) in both non-self-assembled and self-aggregated state was validated by performing time-correlated single-photon counting (TCSPC) experiment having picosecond excitation at 375 nm. A triexponential function was used for fitting the decay curves in each experiment. The components of **NDI-nip** ($\lambda_{monitored}$ = 415 nm) in DMSO solution were 0.162 ns (62 %), 1.275 ns (37 %), 5.381 ns (2 %) with a short average lifetime ($\langle\tau\rangle$) 0.65 ns (Table 1, Figure 8d). Interestingly, the average lifetime of **NDI-nip** got enhanced upon gradual increment of water percentage into the system. At f_w = 60 vol% the components of **NDI-nip** ($\lambda_{monitored}$ = 568 nm) were 0.107 ns (66 %), 7.507 ns (17 %) and 20.903 ns (17 %) having average lifetime of 4.86 ns. At maximum water content (f_w = 99 vol%) the components of **NDI-nip** ($\lambda_{monitored}$ = 579 nm) were 1.663 ns (35 %), 7.348 ns (42 %) and 18.118 ns (23 %), and the average lifetime of **NDI-nip** was 7.77 ns (Table 1, Figure 8d). This long decay

lifetime originates possibly due to the pre-associated excimer formation by **NDI-nip** FONPs in f_w = 99 vol%. Therefore, TCSPC experiment confirmed that the AIE characteristics shown by **NDI-nip** took place via excimer formation.

Table 1. Lifetime values of **NDI-nip** in presence of different fractions of water in DMSO (λ_{ex} = 375 nm).

Fraction of Water (vol%)	$\lambda_{monitored}$ (nm)	τ_1 (a_1) (ns)	τ_2 (a_2) (ns)	τ_3(a_3) (ns)	Average lifetime (τ) (ns)
0	415	0.162	1.275	5.381	0.65
		(0.62)	(0.37)	(0.02)	
60	568	0.107	7.507	20.903	4.86
		(0.66)	(0.17)	(0.17)	
99	579	1.663	7.348	18.118	7.77
		(0.35)	(0.42)	(0.23)	

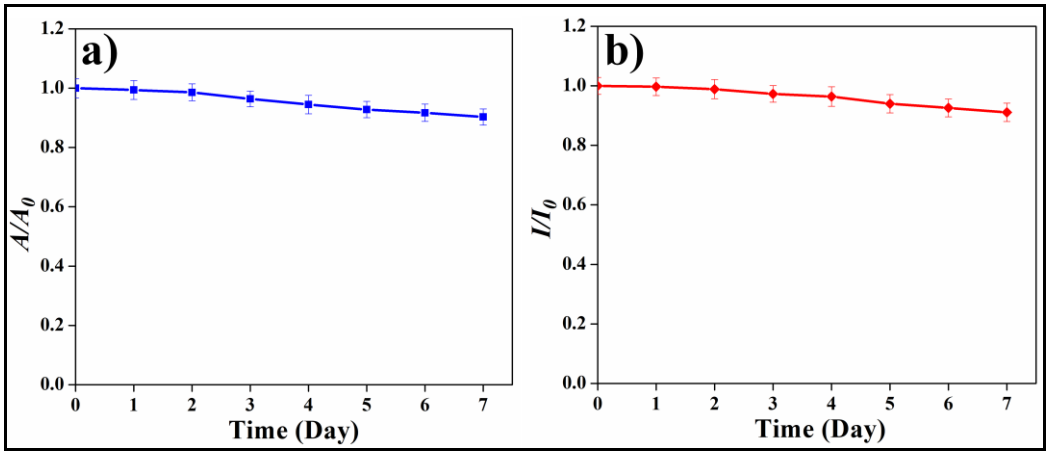

Figure 10. Temporal evolution of (a) the absorbance at 381 nm and (b) fluorescence intensity at 579 nm of 10 μM **NDI-nip** in DMSO-water solvent mixture (f_w = 99 vol%).

Next, time-dependent UV-vis and photoluminescence spectroscopy experiment was performed to examine the stability of **NDI-nip** FONPs in f_w = 99 vol% (self-aggregated state) (Figure 10). **NDI-nip** (10 μM) was used to check the relative absorbance (A/A_o at λ_{max} = 381 nm) and relative fluorescence intensities (I/I_o at λ_{em} = 579 nm) for 7 days. After completion of 7 days,

the relative absorbance and the emission intensities of **NDI-nip** FONPs remained almost unaltered and barely diminished which satisfy its stability in self-aggregated state.

The excitation-dependent fluorescence spectra of **NDI-nip** at f_w = 99 vol% was monitored to observe the influence of the charge-transfer process in the AIE phenomena (Figure 11a). The excitation dependent charge-transfer band (λ_{ex} = 350-450 nm) of **NDI-nip** displayed emission spectra with characteristics similar to that was obtained at λ_{ex} = 350 nm suggesting the enhancement of emission due to charge transfer between the donor-acceptor residues (Figure 11a).[44,47]

Table 2. Photophysical property of **NDI-nip**[a]

Solvent	Δf	λ_{ab} (nm)	λ_{em} (nm)	$\Delta\nu$ (cm^{-1})
Benzene	0.002	383	584	8947
Toluene	0.013	383	583	9010
o-Xylene	0.027	381	579	9057
m-Xylene	0.012	381	573	8979
p-Xylene	0.006	380	574	8954
Chlorobenzene	0.143	384	602	9437

[a]Abbreviation: Δf = solvent polarity parameters, λ_{ab} = absorption maximum, λ_{em} = emission maximum, Δν = Stokes shift. Excitation wavelength (λ_{ex} = 350 nm)

Additionally, intermolecular or intramolecular charge transfer process was envisaged UV-vis and fluorescence spectra of **NDI-nip** in differing solvents having different polarities. The absorbance maxima (λ_{max}) of **NDI-nip** remained almost unaltered in different solvents starting from less polar benzene to moderately polar toluene and finally to comparatively more polar chlorobenzene (Table 2 and Figure 11b). However, from emission spectra of **NDI-nip**, it was observed that with increasing solvent polarity the emission maxima (λ_{em}) steadily got red-shifted from 571 nm to 595 nm (Table 2 and Figure 11c).

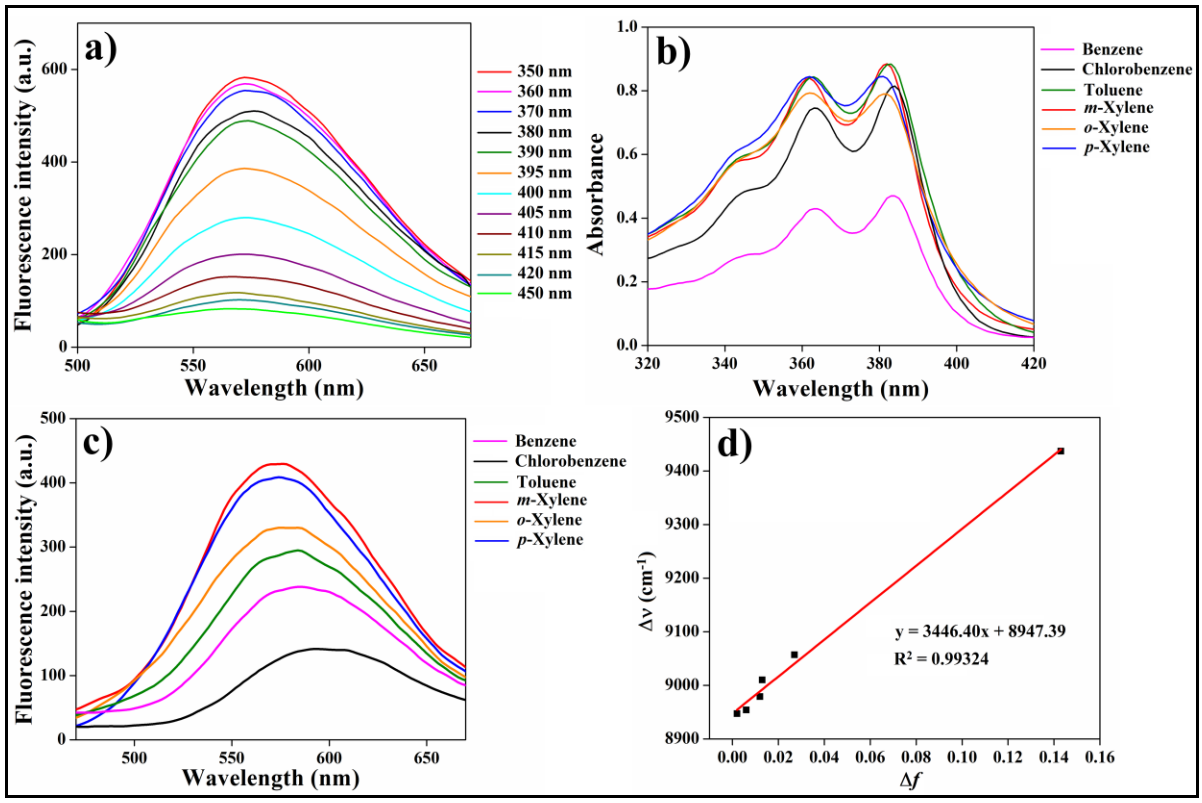

Figure 11. (a) Excitation-dependent emission spectra of **NDI-nip** (10 μM) in 1:99 v/v, DMSO-water, solvent-dependent (b) absorption and (c) emission spectra **NDI-nip** (10 μM). (d) Plot of Stokes shift (Δν) of **NDI-nip** vs solvent polarity parameter (Δf).

The Stokes shift ($\Delta\nu$) of **NDI-nip** in varying solvents of different polarities was estimated, and their solvatochromic properties were quantitatively interpreted by the Lippert-Mataga equation,[50,51]

$$\Delta\nu = \nu_a - \nu_b = \frac{2\Delta f}{hca^3}(\mu_E - \mu_G)^2 + constant \qquad (1)$$

Where, ν_a = maximum absorbance and ν_e = emission wavenumbers, μ_G = dipole moment in the ground state and μ_E = dipole moment in the excited states. h = Planck constant, c = speed of light, a = Onsager solvent cavity radius and n = refractive index of the solvent. The solvent polarity parameter or orientational polarizability (Δf), described in equation 4 which was utilized for the polarity measurement.

$$\Delta f = \frac{\varepsilon - 1}{2\varepsilon + 1} - \frac{n^2 - 1}{2n^2 + 1} \qquad (2)$$

where, ε and n represent static dielectric constant and optical refractive index of the solvent respectively. The linear relationship between Stokes shift ($\Delta\nu$) and solvent polarity parameter (Δf) as well as positive solvatochroism that was found for **NDI-nip** from the Lippert-Mataga plot depict the participation of solvent polarity induced intramolecular charge transfer (ICT) between naphthyl unit as donor moiety and NDI core as the acceptor residue. (Figure 11d). It was observed that the relative fluorescence quantum yield of **NDI-nip** in f_w = 99 vol% was 3.34% (with respect to Quinine hydrogen sulfate), which is comparatively superior to that of the AIE characteristics shown by naphthalene diimide (NDI) derivatives in the aqueous medium.[21] Therefore, it may be concluded that AIE phenomena for **NDI-nip** was observed primarily due the excimer formation in association with ICT during the self-aggregation of the amphiphile.

2.2.6 MEDIA STABILITY AND CYTOCOMPATIBILITY OF NDI-NIP FONPs.

After warranting the stability and all other physicochemical characteristics of the **NDI-nip** AIE-gens, we planned to explore these FONPs in bio-imaging as well as therapeutic applications. Prior to that it was essential to study the suspension stability of **NDI-nip** FONPs in (i) biological milieu and (ii) cytocompatibility against eukaryotic cells. In FBS-DMEM media, **NDI-nip** FONPs (100 μM) was added having FBS concentrations from 0 to 75% and kept for 48 h (Figure 12a). The long-time stability of **NDI-nip** FONPs was also investigated by keeping the mixtures of **NDI-nip** FONPs (100 μM)-FBS (10%)-DMEM media for 10 days (Figure 12b). In both the cases the stability of **NDI-nip** FONPs was ~ 90% (Figure 12). The stability of **NDI-nip** FONPs in biological media is also in concurrence with the respective visual images (Figure 12a). Next the cytocompatibility of **NDI-nip** FONPs (f_w = 99 vol%) was tested by MTT assay in SH-SY5Y (neuroblastoma), A549 (cancer) and NIH3T3 (non-cancer) eukaryotic cells. In all cases, the percentage of alive cells were ~88% after incubated with varying concentrations (10-200 μM) **NDI-nip** FONPs foe 24 h in all type of cells (Figure 12c). Therefore, these **NDI-nip** with superior cytocompatibility could be utilized for cellular imaging and serve as nanocarriers for drug delivery system.

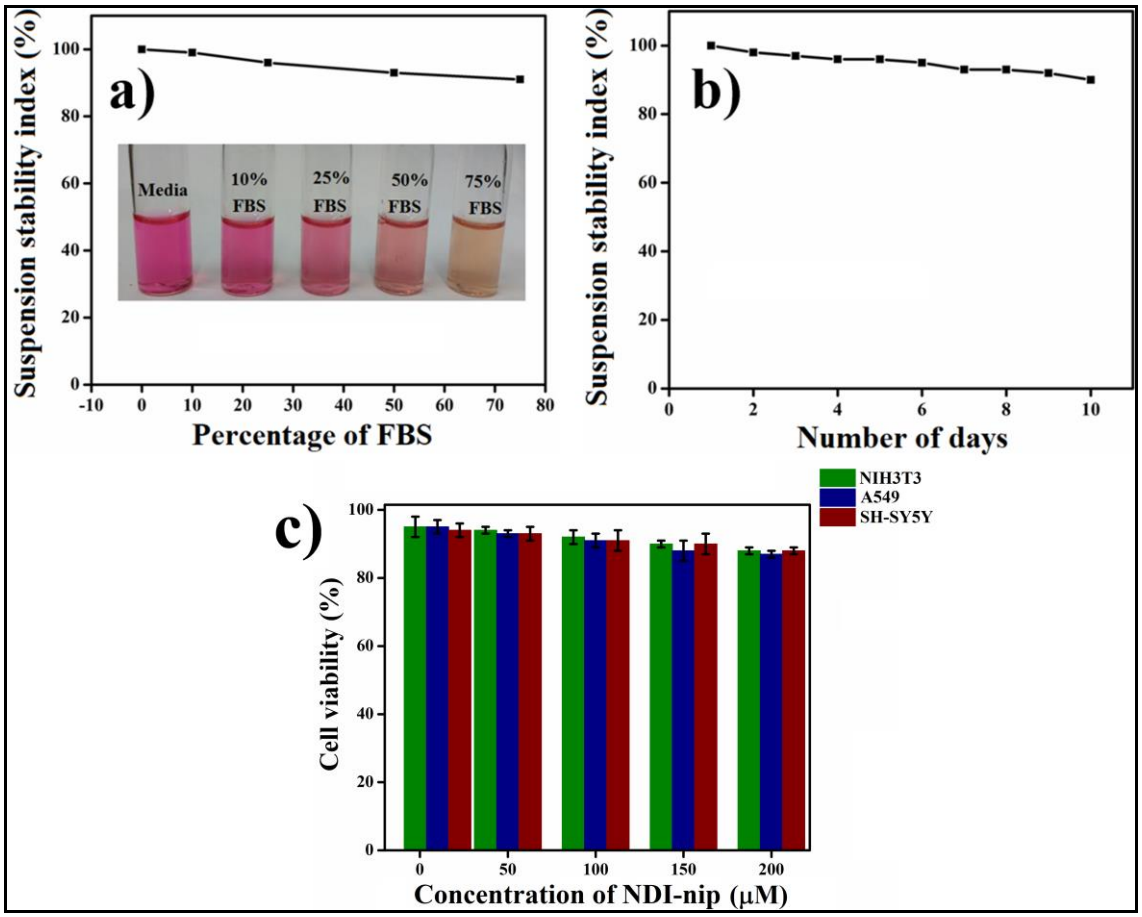

Figure 12. Suspension stability index of **NDI-nip** (100 μM) (prepared in 1:99 (v/v) DMSO-water) in (a) DMEM media supplemented with different percentage of FBS (0-75%) and (b) DMEM media supplemented with 10% of FBS over the 10 days incubation, (c) MTT-based % cell viability of NIH3T3 (non-cancer cells), A549 and SH-SY5Y (cancer cells) in presence of varying concentration of FONPs derived from **NDI-nip** in 1:99 v/v, DMSO-water over 24 h incubation period. Percent errors are within ± 3% in triplicate experiments.

2.2.7 TARGET SPECIFIC BIOIMAGING BY NDI-NIP FONPs.

Considering the notable biocompatibility and stability of this fluorescent probe, initially we investigated its applications in cellular imaging and bio-labelling. To this end, orange emitting **NDI-nip** FONP (100 μM, prepared from f_w = 99 vol%) was incubated separately with non-cancerous NIH3T3 cells and cancerous cell A549 and SH-SY5Y (neuroblastoma) for 12-24 h. The nipecotic acid functionalized **NDI-nip** FONP could selectively diagnose A549 and SH-SY5Y through its eased inclusion owing to the over-

expressing $GABA_A$ receptors in both the cancer cells. All the cells were investigated under fluorescence microscope after completion the 12-24 h incubation.

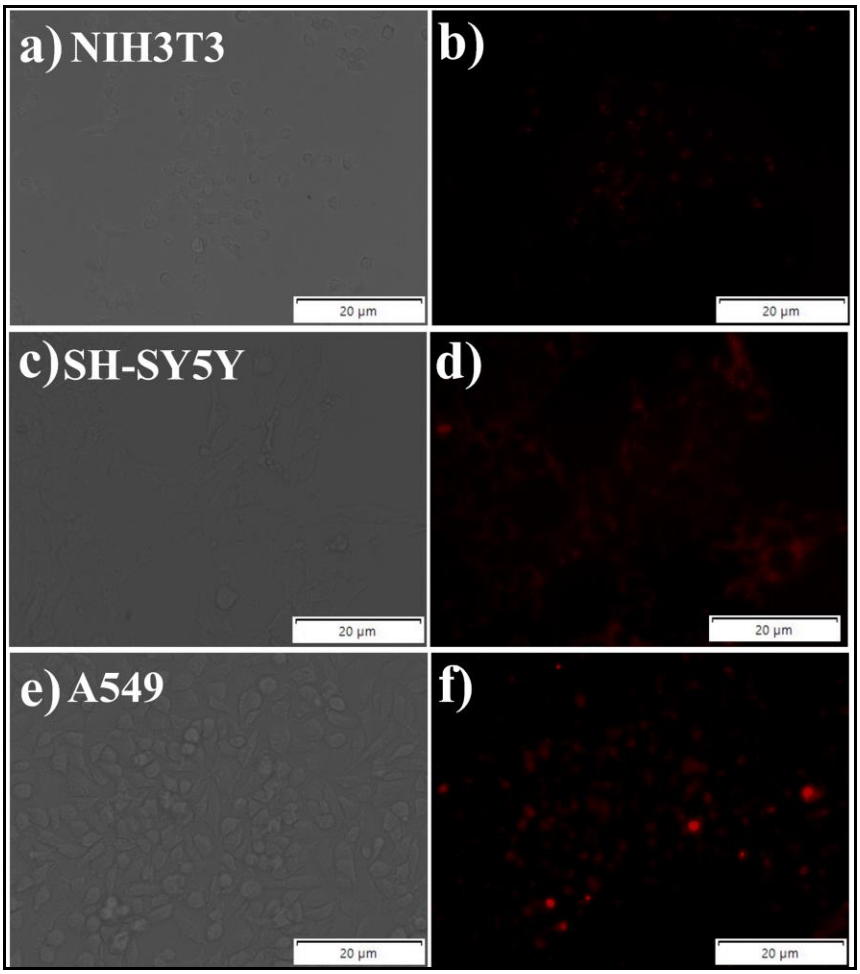

Figure 13. Bright-field, fluorescence microscopic images of cells after 12 h incubation with **NDI-nip** where [**NDI-nip**] = 100 µM, (a,b) NIH3T3, (c,d) SH-SY5Y and (e,f) A549 cells. Scale bars correspond to 20 µm.

In case of non-cancerous NIH3T3 cell, weak red fluorescence was observed inside the cells after 12 h incubation (Figure 13a,b), which got slightly intensified after 24 h incubation having mean fluorescence intensity of 734 (Figure 14a,b,c). This weak to slightly improved fluorescence with time delineates the poor internalization of **NDI-nip** FONP within NIH3T3 cells primarily due to the trivial presence of $GABA_A$ receptor on NIH3T3 cells.

On the other hand, in case of both the cancerous cells (SH-SY5Y and A549), initially weak fluorescence of **NDI-nip** FONP was noted after 12 h incubation (Figure 13c-f), which got

significantly quenched after 24 h (Figure 14d-i). The mean fluorescence intensity of the quenched **NDI-nip** FONP after 24 h was found to be notably low, 157 and 265 for GABA$_A$R enriched cells SH-SY5Y and A549, respectively (Figure 14d,i).

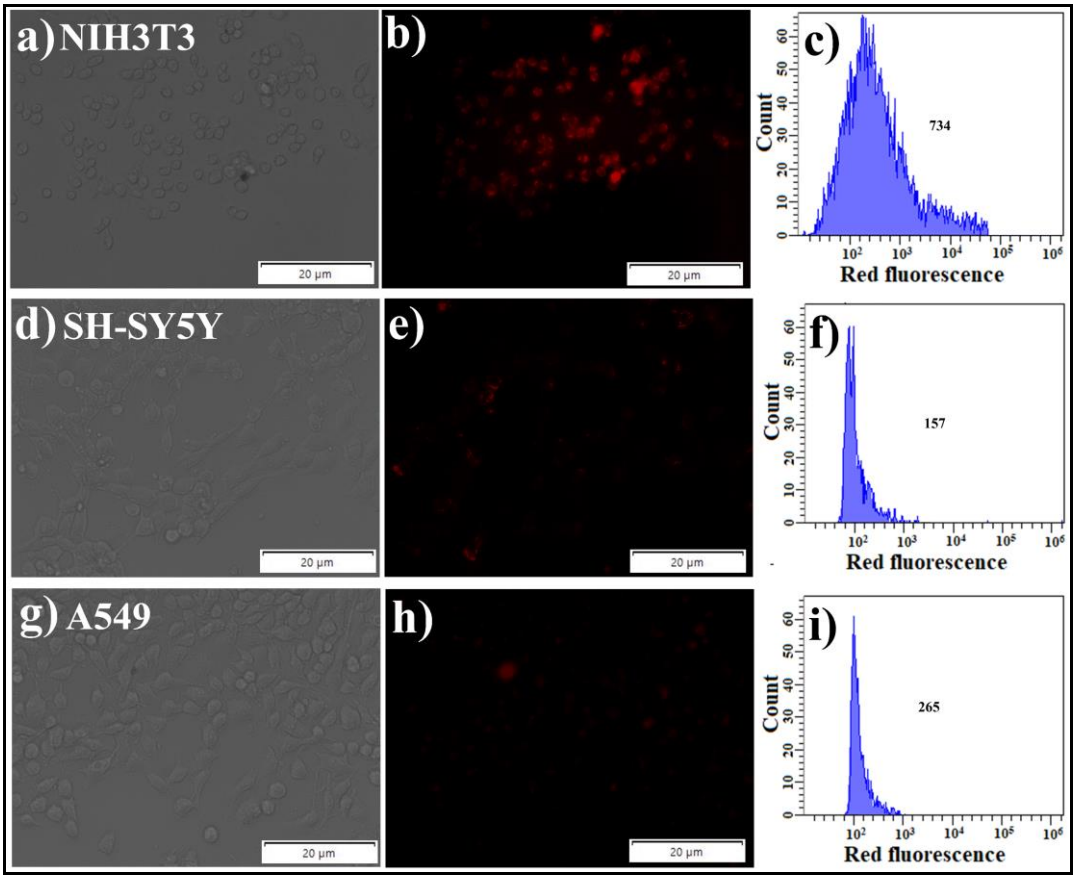

Figure 14. Bright-field, fluorescence microscopic images of cells and corresponding flow cytometric plots after 24 h incubation with **NDI-nip** where [**NDI-nip**] = 100 µM, (a,b,c) NIH3T3, (d,e,f) SH-SY5Y and (g,h,i) A549 cells. Scale bars correspond to 20 µm. The mean fluorescence intensity values are given in the insets.

The observed quenching in the emission of **NDI-nip** FONPs within GABA$_A$R enriched cells might have been originated due to possible interactions between **NDI-nip** and ligand present in GABA$_A$ receptor. Since nipecotic acid shows GABA mimetic actions due to their structural similarity, therefore ligand present in GABA$_A$ receptor could bind with nipecotic acid tagged FONPs resulting in quenching of its fluorescence intensity. Consequently, emission intensity of the **NDI-nip** FONPs started to get quenched possibly from the time of its internalization within these GABA$_A$ receptor enriched cells. As a result, in case of both SH-SY5Y

and A549 cells, weak fluorescence was noted after 12 h incubation, which notably got reduced after 24 h incubation. Thus, considerable quenching of emission intensity after 24 h incubation established the target specific successful internalization of **NDI-nip** FONPs within $GABA_A$ receptor over-expressing RA-differentiated SH-SY5Y cells as well as $GABA_AR$ enriched NSCLC cell, A549 (Figure 14d-i).

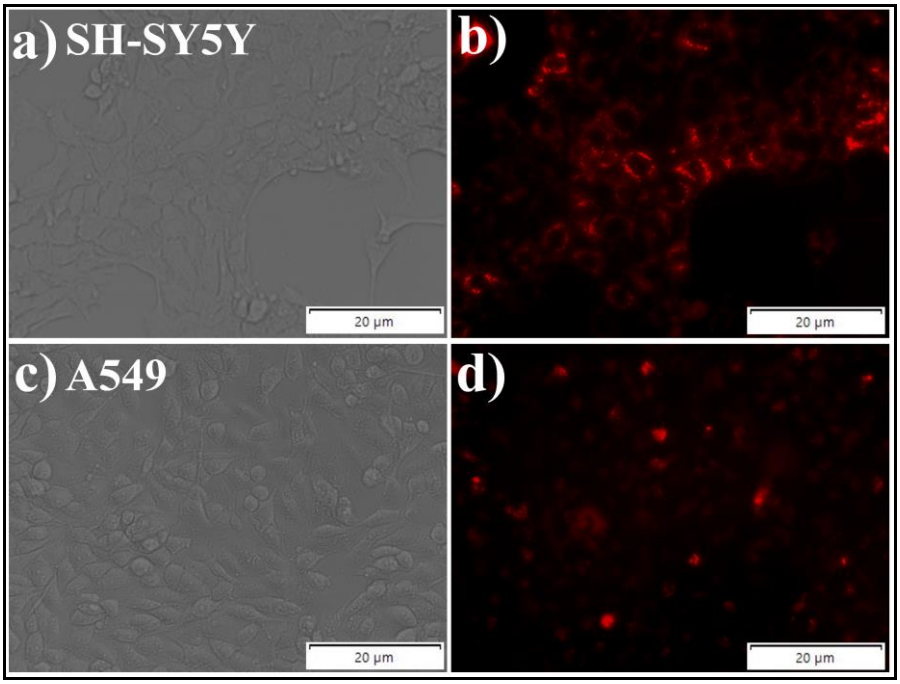

Figure 15. Bright-field, fluorescence microscopic images of cells after 12 h incubation with (**NDI-nip** + GABA) where [**NDI-nip**] = 100 µM, [GABA] = 200 µg/mL, (a,b) SH-SY5Y and (c,d) A549 cells. Scale bars correspond to 20 µm.

To substantiate further the target specific cellular internalization, a mixed solution of **NDI-nip** FONPs (100 µM, prepared from f_w = 99 vol%) and GABA (200 µg/mL) was incubated separately with cancerous cell A549 and SH-SY5Y for 12-24 h. Interestingly, after 12 h incubation, marked improvement in fluorescence intensity of FONPs was observed in the cellular systems (Figure 15). This enhancement in the emission intensity of **NDI-nip** FONPs got remarkably intensified at the cell surface as well as inside the cells after 24 h incubation with the mean fluorescence intensity of 2056 and 1785 for SH-SY5Y and A549, respectively (Figure 16). This is obvious that GABA would exhibit strong binding with the ligand present in $GABA_A$ receptor for natural reasons. In comparison to the nipecotic acid (mimic of GABA), GABA

possess higher affinity to get bind with $GABA_AR$.[52,53] Consequently, the possibility of interactions between the ligand presents in $GABA_A$ receptor (possibly responsible for the quenching of FONP emission) and nipecotic acid of **NDI** got substantially reduced in presence of GABA. Consequently, **NDI-nip** FONPs started to exhibit its intrinsic fluorescence. Therefore, a greater number of **NDI-nip** FONPs that either accumulated on the cell surface or got internalized within the A549 and SH-SY5Y cancerous cells displayed remarkable enhancement in the emission intensity with time (Figure 15,16). Thus, the newly developed **NDI-nip** FONPs successfully emerged as a selective targeted biomarker towards $GABA_A$ receptor enriched cells.

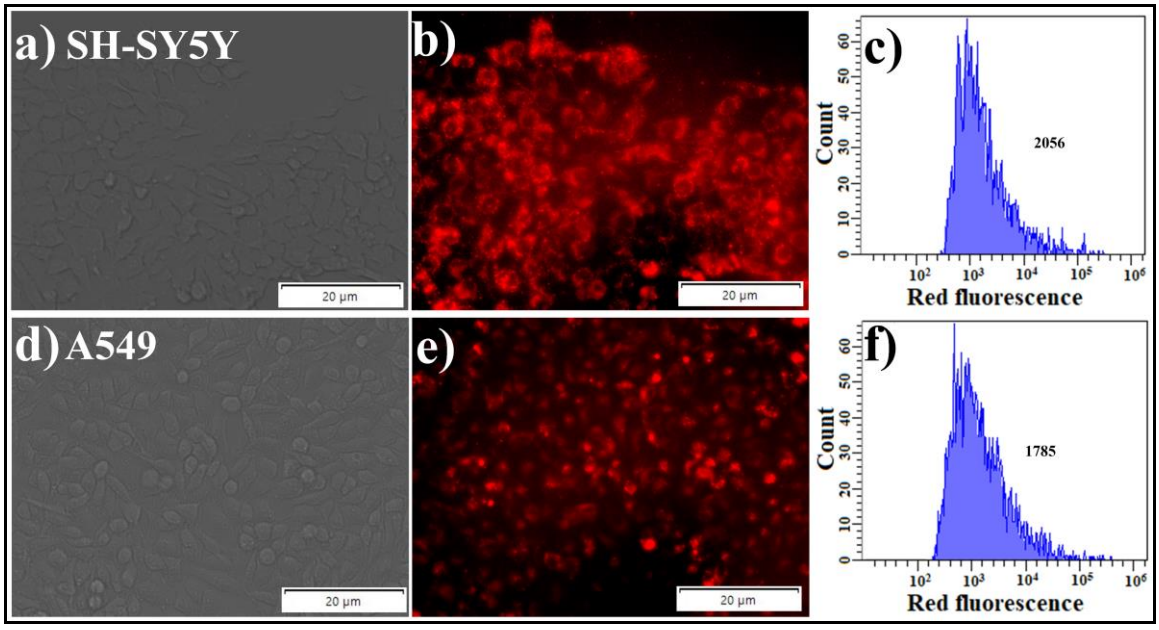

Figure 16. Bright-field, fluorescence microscopic images of cells and corresponding flow cytometric plots after 24 h incubation with (**NDI-nip** + GABA) where [**NDI-nip**] = 100 µM, [GABA] = 200 µg/mL, (a,b,c), SH-SY5Y and (d,e,f) A549 cells. Scale bars correspond to 20 µm. The mean fluorescence intensity values are given in the insets.

After target specific bio imaging of cancer cells by **NDI-nip** we wanted to know the distribution of FONPs in the cells through staining of nuclei. We carried out the experiment of staining of nuclei using Hoechst stain. Hoechst stains are part of a family of blue fluorescent dyes used to stain DNA. $GABA_A$ receptor positive cells (SH-SY5Y and A549) cells were incubated by **NDI-nip** FONPs (100 µM) for 24 h following similar experimental environment

mentioned above in different chamber slides. For both cells (SH-SY5Y and A549) we further incubated GABA (200 μg/mL) for 24 h followed by incubation of **NDI-nip** FONPs (100 μM) for 24 h in another two separated chamber slides. In all four chamber slides we used Hoechst dye to stain nuclei and further observed the distribution of FONPs in microscope (Figure 17).

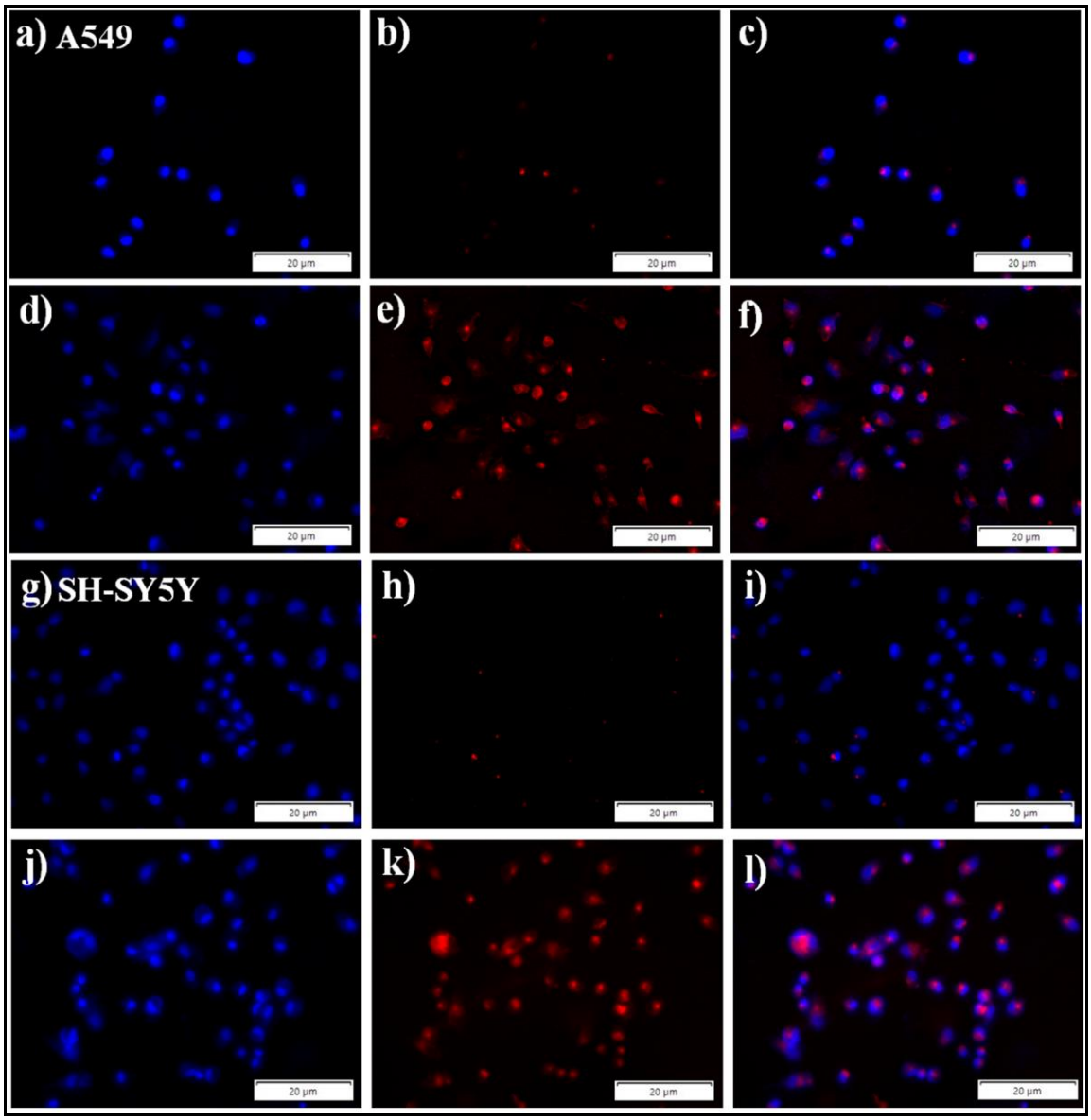

Figure 17. Fluorescence microscopic images of cells with Hoechst nuclei staining. (a-c) A549 cells and (g-i) SH-SY5Y cells incubated with [**NDI-nip**] = 100 μM; (d-f) A549 cells and (j-l) SH-SY5Y cells incubated with [**NDI-nip**] = 100 μM and [GABA] = 200 μg/mL. Scale bars correspond to 20 μm.

In absence of native GABA molecule, the emission intensity of **NDI-nip** FONPs got quenched so that we could not suggests the distribution of FONPs around respective cell lines. As for the $GABA_A$ receptor negative cell line NIH3T3, Hoechst staining experiment was found to be inconclusive due to poor internalization of **NDI-nip** FONPs. On the other hand, in presence of GABA molecule, we observed red fluorescence of the $GABA_A$ receptor positive cells (SH-SY5Y and A549) cells with Hoechst-stained nuclei under the microscope due to native fluorescence of **NDI-nip** FONPs. Thus, distribution of **NDI-nip** FONPs on the cells indicates the cellular internalization in the $GABA_AR$ overexpressed cells (SH-SY5Y and A549) through binding of **NDI-nip** FONPs at the active site of $GABA_A$ receptors.

After successful targeted cellular internalization of **NDI-nip** FONPs into $GABA_AR$ enriched cells, we were curious to investigate the mechanism of fluorescence quenching inside these SH-SY5Y and A549 cells. Nipecotic acid was reported to preferably adopt a binding pose in which the piperidine nitrogen facing to the intracellular side, whereby the carboxylic moiety does the same interactions with the protein observed for the native ligand, GABA.[42] In case of mammals, the heteropentameric $GABA_AR$ were expressed by 19 different subunits.[52-55] The binding sites of $GABA_A$ receptor, a Cys-loop receptor characteristically possess an "aromatic box," where the bound ligand was surrounded by several aromatic amino acid residues. A cation-π interaction between one of these moieties with the natural agonist (GABA) is common.[53] However, the residue type and location are not conserved suggesting that GABA occupies subtly different locations even in such closely related receptors. In $GABA_A$ receptors, L-tyrosine (Tyr) and L-phenylalanine (Phe) residue in loop A of the aromatic box is known to facilitate the cation-π interaction with GABA.[53] On the other hand, Wagner et al. hypothesized that L-arginine (Arg) side chain contacts directly the carboxy group of the GABA molecule that influences GABA binding and unbinding without changing channel gating.[56]

In order to investigate the possible interactions between **NDI-nip** FONPs with the mentioned ligand present in $GABA_A$ receptor, we carried out the photoluminescence study of **NDI-nip** FONPs (f_w = 99 vol%) in presence of those amino acid residues (Tyr, Phe, and Arg) and GABA. Addition of GABA (200 μg/mL) to the solution of **NDI-nip** FONPs did not influence its emission intensity (Figure 18a). As nipecotic is considered to be the mimic of GABA, expectedly interaction between them (if any) will not affect the fluorescence

characteristics of FONPs. Interestingly, addition of 100 μg/mL of each of the amino acids (Tyr, Phe and Arg) separately into the **NDI-nip** FONPs solutions (10 μM, prepared at f_w = 99 vol%) led to the significant quenching of the emission intensity of **NDI-nip** FONPs (Figure 18a).

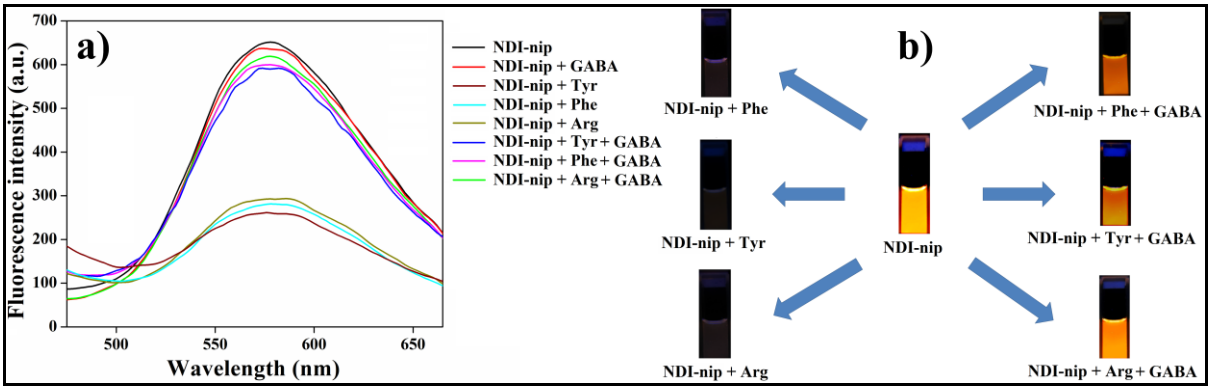

Figure 18. (a) Fluorescence spectra of **NDI-nip** FONPs (10 μM) and (b) Photographs of change in emission intensity **NDI-nip** FONPs (10 μM) in absence and presence of amino acid residues (Tyr, Phe, and Arg) and GABA in (1:99, v/v) DMSO-water solution upon UV-light irradiation (λ_{ex} = 365 nm). [**NDI-nip**] = 10 μM, [Tyr/Phe/Arg] = 100 μg/mL and [GABA] = 200 μg/mL.

This markedly plummeted fluorescence of FONPs in presence of the investigated amino acids (integral residues of $GABA_A$ receptor) established the interaction between **NDI-nip** FONPs with the amino acids. Hence, this observed result demonstrated the plausible mechanism of interaction of **NDI-nip** FONPs with $GABA_A$ receptor enriched cells (SH-SY5Y and A549 cells) that notably quenched its emission. Importantly, addition of the mixed solution of GABA (200 μg/mL) and 100 μg/mL of amino acids (Tyr, Phe and Arg) in separate experiments, reinstated the fluorescence intensity of **NDI-nip** FONPs band signals again (Figure 18a). The GABA molecule naturally has stronger interactions with the mentioned amino acids (being the integral components of $GABA_AR$) in comparison to its mimic nipecotic acid derived **NDI-nip**. Subsequently, **NDI-nip** FONPs could exhibit its intrinsic emission (Figure 18a) similar to that was observed in the preceding cellular studies (Figure 15,16).

Similarly, the macroscopic changes in the emission quenching of **NDI-nip** FONP (10 μM, in f_w = 99 vol%) was observed in presence of 100 μg/mL of Tyr, Phe and Arg (λ_{ex} = 365 nm) because of the interaction between and amino acid residues (Figure 18b). Here too, in the presence of both GABA (200 μg/mL) and each of the investigated amino acid (100 μg/mL), fluorescence restoration of **NDI-nip** FONP was observed due to stronger binding between

GABA to those amino acids compared to that of **NDI-nip**. Accordingly, these amino acids were no longer available to quench the emission of **NDI-nip** FONP and thereby its intrinsic emission got restored (Figure 18b). One of the possible reasons for the fluorescence quenching of **NDI-nip** FONPs could be due to the cation-π interaction with the amino acid (Tyr, Phe, Arg) present in $GABA_AR$ binding sites. Hence, this **NDI-nip** FONP can be successfully utilized as a target specific bio-imaging probe towards $GABA_A$ receptor enriched cell lines.

To establish further the target specificity of the **NDI-nip** FONP to $GABA_AR$ enriched cells, we made use of another NDI derived AIE-gen devoid of nipecotic acid as a control amphiphilic molecule (**NDI-C**, Figure 19). In this NDI derivative, nipecotic acid residue was replaced by benzyl alcohol. This molecule and its physicochemical characterization were previously reported by our research group.[44] The absorption maximum (λ_{max}) was observed at 382 nm for **NDI-C** in f_w = 99 vol%. In the photoluminescence study, **NDI-C** also showed AIE through excimer formation having λ_{em} at 588 nm upon excitation at λ_{ex} = 350 nm in f_w = 99 vol%.

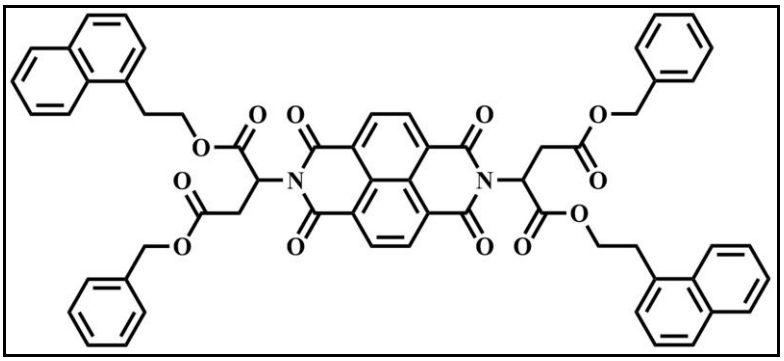

Figure 19. Structure of **NDI-C** amphiphile (control compound).

This orange emitting **NDI-C** FONP (100 μM, prepared from f_w = 99 vol%) was similarly incubated separately with non-cancerous NIH3T3 cells and cancerous cell A549 and SH-SY5Y (neuroblastoma) for 12-24 h. Here too, the cells were investigated under fluorescence microscope after incubation period (Figure 20,21). Moderate to slightly intensified red fluorescence of **NDI-C** FONP was observed in all the investigated cell lines after 12 h incubation (Figure 20). Moreover, the fluorescence intensity got brightly improved in each cell line after 24 h suggesting cellular internalization of a large number of **NDI-C** FONP with time and also the

potent cell-staining ability of **NDI-C** FONP irrespective of the nature of mammalian cells (Figure 21). After 24 h incubation, the mean fluorescence intensity of **NDI-C** FONPs was found to be 1585, 1994, and 2274 in NIH3T3, neuroblastoma cell SH-SY5Y, and A549 cancer cell, respectively (Figure 21). Hence, from the fluorescence microscopic images and flow cytometry data it is evident that despite having varying extent of cell staining ability of **NDI-C** FONPs, it could not exhibit distinct target specificity towards investigated cancer cells presumably due to the absence of nipecotic acid in its molecular framework. Therefore, the nipecotic acid residue present in **NDI-nip** FONPs plays a pivotal role in target specific bio-labeling of the $GABA_AR$ over-expressing cell lines i.e., SH-SY5Y and A549 through fluorescence off mechanism.

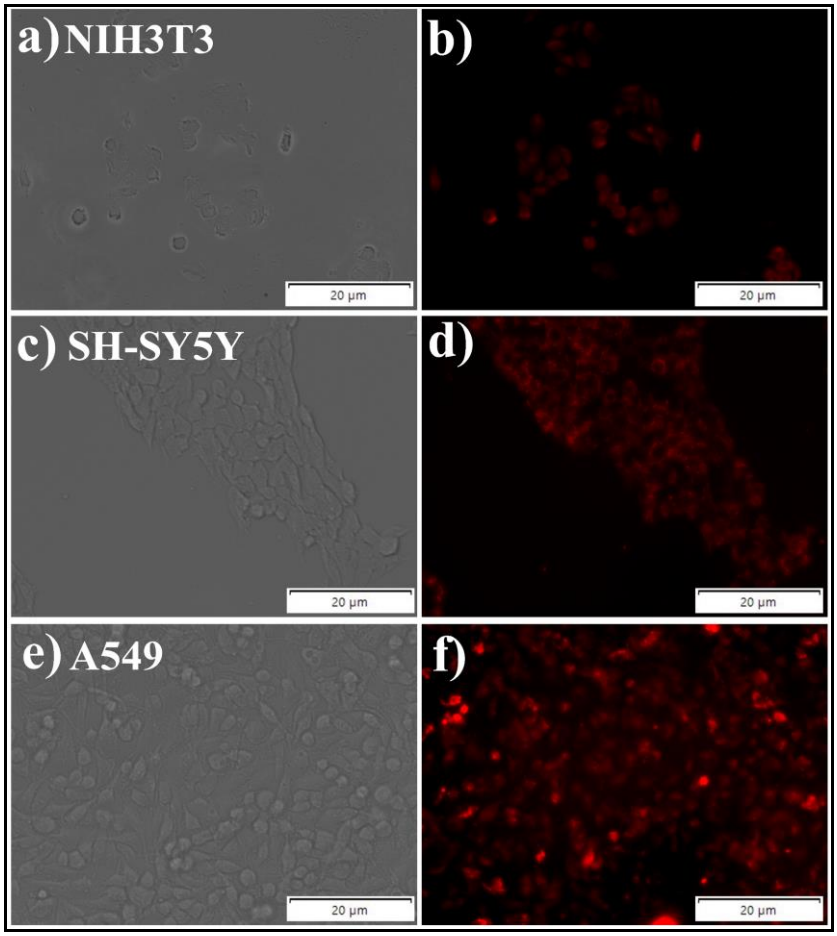

Figure 20. Bright-field, fluorescence microscopic images of cells after 12 h incubation with **NDI-C** where [**NDI-C**] = 100 µM, (a,b) NIH3T3, (c,d) SH-SY5Y and (e,f) A549 cells. Scale bars correspond to 20 µm.

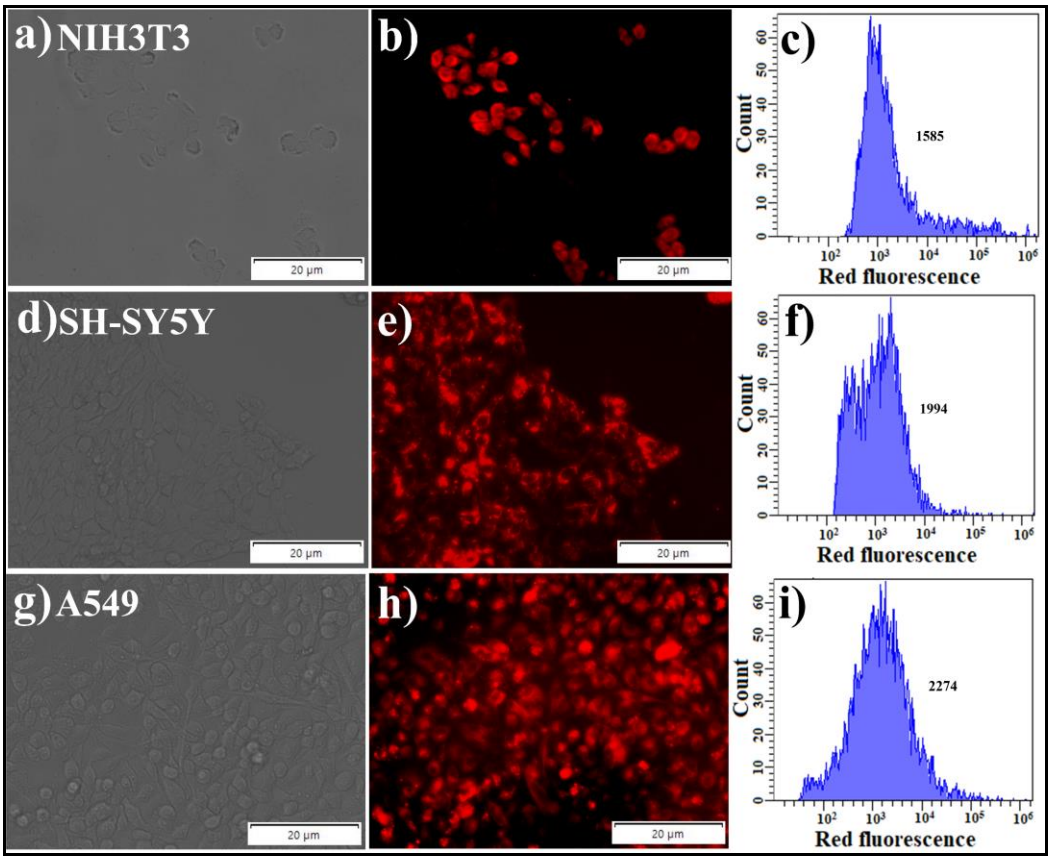

Figure 21. Bright-field, fluorescence microscopic images of cells and corresponding flow cytometric plots after 24 h incubation with **NDI-C** where [**NDI-C**] = 100 µM, (a,b,c) NIH3T3, (d,e,f) SH-SY5Y and (g,h,i) A549 cells. Scale bars correspond to 20 µm. The mean fluorescence intensity values are given in the insets.

2.2.8 DRUG LOADING AND CANCER CELL KILLING EFFICIENCY OF CURCUMIN ENCAPSULATED NDI-NIP FONPs.

Curcumin, also termed diferuloylmethane, a yellow-colored polyphenol extracted from the rhizome of *Curcuma longa* L (South Asian turmeric plant), is a dietary constituent with the demonstrated ability of anti-carcinogenic through diverse mechanisms.[57] The anticancer effects of curcumin have been attributed to the inhibition of metastatic progression, invasion, cancer cell motility in various cancer cells. The primary drawback posed by curcumin is its poor solubility in water and high degradability.[58] In addition to the target specific bio-labeling efficacy of **NDI-nip** FONPs (formed in f_w = 99 vol%), we aim to investigate its capability to act as a target specific cellular transporter.

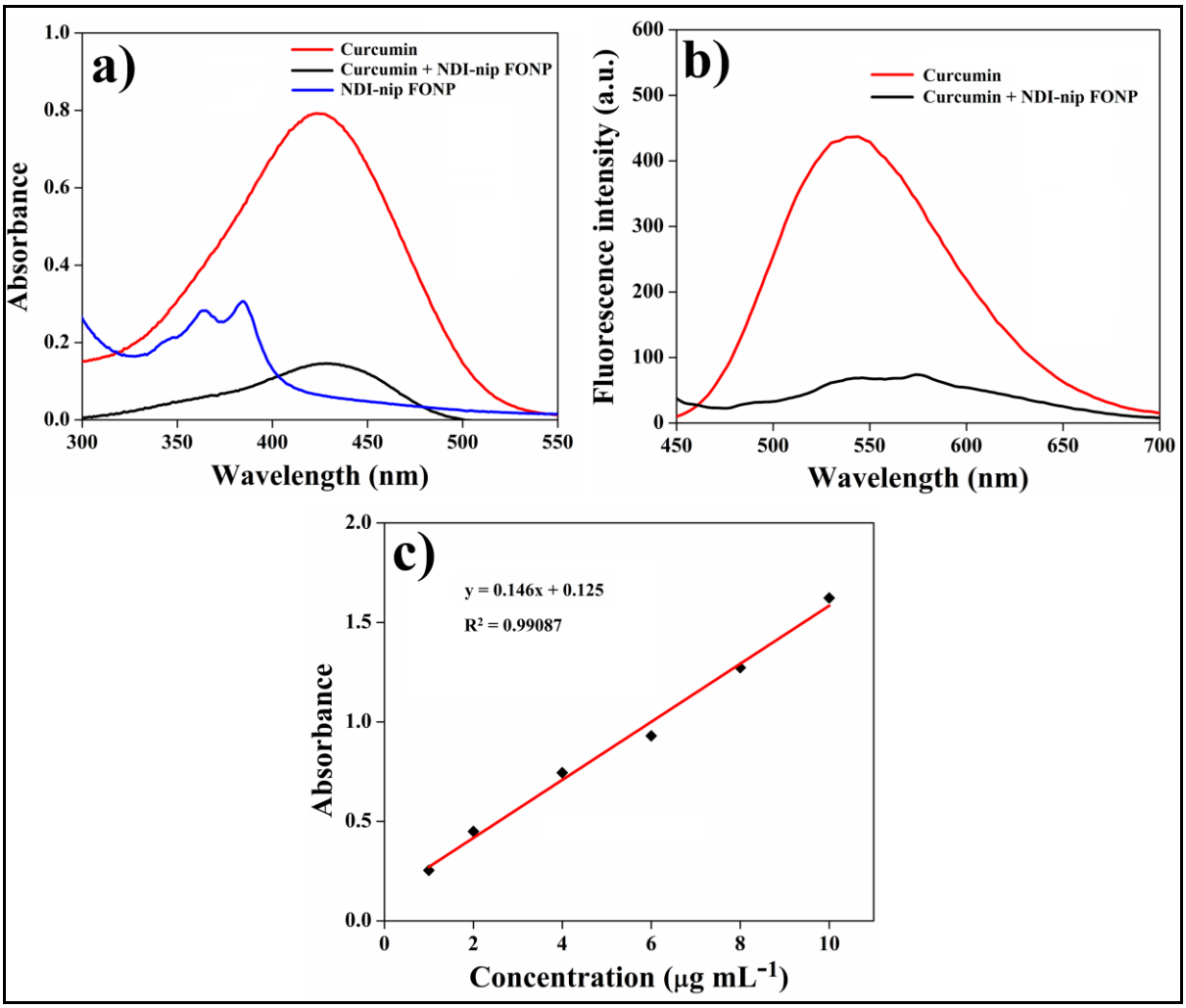

Figure 22. (a) UV-vis spectra of native curcumin, **NDI-nip** in (1:99, v/v DMSO-water solvent mixture), curcumin loaded **NDI-nip** FONP, (b) Fluorescence spectra of native curcumin and curcumin loaded **NDI-nip** FONP and (c) calibration graph of curcumin in methanol

Curcumin was encapsulated in the nano-vehicle at **NDI-nip** FONPs to curcumin ratio of 1:2 (w/w) (included in experimental section). The drug encapsulation was characterized by UV-vis absorption and photoluminescence spectroscopy.[21,59] In UV-vis study, the major peak intensity of curcumin at 425 nm was reduced following encapsulation in FONPs but the spectral pattern of curcumin was retained, which suggests the presence of curcumin in the nano-formulation (Figure 22a). Likewise, drastically plummeted emission intensity of the chromophoric drug curcumin at 542 nm (λ_{ex} = 350 nm) in presence of FONPs in comparison to its native fluorescence signal further confirmed the successful loading of the drug in to the

NDI-nip FONPs (Figure 22b). The loading efficiency of curcumin in **NDI-nip** based FONPs was observed to be 68%, correlating with the standard calibration curve of curcumin (Figure 22c).

Next, we checked the percentage of NIH3T3, A549 and SH-SY5Y cell killing following exposure to both native curcumin (5-100 μM) and curcumin loaded **NDI-nip** FONPs ([curcumin] = 5-100 μM and [**NDI-nip** FONPs] = 2.5-50 μM) for 24 h at a dose dependent manner. A steady enhancement in the percentage killing of SH-SY5Y and A549 was noted upon increasing the concentration of curcumin loaded **NDI-nip** FONPs ([curcumin] = 5-100 μM and [**NDI-nip** FONPs] = 2.5-50 μM), (Figure 23). The killing efficiency of curcumin encapsulated **NDI-nip** FONPs was significantly higher in SH-SY5Y and A549 cells than that in NIH3T3. Following exposure to the highest concentration of curcumin being loaded in **NDI-nip** FONPs ([curcumin] = 100 μM and [**NDI-nip** FONPs] = 50 μM), significantly higher number of SH-SY5Y cells (88 ± 3%) and A549 cells (72 ± 2%) got killed in comparison to that being observed in NIH3T3 cells (37 ± 2%) (Figure 23).

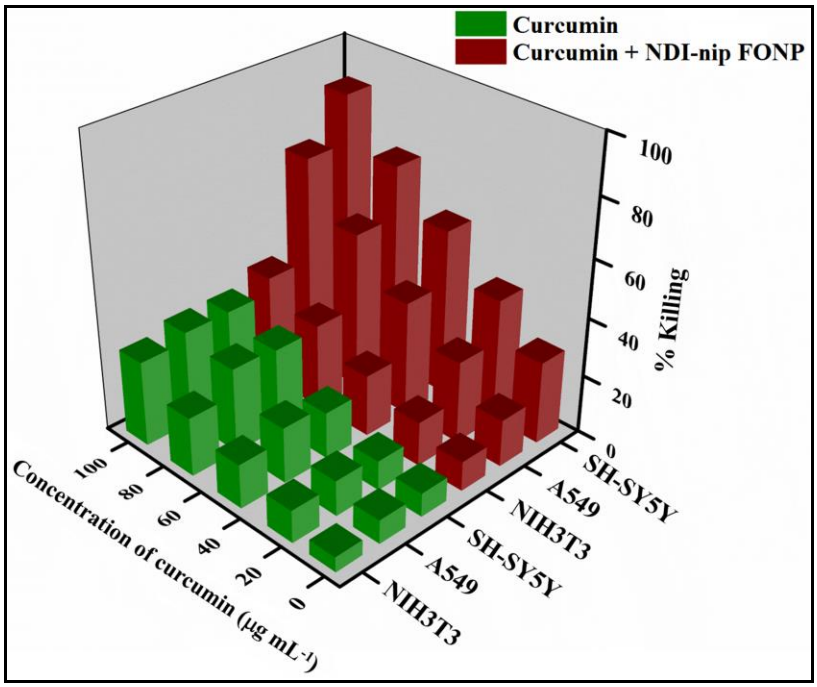

Figure 23. Killing efficiency (determined by MTT assay) of curcumin loaded **NDI-nip** FONPs and free curcumin toward NIH3T3, A549 and SH-SY5Y cells for 24 h. Percent experimental errors are within ±~3% in triplicate experiments.

However, only ~ 32% mammalian cell death was observed upon treatment with highest concentration of native curcumin (100 μM). The significantly higher killing of the cancer cells in contrast to the non-cancer NIH3T3 was due to the presence of overexpressed $GABA_AR$ in SH-SY5Y and A549 cells. Even between the two cancer cells, the killing percentage of the drug encapsulated FONPs in SH-SY5Y cells was slightly higher than in A549 cells due to the higher prominence of $GABA_AR$ in neuroblastoma cell line SH-SY5Y than NSCLC cell line A549. Hence, **NDI-nip** FONPs were target specifically used as a bio-imaging diagnostic tool along with therapeutic ability for $GABA_A$ receptor enriched cell (SH-SY5Y and A549) in comparison to non-cancerous cell (NIH3T3).

2.3 CONCLUSION

In summary, we have designed and prepared L-aspartic acid appended naphthalene diimide (NDI) based amphiphilic compound (**NDI-nip**) having naphthyl and nipecotic acid moieties at both the terminals. Spherical organic nanoparticles having dimension 50-70 nm were formed by **NDI-nip** in DMSO-water binary solvent system through *J*-type aggregation. A weak blue emission was showed by **NDI-nip** in DMSO (i.e., molecularly dissolved state) at λ_{em} = 415 nm. Self-assembly driven aggregation induced orange emission was exhibited by **NDI-nip** through excimer formation at and above f_w = 60 vol%. The fluorescence intensity of the excimer band was successively amplified with gradual addition of water content up to f_w = 99 vol% with emission maximum 579 nm (λ_{ex} = 350 nm). These newly developed orange FONPs, having good cytocompatibility and stability in biological milieu, were efficaciously employed in targeted cellular imaging and also as drug delivery vehicle. Comprising of nipecotic acid unit at both terminals the **NDI-nip** FONPs were subjected towards targeted cellular imaging of $GABA_A$ receptor enriched cells (SH-SY5Y and A549) as nipecotic acid being a conformational β-analog of GABA molecule. Fluorescence intensity of **NDI-nip** got quenched in SH-SY5Y and A549 cells indicating cellular internalization of **NDI-nip** FONPs specifically in those $GABA_AR$ enriched cell line while in presence of native GABA molecule no such prominent quenching was noted. Moreover, these **NDI-nip** FONPs were found highly efficient for encapsulating the anti-cancer drug, curcumin. These drug-loaded nanoparticles exhibited target-specific killing of cancerous SH-SY5Y and A549 cells in contrast to non-cancerous NIH3T3 cells. Hence, **NDI-nip** FONPs

were used as targeted delivery vehicle and bio-imaging diagnostic probe for $GABA_A$ receptor enriched cell (SH-SY5Y and A549) in comparison to non-cancerous cell ($NIH3T3$).

2.4 EXPERIMENTAL SECTION

2.4.1 MATERIALS.

N-(*tert*-butoxycarbonyl)-L-aspartic acid 4-benzyl ester, 1-naphthaleneethanol, 1,4,5,8-Naphthalenetetracarboxylic dianhydride, nipecotic acid and all deuteriated solvents were brought from Sigma-Aldrich. *N*-hydroxysuccinimide (NHS), *N*,*N*-dicyclohexylcarbodiimide (DCC), trifluoroacetic acid (TFA), 4-*N*,*N*-(dimethylamino) pyridine (DMAP), *N*-hydroxybenzotriazole (HOBT), palladium 10% on activated charcoal, reagents of column chromatography and other solvents and chemicals were bought from SRL, India. Cell culture ingredients and all type of cells were bought from Invitrogen and NCCS, Pune India respectively. 300 MHz and 400 MHz AVANCE (Bruker) spectrometer and Bruker Ultraflex MALDI mass spectrometer (2,5-dihydroxy benzoic (DHB) acid as matrix) was used for NMR spectroscopy and to record MALDI-TOF spectra respectively.

2.4.2 SYNTHESIS OF NDI-NIP.

1.0 eqv of 1-naphthaleneethanol and 1.2 eqv of *N*-(tert-butoxycarbonyl)-L-aspartic acid 4-benzyl ester were conjugated using 1.1 eqv of DCC, DMAP and HOBT in dry dichloromethane (DCM). The reaction mixture was stirred for 12 h under N_2 atmosphere. After washing the organic part with HCl (1N) and drying over anhydrous sodium sulfate, the solvent was evaporated and the coupled product was purified by column chromatography (60-120 mesh silica gel) using 1% MeOH in $CHCl_3$ as eluent. The obtained product was debenzylated in methanol under hydrogen (H_2) atmosphere in presence of Pd on activated charcoal. The mixture was filtered in a celite-545 column after overnight stirring at room temperature. The deprotected acid was subjected to NHS activation by using 2.6 eqv of DCC and 2.3 eqv of NHS in dry DMF and stirred overnight under N_2 atmosphere. Nipecotic acid (2 eqv) and dry pyridine (excess) were added to this activated acid. After overnight stirring the DMF was distilled out

from the reaction mixture and nipecotic acid coupled product was purified by column chromatography (100-200 mesh silica gel) where 5 % MeOH in $CHCl_3$ used as the eluent.

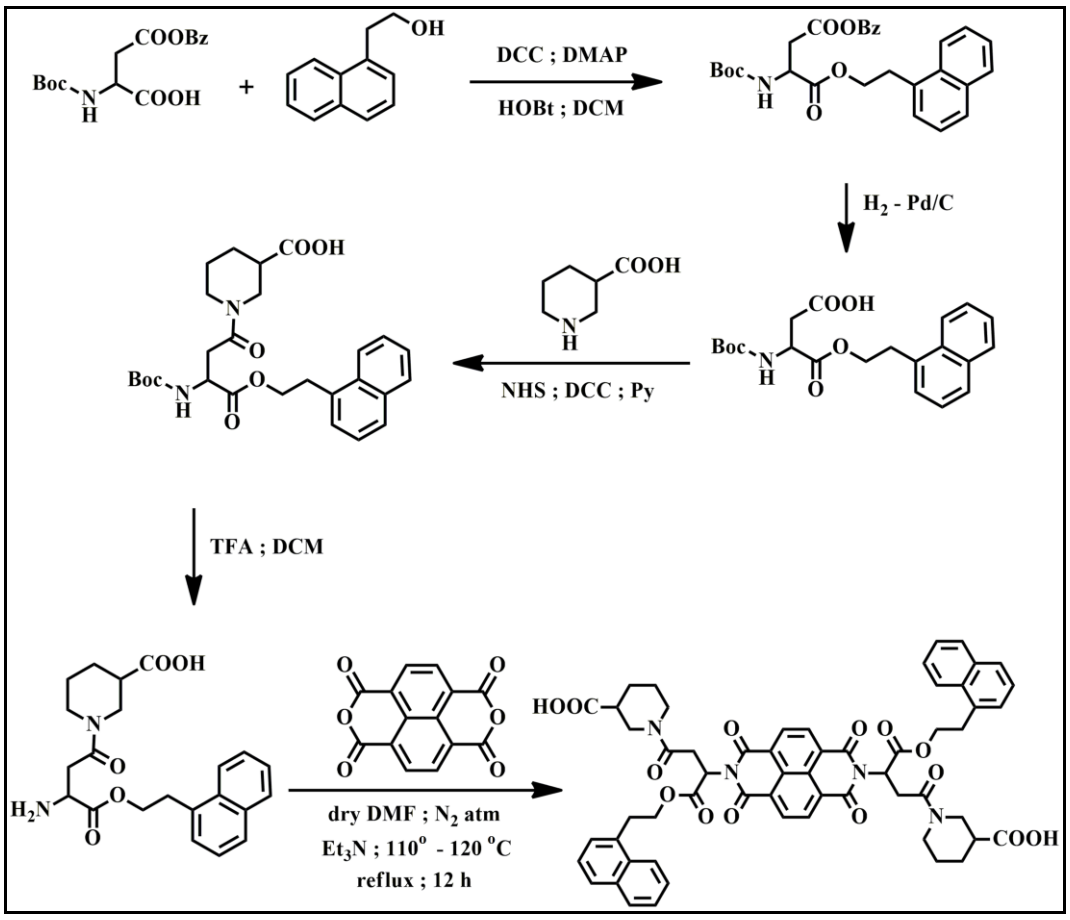

Scheme 1. Synthetic scheme of naphthalene diimide (NDI) based amphiphile, **NDI-nip**.

TFA (1.5 eqv) was used to deprotect the *tert*-butoxycarbonyl group in dry DCM. DCM was evaporated after 4 h of stirring and the concentrated mass was taken in ethyl acetate that was washed with aqueous sodium carbonate solution (10%) and followed by brine solution. The free amine derivative was obtained after evaporating the organic solvent. Finally, condensation of 2.2 eqv of free amine derivative and 1.0 eqv of 1,4,5,8-naphthalenetetracarboxylic dianhydride was carried out at 90 °C for 12 h in dry DMF under inert atmosphere. DMF was removed and DCM was used to dissolved the crude mass which was then washed with water. To obtain the pure **NDI-nip**, the condensed product was purified by column chromatography (100-200 mesh silica gel, 5% MeOH in $CHCl_3$ as an eluent) followed by washing with diethyl ether (Figure 1 and Scheme 1).

2.4.3 PREPARATION OF SAMPLES FOR SELF-ASSEMBLY.

NDI-nip was dissolved in DMSO to prepare the stock solution of 10 mM concentration. To achieve different composition needed for following experiments, required amount aliquot was added to the varying compositions of DMSO-water binary solvent mixture in various ratios from this stock solution of **NDI-nip** in DMSO. Detailed characterization data of the self-aggregated **NDI-nip** in varying compositions of DMSO-water such as transmission electron microscopy (TEM), field emission scanning electron microscopy (FESEM), atomic force microscopy (AFM), dynamic light scattering (DLS), FTIR, solvent-dependent ^{1}H-NMR, fluorescence microscopic study, quantum yield (QY) measurement and time resolved study have been carried out with the prepared stock solution.

2.4.4 TRANSMISSION ELECTRON MICROSCOPY (TEM) STUDY.

NDI-nip (10 μM) solution in (1:99 v/v) DMSO-water (f_w = 99 vol%) was deposited on a 300-mesh carbon-coated copper grid and dried. Negative staining of the copper grid was done with freshly prepared 1 μL of uranyl acetate solution (1% w/v), and a filter paper was used to blot the excess solution. Before taking the image in transmission electron microscopic, the sample was dried for 4 h in vacuum. The TEM images were taken in JEOL JEM 2010 microscope.

2.4.5 FIELD-EMISSION SCANNING ELECTRON MICROSCOPY (FE-SEM) STUDY.

To obtain FESEM images, a JEOL-6700F microscope was used. 5 μL of **NDI-nip** having concentration of 10 μM solution in f_w = 99 vol% was used to drop cast on a coverslip. After drying it for overnight, the FESEM images were taken.

2.4.6 ATOMIC FORCE MICROSCOPY (AFM) STUDY.

Veeco, model AP0100 instrument was used to capture the AFM images of **NDI-nip**. 10 μL of solution of **NDI-nip** having concentration of 10 μM in f_w = 99 vol% was deposited on freshly cleaved (1 cm × 1 cm) mica. Before taking the AFM images, it was dried overnight.

2.4.7 DYNAMIC LIGHT SCATTERING (DLS) STUDY.

To determine the mean hydrodynamic diameter (D_h) of **NDI-nip** (10 μM) in f_w = 99 vol% we performed DLS study using a fixed-angle apparatus (Zen 3690 Zetasizer Nano ZS

instrument (Malvern Instrument Ltd.). Measurement of the scattering intensity was done at an angle of 175°.

2.4.8 UV-VISIBLE STUDY.

PerkinElmer Lambda 25 spectrophotometer was used to record UV-vis spectra. UV-vis spectra of **NDI-nip** (10 μM) were performed in various solvent compositions of DMSO-water changing the water content from f_w = 0 vol% to f_w = 99 vol%. The relative absorbance (A/A_0) of **NDI-nip** (10 μM) was studied for 7 days, where A_0 = original absorbance and A = absorbance at different days. To observe the intramolecular charge transfer (ICT) process, we have recorded UV-vis spectra of **NDI-nip** (50 μM) in various organic solvents (benzene, chlorobenzene, *o*-xylene, *m*-xylene, *p*-xylene and toluene) of different polarities.

2.4.9 FTIR STUDY.

PerkinElmer Spectrum 100 FTIR spectrometer was used for FTIR measurements. FTIR spectra of **NDI-nip** were performed in the $CHCl_3$ (in non-self-assembled state) and in the self-aggregated state (f_w = 99 vol%) at room temperature. 1 mm CaF_2 cell was used to perform all the experiments of FTIR study.

2.4.10 SOLVENT-DEPENDENT ^{1}H-NMR STUDY.

Solvent dependent ^{1}H-NMR study was performed with a Avance 300 MHz (Bruker) spectrometer. The spectra of **NDI-nip** (1 mM) in DMSO-d_6 and in several solvent systems (2:1 (v/v) and 1:1 (v/v) of DMSO-d_6-D_2O) were recorded.

2.4.11 FLUORESCENCE MICROSCOPY STUDY.

Drop casting of 10 μL solution of **NDI-nip** having concentration 10 μM in f_w = 99 vol% was performed on a glass slide. After that, images were taken under fluorescence microscope (Olympus IX83 inverted) at 40x magnification.

2.4.12 PHOTOLUMINESCENCE STUDY.

Varian Cary Eclipse luminescence spectrometer was used to record the fluorescence spectra of the **NDI-nip** (10 μM) solutions in f_w = 0-99 vol% (excitation wavelength (λ_{ex}) = 350

nm). We measured concentration dependent emission of **NDI-nip** in 60% water content in DMSO. pH-dependent fluorescence spectra of **NDI-nip** (10 μM) in different pH (pH = 3.0-7.0) were investigated to check the effect of pH in emission and aggregation property of **NDI-nip**. We also checked excitation dependent emission spectra of **NDI-nip** (10 μM) in f_w = 99 vol% with excitation range 350-450 nm. Relative fluorescence intensity (I/I_o) of **NDI-nip** FONPs (in f_w = 99 vol%) was studied 7 days where, I_o = original fluorescence intensity and I = fluorescence intensity at different days of **NDI-nip** FONPs respectively. Photoluminescence study of **NDI-nip** (10 μM) were also carried out in different organic solvents (benzene, chlorobenzene, *o*-xylene, *m*-xylene, *p*-xylene and toluene) of varying polarities for monitoring the ICT. Interaction between **NDI-nip** (10 μM) with 100 μg/mL of L-phenylalanine (Phe), L-tyrosine (Tyr), L-arginine (Arg) and native GABA (200 μg/mL) were recorded by photoluminescence study.

2.4.13 QUANTUM YIELD (QY) MEASUREMENT.

Quantum yields are usually calculated with respect to an optical dilute standard fluorophore solution having a well-known QY (ϕ_s). The Parker-Rees method was used to determine the QYs (ϕ_u) of the unknown fluorophore.

$$\emptyset_u = \left(\frac{A_s F_u n_u^2}{A_u F_s n_s^2}\right)\emptyset_s \qquad (3)$$

Here, A_u and A_s were the absorbance of unknown sample and reference sample at the excitation wavelength respectively. Exciting at the same excitation wavelength, the area of the integrated fluorescence intensity for the unknown sample and known sample were F_u and F_s respectively. A solution having similar absorbance (<0.01) was used to measure the QY. n_u = the refractive indices of the solvents in which the unknown was prepared and n_s = the refractive indices of the solvents in which the standard samples were prepared. Here, we have chosen quinine sulfate dissolved in 0.1 M sulfuric acid (H_2SO_4) as the standard and its QY (ϕ_s) = 54.0%.

2.4.14 TIME RESOLVED STUDY.

A picosecond diode laser IBH-405 was used to perform time correlation single photon count (TCSPC) measurement. **NDI-nip** (10 μM) solution was excited at 375 nm followed by

monitoring of the emission at 415 nm for only DMSO and at 579 nm for f_w = 99 vol%. IBH DAS6 software was used to analyze the fluorescence decays. the experimental time resolved fluorescence decay $p(t)$ was analyzed using following equation 2.

$$p(t) = b + \sum_{i}^{n} \alpha_i \exp\left(-\frac{t}{\tau_i}\right) \quad (4)$$

where n = number of discrete emissive species, b = baseline correction ("dc" offset), α_i were the pre-exponential factors and τ_i were excited state fluorescence lifetimes associated with the ith component. Equation 3 was utilized to calculate the average lifetime of multiexponential decays.

$$< \tau > = \sum_{i=1}^{n} \alpha_i \tau_i \quad (5)$$

Where $\alpha_i = \frac{\alpha_i}{\sum \alpha_i}$ which denotes the contribution of a decay component.

2.4.15 CELL CULTURE.

A549, SHSY-5Y (cancer cells) and NIH3T3 (normal cells) were cultured using 10% FBS, streptomycin and penicillin in DMEM media while keeping in incubator (5% CO_2, 37 °C). Solution of 10 μM all-trans-retinoic acid (RA) in DMSO was used to differentiate SH-SY5Y cells for 7 to 10 days with varying retinoic acid-containing media on alternate days. We performed cytocompatibility, bioimaging, MTT assay and all other biological experiments with those treated cells. **NDI-nip** FONPs prepared at f_w = 99 vol% was used to perform all the cellular experiments.

2.4.16 STABILITY EXPERIMENTS AND CYTOCOMPATIBILITY OF NDI-NIP FONPs.

The stability of 100 μM of **NDI-nip** FONPs (in f_w = 99 vol%) was investigated in biological milieu by adding **NDI-nip** FONPs in the FBS-supplemented media and kept for a long-time duration. The suspension stability index (SSI) of **NDI-nip** FONPs was determined by recording the absorbance at 381 nm (corresponding to the λ_{max} of **NDI-nip** in f_w = 99 vol%) at various time intervals.

Suspension stability index (SSI) = $(A_t/A_o) \times 100$ where A_t = absorbance of the solutions at different time intervals and A_o = initial absorbance of the solutions at 381 nm for **NDI-nip** FONPs, respectively.

MTT assay was performed to investigate cytocompatibility of **NDI-nip** FONPs in f_w = 99 vol%). In this assay, mitochondrial dehydrogenase excreting from viable cells reduced the soluble tetrazolium gets into insoluble formazan. Spectrophotometric method was used to estimate the amount of insoluble formazan dissolving in DMSO. The production of formazan is proportional to the quantity of alive cells. First, A549, SHSY-5Y and NIH3T3 cells (2×10^4 cells per well) were incubated in a 96-well plate for 24 h (5% CO_2, 37 °C). Next, all the cells were treated with 10-200 μM of **NDI-nip** FONPs (f_w = 99 vol%) for 24 h. Addition of 10 μL of MTT stock solution (5 mg mL^{-1}) was carried out into the cells which were incubated further for 4 h. After the incubation, Bio Tek1 Elisa Reader was used to record the absorbance of the precipitated formazan which was solubilized in DMSO (λ_{ex} = 570 nm). The number of alive cells was calculated as % viability by following the equation

% viability = (A_{570} (treated cells) – background) / (A_{570} (untreated cells) – background) × 100

2.4.17 BIOIMAGING.

A549, SH-SY5Y and NIH3T3 cells were cultured in a chamber slide. After that, cells were incubated with i) **NDI-nip** FONPs (100 μM, f_w = 99 vol%), ii) **NDI-nip** FONPs (100 μM, f_w = 99 vol%) + GABA (200 μg/mL), iii) **NDI-C** (NDI derivative control compound devoid of nipecotic acid moiety) FONPs (100 μM, f_w = 99 vol%) for 12 h and 24 h. Washing of cells were done with phosphate buffer saline (PBS) (three times). After that, 4% paraformaldehyde was used for fixing. Next, glycerol (50%) was used to mount and the glass slide was covered with a cover slip for 24 h. IX83 inverted microscope at 20x magnification was used for cellular imaging.

To check the distribution of **NDI-nip** FONPs (100 μM, fw = 99 vol%) in A549 (cancer) and SH-SY5Y (cancer) cells, the compound was incubated by following the above procedure. Washing of cells were done with PBS (two times). After that 1 μl Hoechst stain dissolved in 1 ml PBS was incubated in both the treated cells for 15 min in dark. Next fixing and mounting with 4% paraformaldehyde and 50% glycerol was done. After that glass slides were covered with cover slips and IX83 inverted microscope at 20x magnification was used for imaging.

2.4.18 FLOW CYTOMETRY.

We incubated i) **NDI-nip** FONPs (100 μM, f_w = 99 vol%), ii) **NDI-nip** FONPs (100 μM, f_w = 99 vol%) + GABA (200 μg/mL), iii) **NDI-C** FONPs (100 μM, f_w = 99 vol%) with NIH3T3, SH-SY5Y and A549 cells for 24 h. In order to remove the excess compounds from cell medium, we washed all the treated cells using DMEM media and PBS buffer after incubation. Cells were trypsinized and centrifuge for 5 min. The flow cytometric experiment was carried out with the precipitated cells suspended in PBS (500 μL) after centrifugation. BD FACS Aria™ III flow cytometer was employed to inspect the cells at emission wavelength using a 510 ± 40 nm bandpass filter upon excitation at 405 nm.

2.4.19 TREATING CELLS WITH CURCUMIN-LOADED NDI-NIP FONPs.

Curcumin (2 mg) and **NDI-nip** (1 mg) were dissolved in 200 μL of DMSO in 2:1 w/w ratio. To attain the required 1:99 v/v DMSO-water mixed solvent ratio, 19.8 mL of Milli-Q water was added into this solution. The mixture was then homogenized using vortex for 10 min. Separation of the drug-encapsulated FONPs was carried out by centrifugation (10000 rpm, 1 h). After dispersing the pellet in 1:99 v/v DMSO-water, 100 μL of aliquot was diluted to 1 mL of methanol to estimate the quantity of loaded curcumin. Measurement of the absorbance of the yellow-colored solution was calculated at 425 nm and a standard calibration curve was used for quantification of curcumin. The standard calibration curve was prepared by gradual dilution of a stock curcumin solution in methanol and the absorbance was recorded at 425 nm. Following equation was used to determine the loading efficiency (LE) of the curcumin:

LE = [(Amount of curcumin loaded in FONPs) / (Amount of curcumin used for loading)] × 100

In an another MTT assay, SHSY-5Y, A549 and NIH3T3 cells were incubated separately with both native curcumin (5-100 μM) and curcumin-loaded **NDI-nip** FONP ([curcumin] = 5-100 μM and [**NDI-nip** FONPs] = 2.5-50 μM) for 24 h in 96-well plates. Equation 1 was used to determine the % of cell killing efficiency by the native curcumin and curcumin-encapsulated **NDI-nip** FONP.

2.5 CHARACTERIZATION DATA

NDI-nip: ^{1}H-NMR (500 MHz, $CDCl_3$, 25 °C): δ/ppm: 8.58 (s, 4H, NDI core), 8.11 (d, 2H, ,C-8 proton of naphthyl ring), 8.02 (d, 2H, C-5 proton of naphthyl ring), 7.85-7.91 (m, 2H, C-4 proton of naphthyl ring), 7.31-7.42 (m, 4H, C-3, C-6 proton of naphthyl ring), 7.18-7.30 (m, 2H, C-7 proton of naphthyl ring), 7.02 (d, 2H, C-2 proton of naphthyl ring), 4.76-4.83 (m, 2H, chiral centre of L-aspartic acid residue), 4.49-4.62 (m, 2H, -O-C$\underline{H}_2$-CH_2-C_6H_7), 3.38-3.82 (m, 12H, -O-CH_2-C$\underline{H}_2$-C_6H_7, C-2, C-5 proton of nipecotic acid residue), 2.28-2.47 (m, 6H, methylene proton od L-aspartic acid residue, C-3 proton of nipecotic acid residue), 1.09-1.38 (m, 4H, C-3 and C-4 proton of nipecotic acid residue).

^{13}C-NMR (100 MHz, $CDCl_3$): 171.26, 170.75, 169.37, 162.21, 136.96, 133.85, 132.00, 130.93, 129.28, 128.64, 128.35, 126.98, 126.49, 125.78, 125.13, 123.37, 95.89, 54.59, 44.73, 43.11, 39.89, 31.45, 29.85, 23.19, 20.27.

MALDI-TOF MS: m/z: 1028.35 $[M]^+$ (calculated); 1028.037 (found).

2.6 SPECTRA

2.6.1 ^{1}H-NMR SPECTRUM.

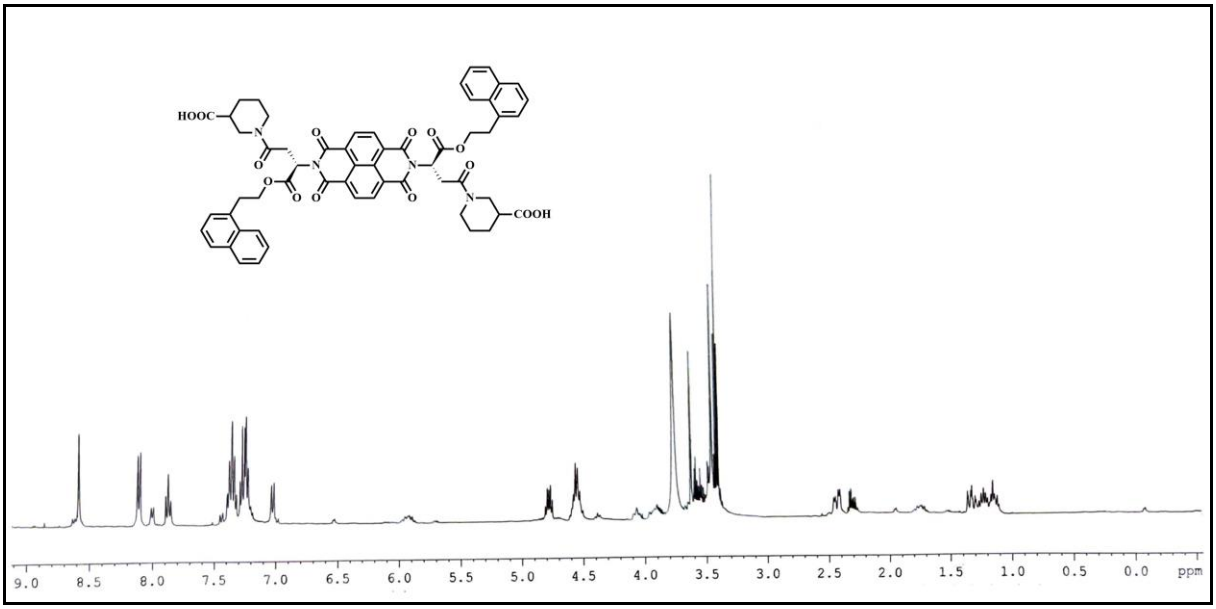

2.6.2 ^{13}C-NMR SPECTRUM.

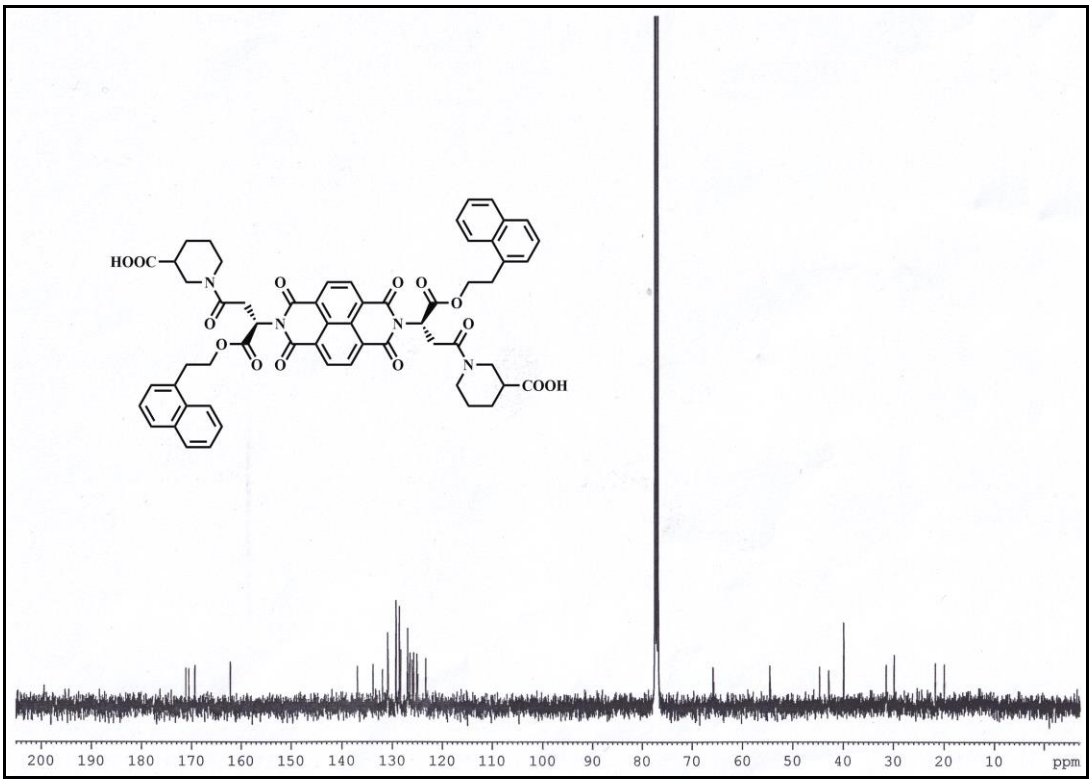

2.6.3 MALDI-TOF MASS SPECTRUM.

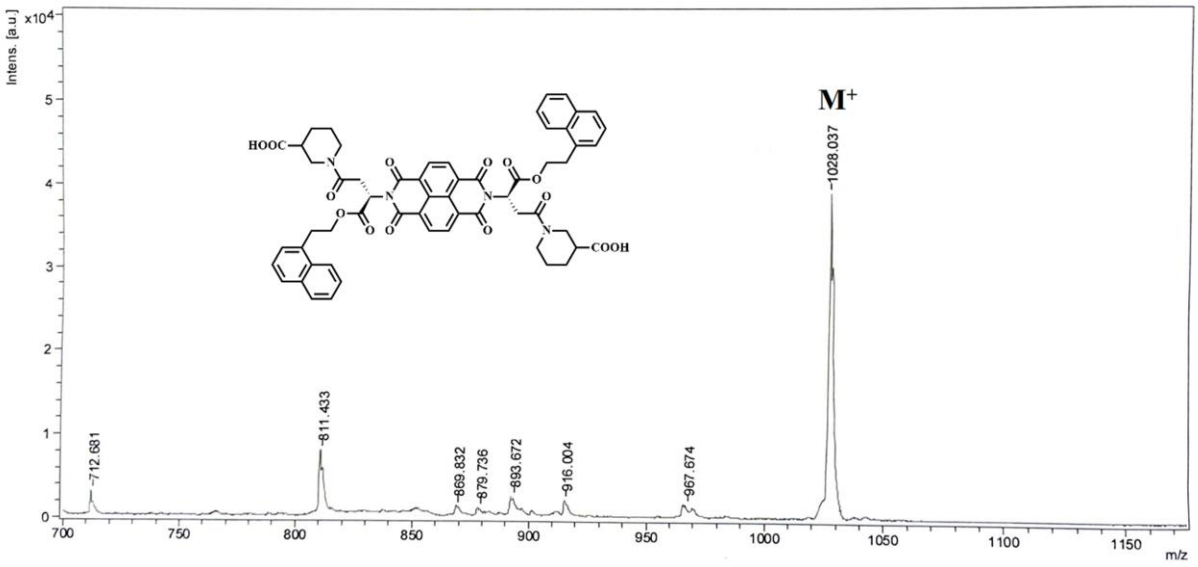

2.7 REFERENCES

[1] Yao, J.; Yang, M.; Duan, Y. Chemistry, Biology, and Medicine of Fluorescent Nanomaterials and Related Systems: New Insights into Biosensing, Bioimaging, Genomics, Diagnostics, and Therapy. *Chem. Rev*. **2014**, *114*, 6130-6178.

[2] Kobayashi, H.; Ogawa, M.; Alford, R.; Choyke, P. L.; Urano, Y. New Strategies for Fluorescent Probe Design in Medical Diagnostic Imaging. *Chem. Rev.* **2010**, *110*, 2620-2640.

[3] Peng, H. S.; Chiu, D. T. Soft Fluorescent Nanomaterials for Biological and Biomedical Imaging. *Chem. Soc. Rev.* **2015**, *44*, 4699-4722.

[4] Desmonts, L. B.; Reinhoudt, D. N.; Calama, M. C. Design of Fluorescent Materials for Chemical Sensing. *Chem. Soc. Rev.* **2007**, *36*, 993-1017.

[5] Wolfbeis, O. S. An Overview of Nanoparticles Commonly used in Fluorescent Bioimaging. *Chem. Soc. Rev.* **2015**, *44*, 4743-4768.

[6] Zhang, X.; Zhang, X.; Wang, S.; Liu, M.; Zhang, Y.; Tao, L.; Wei, Y. Facile Incorporation of Aggregation-Induced Emission Materials into Mesoporous Silica Nanoparticles for Intracellular Imaging and Cancer Therapy. *ACS Appl. Mater. Interfaces* **2013**, *5*, 1943-1947.

[7] Das, K.; Sarkar, S.; Das, P. K. Fluorescent Indicator Displacement Assay: Ultrasensitive Detection of Glutathione and Selective Cancer Cell Imaging. *ACS Appl. Mater. Interfaces* **2016**, *8*, 25691-25701.

[8] Li, J.; Zhu, J. Quantum Dots for Fluorescent Biosensing and Bio-imaging Applications. *Analyst* **2013**, *138*, 2506-2515.

[9] Peynshaert, K.; Manshian, B. B.; Joris, F.; Braeckmans, K.; De Smedt, S. C.; Demeester, J.; Soenen, S. J. Exploiting Intrinsic Nanoparticle Toxicity: The Pros and Cons of Nanoparticle-Induced Autophagy in Biomedical Research. *Chem. Rev*. **2014**, *114*, 7581-7609.

[10] Hong, Y.; Lam, J. W. Y.; Tang, B. Z. Aggregation-Induced Emission: Phenomenon, Mechanism and Applications. *Chem. Commun*. **2009**, 4332-4353.

[11] Yuan, W. Z.; Lu, P.; Chen, S.; Lam, J. W. Y.; Wang, Z.; Liu, Y.; Kwok, H. S.; Ma, Y.; Tang, B. Z. Changing the Behavior of Chromophores from Aggregation-Caused Quenching to Aggregation-Induced Emission: Development of Highly Efficient Light Emitters in the Solid State. *Adv. Mater*. **2010**, *22*, 2159-2163.

[12] Thompson, R. B. *Fluorescence Sensors and Biosensors*, CRC: Boca Raton, **2006**.

[13] Hong, Y.; Lam, J. W. Y.; Tang, B. Z. Aggregation-Induced Emission. *Chem. Soc. Rev*. **2011**, *40*, 5361-5388.

[14] Zhang, X.; Zhang, X.; Tao, L.; Chi, Z.; Xu, J.; Wei, Y. Aggregation Induced Emission-based Fluorescent Nanoparticles: Fabrication Methodologies and Biomedical Applications. *J. Mater. Chem. B* **2014**, *2*, 4398-4414.

[15] Gao, M.; Tang, B. Z. Aggregation-Induced Emission Probes for Cancer Theranostics. *Drug Discov. Today* **2017**, *22*, 1288-1294.

[16] Feng, G.; Liu, B.; Aggregation-Induced Emission (AIE) Dots: Emerging Theranostic Nanolights. *Acc. Chem. Res*. **2018**, *51*, 1404-1414.

[17] Wang, D.; Lee, M. M. S.; Xu, W.; Kwok, R. T. K.; Lam, J. W. Y.; Tang, B. Z. Theranostics based on AIEgens. *Theranostics* **2018**, *8*, 4925-4956.

[18] Wu, W.; Li, Z. Nanoprobes with Aggregation-Induced Emission for Theranostics. *Mater. Chem. Front*. **2021**, *5*, 603-626.

[19] Kaeser, A.; Schenning, A. P. H. J. Fluorescent Nanoparticles based on Self-Assembled π-Conjugated Systems. *Adv. Mater.* **2010**, *22*, 2985-2997.

[20] Kaeser, A.; Fischer, I.; Abbel, R.; Besenius, P.; Dasgupta, D.; Gillisen, M. A. J.; Portale, G.; Stevens, A. L.; Herz, L. M.; Schenning, A. P. H. J. Side Chains Control Dynamics and Self-Sorting in Fluorescent Organic Nanoparticles. *ACS Nano* **2013**, *7*, 408-416.

[21] Choudhury, P.; Das, K.; Das, P. K. L-Phenylalanine-Tethered, Naphthalene Diimide-based, Aggregation-Induced, Green-Emitting Organic Nanoparticles. *Langmuir* **2017**, *33*, 4500-4510.

[22] Ghosh, A. K.; Choudhury, P.; Das, P. K. Fabrication of Orange-Emitting Organic Nanoparticle-Protamine Conjugate: Fluorimetric Sensor of Heparin. *Langmuir* **2019**, *35*, 15180-15191.

[23] Mihic, S. J.; Harris, R. A. GABA and the $GABA_A$ Receptor. *Alcohol Health Res World* **1997**, *21*, 127-131.

[24] Chebib, M.; Johnston, G. A. R. The 'ABC' of GABA Receptors: A Brief Review. *Clin. Exp. Pharmacol.* **1999**, *26*, 937-940.

[25] Fritschy, J. M.; Panzanelli, P. $GABA_A$ Receptors and Plasticity of Inhibitory Neurotransmission in the Central Nervous System. *Eur. J. Neurosci*. **2014**, *39*, 1845-1865.

[26] Sigel, E.; Steinmann, M. E. Structure, Function, and Modulation of $GABA_A$ Receptors. *J. Biol. Chem.* **2012**, *287*, 40224-40231.

[27] Macdonald, R.L.; Olsen, R.W. $GABA_A$ Receptor Channels. *Annu. Rev. Neurosci*. **1994**, *17*, 569-602.

[28] Sieghart, W. Structure and Pharmacology of □-Aminobutyric $Acid_A$ Receptor Subtypes. *Pharmacol. Rev.* **1995**, *47*, 181-234.

[29] Bradford, H.F. Glutamate, GABA and Epilepsy. *Prog. Neurobiol*. **1995**, *47*, 477-511.

[30] Kleppner, S. R.; Tobin, A. J. GABA Signalling: Therapeutic Targets for Epilepsy, Parkinson's Disease and Huntington's Disease. *Expert Opin. Ther. Targets* **2001**, *5*, 219-239.

[31] Kalueff, A. V.; Nutt, D. J. Role of GABA in Anxiety and Depression. *Depress. Anxiety* **2007**, *24*, 495-517.

[32] Braat, S.; Kooy, R. F. The $GABA_A$ Receptor as a Therapeutic Target for Neurodevelopmental Disorders. *Neuron* **2015**, *86*, 1119-1130.

[33] Rudolph, U.; Möhler, H. GABA-based Therapeutic Approaches: $GABA_A$ Receptor Subtype Functions. *Curr. Opin. Pharmacol.* **2006**, *6*, 18-23.

[34] Antkowiak, B.; Rammes, G. GABA(A) Receptor-Targeted Drug Development-New Perspectives in Perioperative Anesthesia. *Expert Opin. Drug. Discov.* **2019**, *14*, 683-699.

[35] Prescot, A. P.; Prisciandaro, J. J.; Miller, S. R.; Ingenito, G.; Kondo, D. G.; Renshaw, P. F. Two-Dimensional Proton Magnetic Resonance Spectroscopy Versus J-Editing for GABA Quantification in Human Brain: Insights from a GABA-Aminotransferase Inhibitor Study. *Scientific Reports* **2018**, *8*, 13200.

[36] Wang, T.; Muthuswamy, J. Immunosensor for Detection of Inhibitory Neurotransmitter Gamma-Aminobutyric Acid using Quartz Crystal Microbalance. *Anal. Chem*. **2008**, *80*, 8576-8585.

[37] Marvin, J. S.; Shimoda, Y.; Magloire, V.; Leite, M.; Kawashima, T.; Jensen, T. P.; Kolb, I.; Knott, E. L.; Novak, O.; Podgorski, K.; Leidenheimer, N. J.; Rusakov, D. A.; Ahrens, M. B.; Kullmann, D. M.; Looger, L. L. A Genetically Encoded Fluorescent Sensor for in Vivo Imaging of GABA. *Nat. Methods* **2019**, *16*, 763-770.

[38] Lee, J. H.; Chae, E. J.; Park, S. J.; Choi, J.W. Label- Free Detection of γ- Aminobutyric Acid based on Silicon Nanowire Biosensor. *Nano Converg.* **2019**, *6*, 13.

[39] Jinnarak, A.; Teerasong, S. A Novel Colorimetric Method for Detection of Gamma-Aminobutyric Acid based on Silver Nanoparticles. *Sensor. Actuat. B Chem.* **2016**, *229*, 315-320.

[40] Meeploy, M.; Deewatthanawong, R.; Determination of γ-Aminobutyric Acid (GABA) in Rambutan Fruit Cv. Rongrian by HPLC-ELSD and Separation of GABA from Rambutan Fruit using Dowex 50W-X8 Column. *J. Chromatogr. Sci*. **2016**, *54*, 445-452.

[41] Quandt, G.; Höfner, G.; Wanner, K. T. Synthesis and Evaluation of N-Substituted Nipecotic Acid Derivatives with an Unsymmetrical Bis-Aromatic Residue Attached to a Vinyl Ether Spacer as Potential GABA Uptake Inhibitors. *Bioorg. Med. Chem*. **2013**, *21*, 3363-3378.

[42] Hellenbrand, T.; Höfner, G.; Wein, T.; Wanner, K. T. Synthesis of 4-Substituted Nipecotic Acid Derivatives and Their Evaluation as Potential GABA Uptake Inhibitors. *Bioorg. Med. Chem*. **2016**, *24*, 2072-2096.

[43] Kokado, K.; Chujo, Y. Multicolor Tuning of Aggregation-Induced Emission Through Substituent Variation of Diphenyl-o-carborane. *J. Org. Chem.* **2011**, *76*, 316-319.

[44] Choudhury, P.; Sarkar, S.; Das, P. K. Tunable Aggregation-Induced Multicolor Emission of Organic Nanoparticles by Varying the Substituent in Naphthalene Diimide. *Langmuir* **2018**, *34*, 14328-14341.

[45] Kumar, M.; George, S. J. Green Fluorescent Organic Nanoparticles by Self-Assembly Induced Enhanced Emission of a Naphthalene Diimide Bola Amphiphile. *Nanoscale* **2011**, *3*, 2130-2133.

[46] Kobaisi, M. A.; Bhosale, S. V.; Latham, K.; Raynor, A. M.; Bhosale, S. V. Functional Naphthalene Diimides: Synthesis, Properties, and Applications. *Chem. Rev*. **2016**, *116*, 11685-11796.

[47] Kulkarni, C.; Periyasamy, G.; Balasubramanian, S.; George, S. J. Charge-Transfer Complexation Between Naphthalene Diimides and Aromatic Solvents. *Phys. Chem. Chem. Phys*. **2014**, *16*, 14661-14664.

[48] Andersson, H.; Björnström, K.; Eintrei, C.; Sundqvis, T. Orexin A Phosphorylates the γ-Aminobutyric Acid Type A Receptor β_2 Subunit on a Serine Residue and Changes the Surface Expression of the Receptor in SH-SY5Y Cells Exposed to Propofol. *J. Neurosci. Res.* **2015**, *93*, 1748-1755.

[49] Zhang, X.; Zhang, R.; Zheng, Y.; Shen, J.; Xiao, D.; Li, J.; Shi, X.; Huang, L.; Tang, H.; Liu, J.; He, J.; Zhang, H. Expression of Gamma-Aminobutyric Acid Receptors on Neoplastic Growth and Prediction of Prognosis in Non-Small Cell Lung Cancer. *J. Transl. Med.* **2013**, *11*, 102.

[50] Lippert, V. E. Dipolmoment und elektronenstruktur von angeregten molekülen. *Z. Naturforschg.* **1955**, *10a*, 541-545.

[51] Mataga, N.; Kaifu, Y.; Koizumi, M. Solvent Effects Upon Fluorescence Spectra and the Dipole Moments of Excited Molecules. *Bull. Chem. Soc. Jpn.* **1956**, *29*, 465-470.

[52] Puthenkalam, R.; Hieckel, M.; Simeone, X.; Suwattanasophon, C.; Feldbauer, R. V.; Ecker, G. F.; Ernst, M. Structural Studies of $GABA_A$ Receptor Binding Sites: Which Experimental Structure Tells us What? *Front. Mol. Neurosci.* **2016**, *9*, 44.

[53] Lummis, S. C. R. Locating GABA in GABA Receptor Binding Sites. *Biochem. Soc. Trans*. **2009**, *37*, 1343-1346.

[54] Zhu, S.; Noviello, C. M.; Teng, J.; Walsh Jr, R. M.; Kim, J. J.; Hibbs, R. E. Structure of a Human Synaptic $GABA_A$ Receptor. *Nature* **2018**, *559*, 67-72.

[55] Miller. P. S.; Aricescu, A. R. Crystal Structure of a Human $GABA_A$ Receptor. *Nature* **2014,** *512*, 270-275.

[56] Wagner, D. A.; Czajkowski, C.; Jones, M. V. An Arginine Involved in GABA Binding and Unbinding but not Gating of the $GABA_A$ Receptor. *J. Neurosci*. **2004**, *24*, 2733-2741.

[57] Zhai, K.; Brockmüller, A.; Kubatka, P.; Shakibaei, M.; Büsselberg, D. Curcumin's Beneficial Effects on Neuroblastoma: Mechanisms, Challenges, and Potential Solutions. *Biomolecules* **2020**, *10*, 1469-1496.

[58] Anand, P.; Kunnumakkara, A. B.; Newman, R. A.; Aggarwal, B. B. Bioavailability of Curcumin: Problems and Promises. *Mol. Pharmaceutics* **2007**, *4*, 807-818.

[59] Li, H.; Zhang, N.; Hao, Y.; Wang, Y.; Jia, S.; Zhang, H.; Zhang, Y.; Zhang, Z. Formulation of Curcumin Delivery with Functionalized Single-Walled Carbon Nanotubes: Characteristics and Anticancer Effects In Vitro. *Drug Delivery* **2014**, *21*, 379-387.

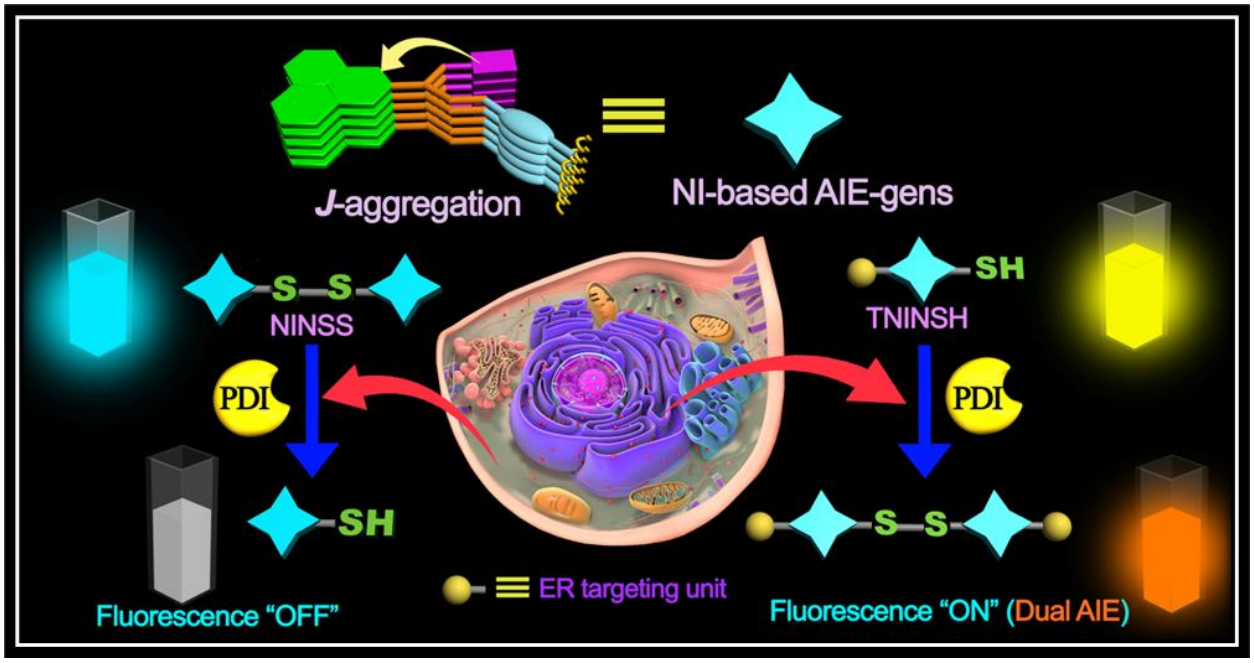

Naphthalimide based AIEgens for Sensing Protein Disulfide Isomerase through Thiol-Disulfide Redox Exchange

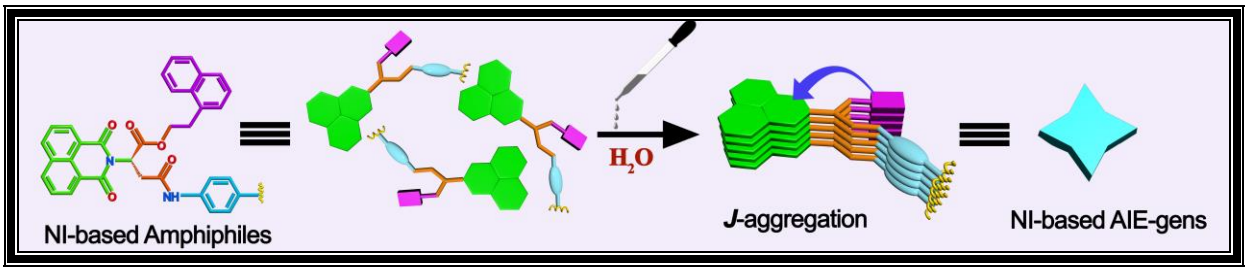

Architecting and Analyzing Naphthalimide-Centered Fluorescent Organic Nanoparticles: A Comprehensive Study in Design, Development, and Characterization

3A.1 INTRODUCTION

Fluorescent probes have emerged as indispensable tools within the realms of sensing, bioimaging, and diagnosis, owing to their innate and remarkable advantages encompassing heightened sensitivity, exceptional versatility, and non-invasive nature. This convergence of traits has propelled their utilization across diverse fields, empowering researchers and medical practitioners alike to glean intricate insights and facilitate precise analyses.[1-5] Among the plethora of luminescent probes that have been investigated (such as organic dyes, conjugated polymers, organic nanoparticles, inorganic quantum dots, metallic nanoclusters),[5-10] a distinctive category deserving particular attention is that of fluorescent organic nanoparticles (FONPs). These entities possess a trifecta of alluring attributes, namely chemical stability, facile tunability, and inherent biocompatibility. Such attributes render FONPs an enticing platform for various applications, ranging from scientific research to clinical practice.[11,12] Nevertheless, the expedition of FONPs is not devoid of challenges, with a noteworthy impediment taking the form of aggregation-caused quenching (ACQ). This phenomenon, wherein the luminescence of FONPs is stifled due to their aggregation, imposes a substantive limitation on their potential applications.[13,14] A pivotal breakthrough emerged in the scientific landscape with the revelation of aggregation-induced emission (AIE) by Tang and his collaborators in 2001. This paradigm-shifting concept unveiled an intriguing behavior exhibited by small organic molecules: while these molecules exhibited subdued or negligible fluorescence in a solvated state, while they remarkably emitted robust fluorescence once subjected to aggregation.[15-18] The realm of FONPs has undergone a revolutionary evolution, expanding exponentially over the past two decades. Researchers have embarked on a voyage of innovation, diligently diversifying and enriching the structural repertoire of FONPs, a testament to the transformative power of the AIE phenomenon.[19-22] In light of this burgeoning landscape, a critical imperative has emerged: the fabrication of AIE-based FONPs hailing from π-conjugated chromophoric molecules, which are endowed with specific motifs designed to interact with and target particular entities of interest.[23-26] This pursuit has transcended the confines of mere academic curiosity, extending its tendrils into the practical domains of scientific inquiry and real-world applicability. The development of these tailored FONPs

harbors immense promise, poised to unravel new dimensions in sensing, imaging, and diagnostic, and thereby, elevating frontiers of knowledge and medical prowess.

Protein Disulfide Isomerase (PDI) is a 57-kDa oxidoreductase with molecular chaperone functions in cellular balance.[27,28] It aids protein folding in the endoplasmic reticulum (ER) by forming disulfide bonds. PDI's dual role involves oxidizing in ER and reducing outside. Its chaperone function depends on redox state, influencing substrate entry.[28] PDI's impact spans cancer, where it aids growth and metastasis, potentially through ER stress-related pathways. Targeting PDI could trigger cancer cell death via UPR activation, making it a potential cancer therapy target.[29,30]

Hence, the precise sensing of Protein Disulfide Isomerase (PDI) across its dynamic range of redox states assumes paramount significance, given its intricate physiological behavior *in vitro* and *in vivo*. To date, an array of methodologies has been meticulously devised to scrutinize PDI's enzymatic activity.[31] Nevertheless, the landscape remains conspicuously sparse in terms of fluorometric diagnostic probes dedicated to PDI exploration. It is within this context that we have embarked upon a pioneering endeavor, culminating in the synthesis of amphiphiles based on the 1,8-naphthalimide (NI) scaffold. These novel amphiphiles are ingeniously tailored to encompass thiol (-SH) and disulfide (-S-S-) moieties, strategically positioned to facilitate the comprehensive analysis of PDI's intricate redox behavior (Figure 1). As a remarkable testament to the intricacy and versatility of these newly crafted amphiphiles, both thiol-containing variants (**NISH** & **TNINSH**) and their disulfide-bearing counterparts (**NISS** & **NINSS**) orchestrated the spontaneous assembly of organic nanoparticles. This self-assembly phenomenon was driven by the *J*-type aggregation mechanism within a solvent milieu of dimethyl sulfoxide (DMSO) and water (f_w = 99 vol%). Among this intriguing ensemble of amphiphiles, namely **NINSS** and **TNINSH**, emerged as heralds of a fascinating phenomenon-"Aggregation-Induced Emission (AIE)". This phenomenon bestowed **NINSS** and **TNINSH** with a distinctive fluorescence signature, characterized by vibrant blue and yellow emissions peaking at 470 nm and 550 nm, respectively, in 1:99 (v/v) DMSO-water solvent mixture. Harnessing the potent fluorescence characteristics of the **NINSS** and **TNINSH**-based Fluorescent Organic Nanoparticles (FONPs), we embarked upon an exploration of PDI's redox status. This exploration spanned the gamut from controlled laboratory experiments (*in vitro*)

to venturing into the complex tapestry of living organisms (*in vivo*). The utility of these tailored FONPs was elegantly channeled towards the probing and deciphering of PDI's redox intricacies for unraveling the enzyme's multifaceted behavior and functioning within the biological contexts. This innovative approach stands as a testament to the remarkable synergy between chemical ingenuity and biological inquiry, opening up vistas of understanding and potential therapeutic avenues in the enthralling realms of PDI-mediated physiological processes.

Within this specific subsection (Chapter 3A), our focus converges upon exploration encompassing the conceptualization and realization of amphiphiles centered around the foundational 1,8-naphthalimide moiety (NI). Delving into the nuances of design and the meticulous process of development, we unveil the unique attributes and functionalities inherent to these NI-based amphiphiles (**NISH**, **NISS**, **NINSS** and **TNINSH**). Furthermore, our discourse extends to the meticulous endeavor of characterization, where we scrutinize and elucidate the distinctive features and behaviors exhibited by these innovative amphiphilic constructs. Through this comprehensive examination, we endeavor to unravel the underlying principles and unveil the intricate tapestry that constitutes the realm of NI-based amphiphiles, shedding light on their structural, functional, and performance aspects.

3A.2 RESULTS AND DISCUSSION

3A.2.1 DESIGNING OF THE NAPHTHALIMIDE BASED AIE-GENS.

Development of supramolecular AIEgens is primarily administered through self-assembly by variation in molecular architecture of the building constituent comprising of chromophoric unit. Building blocks spontaneously get associated to form ordered architectures, which enables these materials with diverse morphologies, tunable designs and stimuli responsiveness. Thus, molecular architecting plays the crucial role in order to construct small amphiphilic AIE-gens with target specific motif. In principle, fluorescent nature of AIEgens is originated owing to restriction of intermolecular motion (RIM) which in turn governed by non-planarity/propeller shape of building block.[16-17] To expedite AIE phenomena in self-aggregated state, rotations are restricted through physical constraints that block the nonradiative pathway and therefore enable the excitons to decay radiatively. In this context, conjugated organic luminescent molecules with donor (D)-acceptor (A) scaffold have been

emerged as attractive multifunctional systems that facilitate the charge transfer process resulting in emission modulation.[24,26,32,33]

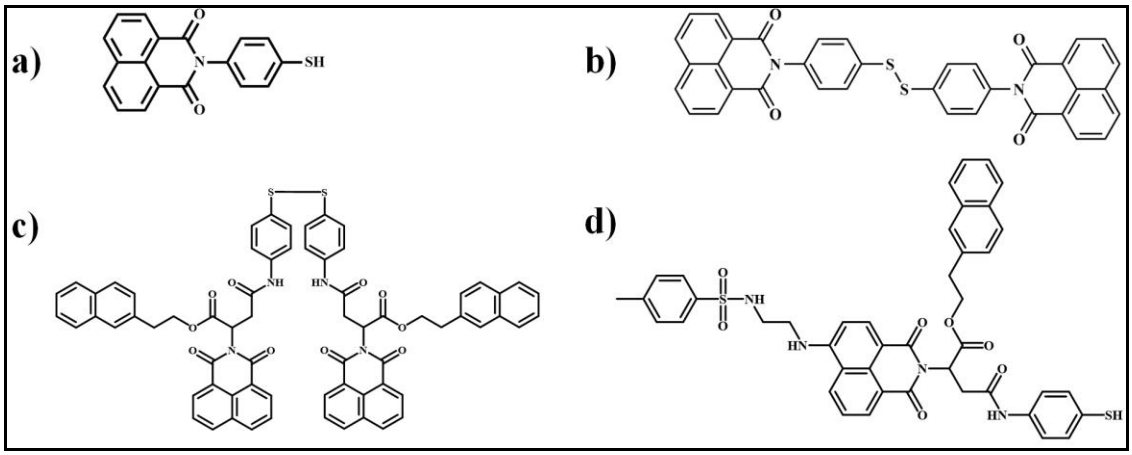

Figure 1. Molecular structure of NI-based amphiphiles: (a) **NISH**, (b) **NISS**, (c) **NINSS** and (d) **TNINSH**.

Herein, we used 1,8-Naphthalimides (NIs) as building block for developing AIE-gens. Considering its unique photophysical properties and prominent advantages such as large Stokes shift, photostability and cytocompatibility, NI derivatives are extensively used in developing AIEgens.[34,35] *N*-Functionalization of electron deficient NI core or introduction of electron-donating substituents at the 4th position of the NI core can authorize intramolecular charge transfer (ICT) from electron rich (donor) ligands to electron deficient (acceptor) molecular backbone.[36-38] This may have significant contribution towards achieving AIE due to RIM generated from planarity forfeiture of molecule in self-aggregated state. To analyze the redox behavior of dithiol-disulfide oxidoreductase, protein disulfide isomerase (PDI), we introduced thiol and disulfide functionalization within molecular framework of NI derivatives, **NISH** and **NISS** (Figure 1). Alongside, we developed other NI derivative, **NINSS** where NI-core was attached with π-electron donating naphthyl moiety via L-aspartic acid and functionalized with disulfide unit (Figure 1). Considering high abundance of PDI in endoplasmic reticulum (ER), we synthesized another NI-derivative, **TNINSH** (Figure 1) comprising of N-tosyl-ethylenediamine as ER-targeting moiety. Naphthyl residue present in molecular framework may engendered hydrophobic interaction and π-π stacking during self-aggregation. Subsequently, charge transfer may occur from electron donating naphthyl residue to electron-acceptor NI core to instigate AIE. Moreover, chiral L-aspartic acid is anticipated to persuade

non-planarity in molecular skeleton, which can promote RIM, a prerequisite for exhibiting AIE (Scheme 1).

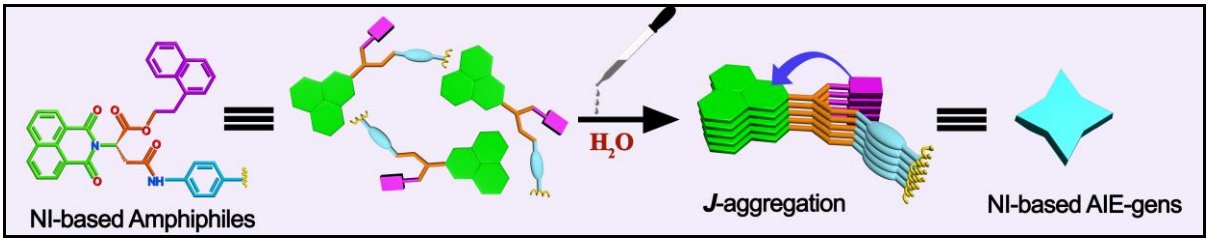

Scheme 1. Schematic representation of self-assembly induced fabrication of NI-based AIE-gens from naphthalimide based amphiphiles. AIE: aggregation-induced emission.

3A.2.2 SELF-ASSEMBLY OF NI-BASED AMPHIPHILES.

Self-assembly and aggregation pattern of synthesized NI-derivatives (**NISH, NISS, NINSS** and **TNINSH**) were investigated by spectroscopic and microscopic methods. NI-based amphiphiles were completely soluble in DMSO. Addition of small amount of water into DMSO solutions of **NISH**, **NISS**, **NINSS** and **TNINSH** showed macroscopic translucency signifying the formation of self-aggregated structures by NI-based amphiphiles in DMSO-H_2O (Figure 2a,c,e,g). For all NI-derivatives, transparent solutions converted into translucent solutions without precipitation on and above 40% water in DMSO (f_w = 40 vol%). The translucent solution was unswerving up to maximum water composition (f_w = 99 vol%) by virtue of self-assembly. Emissive behavior of these NI-derived organic nanoparticles was observed in varying compositions of DMSO-H_2O under UV torch exposure (λ_{ex} = 365 nm). Organic nanoparticles formed by **NISH** and its dimer **NISS** in DMSO-water were found to be non-fluorescent (Figure 2b,d). In case of **NINSS**, DMSO solution (molecularly state) was weakly or non-fluorescent. Addition of H_2O to this DMSO solution led to blue emission at f_w = 40 vol% and the emission intensity got maximized at f_w = 99 vol% (Figure 2f). Electron donating naphthyl moiety in **NINSS** might have facilitated charge transfer induced AIE in self-aggregated state in comparison to non-fluorescent **NISS**. Similarly, DMSO solution of **TNINSH** showed weak blue emission at 365 nm under UV light exposure. Gradual addition of H_2O into DMSO solution led to decrease in fluorescence intensity up to <30% water content (Figure 2h). At 40 vol% and beyond water concentration, blue emission color got transformed to faint yellow. The intensity of yellow emission augmented with increase in H_2O up to f_w = 99 vol% (Figure 2h). These

findings delineate that both **NINSS** and **TNINSH** exhibited self-assembly engendered AIE in DMSO-water. AIE for **TNINSH** FONPs was observed at higher emission wavelength (yellow) and blue emission was observed for **NINSS** FONPs.

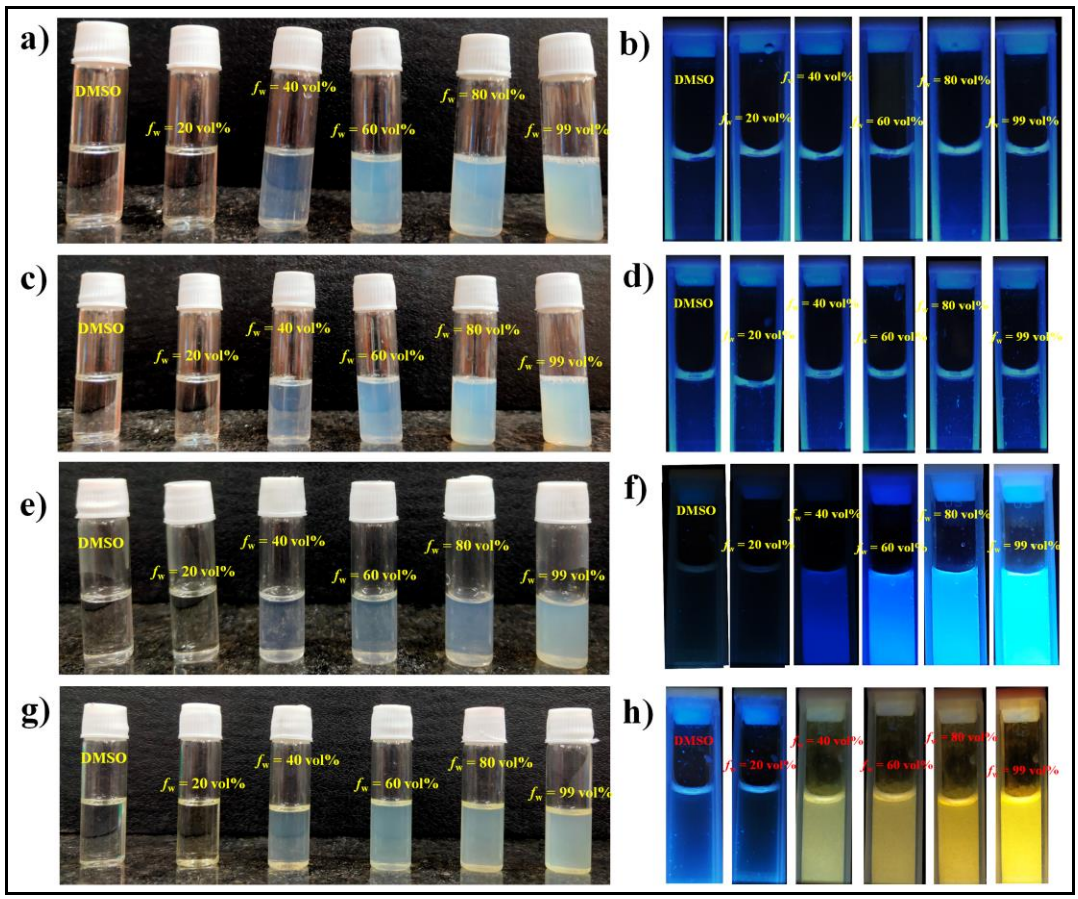

Figure 2. (a), (c), (e), (g) Photograph of formation of translucent solutions and (b), (d), (f), (h) photograph of change in emission color for **NISH**, **NISS**, **NINSS** and **TNINSH** ([NI-based amphiphiles] = 50 μM; UV-light irradiation, λ_{ex} at 365 nm) with increase in water content in DMSO, respectively.

3A.2.3 MICROSCOPIC AND DLS STUDY.

Morphology of self-aggregated structures of NI-derivatives at f_w = 99 vol% was investigated by different microscopy. Negatively stained TEM images suggest formation of spherical aggregates of NI-amphiphiles (25 μM) in 1:99 (v/v) DMSO-water having diameters ~50-120 nm (Figure 3a,d,g,j). Solid physical appearance of organic nanoparticles was denoted by vague contrast of spherical particles. Formation of spherical shaped organic nanoparticles with

similar dimension was also evident from respective FESEM images of NI-derivatives (25 μM) in f_w = 99 vol% (Figure 3b,e,h,k).

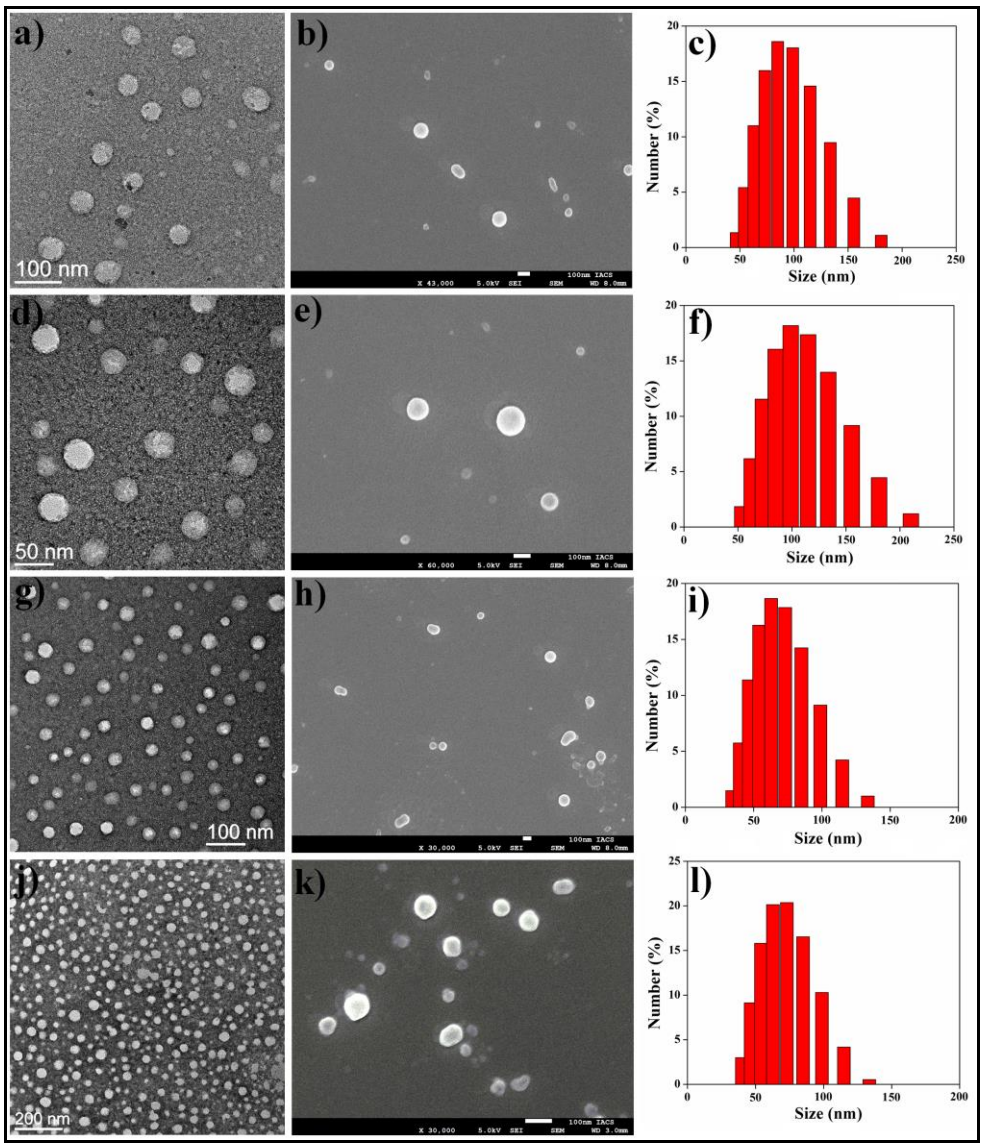

Figure 3. Figure 3. (a), (d), (g), (j) Negatively stained TEM images, (b), (e), (h), (k) FESEM images and (c), (f), (i), (l) DLS plot of particles size distribution of **NISH**, **NISS**, **NINSS** and **TNINSH** in (1:99, v/v) DMSO-water binary solvent mixture ([NI-based amphiphiles] = 25 μM) respectively.

Dynamic light scattering (DLS) study also delineated the mean hydrodynamic diameter (D_h) of NI-based organic nanoparticles around 50-120 nm in its self-assembled state (f_w = 99 vol%) (Figure 3c,f,i,l). Correlograms of corresponding DLS studies were provided in Figure 4.

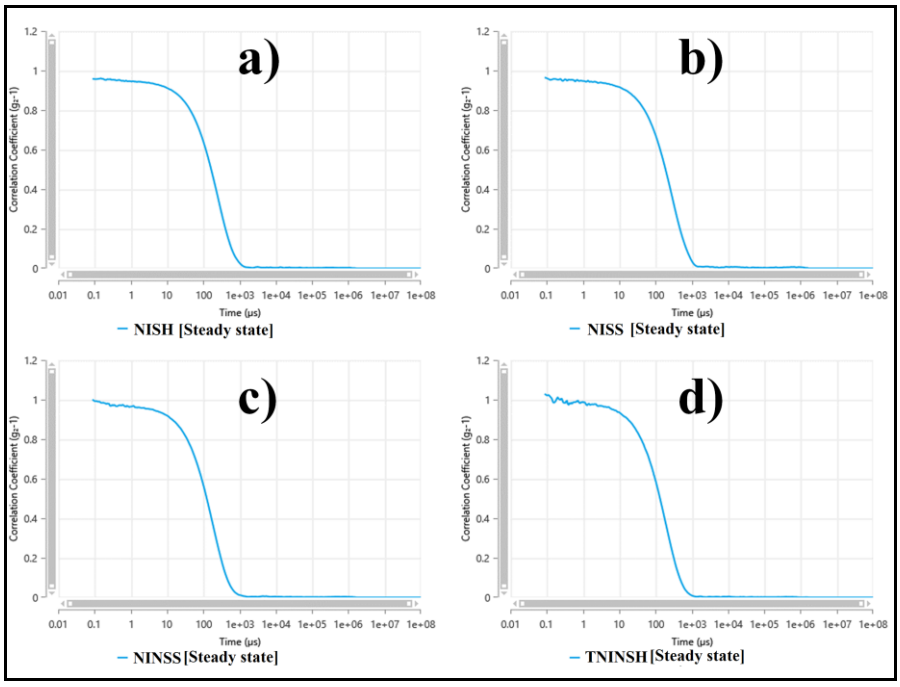

Figure 4. Correlogram of DLS plots of (a) **NISH**, (b) **NISS**, (c) **NINSS**, (d) **TNINSH** in 1:99 (v/v) DMSO-water binary solvent mixture.

3A.2.4 SPECTROSCOPIC STUDY FOR SELF-ASSEMBLY.

Upon confirmation on the formation of fluorescent organic nanoparticles (FONPs) by **NINSS** and **TNINSH**, we investigated mechanistic pathway for self-aggregation by different spectroscopy. UV-vis spectra of **NINSS** and **TNINSH** (20 µM) in pure DMSO (non-self-aggregated) exhibited characteristics absorbance peak around 300-370 nm with absorption maxima (λ_{max}) at 334 nm (Figure 5a,b). This may be accredited to π-π* transition polarized along the long axis of naphthalimide chromophore.[24,26,35] Upon successive increment in H_2O percentage in DMSO, steady bathochromic shifting of absorption maxima was observed and the λ_{max} was noticed at 343 nm and 348 nm for **NINSS** and **TNINSH**, respectively at f_w = 99 vol% (Figure 3a,b). Red shifting of λ_{max} upon gradual inclusion of water illustrated self-assembly driven construction of organic nanoparticles possibly via *J*-aggregation (head-to-tail arrangement) for **NINSS** and **TNINSH** FONPs (Scheme 1). Similarly, **NISH** and **NISS** formed self-assembly directed non-fluorescent organic nanoparticles (Figure 5c,d).

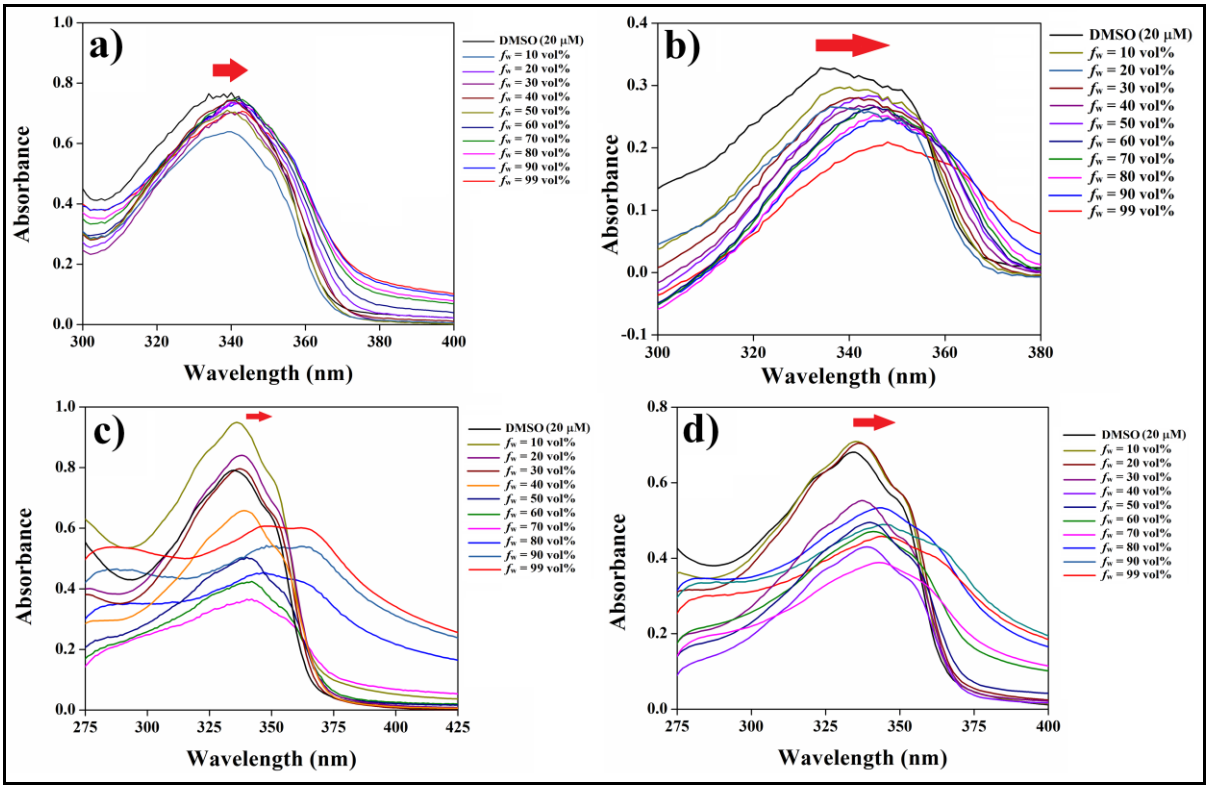

Figure 5. UV-visible spectra of (a) **NINSS** (20 μM), (b) **TNINSH** (20 μM), (c) **NISH** (20 μM) and (d) **NISS** (20 μM) in varying DMSO-water solvent mixtures.

Moreover, a meticulous exploration of steady-state fluorescence anisotropy was undertaken with regards to the NI derivatives, with the primary objective of probing the intricate microenvironment inherent to the aggregated structures. To this end, a probing agent by the name of 1,6-diphenyl-1,3,5-hexatriene (DPH) was introduced, esteemed for its capacity to intercalate within the hydrophobic interior of these aggregates. The manifestation of an elevated steady-state anisotropy (denoted as "r" value) serves as a reliable indicator of the constrained mobility experienced by DPH within environments characterized by diminished polarity and augmented hydrophobicity, emblematic of the aggregate structures. Remarkably, an unequivocal augmentation in the *r*-value was unmistakably observed across all the NI derivatives, aligning harmoniously with the gradual augmentation in water content within the solvent matrix comprising dimethyl sulfoxide (DMSO) (f_w = 50% to 99%). This salient observation, aptly chronicled within Table 1, crystallizes the pivotal inference that the **NISH**, **NISS**, **NINSS**, and **TNINSH** entities effortlessly usher forth the genesis of resolute and stable

organic nanoparticles within the dynamic confines of the DMSO-water amalgamation, particularly at elevated water contents. This poignant revelation, elegantly unveiled through the lens of steady-state fluorescence anisotropy, stands as an irrefutable testament to the triumphant establishment of robust organic nanoparticle formation by **NISH**, **NISS**, **NINSS**, and **TNINSH** in DMSO-water solvent system through self-assembly.

Table 1. Steady-state fluorescence anisotropy (r) of DPH with **NISH**, **NISS**, **NINSS** and **TNINSH** in different ratios of DMSO-water solvent mixture.

Amphiphile	f_w = 50 %	f_w = 75 %	f_w = 99 %
NISH	0.092	0.105	0.161
NISS	0.087	0.117	0.172
NINSS	0.069	0.120	0.228
TNINSH	0.089	0.144	0.283

Subsequently, an insightful exploration was undertaken through the prism of circular dichroism (CD) spectroscopy, aimed at delving into the intricate supramolecular attributes inherent to the aggregates fashioned from the NI derivatives. Intriguingly, when scrutinized within DMSO solutions, all the NI derivatives did not manifest any distinctive CD signals, a noteworthy observation underscored in Figure 6. However, a striking departure from this norm was unequivocally unveiled when the solvent composition reached f_w = 99%. Within this intriguing context, the CD spectra exhibited a remarkable dichotomy-a robust positive band characterized by peak wavelengths of 208 nm, 217 nm, 215 nm, and 212 nm, counterbalanced by a salient and pronounced negative band resonating at 257 nm, 261 nm, 243 nm, and 259 nm, corresponding to **NISH**, **NISS**, **NINSS**, and **TNINSH** FONPs, respectively (Figure 6). Evidently, these CD spectroscopic observations evinced a transformative metamorphosis in the supramolecular configuration of the NI-amphiphiles, specifically upon their transition into the aggregated state. A distinctive pattern emerged, wherein the NI-amphiphiles in their aggregated form exhibited a striking negative cotton effect, an optical phenomenon that was conspicuously absent in their monomeric counterparts. The emergence of this chiral bias within the supramolecular arrangement of the NI-derivatives was postulated to be steered by

the influential presence of chiral L-aspartic acid, an integral constituent of the self-aggregated state. This captivating revelation underscores the impact exerted by molecular interactions and asymmetrical architectural motifs on the chiral landscape of the NI-amphiphile aggregates, lending a new layer of understanding to their nuanced self-organization.

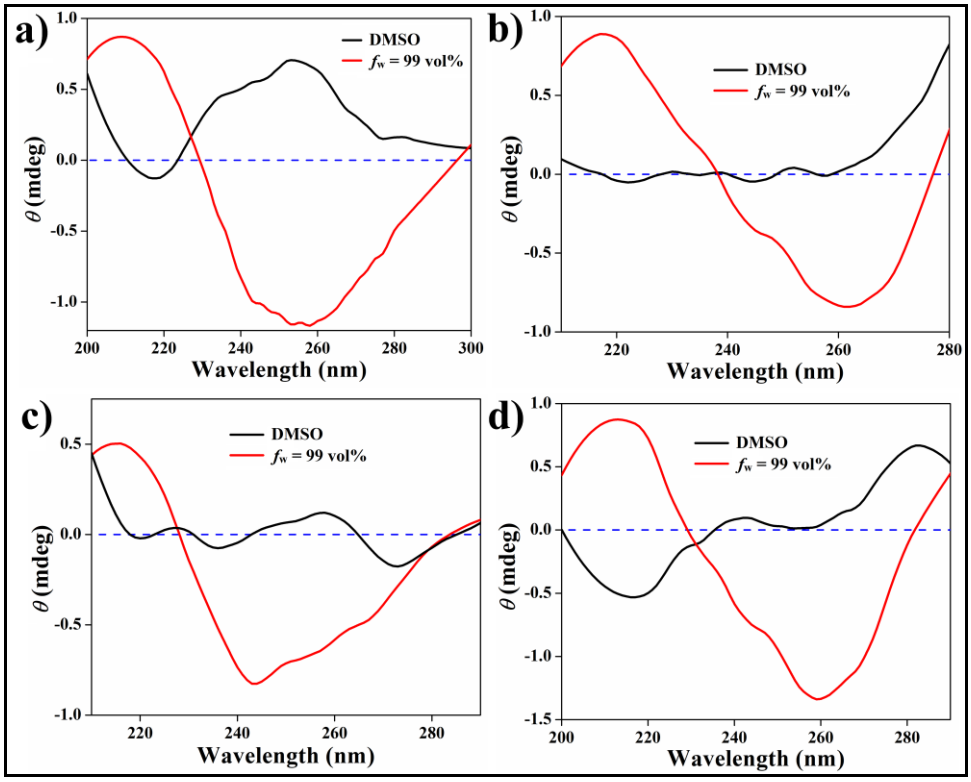

Figure 6. CD spectra of (a) **NISH**, (b) **NISS**, (c) **NINSS** and (d) **TNINSH** in DMSO and 1:99 v/v DMSO-water system. ([NI-based amphiphiles] = 25 μM)

3A.2.5 INTERMOLECULAR NONCOVALENT INTERACTIONS IN SELF-ASSEMBLY.

Participation of the different non-covalent interactions in this self-assembly driven formation of aggregated nanoparticles was investigated by Fourier transform infrared (FTIR) and solvent-dependent ^{1}H-NMR spectroscopy (Figures 7,8). In the FTIR spectrum of **NISH** and **NINSS** in $CHCl_3$ (non-aggregated state), transmittance peaks were observed at approximately $\nu_{C\text{-}N}$ (C-N stretching) = 1241, and 1232 cm^{-1}, respectively and $\nu_{C=O}$ (imide, stretching) = 1775 and 1773 cm^{-1}, respectively (Figure 7a,b). These peaks got shifted to $\nu_{C\text{-}N}$ (C-N stretching) = 1227 cm^{-1} (broad band) and 1218 cm^{-1}, $\nu_{C=O}$ (imide, stretching) = 1763 cm^{-1} and 1743 cm^{-},^{1} respectively, in (2:1, v/v) DMSO-d_6-D_2O solvent mixture. In (1:1, v/v) DMSO-d_6-D_2O solvent mixture these

characteristic peaks further shifted to ν_{C-N} (C-N stretching) = 1203 cm^{-1} (broad band) and 1207 cm^{-1}, $\nu_{C=O}$ (imide, stretching) = 1735 cm^{-1} and 1731 cm^{-1}, respectively (Figure 7a,b). These shifting and broadening in stretching frequencies of the peaks in DMSO-d_6-D_2O solvent mixtures compared to that in $CHCl_3$ (non-aggregated state), signify the involvement of intermolecular hydrogen bonding during the process of self-assembly induced formation of **NISH** and **NISS** organic nanoparticles.

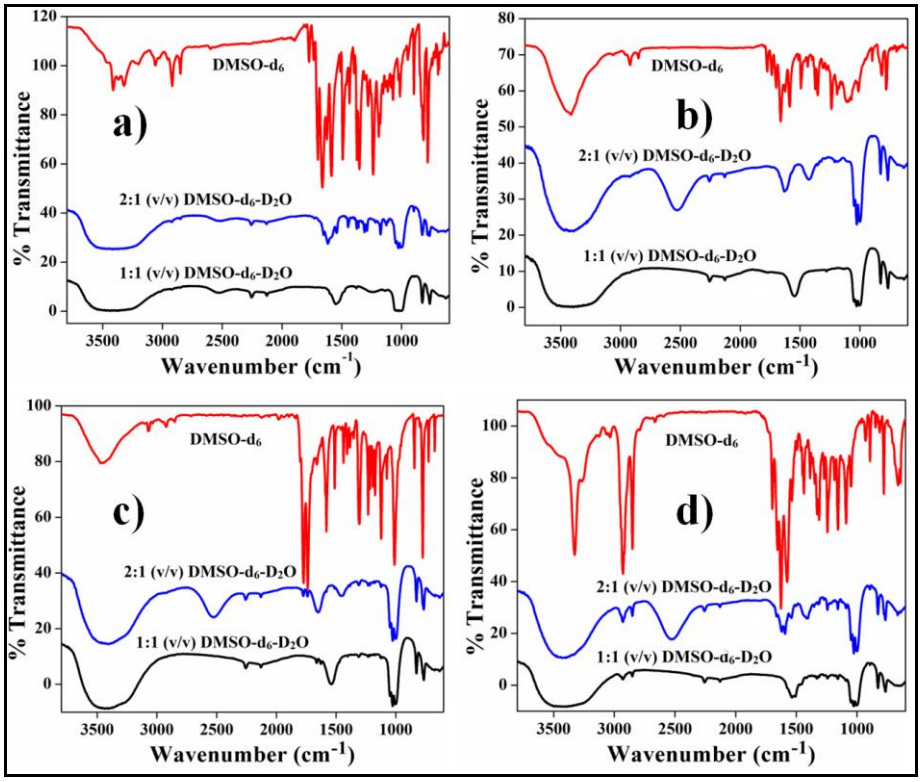

Figure 7. FTIR Spectra of (a) **NISH**, (b) **NISS**, (c) **NINSS** and (d) **TNISNH** in their self-assembled and non-self-aggregated state.

To the same end, in the FTIR spectrum of **NINSS** and **TNINSH**, transmittance peaks in non-aggregated state (in $CHCl_3$) displayed at ν_{N-H} (amide A) = 3379-3550 cm^{-1} and 3253-3368 cm^{-1} respectively, $\nu_{C=O}$ (amide I, stretching) = 1683 cm^{-1} and 1697 cm^{-1} respectively and for ν_{N-H} (amide II, bending) = 1637 and 1578 cm^{-1} (Figure 7c,d). Shifting of these respective peaks of **NINSS** and **TNINSH** to ν = 3225-3613 cm^{-1} (broad band) and 3157-3630 cm^{-1} respectively, for ν_{N-H} (amide A) = 1631 cm^{-1} and 1652 cm^{-1} respectively, and for $\nu_{C=O}$ (amide I, stretching) = 1583 cm^{-1} and 1572 cm^{-1} respectively, were attributed to the self-aggregated state (2:1, v/v) in DMSO-d_6-D_2O solvent mixture. The corresponding peaks of **NINSS** and **TNINSH** got further shifted to ν

= 3117-3687 cm^{-1} (broad band) and 3043-3727 cm^{-1}, respectively, for ν_{N-H} (amide A) = 1606 cm^{-1} and 1623 cm^{-1}, respectively, and for $\nu_{C=O}$ (amide I, stretching) = 1509 cm^{-1} and 1566 cm^{-1}, respectively, in (1:1, v/v) DMSO-d_6-D_2O solvent mixture (Figure 7c,d). These shifting in the stretching and bending frequencies of the peaks in DMSO-d_6-D_2O solvent systems might be originated due to involvement of intermolecular hydrogen bonding between the amide N–H and carbonyl (C=O) (i.e., N–H···O=C) during self-assembly of **NINSS** and **TNINSH**.

In solvent-dependent ^{1}H-NMR study, the aromatic protons of **NISH** exhibited characteristic sharp ^{1}H-NMR signals in the region δ = 8.4-8.6 ppm (C2,C4,C5 & C7 of NI), δ = 7.8-7.9 ppm (C3 & C6 of NI) and δ = 7.4-7.6 ppm (phenyl ring) in DMSO-d_6, illustrating its non-aggregated state (Figure 8a). With gradual increase in the D_2O content, the characteristic NMR signal got upfield shifted with reduced peak intensity. At (1:1, v/v) DMSO-d_6-D_2O solvent mixture, ^{1}H-NMR signals of the NI aromatic core and the phenyl ring were broadened and shifted to δ = 8.2 ppm, δ = 7.4-7.5 ppm and δ = 7.2-7.3 ppm (phenyl ring) for the respective protons (Figure 8a). **NISS** in DMSO-d_6 showed sharp NMR signals in the region δ = 8.4-8.6 ppm (C2,C4,C5 & C7 of NI), δ = 7.8-7.9 ppm (C3 & C6 of NI) and δ = 7.5-7.6 ppm (phenyl rings) for respective protons, which got shifted and broadened after gradual addition of D_2O content (Figure 8b). At (1:1, v/v) DMSO-d_6-D_2O solvent mixture, ^{1}H-NMR signals of the NI aromatic core and the phenyl ring of **NISS** got broadened and shifted to δ = 7.9-8.1 ppm, δ = 7.3-7.4 ppm and δ = 7.2-7.25 ppm (phenyl rings). Similarly, the ^{1}H-NMR signal of the aromatic protons were observed for **NINSS** in the region δ = 8.4-8.5 ppm (C2,C4,C5 & C7 of NI core), 8.2-8.3 (C3 & C6 of NI core), δ = 7.7-7.9 ppm (phenyl rings) and δ = 7.4-7.6 ppm (naphthyl rings) (Figure 8c). Upfield shifting of the characteristics NMR signals with diminished peak intensity was witnessed upon gradual addition of D_2O content in DMSO-d_6. Various ^{1}H-NMR signals for aromatic protons of the **NINSS** got broadened and shifted to δ = 7.9-8.2 ppm (NI-core), δ = 7.5-7.7 ppm (phenyl ring) and δ = 7.15-7.25 ppm (naphthyl ring) and at (1:1, v/v) DMSO-d_6-D_2O. Furthermore, the solvent-dependent ^{1}H-NMR spectrum of **TNINSH** in non-self-aggregated state (DMSO-d_6) displayed different characteristic aromatic ^{1}H-NMR signals in the region δ = 8.3-8.6 ppm (aromatic core of NI), δ = 7.8-8.1 ppm (various protons of phenyl and naphthyl ring) and δ = 7.4-7.7 ppm (various protons of phenyl and naphthyl ring) (Figure 8d). After gradual inclusion of D_2O content, here too the NMR signal got upfield shifted with reduced

peak intensity. At (1:1, v/v) DMSO-d_6-D_2O solvent mixture, ^{1}H-NMR signals of the aromatic protons of NI core, the phenyl and naphthyl ring were broadened and shifted to δ = 8.0-8.2 ppm, δ = 7.5-7.7 ppm and δ = 7.2-7.4 ppm. In the non-self-assembled state, no effective π–π stacking as well as hydrophobic interactions was involved. With gradual increase in D_2O content, initiation of self-assembly facilitates the non-covalent interactions (such as π–π stacking, hydrophobic interaction) between the aromatic residues of the molecular framework. These spectroscopic evidences confirmed the involvement of non-covalent interactions during the formation of self-assembled organic nanoparticles.

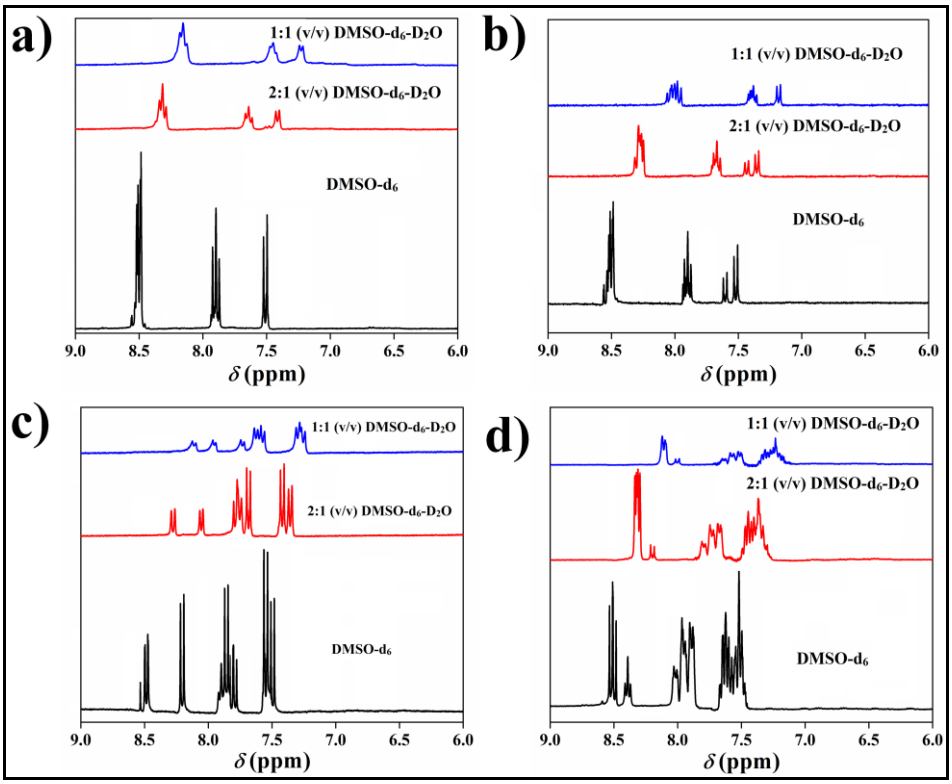

Figure 8. Solvent dependent ^{1}H-NMR of (a) **NISH**, (b) **NISS**, (c) **NINSS** and (d) **TNINSH**.

3A.2.6 FLUORESCENCE STUDY

The changes in emission color of **NINSS** and **TNINSH** FONPs upon UV irradiation intrigued us to explore emissive behavior of the same in varying composition of DMSO-water. **NINSS** (20 μM) in DMSO displayed weak fluorescence having emission maxima (λ_{em}) at 390 nm upon excitation at 350 nm (Figure 9a). Gradual addition of water caused reduction in monomeric peak intensity and after 30 vol% water content, a new excimer peak was appeared

with λ_{em} at 470 nm. Emission intensity of excimer peak steadily got improved with increase in water content and it was maximum at f_w = 99 vol% (Figure 9a).

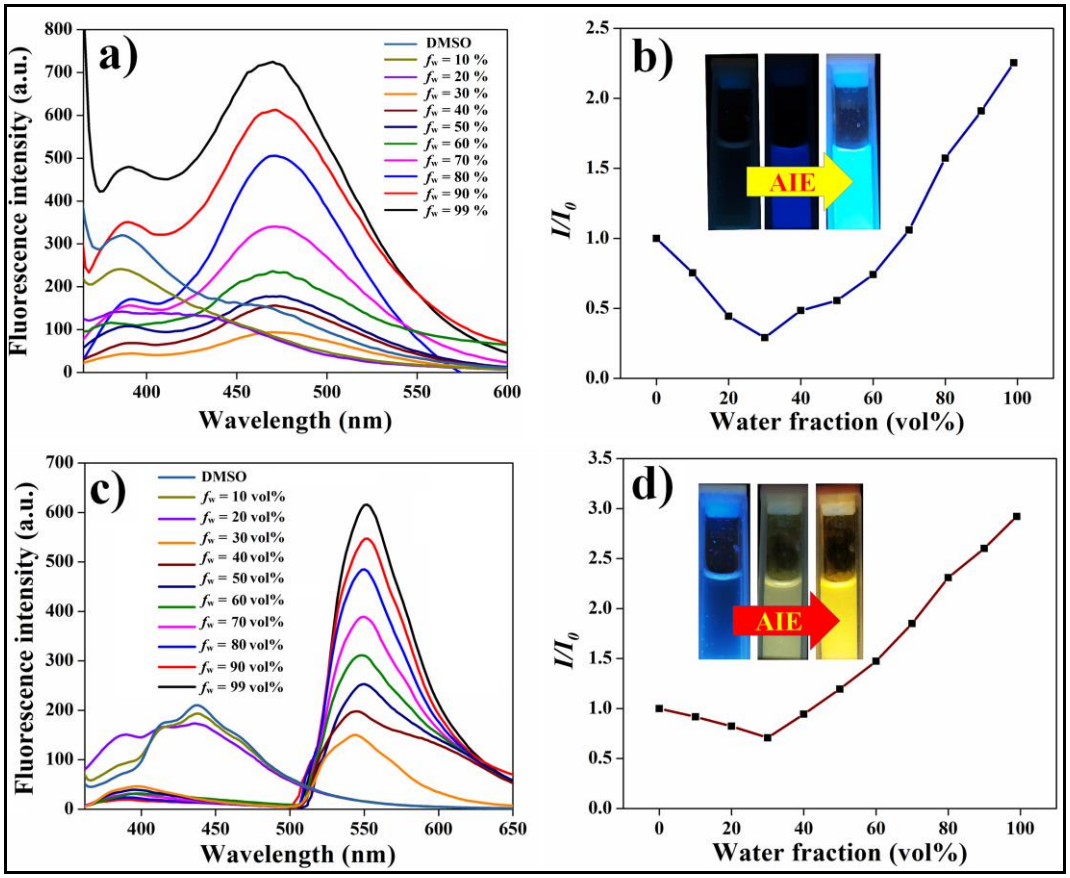

Figure 9. Fluorescence spectra (λ_{ex} = 350 nm) of (a) **NINSS** (20 μM) and (c) **TNINSH** (20 μM) in DMSO-water solvent mixture; Plot of relative emission intensity (I/I_0) vs the fraction of water in DMSO of (b) **NINSS** and (d) **TNINSH**.

Similarly, fluorescence spectra of **TNINSH** (20 μM) in DMSO exhibited λ_{em} at 435 nm (λ_{ex} = 350 nm, Figure 9c). The monomeric peak emission intensity of **TNINSH** got diminished upon gradual insertion of water in DMSO. At 30 vol% water, a new excimer peak with λ_{em} at 543 nm was observed upon excitation at 350 nm. With increasing amount of H_2O, continuous improvement in excimer peak intensity was observed being maximum at f_w = 99 vol% having λ_{em} = 551 nm (Figure 9c). Upon addition of H_2O, red shift in excimer peak of **TNINSH** FONPs was observed from 543 nm to 551 nm. Overall, a bathochromic shift of 80 nm & 116 nm and marked enhancement in emission intensity in self-aggregated state were observed compared to monomeric peaks of **NINSS** and **TNINSH**, respectively (Figure 9b,d). Thus, **NINSS** and

TNINSH exhibited AIE originated via excimer formation leading to the development of FONPs. **NINSS** and **TNINSH** showed blue and green dotted FONPs at f_w = 99 vol% in the respective fluorescence microscopic images that captured using blue and green filter (Figure 10).

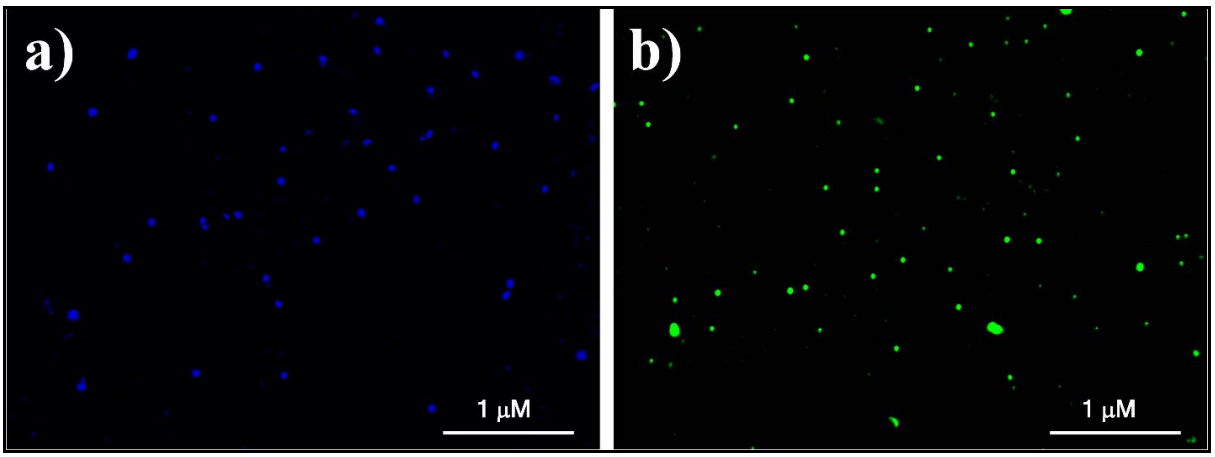

Figure 10. Fluorescence microscope images of (a) **NINSS** FONPs and (b) **TNINSH** FONPs in (1:99, v/v) DMSO-water mixture.

NISH and **NISS** did not exhibit any notable fluorescence signal in self-assembled state ascertaining its non-emissive nature (Figure 11). In absence of any prominent electron donating moiety, both **NISH** and **NISS** did not exhibit any emissive property in its self-assembled state as well as in non-self-aggregated state.

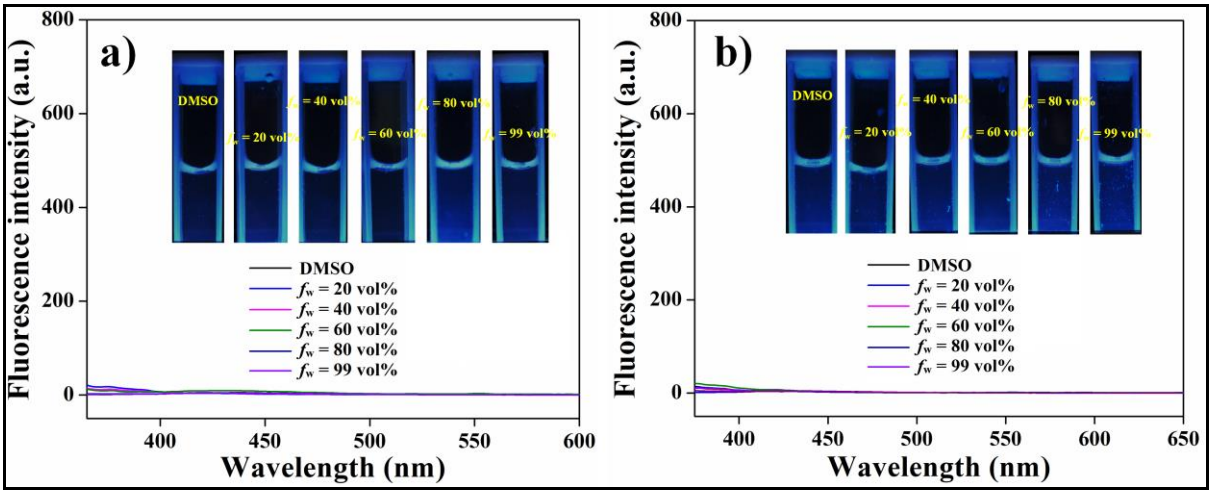

Figure 11. Fluorescence spectra (λ_{ex} = 350 nm) of (a) **NISH** (20 μM) and (b) **NISS** (20 μM) FONPs in DMSO-water mixture (inset: UV irradiated (λ_{ex} = 365 nm) images).

Table 2. Lifetime values of **NINSS** in presence of different fractions of water in DMSO (λ_{ex} = 360 nm)

Fraction of Water (vol%)	$\lambda_{monitored}$ (nm)	τ_1 (ns) (a_1)	τ_2 (ns) (a_2)	τ_3 (ns) (a_3)	Average lifetime (τ) (ns)
0	390	1.16	1.93	10.04	1.43
		(0.63)	(0.29)	(0.08)	
50	470	8.96	28.81	1.37	4.88
		(0.39)	(0.41)	(0.20)	
99	470	8.78	28.57	1.56	5.22
		(0.40)	(0.39)	(0.21)	

Table 3. Lifetime values of **TNINSH** in presence of different fractions of water in DMSO (λ_{ex} = 360 nm)

Fraction of Water (vol%)	$\lambda_{monitored}$ (nm)	τ_1 (ns) (a_1)	τ_2 (ns) (a_2)	τ_3 (ns) (a_3)	Average lifetime (τ) (ns)
0	435	2.56	1.13	7.75	1.59
		(0.29)	(0.56)	(0.15)	
50	550	10.08	22.59	2.23	4.95
		(0.24)	(0.37)	(0.39)	
70	550	8.29	21.63	2.58	5.21
		(0.43)	(0.21)	(0.36)	
99	550	10.44	22.93	3.62	6.54
		(0.39)	(0.19)	(0.42)	

To further ascertain emissive nature of **NINSS** and **TNINSH** FONPs (20 μM), we performed time-correlated single-photon counting (TCSPC) experiment having picosecond excitation at 360 nm. A triexponential function was utilized for fitting decay curves in each

experiment. For **NINSS** and **TNINSH** dissolved in DMSO, fluorescence was monitored at λ_{mon} = 390 nm and 435 nm, respectively. The average lifetime ($\langle\tau\rangle$) of **NINSS** (λ_{mon} = 390 nm) in DMSO was 1.43 ns (Table 2, Figure 12a). The $\langle\tau\rangle$ of **NINSS** got increased upon increment of H_2O content in DMSO. At f_w = 50 vol%, the $\langle\tau\rangle$ of **NINSS** FONPs was 4.88 ns and that was 5.22 ns (λ_{mon} = 470 nm) in f_w = 99 vol%. Similarly, the $\langle\tau\rangle$ in DMSO solution of **TNINSH** (λ_{mon} = 435 nm) was 1.59 ns (Table 3, Figure 12b). Enhancement in the $\langle\tau\rangle$ of **TNINSH** was noted upon addition of H_2O in DMSO. The $\langle\tau\rangle$ of **TNINSH** FONPs (λ_{mon} = 550 nm) was 4.95 ns, 5.21 ns and 6.54 ns at f_w = 50, 70 and 99 vol%, respectively. This long decay lifetime with increasing H_2O in DMSO originates possibly due to pre-associated excimer formation by **NINSS** and **TNINSH** FONPs. Relative fluorescence quantum yield (QY) of **NINSS** and **TNINSH** FONPs at f_w = 99 vol% was 6.14% and 4.37 % (with respect to Quinine hydrogen sulfate).

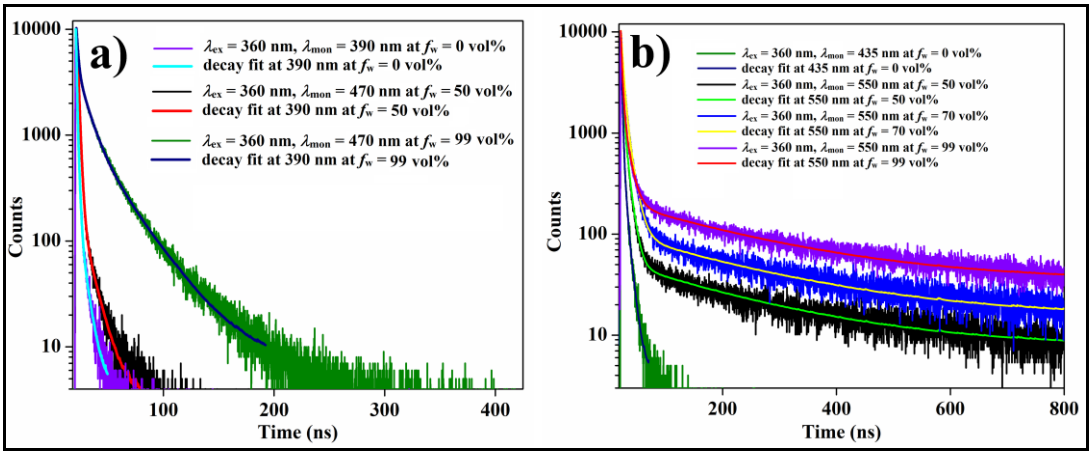

Figure 12. TCSPC decay profiles of (a) **NINSS** monitored at 390 nm (DMSO), 470 nm (f_w = 50 vol%) and 470 nm (f_w = 99 vol%) and (b) **TNINSH** monitored at 435 nm (DMSO), 550 nm (f_w = 50 vol%), 550 nm (f_w = 70 vol%) and 550 nm (f_w = 99 vol%) upon excitation at 360 nm.

Next, we were intrigued to examine the stability of the **NINSS** and **TNINSH** FONPs in the self-aggregated state. To this end, we recorded time-dependent UV-visible and fluorescence spectra of the organic nanoparticles at f_w = 99 vol % (Figure 13). The relative absorbance (A/A_o at λ_{max} = 334 nm) and relative emission intensity (I/I_o at λ_{em} = 470 nm and 550 nm respectively for **NINSS** and **TNINSH**) were monitored at different times interval (up to 7 days) for 20 μM of **NINSS** and **TNINSH** in 1:99 (v/v) DMSO-water. In case of both the FONPs (20 μM), the absorbance and the fluorescence intensities persisted almost unaltered and marginally

diminished by ~10-12% after 7 days suggesting superior stability of **NINSS** and **TNINSH** FONPs at their self-assembled state (Figure 13).

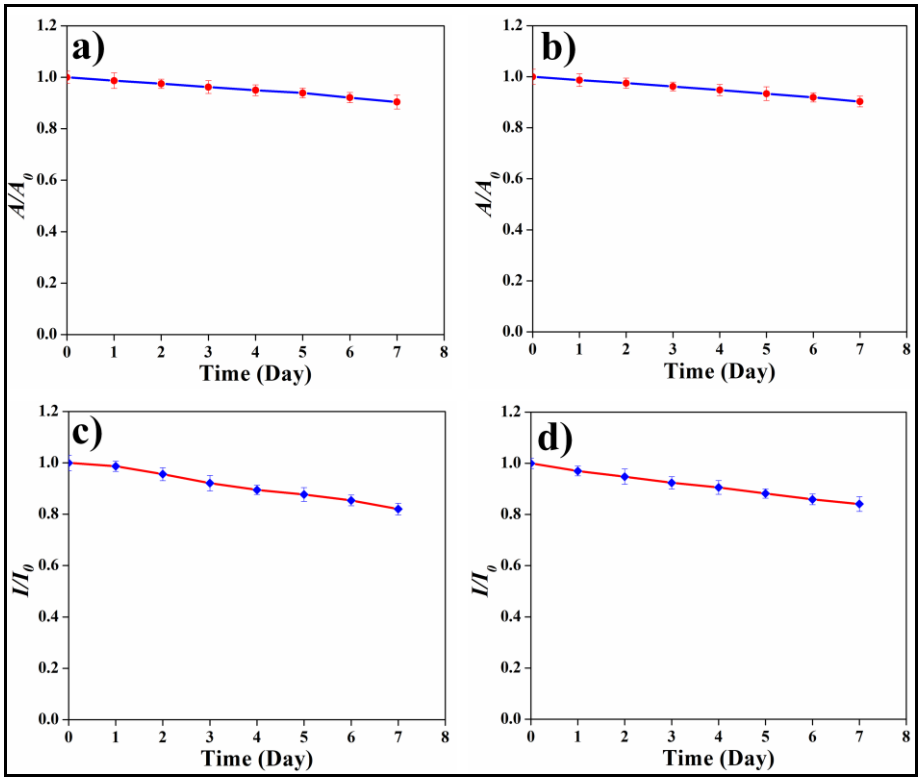

Figure 13. Temporal evolution of the absorbance at 334 nm for (a) **NINSS** [20 μM] and (c) **TNINSH** [20 μM] and the fluorescence intensity at 470 nm for (c) **NINSS** [20 μM] and 550 nm for **TNINSH** [20 μM] in DMSO-water solvent mixture (f_w = 99 vol%) respectively.

Fluorescence spectra pertaining to the **NINSS** and **TNINSH** FONPs were meticulously captured within an assorted array of solvent systems, namely PEG/H2O, THF/H2O, and PEG/THF, with the primary aim of unraveling the profound influence of the environment's polarity and viscosity on their distinctive fluorescence behavior. Notably, a consistent and intriguing trend unfurled across both categories of FONPs. Evidently, the fluorescence intensity exhibited a palpable elevation in tandem with the augmentation of PEG concentrations within the aqueous or THF solvents (Figure 14). Similarly, a parallel escalation was discerned as the THF content was enhanced within the aqueous medium, a noteworthy phenomenon beautifully captured within Figure 14. This augmentation in fluorescence intensity finds its roots in a discernible constraint imposed upon the rotational motion of the

probing entities-namely, the FONPs-within domains characterized by elevated viscosities or a more subdued polarity. The underpinning principle is elegantly encapsulated by the theory of an energy barrier, an influential factor that engenders a deliberate deceleration in the overall rotational dynamics. Consequently, this orchestrated slowdown culminates in a reduction of non-radiative decay pathways, thereby paving the way for an amplified emission phenomenon. In essence, the intricate interplay between viscosity, polarity, and molecular mobility orchestrates a symphony where the FONPs' fluorescence is propelled to higher intensities, effectively unraveling a captivating nexus between the intricate solvation environment and the manifestation of luminous emissions from these enigmatic nanoparticles.

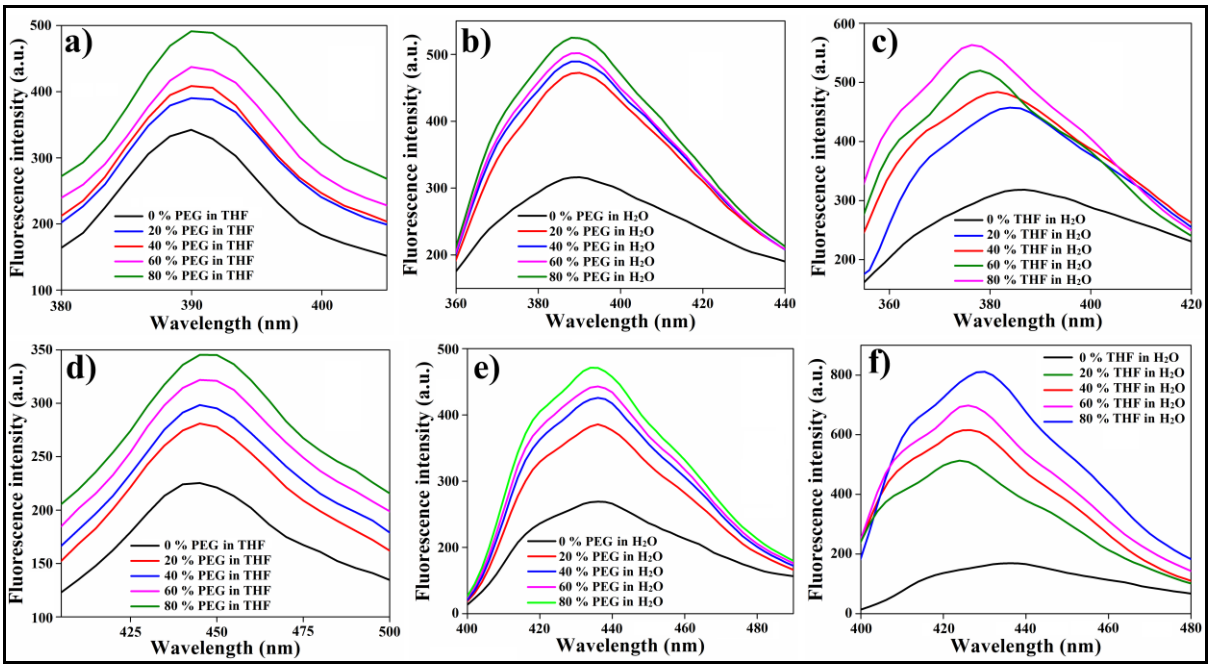

Figure 14. Fluorescence spectra of **NINSS** FONPs (20 μM) and **TNINSH** FONPs (20 μM) in (a), (d) PEG-THF system, (b), (e) PEG-water system and (c), (f) THF-water system, respectively; (λ_{ex} = 350 nm).

3A.3 CONCLUSION

In a comprehensive culmination, our endeavor has encompassed the ingenious design and meticulous development of a novel class of amphiphiles, rooted in the naphthalimide (NI) framework. Distinctively embellished with thiol moieties, exemplified by **NISH** and **TNINSH**, as well as disulfide entities, embodied within **NISS** and **NINSS**, these amphiphiles form the

cornerstone of our innovative approach. Through an orchestrated process of self-assembly, harnessed by the captivating phenomenon of *J*-type aggregation, these NI-derived amphiphiles seamlessly orchestrated the emergence of exquisitely spherical organic nanoparticles. Ranging in size from 50 to 120 nanometers, these nanoparticles sprang forth within the dynamic embrace of a precisely balanced 1:99 (v/v) DMSO-H_2O medium. An emblematic manifestation of the prowess underlying molecular self-organization, this assembly process unveiled a captivating interplay of forces, resulting in the formation of distinctively spherical nanostructures. Within the realm of their self-aggregated state, notably attained at and beyond f_w = 30 vol%, a beguiling phenomenon-Aggregation-Induced Emission (AIE)-came to the forefront. This intriguing behavior was underpinned by the formation of luminous excimers, marking a pivotal milestone in our exploration. The culmination of this phenomenon unfurled through a meticulously orchestrated enhancement in the emission intensity of the excimer peak, with **NINSS** and **TNINSH** leading the charge. A continuous increase in emission intensity was achieved through the gradual inclusion of water, maximizing at f_w = 99 vol%, an endeavor underscored by emission wavelengths of 470 nm and 550 nm, elegantly spurred by an excitation wavelength of 350 nm. In this intricate mosaic of scientific inquiry, design ingenuity, and luminous expression, our comprehensive exploration contributes substantively to the burgeoning domain of molecular self-assembly, offering a glimpse into the multifaceted interplay of intricate molecular interactions and emergent phenomena, thereby expanding the horizons of nanoscale architecture and luminescence dynamics.

Henceforth, within the subsequent segment of this chapter, delineated as Chapter 3B, our trajectory shifts emphatically towards an incisive exploration. In this pivotal subsection, the spotlight converges onto a discerning foray-the probing study of Protein Disulfide Isomerase (PDI)-an endeavor skillfully facilitated by our newly devised **NINSS** and **TNINSH** Fluorescent Organic Nanoparticles (FONPs). This analytical journey is underpinned by a strategic leverage of their Aggregation-Induced Emission (AIE) characteristic, an intrinsic attribute meticulously woven into the fabric of their architecture. The resolute objective of this scientific expedition lies in unraveling the intricate machinations of PDI's behavior, thereby harnessing the illuminating prowess of AIE-enabled FONPs as beacons to illuminate the enigmatic pathways of this crucial biochemical actor.

3A.4 EXPERIMENTAL SECTION

3A.4.1 MATERIALS.

1,8-Naphthalic anhydride, 4-benzyl N-Boc-L-aspartate, 1-naphthaleneethanol, 4-aminophenyl disulfide, N-tosylethylenediamine, and all deuteriated solvents were bought from Sigma-Aldrich. 4-aminothiophenol and 4-bromo-1,8-naphthalenedicarboxylic anhydride purchased from TCI chemicals, India. 1-Hydroxy-2,5-pyrrolidinedione (NHS), *N,N'*-Dicyclohexylcarbodiimide (DCC), trifluoroacetic acid (TFA), N,N-Dimethylpyridin-4-amine (DMAP), 1,2,3-benzotriazol-1-ol (HOBt), palladium 10% on activated carbon powder, column chromatography reagents and other solvents and chemicals were acquired from SRL, India. 300 MHz and 400 MHz AVANCE (Bruker) spectrometer was used for NMR spectroscopy and Bruker Ultraflex MALDI mass spectrometer (2,5-dihydroxy benzoic (DHB) acid as matrix) was used to record MALDI-TOF spectra.

3A.4.2 SYNTHESIS OF NAPHTHALIMIDE DERIVATIVES.

To prepare **NISH**, condensation of 1.0 equiv of 4-aminothiophenol and 1.0 equiv of 1,8-naphthalic anhydride was carried out at 75 °C in dry ethanol (EtOH) under N_2 atmosphere for 12 h. After removal of EtOH, dichloromethane (DCM) was used to dissolve the crude mass, and then washed with water. Next, purification of the condensed product was done by column chromatography (100-200 mesh silica gel, 3% MeOH in $CHCl_3$ as an eluent) followed by washing with diethyl ether to obtain the pure **NISH** (Figure 1a, Scheme 2).

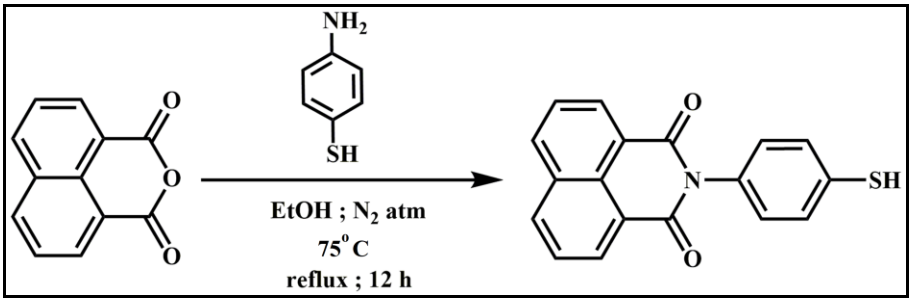

Scheme 2. Synthetic scheme for **NISH** amphiphile.

Next, to prepare **NISS**, 2.0 equiv of 1,8-naphthalic anhydride and 1 equiv of 4-aminophenyl disulfide were taken in dry EtOH and refluxed at 75 °C for 12 h. The residue

obtained after exclusion of EtOH was dissolved in DCM followed by washing with water. Next, we purified the condensed product using column chromatography (100-200 mesh silica gel using 2% MeOH/$CHCl_3$ as eluent) to get pure **NISS** (Figure 1b, Scheme 3).

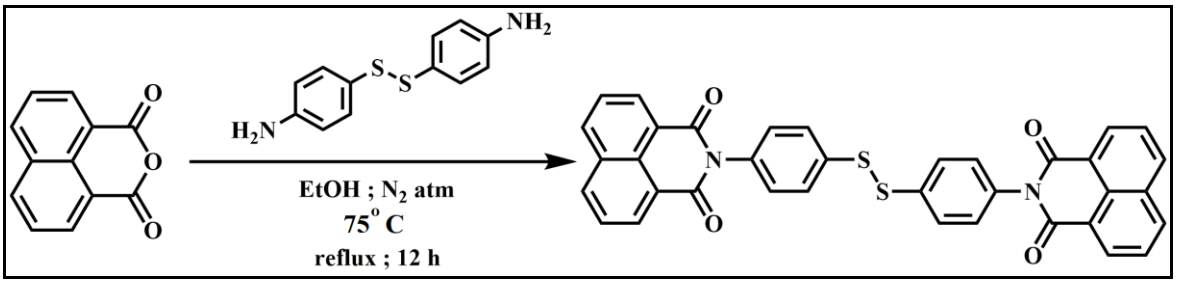

Scheme 3. Synthetic scheme for **NISS** amphiphile.

In order to synthesize **NINSS**, first 1.0 equiv of 1-naphthaleneethanol and 1.2 equiv of *N*-(*tert*-butoxycarbonyl)-L-aspartic acid 4-benzyl ester were conjugated using 1.1 equiv of DCC, DMAP and HOBt in dry DCM. The reaction mixture was stirred for 12 h under N_2 atmosphere. After washing the organic part with HCl (1N) and drying over anhydrous sodium sulfate, the solvent was evaporated and the coupled product was purified by column chromatography (60-120 mesh silica gel) using 1% MeOH in $CHCl_3$ as eluent. Next, deprotection of the BOC group was carried out using TFA (~1.5 equiv) in dry DCM for 5 h. After removing the solvent, the crude mass taken in ethyl acetate was worked-up with 10% aqueous Na_2CO_3 solution and water. The organic part was evaporated to obtain a free amine. Finally, 1,8-naphthalic anhydride (1.0 equiv) and free amine derivative (1.2 equiv) were heated (75 °C, 12 h) in dry EtOH. After solvent removal, the crude mass was solubilized in DCM and washed with water. The product was collected from the DCM part. Purification of the condensed product was performed by column chromatography (100-200 mesh silica gel, 3% MeOH/$CHCl_3$ as an eluent) and washed with diethyl ether to obtain the product. The obtained product was debenzylated in methanol under hydrogen (H_2) atmosphere in presence of Pd on activated charcoal. The mixture was filtered in a celite-545 column after overnight stirring at room temperature. The deprotected acid was subjected to NHS activation by using 2.6 equiv of DCC and 2.3 equiv of NHS in dry DMF and stirred overnight under N_2 atmosphere. 4-Aminophenyl disulfide (1.0 equiv) and dry pyridine (excess) were added to this activated acid. After overnight stirring the DMF was distilled out from the reaction mixture and coupled product was purified by column chromatography (100-

200 mesh silica gel, 5 % MeOH in $CHCl_3$ used as the eluent) followed by washing with diethyl ether (Figure 1c, Scheme 4).

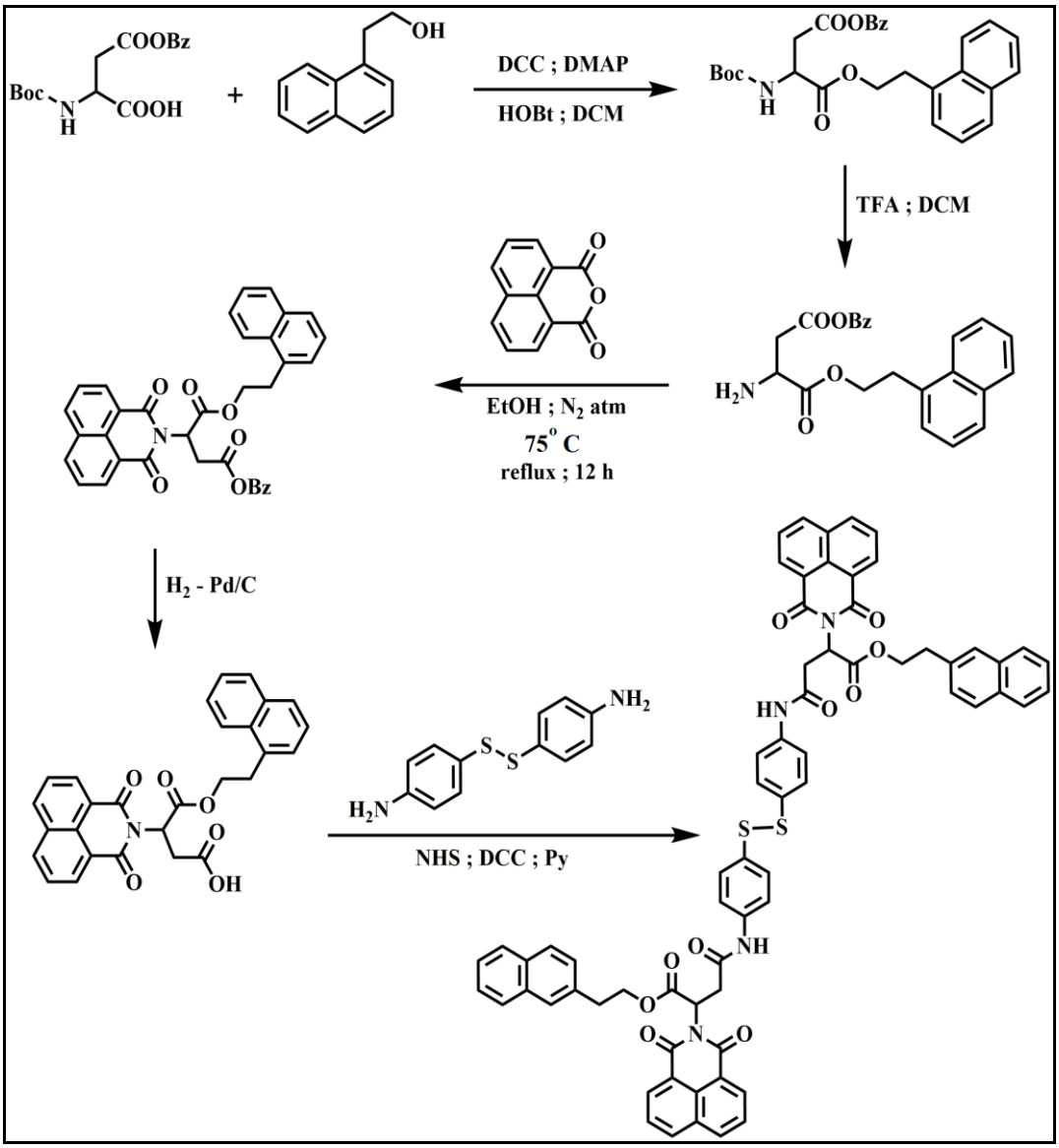

Scheme 4. Synthetic scheme for **NINSS** amphiphile.

To synthesize **TNINSH**, at first, coupling reaction between N-(*tert*-butoxycarbonyl)-L-aspartic acid 4-benzyl ester (1.2 equiv) and 1-naphthaleneethanol (1.0 equiv) was carried out using DCC (1.1 equiv), HOBt (1.1 equiv) DMAP (1.1 equiv), in dry DCM. The reaction mixture was stirred for 12 h under nitrogen atmosphere. 1N HCl was used to wash the organic part and consequently it was dried over anhydrous Na_2SO_4. The residue obtained after evaporation was

purified by column chromatography using 60-120 mesh silica gel as the stationary phase and the eluent was 1% methanol in chloroform. The BOC group was deprotected in 5 h using TFA (~1.5 equiv) in dry DCM. After solvent removal, the crude mass taken in ethyl acetate was twice washed with 10% aqueous Na_2CO_3 solution and water. Drying and evaporation of the solvent resulted in the formation of free amine. On the other hand, 4-bromo-1,8-naphthalene anhydride (1.0 equiv) and *N*-tosylethylenediamine (1.5 equiv) were dissolved in methoxy-ethanol and heated at 120 °C for 4 h under reflux conditions. The reaction mixture was cooled to room temperature and poured into 50 mL of ice-cold distilled water. The mixture was filtered, and the filtrate was vacuum-evaporated to get a yellow solid. This solid was purified in 100-200 mesh silica gel chromatography using 3% methanol in chloroform (v/v) as the eluent to obtain the product. After that, the free amine (1.2 equiv) and naphthalene anhydride derivative (1.0 equiv) were heated (75 °C, 12 h) in dry EtOH. The reaction mixture was cooled to room temperature and EtOH was evaporated. The crude mass was solubilized in DCM and washed with water. The expected product was collected from the DCM part. Purification of the condensed product was performed by column chromatography (100-200 mesh silica gel, 5% MeOH/$CHCl_3$ as an eluent) and washed with diethyl ether to obtain the product. The hydrogenation reaction of the obtained product (in the preceding step) was carried out in the presence of Pd on activated charcoal in dry tetrahydrofuran (THF) and the reaction mixture was stirred overnight at room temperature to deprotect the benzyl protection. The whole mixture was filtered in a $Celite_{545}$ column where hot THF was used as the eluent. The THF was then removed completely with a vacuum pump to get the acid. NHS activation of the acid was performed by using the previously formed acid, DCC (2.6 equiv), and NHS (2.3 equiv) in dry DMF and stirred overnight under N_2 atmosphere. To this activated acid, 4-aminothiophenol (1.0 equiv) and dry pyridine (excess) were added. The reaction mixture was stirred overnight and the DMF was distilled out under vacuum. The residue mixture was then purified through column chromatography by using 100-200 mesh silica gel and 5% MeOH/$CHCl_3$ as the eluent to obtain pure **TNINSH** (Figure 1d, Scheme 5).

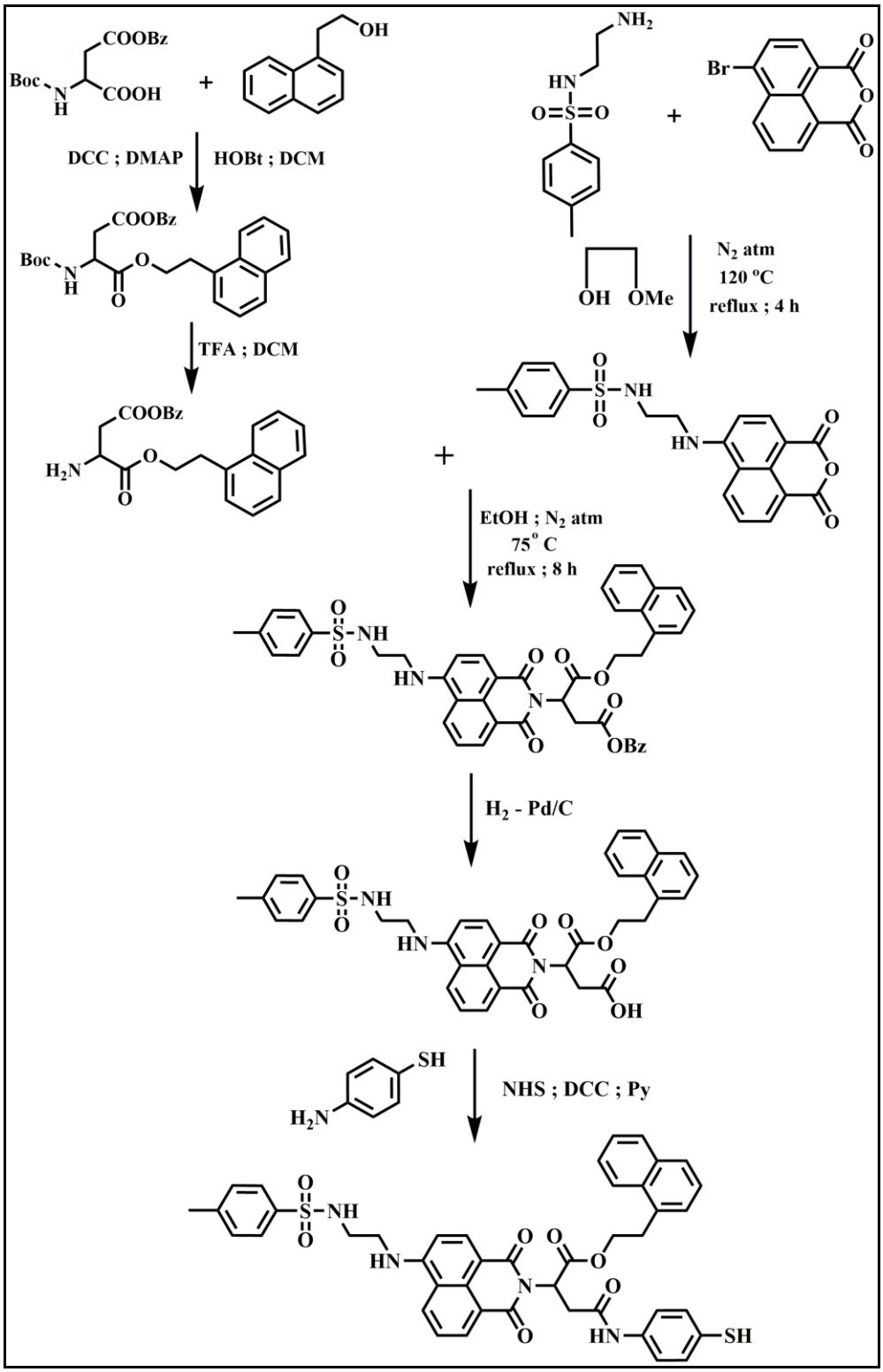

Scheme 5. Synthetic scheme for **TNINSH** amphiphile.

3A.4.3 PREPARATION OF SAMPLE.

All the naphthalimide derivatives (**NISH**, **NISS**, **NINSS** and **TNINSH**) were dissolved in DMSO to prepare the stock solution of 10 mM concentration. To achieve different composition needed for subsequent experiments, required amount aliquot was added to the varying compositions of DMSO-water binary solvent mixture in various ratio from this stock solutions in DMSO.

3A.4.4 TRANSMISSION ELECTRON MICROSCOPY (TEM) STUDY.

NISH, **NISS**, **NINSS** and **TNINSH** (25 μM) solution in (1:99 v/v) DMSO-water (f_w = 99 vol%) was deposited on a 300-mesh carbon-coated copper grid and dried. Negative staining of the copper grid was done with freshly prepared 1 μL of uranyl acetate solution (1% w/v), and a filter paper was used to blot the excess solution. Before taking the image in transmission electron microscopic, the sample was dried for 4 h in vacuum. The TEM images were taken in JEOL JEM 2010 microscope.

3A.4.5 FIELD-EMISSION SCANNING ELECTRON MICROSCOPY (FESEM) STUDY.

To obtain FESEM images, a JEOL-6700F microscope was used. 5.0 μL of **NISH**, **NISS**, **NINSS** and **TNINSH** having concentration of 25 μM solution in f_w = 99 vol% was used to drop cast on a coverslip. After drying it for overnight, the FESEM images were taken.

3A.4.6 DYNAMIC LIGHT SCATTERING (DLS) STUDY.

To determine the mean hydrodynamic diameter (D_h) of **NISH, NISS, NINSS** and **TNINSH** (25 μM) in f_w = 99 vol% we performed DLS study using a fixed-angle apparatus (Zen 3690 Zetasizer Nano ZS instrument (Malvern Instrument Ltd.). Measurement of the scattering intensity was done at an angle of 175°.

3A.4.7 UV-VISIBLE STUDY.

Agilent Cary 60 spectrophotometer was used to record UV-vis spectra. UV-vis spectra of **NISH**, **NISS**, **NINSS** and **TNINSH** (20 μM) were performed in various solvent compositions of DMSO-water changing the water content from f_w = 0 vol% (non-self-assembled state) to f_w = 99

vol% (self-assembled state). The relative absorbance (A/A_o) of **NINSS** and **TNINSH** (10 μM) was studied for 7 days, where A_o = original absorbance and A = absorbance at different days.

3A.4.8 STEADY-STATE FLUORESCENCE ANISOTROPY STUDY.

Fluorescence spectra were recorded using the hydrophobic fluorescent probe 1,6-diphenyl-1,3,5-hexatriene (DPH) in a Varian Cary Eclipse fluorescence spectrophotometer. The steady-state anisotropy (r) of DPH was measured in individual solution of **NISH**, **NISS**, **NINSS** and **TNINSH** in different solvent compositions of DMSO-water. A stock solution of DPH (0.2 mM) was prepared in tetrahydrofuran (THF), and in each investigating solution (1 mL) the final concentration of DPH was maintained at 1 μM. The DPH included **NISH**, **NISS**, **NINSS** and **TNINSH** solutions were excited at 325 nm. The emission intensity was measured at 450 nm using an emission cutoff filter at 430 nm to avoid any scattering due to turbidity of the solution. The excitation and emission slit widths were kept at 5 nm. The fluorescence anisotropy (r) was calculated by the instrument software using following equation,

$$r = \frac{(I_{VV} - G I_{VH})}{(I_{VV} + 2G I_{VH})} \quad (1)$$

where I_{VV} and I_{VH} are the intensities of the emission spectra obtained with vertical and horizontal polarization (for vertically polarized light), respectively, and G = I_{HV}/I_{HH} is the instrumental correction factor, where I_{HV} and I_{HH} are the emission intensities obtained with vertical and horizontal polarization (for horizontally polarized light), respectively. The fluorescence measurements were performed at least five times for each sample at 25 °C.

3A.4.9 CIRCULAR DICHROISM (CD) STUDY.

CD spectra of **NISH**, **NISS**, **NINSS** and **TNINSH** (25 μM) in DMSO (non-self-assembled state) and 1:99 v/v DMSO-water system (self-aggregated state) were recorded by using a quartz cuvette of 1 mm path length in a JASCO J-815 CD spectropolarimeter.

3A.4.10 FTIR STUDY.

PerkinElmer Spectrum 100 FTIR spectrometer was used for FTIR measurements. FTIR spectra of **NISH**, **NISS**, **NINSS** and **TNINSH** were performed in the $CHCl_3$ (in non-self-

assembled state) and in the self-aggregated state (f_w = 99 vol%) at room temperature. 1 mm CaF2 cell was used to perform all the experiments of FTIR study.

3A.4.11 SOLVENT-DEPENDENT ^{1}H-NMR STUDY.

Solvent dependent ^{1}H-NMR study was performed with a Avance 300 MHz (Bruker) spectrometer. The spectra **NISH**, **NISS**, **NINSS** and **TNINSH** (1 mM) in DMSO-d_6 and in several solvent systems (2:1 (v/v) and 1:1 (v/v) of DMSO-d_6-D_2O) were recorded.

3A.4.12 PHOTOLUMINESCENCE STUDY.

Agilent Cary Eclipse luminescence spectrometer was used to record the fluorescence spectra of the **NISH**, **NISS**, **NINSS** and **TNINSH** (20 μM) solutions in f_w = 0-99 vol% (excitation wavelength (λ_{ex}) = 350 nm). Relative fluorescence intensity (I/I_o) of **NINSS** and **TNINSH** FONPs (in f_w = 99 vol%) was studied 7 days where, I_o = original fluorescence intensity and I = fluorescence intensity at different days of **NINSS** and **TNINSH** FONPs respectively. We also monitored the fluorescence dependence from environment polarity at different viscosity (e.g., PEG/H_2O, THF/H_2O, PEG/THF mixtures) to check fluorescence dependency on the polarity and viscosity of **NINSS** and **TNINSH** FONPs.

3A.4.13 FLUORESCENCE MICROSCOPIC STUDY.

Drop casting of 10 μL solution of **NINSS** and **TNINSH** having concentration 20 μM in f_w = 99 vol% was performed on a glass slide. After that, images were taken under fluorescence microscope (Olympus IX83 inverted) at 40x magnification.

3A.4.14 QUANTUM YIELD (QY) MEASUREMENT.

QYs are generally measured relative to an optical dilute standard fluorophore solution that exhibits a well-known quantum yield (ϕ_s). The quantum yields of the unknown fluorophore (ϕ_u) were determined by using the Parker-Rees method.

Equation

$$\emptyset_u = \left(\frac{A_s F_u n_u^2}{A_u F_s n_s^2}\right)\emptyset_s \qquad (2)$$

Here, A_u = the absorbance of unknown sample at the excitation wavelength, A_s = the absorbance of reference sample at the excitation wavelength, F_u = the total area of integrated fluorescence intensity for the unknown sample when excited at the same excitation wavelength, and F_s = the area of the integrated fluorescence intensity for the known sample when excited at the same excitation wavelength. We used a solution with similar absorbance (<0.01) for the determination of quantum yield. The refractive indices of the solvents in which the unknown and the standard samples were prepared are given by n_u and n_s respectively. Here, in our study we have chosen quinine sulfate in 0.1 M sulfuric acid (H_2SO_4) as the standard and its QY (ϕ_s) is known to be 54.0%.

3A.4.15 TIME RESOLVED STUDY.

A picosecond diode laser IBH-405 was used to perform time correlation single photon count (TCSPC) measurement. **NINSS** and **TNINSH** (20 μM) solution were excited at 360 nm followed by monitoring of the emission at 390 and 435 nm for only DMSO and at 470 and 550 nm for f_w = 99 vol%, respectively. IBH DAS6 software was used to analyze the fluorescence decays. the experimental time resolved fluorescence decay $p(t)$ was analyzed using following equation 2.

$$p(t) = b + \sum_{i}^{n} \alpha_i \exp\left(-\frac{t}{\tau_i}\right) \quad (3)$$

where n = number of discrete emissive species, b = baseline correction ("dc" offset), α_i were the pre-exponential factors and τ_i were excited state fluorescence lifetimes associated with the ith component. Equation 3 was utilized to calculate the average lifetime of multiexponential decays.

$$< \tau > = \sum_{i=1}^{n} \alpha_i \tau_i \quad (4)$$

Where $\alpha_i = \frac{\alpha_i}{\sum \alpha_i}$ which denotes the contribution of a decay component.

3A.5 CHARACTERIZATION DATA

NISH: ^{1}H-NMR (400 MHz, DMSO-d_6, 25 °C): δ/ppm: 8.42-8.64 (m, 4H, C-2, C-4, C-5 and C-7 proton of naphthalimide core), 7.81-7.93 (m, 2H, C-3 and C-6 proton of NI core), 7.47-7.68 (m, 4H, C-2, C-3, C-5 and C-6 proton of aminothiophenol ring). ^{13}C-NMR (100 MHz, DMSO-d_6): 159.26, 138.25, 128.50, 127.59, 124.15, 123.66, 121.41, 117.15, 116.05. MALDI-TOF MS: *m*/*z*: 305.3510 $[M]^+$ (calculated); 306.316 $[M+H]^+$, 328.555 $[M+Na]^+$, 344.590 $[M+K]^+$ (found).

NISS: ^{1}H-NMR (400 MHz, DMSO-d_6, 25 °C): δ/ppm: 8.47-8.59 (m, 4H, C-2, C-4, C-5 and C-7 proton of both naphthalimide core unit), 7.82-7.94 (m, 2H, C-3 and C-6 proton of both NI core), 7.70-7.78 (m, 2H, C-2 and C-6 proton of phenyl rings), 7.62-7.69 (m, 2H, C-3 and C-5 proton of phenyl ring). ^{13}C-NMR (100 MHz, DMSO-d_6): 161.23, 141.07, 139.49, 132.75, 131.15, 129.52, 126.42, 125.03, 123.35. MALDI-TOF MS: *m*/*z*: 608.086 $[M]^+$ (calculated); 609.081 $[M+H]^+$, 631.035 $[M+Na]^+$, 647.039 $[M+K]^+$ (found).

NINSS: ^{1}H-NMR (400 MHz, $CDCl_3$, 25 °C): δ/ppm: 8.38-8.49 (m, 12H, naphthalimide core), 8.06-8.13 (m, 4H, C-3 and C-5 proton of phenyl rings), 7.65-7.77 (m, 10H, C-2 and C-6 protons of phenyl rings and C-4, C-5, C-8 protons of naphthyl rings), 7.49-7.62 (m, 8H, C-1,C-3,C-6 ring and C-7 protons of naphthyl rings), 4.68-4.73 (t, 2H, chiral centre of L-aspartic acid residue), 4.37-4.42 (t, 4H, -O-C$\underline{H}_2$-CH_2-$C_{10}H_7$), 3.10-3.23 (m, 8H, -O-CH_2-C$\underline{H}_2$-$C_{10}H_7$ and methylene protons of L-aspartic acid residue).^{13}C-NMR (100 MHz, $CDCl_3$): 172.26, 169.95, 158.08, 138.51, 138.39, 138.23, 137.20, 136.49, 134.95, 132.85, 132.12, 131.42, 130.69, 128.35, 127.51, 124.15, 123.45, 68.89, 62.37, 34.54, 29.97. MALDI-TOF MS: *m*/*z*: 1147.296 $[M]^+$ (calculated); 1147.295 $[M]^+$ (found).

TNINSH: ^{1}H-NMR (400 MHz, $CDCl_3$, 25 °C): δ/ppm: 8.48-8.56 (m, 1H, C-7 proton of NI core), 8.36-8.42 (m, 1H, C-2 and C-5 proton of NI core), 7.93-8.16 (m, 2H, C-5 and C-8 proton of naphthyl ring), 7.82-7.89 (m, 2H, C-3 and C-5 proton of phenyl ring of aminothiophenol unit), 7.75-7.78 (m, 1H, C-4 proton of naphthyl ring), 7.25-7.61 (m, 10H, C-1, C-3, C-6, C-7 of naphthyl ring, C-2 and C-6 proton of phenyl ring of aminothiophenol unit and all protons of phenyl ring of tosyl unit), 7.09-7.02 (C-3 of NI core), 4.63-4.69 (m, 1H, chiral centre of L-aspartic acid residue), 4.38-4.43 (m, 2H, -O-C$\underline{H}_2$-CH_2-$C_{10}H_7$), 3.33-3.39 (m, 2H, -NH-C$\underline{H}_2$-CH_2-NH_2-SO_2-

PhMe), 3.05-3.14 (m, 6H, -O-CH_2-C$\underline{H}_2$-$C_{10}H_7$, methylene protons of L-aspartic acid residue and -NH-CH_2-C$\underline{H}_2$-NH_2-SO_2-PhMe), 2.37 (s, 3H, -NH-CH_2-C$\underline{H}_2$-NH_2-SO_2-Ph-C$\underline{H}_3$).^{13}C-NMR (100 MHz, $CDCl_3$): 177.86, 174.75, 158.58, 157.11, 140.39, 139.83, 137.50, 137.09, 135.95, 134.15, 132.62, 131.42, 129.09, 128.15, 127.25, 126.96, 126.06, 123.65, 122.31, 119.79, 117.37, 112.48, 64.29, 57.47, 48.16, 42.56, 32.64, 25.97, 21.07. MALDI-TOF MS: *m/z*: 786.218 $[M]^+$ (calculated); 786.225 $[M]^+$, 825.058 $[M+K]^+$ (found).

3A.6 SPECTRA

3A.6.1 ^{1}H-NMR SPECTRA

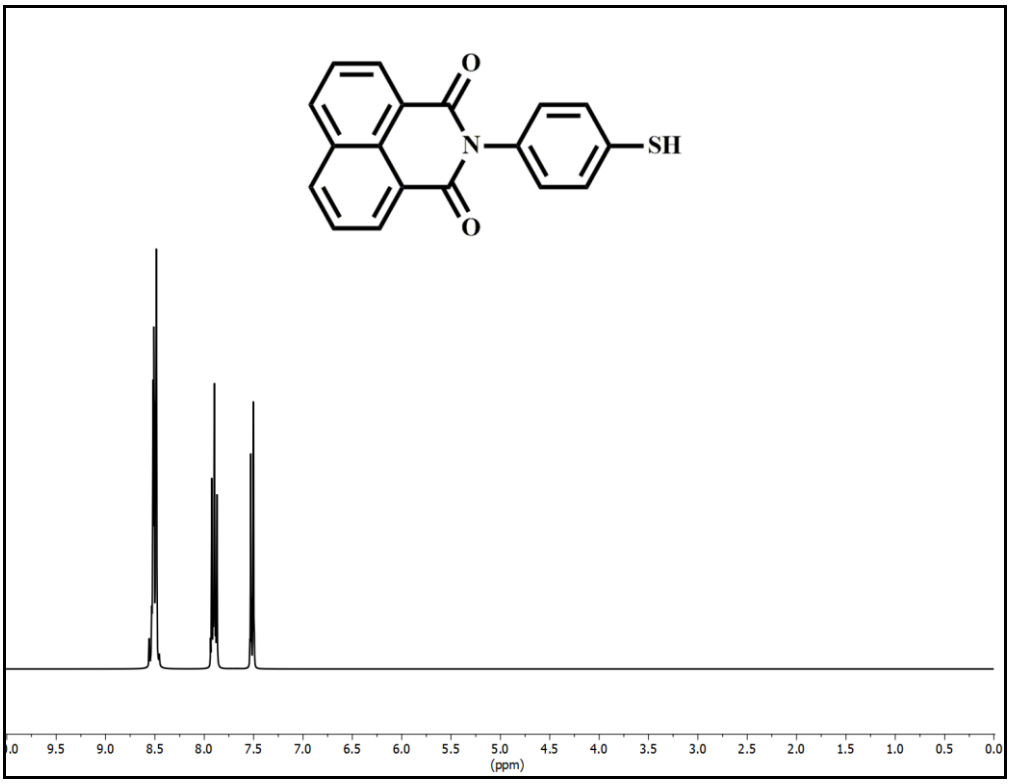

Figure 15. ^{1}H-NMR spectrum of **NISH**.

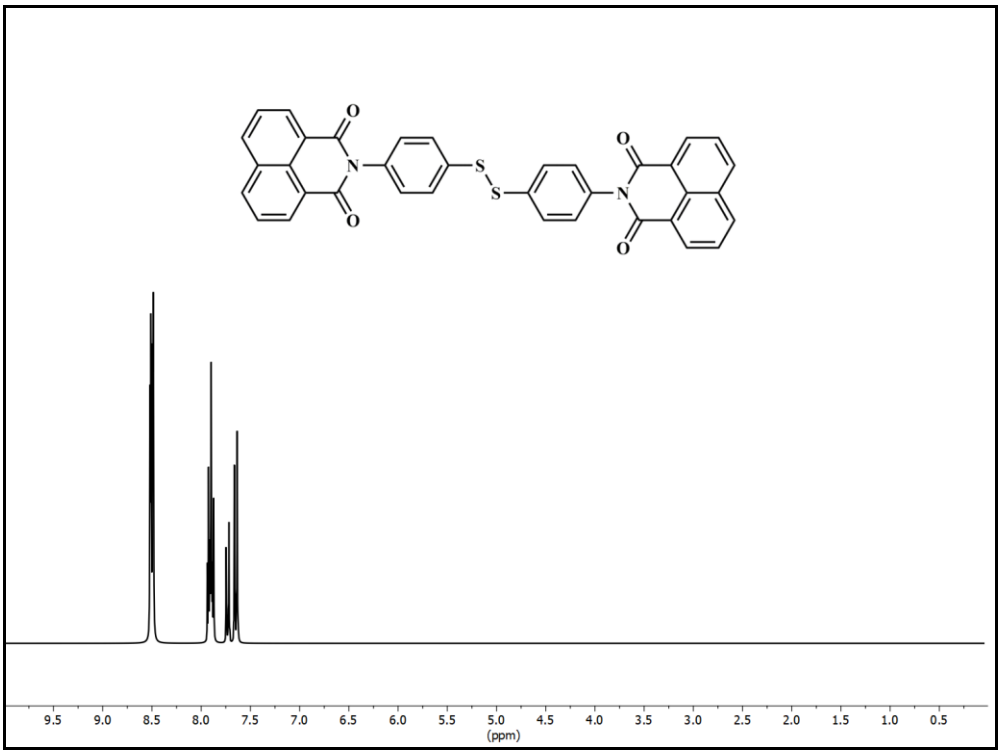

Figure 16. ^{1}H-NMR spectrum of **NISS**.

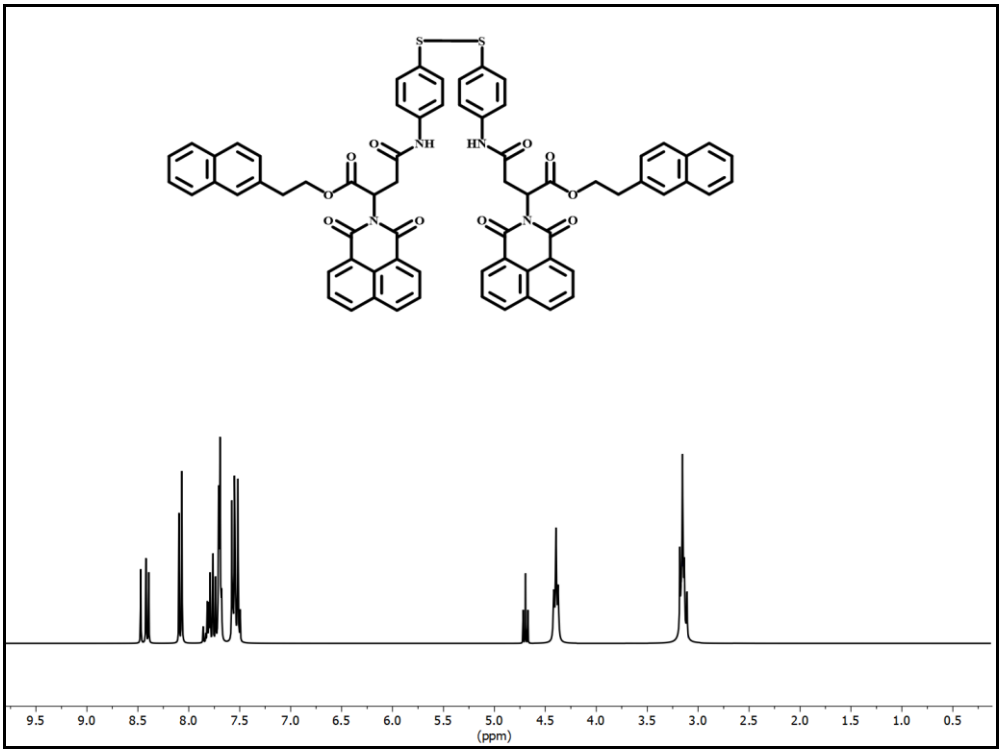

Figure 17. ^{1}H-NMR spectrum of **NINSS**.

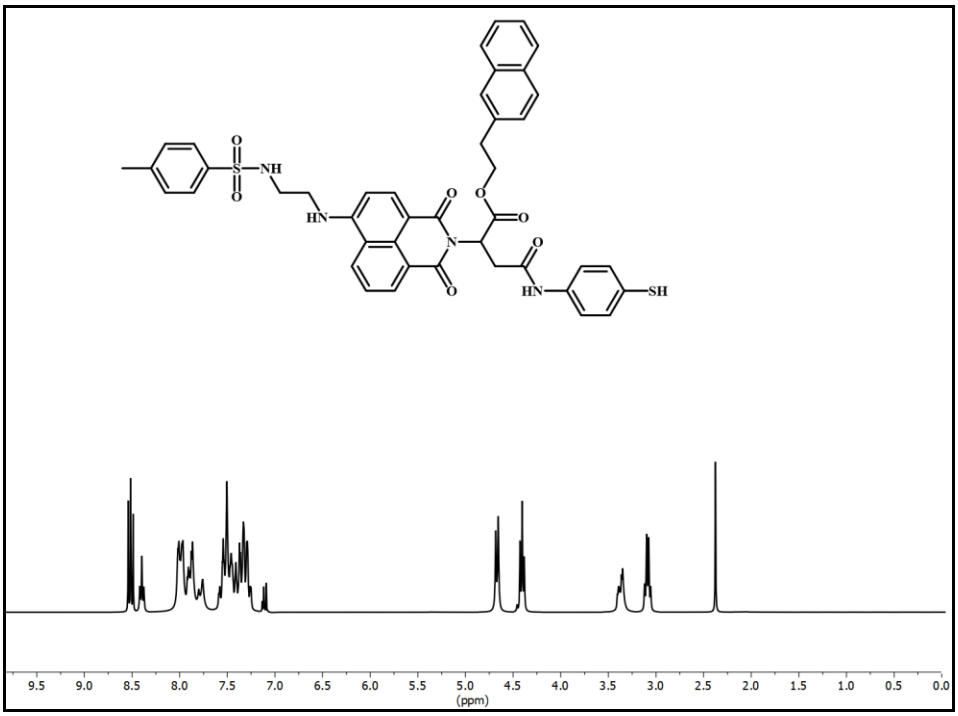

Figure 18. ^{1}H-NMR spectrum of **TNINSH**.

3A.6.2 ^{13}C-NMR SPECTRA.

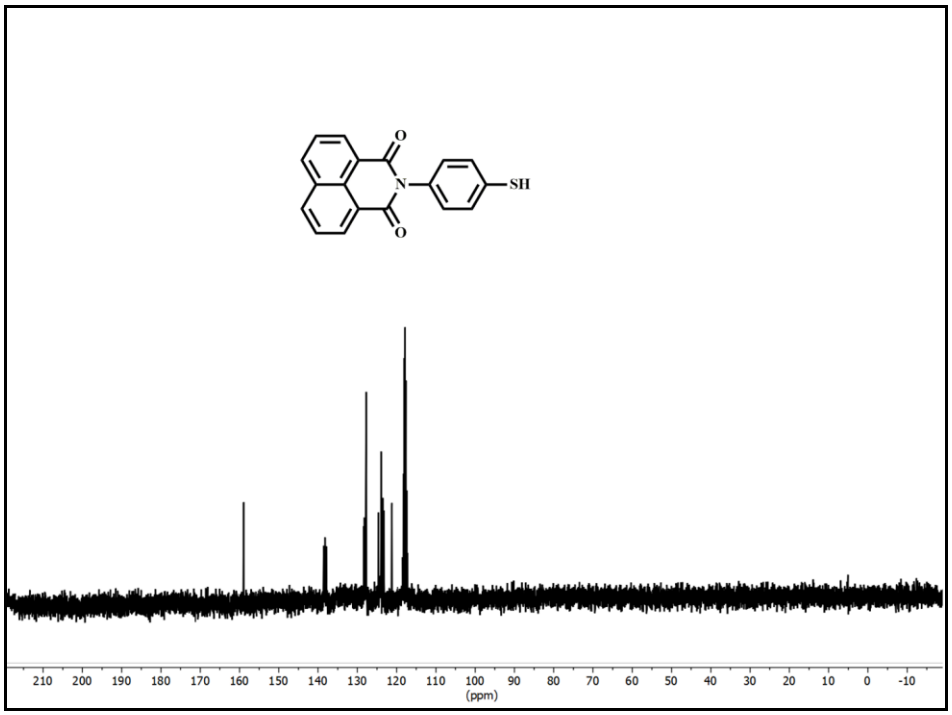

Figure 19. ^{13}C-NMR spectrum of **NISH**.

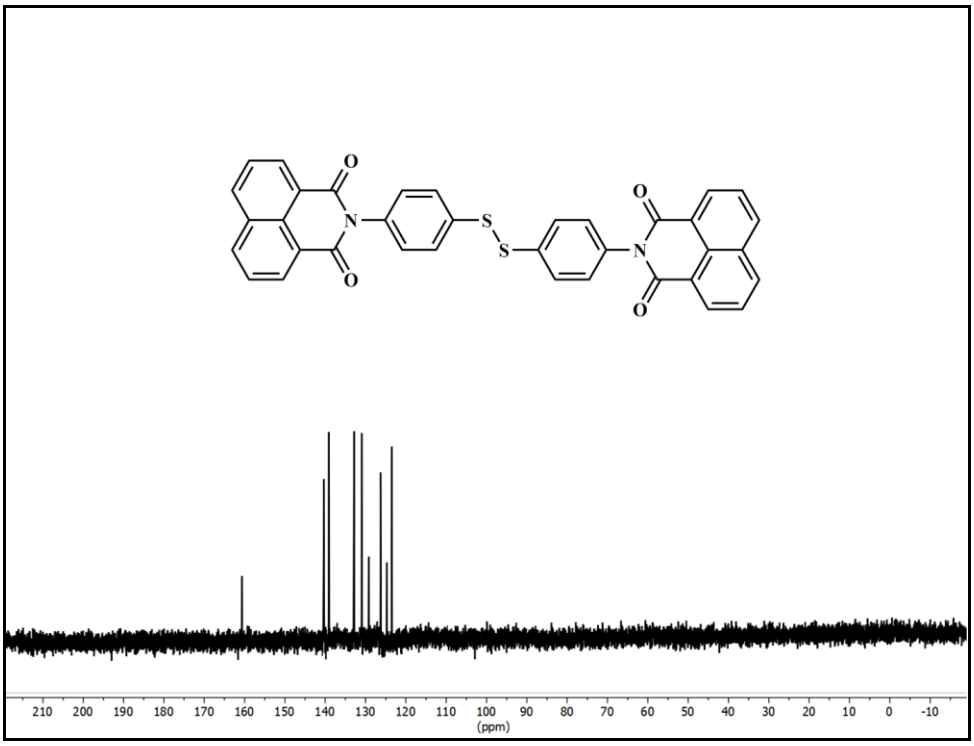

Figure 20. ^{13}C-NMR spectrum of **NISS**.

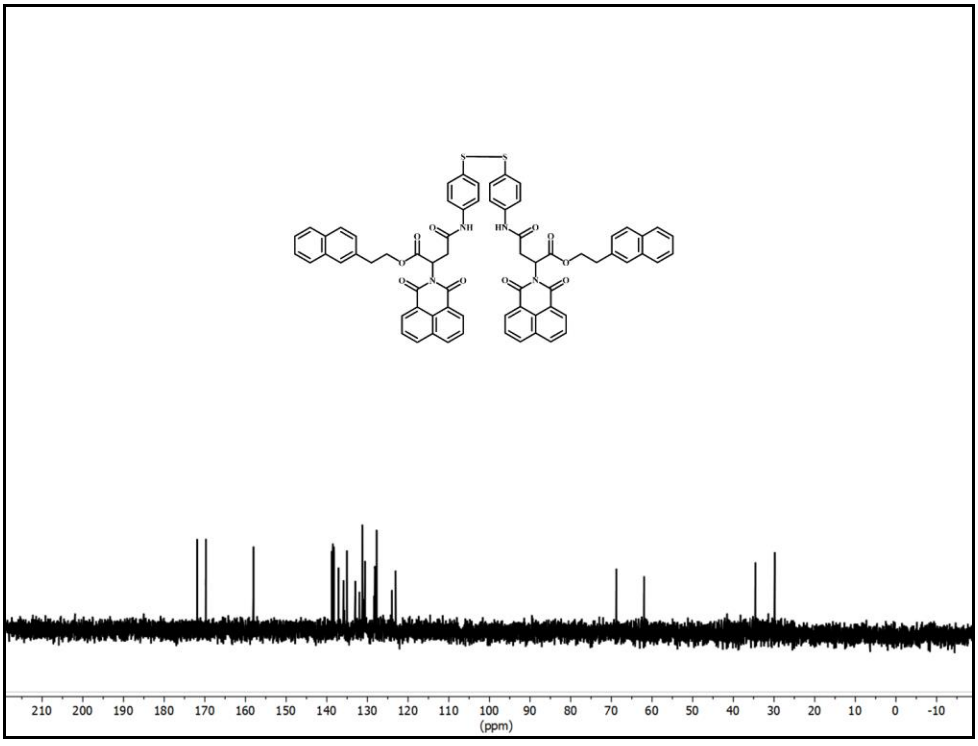

Figure 21. ^{13}C-NMR spectrum of **NINSS**.

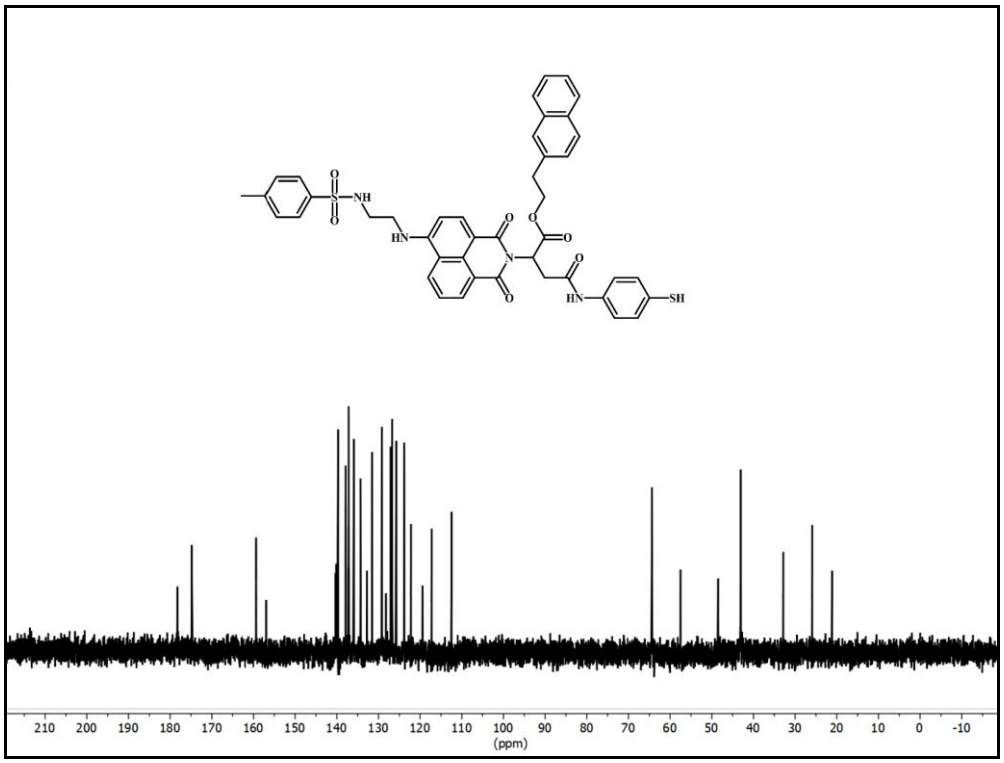

Figure 22. ^{13}C-NMR spectrum of **TNINSH**.

3A.6.3 MALDI-TOF MASS SPECTRA

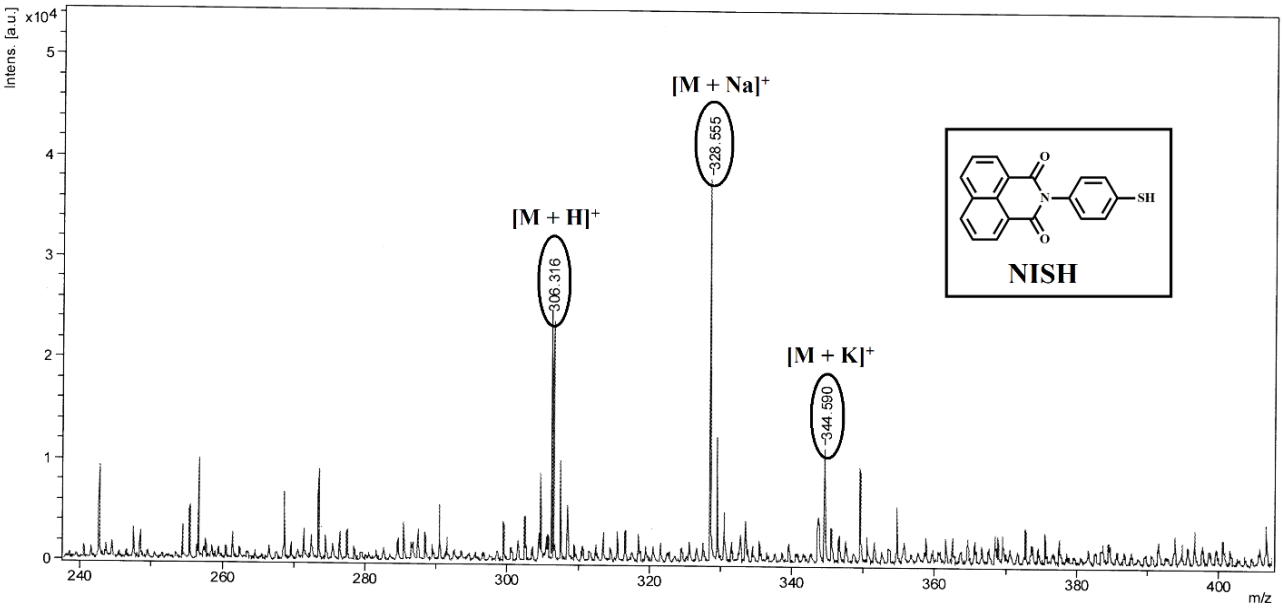

Figure 23. MALDI-TOF mass spectrum of **NISH**.

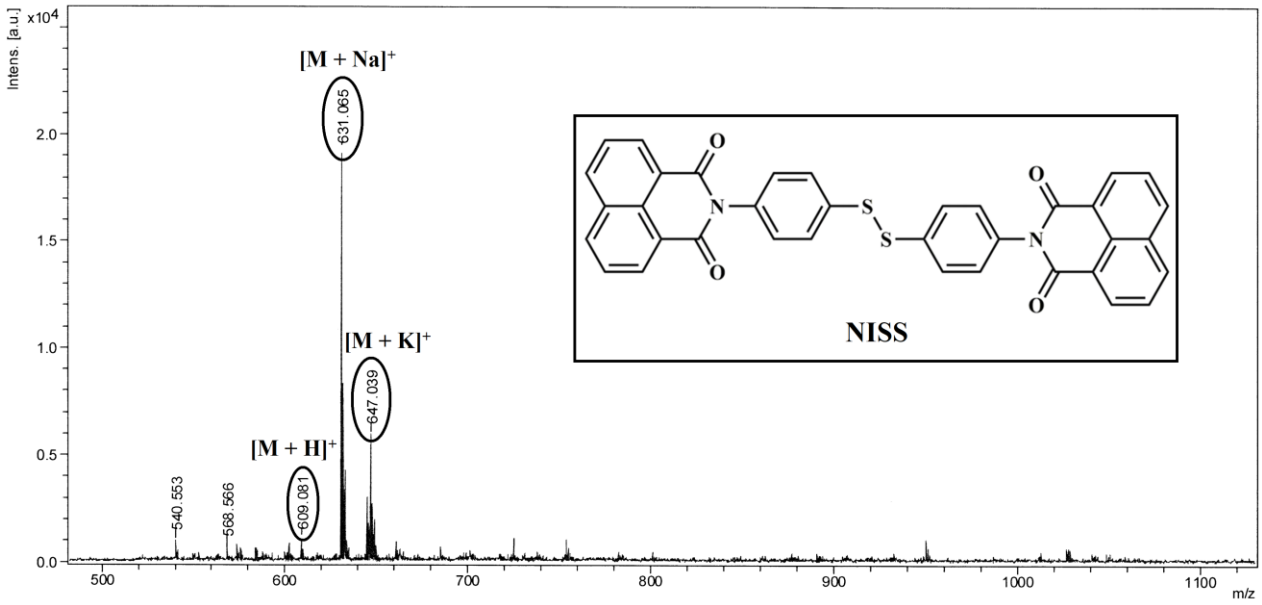

Figure 24. MALDI-TOF mass spectrum of **NISS**.

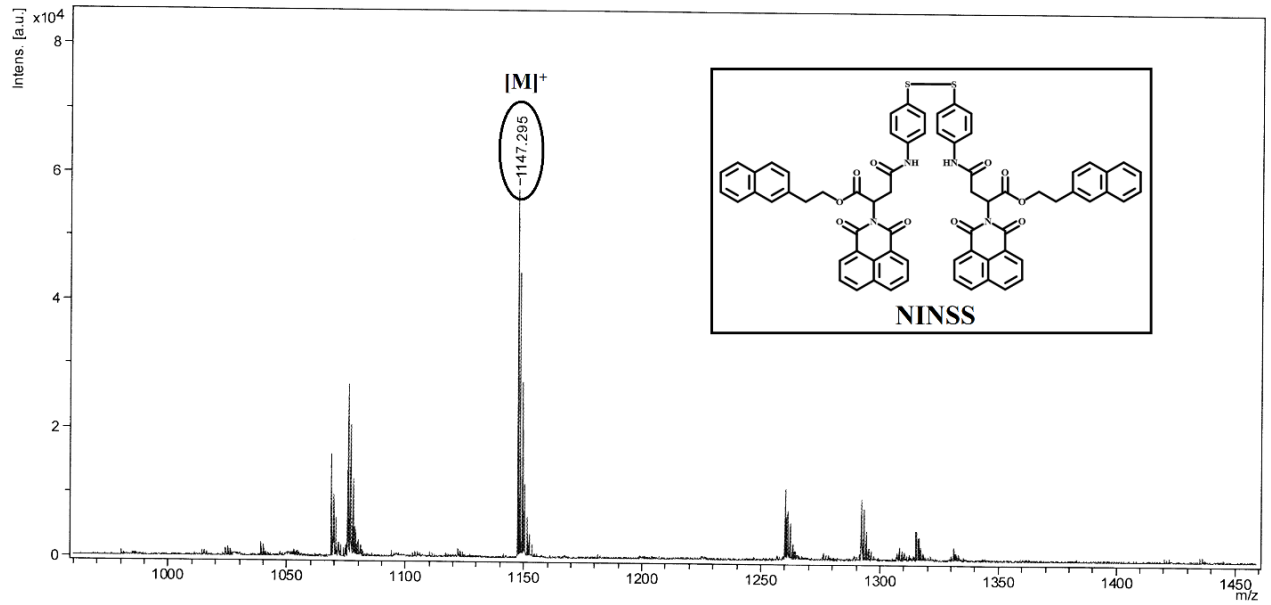

Figure 25. MALDI-TOF mass spectrum of **NINSS**.

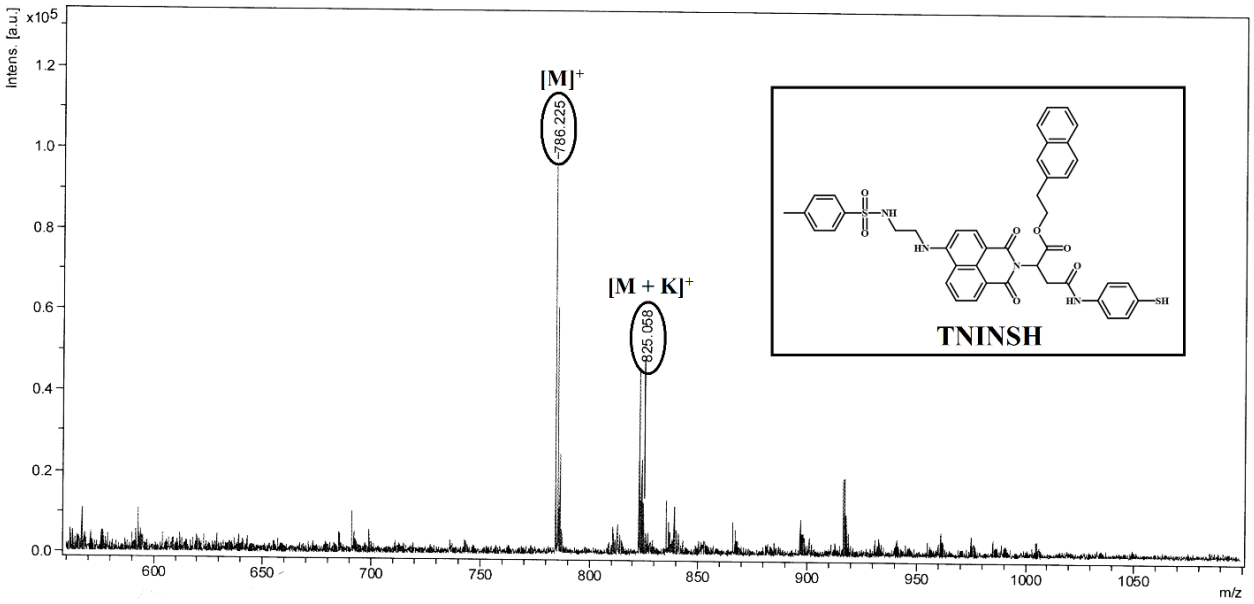

Figure 25. MALDI-TOF mass spectrum of **NINSS**.

3A.7 REFERENCES

[1] Yao, J.; Yang, M.; Duan, Y. Chemistry, Biology, and Medicine of Fluorescent Nanomaterials and Related Systems: New Insights into Biosensing, Bioimaging, Genomics, Diagnostics, and Therapy. *Chem. Rev*. **2014**, *114*, 6130-6178.

[2] Ueno, T.; Nagano, T. Fluorescent Probes for Sensing and Imaging. *Nat. Methods* **2011**, *8*, 642-645.

[3] Desmonts, L. B.; Reinhoudt, D. N.; Calama, M. C. Design of Fluorescent Materials for Chemical Sensing. *Chem. Soc. Rev.* **2007**, *36*, 993-1017.

[4] Wolfbeis, O. S. An Overview of Nanoparticles Commonly used in Fluorescent Bioimaging. *Chem. Soc. Rev.* **2015**, *44*, 4743-4768.

[5] Peng, H. S.; Chiu, D. T. Soft Fluorescent Nanomaterials for Biological and Biomedical Imaging. *Chem. Soc. Rev.* **2015**, *44*, 4699-4722.

[6] Svechkarev, D.; Mohs, A. M. Organic Fluorescent Dye-based Nanomaterials: Advances in the Rational Design for Imaging and Sensing Applications. *Curr. Med. Chem*. **2019**, *26*, 4042-4064.

[7] Thomas, S. W.; Joly, G. D.; Swager, T. M. Chemical Sensors Based on Amplifying Fluorescent Conjugated Polymers. *Chem. Rev.* **2007**, *107*, 1339-1386.

[8] Li, Z.; Sun, Q.; Zhu, Y.; Tan, B.; Xu, Z. P.; Dou, S. X. Ultra-small Fluorescent Inorganic Nanoparticles for Bioimaging. *J. Mater. Chem. B* **2014**, *2*, 2793-2818.

[9] Li, J.; Zhu, J. Quantum Dots for Fluorescent Biosensing and Bio-imaging Applications. *Analyst* **2013**, *138*, 2506-2515.

[10] Li, J.; Zhu, J. J.; Xu, K. Fluorescent Metal Nanoclusters: From Synthesis to Applications. *Trends Analyt. Chem.* **2014**, *58*, 90-98.

[11] Wani, W. A.; Shahid, M.; Hussain, A.; AlAjmi, M. F. Fluorescent Organic Nanoparticles: New Generation Materials with Diverse Analytical and Biomedical Applications. *Springer*, Singapore, **2018**.

[12] Tang, F.; Wang, C.; Wang, J.; Wang, X.; Li, L. Fluorescent Organic Nanoparticles with Enhanced Fluorescence by Self-Aggregation and their Application to Cellular Imaging. *ACS Appl. Mater. Interfaces* **2014**, *6*, 18337-18343.

[13] Yuan, W. Z.; Lu, P.; Chen, S.; Lam, J. W. Y.; Wang, Z.; Liu, Y.; Kwok, H. S.; Ma, Y.; Tang, B. Z. Changing the Behavior of Chromophores from Aggregation-Caused Quenching to Aggregation-Induced Emission: Development of Highly Efficient Light Emitters in the Solid State. *Adv. Mater.* **2010**, *22*, 2159-2163.

[14] Thompson, R. B. *Fluorescence Sensors and Biosensors*, CRC: Boca Raton, **2006**.

[15] Luo, J.; Xie, Z.; Lam, J. W. Y.; Cheng, L.; Chen, H.; Qiu, C.; Kwok, H. S.; Zhan, X.; Liu, Y.; Zhu, D.; Tang, B. Z. Aggregation-Induced Emission of 1-methyl-1,2,3,4,5-pentaphenylsilole. *Chem. Commun.* **2001**, 1740-1741.

[16] Hong, Y.; Lam, J. W. Y.; Tang, B. Z. Aggregation-Induced Emission: Phenomenon, Mechanism and Applications. *Chem. Commun.* **2009**, 4332-4353.

[17] Hong, Y.; Lam, J. W. Y.; Tang, B. Z. Aggregation-Induced Emission. *Chem. Soc. Rev.* **2011**, *40*, 5361-5388.

[18] Chen, Y.; Lam, J. W. Y.; Kwok, R. T. K.; Liu, B.; Tang, B. Z. Aggregation-Induced Emission: Fundamental Understanding and Future Developments. *Mater. Horiz.* **2019**, *6*, 428-433.

[19] Zhang, X.; Zhang, X.; Tao, L.; Chi, Z.; Xu, J.; Wei, Y. Aggregation Induced Emission-based Fluorescent Nanoparticles: Fabrication Methodologies and Biomedical Applications. *J. Mater. Chem. B* **2014**, *2*, 4398-4414.

[20] Wu, W.; Li, Z. Nanoprobes with Aggregation-Induced Emission for Theranostics. *Mater. Chem. Front.* **2021**, *5*, 603-626.

[21] Yang, B.; Zhang, X.; Zhang, X.; Huang, Z.; Wei, Y.; Tao, L. Fabrication of Aggregation-Induced Emission based Fluorescent Nanoparticles and Their Biological Imaging Application: Recent Progress and Perspectives. *Mater. Today* **2016**, *19*, 284-291.

[22] Cai, X.; Liu, B. Aggregation-Induced Emission: Recent Advances in Materials and Biomedical Applications. *Angew. Chem. Int. Ed.* **2020**, *59*, 9868-9886.

[23] Kaeser, A.; Schenning, A. P. H. J. Fluorescent Nanoparticles based on Self-Assembled π-Conjugated Systems. *Adv. Mater.* **2010**, *22*, 2985-2997.

[24] Ghosh, A. K.; Choudhury, P.; Das, P. K. Fabrication of Orange-Emitting Organic Nanoparticle-Protamine Conjugate: Fluorimetric Sensor of Heparin. *Langmuir* **2019**, *35*, 15180-15191.

[25] Kaeser, A.; Fischer, I.; Abbel, R.; Besenius, P.; Dasgupta, D.; Gillisen, M. A. J.; Portale, G.; Stevens, A. L.; Herz, L. M.; Schenning, A. P. H. J. Side Chains Control Dynamics and Self-Sorting in Fluorescent Organic Nanoparticles. *ACS Nano* **2013**, *7*, 408-416.

[26] Ghosh, A. K.; Chowdhury. M.; Das, P. K. Nipecotic-Acid-Tethered, Naphthalene-Diimide-Based, Orange-Emitting Organic Nanoparticles as Targeted Delivery Vehicle and Diagnostic Probe toward $GABA_A$-Receptor-Enriched Cancer Cells. *ACS Appl. Bio Mater.* **2021**, *4*, 7563-7577.

[27] Wilkinson, B.; Gilbert, H. F. Protein Disulfide Isomerase. *Biochimica et Biophysica Acta* **2004**, *1699*, 35-44.

[28] Noiva, R. Protein Disulfide Isomerase: The Multifunctional Redox Chaperone of the Endoplasmic Reticulum. *Semin. Cell Dev. Biol.* **1999**, *10*, 481-493.

[29] Xu, S.; Sankar, S.; Neamati, N. Protein Disulfide Isomerase: A Promising Target for Cancer Therapy. *Drug Discov. Today* **2014**, *19*, 222-240.

[30] Khan, M. M. G.; Simizu, S.; Kawatani, M.; Osada, H. The Potential of Protein Disulfide Isomerase as a Therapeutic Drug Target. *Oncol. Res.* **2011**, *19*, 445-453.

[31] Watanabe, M. M.; Laurindo, F. R. M.; Fernandes, D. C. Methods of Measuring Protein Disulfide Isomerase Activity: A Critical Overview. *Front. Chem.* **2014**, *2*, 73.

[32] Kokado, K.; Chujo, Y. Multicolor Tuning of Aggregation-Induced Emission Through Substituent Variation of Diphenyl-o-carborane. *J. Org. Chem.* **2011**, *76*, 316-319.

[33] Choudhury, P.; Sarkar, S.; Das, P. K. Tunable Aggregation-Induced Multicolor Emission of Organic Nanoparticles by Varying the Substituent in Naphthalene Diimide. *Langmuir* **2018**, *34*, 14328-14341.

[34] Banerjee, S.; Veale, E. B.; Phelan, C. M.; Murphy, S. A.; Tocci, G. M.; Gillespie, L. J.; Frimannsson, D. O.; Kelly, J. M.; Gunnlaugsson, T. Recent Advances in the Development of 1,8-Naphthalimide based DNA Targeting Binders, Anticancer and Fluorescent Cellular Imaging Agents. *Chem. Soc. Rev.* **2013**, *42*, 1601-1618.

[35] Geraghty, C.; Wynne, C.; Elmes, R. B. P. 1,8-Naphthalimide Based Fluorescent Sensors For Enzymes. *Coord. Chem. Rev.* **2021**, *437*, 213713.

[36] Gopikrishna, P.; Meher N.; Iyer, P. K. Functional 1,8-Naphthalimide AIE/AIEEgens: Recent Advances and Prospects. *ACS Appl. Mater. Interfaces* **2018**, *10*, 12081-12111.

[37] Duke, R. M.; Veale, E. B.; Pfeffer, F. M.; Kruger, P. E.; Gunnlaugsson, T. Colorimetric and Fluorescent Anion Sensors: An Overview of Recent Developments in the Use of 1,8-Naphthalimide-Based Chemosensors. *Chem. Soc. Rev.* **2010**, *39*, 3936-3953.

[38] Lin, H. H.; Chan, Y. C.; Chen, J. W.; Chang, C. C. Aggregation-Induced Emission Enhancement Characteristics of Naphthalimide Derivatives and Their Applications in Cell Imaging. *J. Mater. Chem.* **2011**, *21*, 3170-3177.

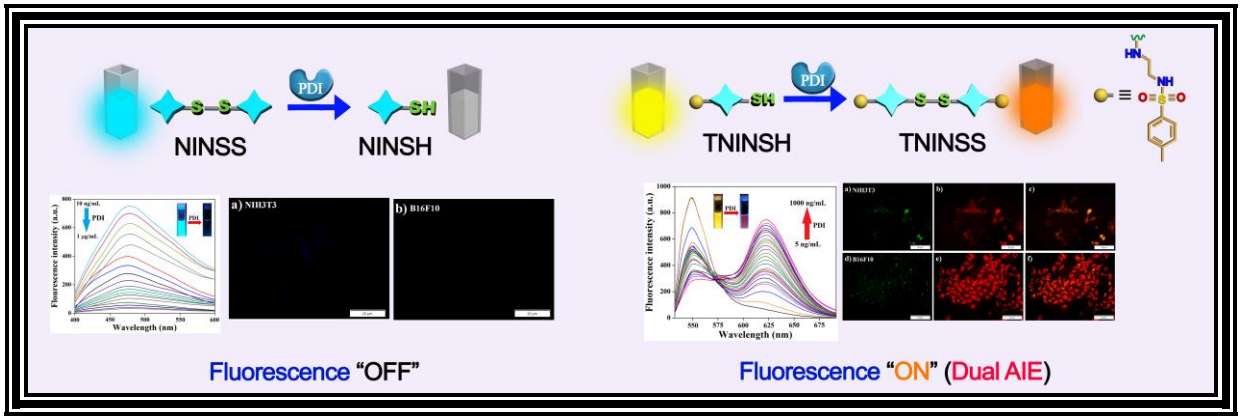

AIE-Active Naphthalimide based FONPs: Probing Protein Disulfide Isomerase via Thiol-Disulfide Redox Exchange

3B.1 INTRODUCTION

Belonging to the thioredoxin superfamily, protein disulfide isomerase (PDI) emerges as a 57-kDa dithiol-disulfide oxidoreductase, endowed with the multifaceted attributes of a molecular chaperone that intricately safeguards cellular equilibrium.[1,2] PDI's prominence is accentuated within the endoplasmic reticulum (ER), where its overexpression predominates, positioning it as a pivotal catalyst orchestrating the intricate ballet of protein folding through the mediation of disulfide formation, cleavage, and rearrangement.[3-6] In the ER milieu, PDI assumes the role of an oxidase, adeptly constructing disulfide bonds within nascent secretory proteins.[7,8] Concurrently, PDI navigates the terrain of reducing disulfide bonds in target proteins, extending its influence across cell surfaces, cytoplasmic realms, and even within endosomes.[8,9] The oscillation between its oxidized and reduced states dictates a dynamic conformational dance, with an open configuration welcoming chaperone substrates and a closed state inhibiting their ingress during protein folding, thus substantiating its role as a master orchestrator of folding events.[3,6,10-12]] PDI's far-reaching impact transcends cellular boundaries, actively participating in the intricate tapestry of proliferation, survival, and metastasis within various cancers. [13-18] Anchoring itself within an array of cellular processes, including the hallmark Unfolded Protein Response (UPR) signaling and the orchestration of apoptosis, PDI emerges as a pivotal influencer within the choreography of cancer's physiological landscape.[17-19] In this unfolding scientific narrative, a diverse array of assays has emerged to monitor PDI's dynamic activity, a testament to its multifaceted nature.[20] However, within the realm of PDI sensing and detection, an intriguing void exists. Reports delineating the *in-vitro* or intracellular detection of PDI utilizing diagnostic probes remain strikingly scarce, beckoning for innovative exploration and the unveiling of untapped diagnostic frontiers.

Preceding to the previous subsection of chapter 3 (Chapter 3A), our investigative journey led us to harness the potent attributes of Fluorescent Organic Nanoparticles (FONPs) arising from both **TNINSH** and **NINSS** as tools for scrutinizing the redox dynamics of the PDI enzyme. This choice was ingeniously underpinned by the presence of thiol and disulfide functional groups intricately woven into the molecular architecture of the NI-derivatives; a

composition that stands poised to seamlessly interface with the oxidoreductase realm inhabited by PDI. Our hypothesis resonated with the potential to exploit the mechanism of thiol-disulfide exchange; a process ideally suited for potential interactions with PDI. In a controlled *in-vitro* milieu, the PDI enzyme orchestrates an intricate symphony of events, ranging from the oxidation of protein sulfhydryl groups to the reduction and isomerization of protein disulfide bonds. This complex interplay pivots on the dynamic redox state of the active-site cysteines, as elucidated in pertinent literature. Within this rich biochemical context, our focus was adeptly directed towards the emissive attributes inherent to the synthetically crafted **NINSS** and **TNINSH** FONPs.

Accordingly, in Chapter 3B, our dedicated attention converges with utmost precision upon probing the intricate behavior of PDI. The fluorescence characteristics inherent to **NINSS** and **TNINSH** FONPs were strategically harnessed to delve into the redox dynamics of PDI. The fluorescence intensity of **NINSS** FONPs experienced a discernible quenching effect in the presence of PDI, attributed to the reduction of disulfide bonds to thiols catalyzed by PDI. In stark contrast, **TNINSH** FONPs, which incorporated an ER-targeting N-tosylethylenediamine motif (referred to as 'T'), exhibited a remarkable augmentation in aggregation-induced emission (AIE) with a notable bathochromic shift in the fluorescence signal. This shift stemmed from the formation of disulfide linkages, facilitated by thiol oxidation induced by PDI. The prowess of **NINSS** and **TNINSH** FONPs as potent tools for AIE-based fluorometric sensing of PDI's oxidoreductase activity stood undeniable. With a remarkable detection limit encompassing ~12.6-17.7 ng/mL for **NINSS** and ~11.7-16.5 ng/mL for **TNINSH**, these biocompatible FONPs exhibited remarkable efficiency in discerning PDI's presence. Further, the distinctive attributes of these FONPs culminated in the successful and selective diagnosis of cancerous (B16F10) cells, effectively demarcating them from their non-cancerous counterparts (NIH3T3), a feat attributed to the overexpression of PDI within the cancer cell milieu. In essence, the tandem of **NINSS** and **TNINSH** FONPs emerges as a potent diagnostic duo, offering selective and sensitive analysis of PDI's redox state, ingeniously harnessed through their innate AIE phenomenon.

3B.2 RESULTS AND DISCUSSION

3B.2.1 PDI SENSING BY NINSS AND TNINSH FONPs.

Utilizing Fluorescent Organic Nanoparticles (FONPs) derived from **TNINSH** and **NINSS**, we probe the redox behavior of protein disulfide isomerase (PDI). Thiol and disulfide groups within these Naphthalimide-based constructs offer an avenue to sense PDI through thiol-disulfide exchange. PDI's multifaceted enzymatic activities, involving oxidation and reduction of sulfhydryl/disulfide bonds, find focus here. Employing synthesized FONPs, we leverage their emissive properties to scrutinize PDI's redox activity, aiming to establish them as sensitive and selective enzyme biomarkers in an innovative manner.

To this account, we attempted to detect PDI by **NINSS** and **TNINSH** FONPs prepared in 1:99 (v/v) DMSO-water. At first, PDI responsive experiments were carried out at pH 7.4 (10 mM phosphate buffer) using 25 μM of both FONPs. Upon addition of 10 ng/mL of PDI led to marginal decrease in emission intensity of **NINSS** FONPs at λ_{em} = 470 nm (Figure 1a). In case of **TNINSH** FONPs (25 μM), gradual inclusion of PDI firstly led to diminution in emission intensity at λ_{em} = 551 nm with concomitant generation of new fluorescence peak at λ_{em} = 625 nm (Figure 1c). Steady quenching of fluorescence intensity of **NINSS** FONPs was noted up to 75 ng/mL of PDI (Figure 1b). Quenching in fluorescence might have been taken place due to reduction of disulfide bond of **NINSS** by PDI to its thiol state (**NINSH**, Figure 2a). Further addition of PDI led to subsequent quenching of **NINSS** FONPs, which was however sporadic in nature in few instances (Figure 1a,b). On the other hand, PDI mediated oxidation of thiol present in **TNINSH** possibly led to the formation of disulfide comprising **TNINSS** (Figure 2c) that resulted in AIE at λ_{em} = 625 nm. This enrichment of fluorescence signal with a bathochromic shift might be attributed to this **TNINSS** formed upon oxidation of **TNINSH**. However, reducing emission intensity of **TNINSH** FONPs and increasing fluorescence intensity **TNINSS** were not in linearity with further increment in PDI concentration (Figure 1c,d). During enzymatic reduction of **NINSS** to **NINSH**, PDI also got converted to its oxidized form. Thus, beyond a critical concentration of PDI, amount of **NINSH** and oxidative form of PDI get enhanced during enzymatic reduction of **NINSS**. Subsequently, some amount of **NINSH** possibly got oxidized by the produced oxidative form of PDI to **NINSS** in a reversible manner (Figure 2a). Subsequently, irregular emission quenching was noted owing to the recovered AIE of reversely formed **NINSS** (Figure 1a,b, 2a). Similarly, during enzymatic oxidation of **TNINSH**

to **TNINSS**, conversion of PDI to its reduced state was also took place. Thus, amount of **TNINSS** and reduced form of PDI obviously will get increased beyond a critical concentration of PDI. Consequently, some quantity of **TNINSS** could be converted back to its monomeric form, **TNINSH** via reductive cleavage of disulfide by reduced form of PDI (Figure 2c). Hence, irregular emission quenching at λ_{em} = 551 nm and non-linear fluorescence enhancement at λ_{em} = 625 nm were observed owing to recovered AIE of reversely formed **TNINSH** (Figure 1c,d, 2c).

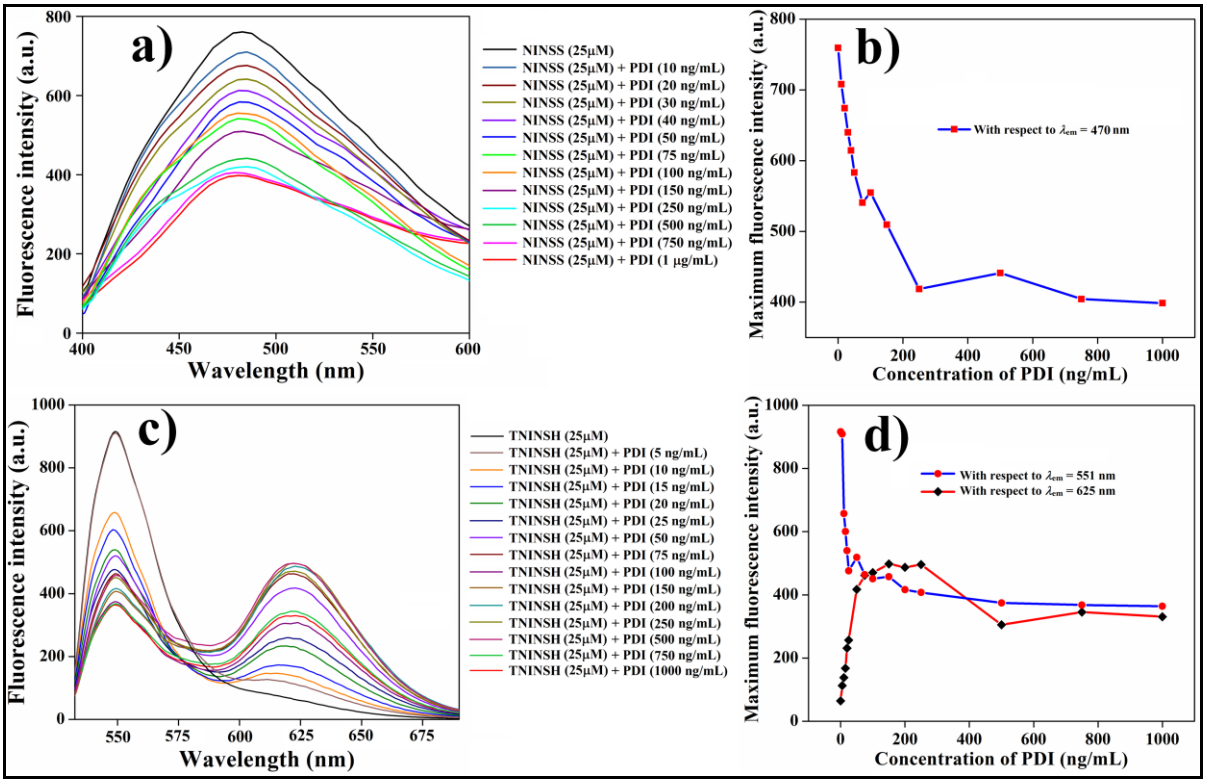

Figure 1. Fluorescence spectra of (a) **NINSS** FONPs (25 μM), (c) **TNINSH** FONPs (25 μM) in presence of PDI (without GSH and GSSG respectively) in (1:99, v/v) DMSO-PBS (pH = 7.4, 10 mM); Corresponding plot of maximum emission intensity of (b) **NINSS** FONPs (25 μM) (d) **TNINSH** FONPs (25 μM) vs PDI concentration (λ_{ex} = 350 nm).

These observations are in concurrence with that of the physiological system where disulfide gets reduced to dithiol and thiol gets oxidized to disulfide with concomitant formation of disulfide in PDI and dithiol containing PDI. To complete the catalytic cycle, reductants, such as glutathione (GSH), NADPH and dithiothreitol (DTT), serve as terminal electron donors to reduce disulfide in PDI back to its dithiol state and glutathione disulfide (GSSG) act as terminal electron acceptors to oxidize dithiol back to disulfide state.[8] Thereby, we carried out the same PDI sensing by **NINSS** and **TNINSH** FONPs in presence of GSH (25

μM) as reductant and GSSG (25 μM) as oxidant, respectively. Interestingly, fluorescence intensity of **NINSS** FONP steadily plummeted with increase in PDI concentration without any irregular changes in presence of GSH (Figure 3a,b).

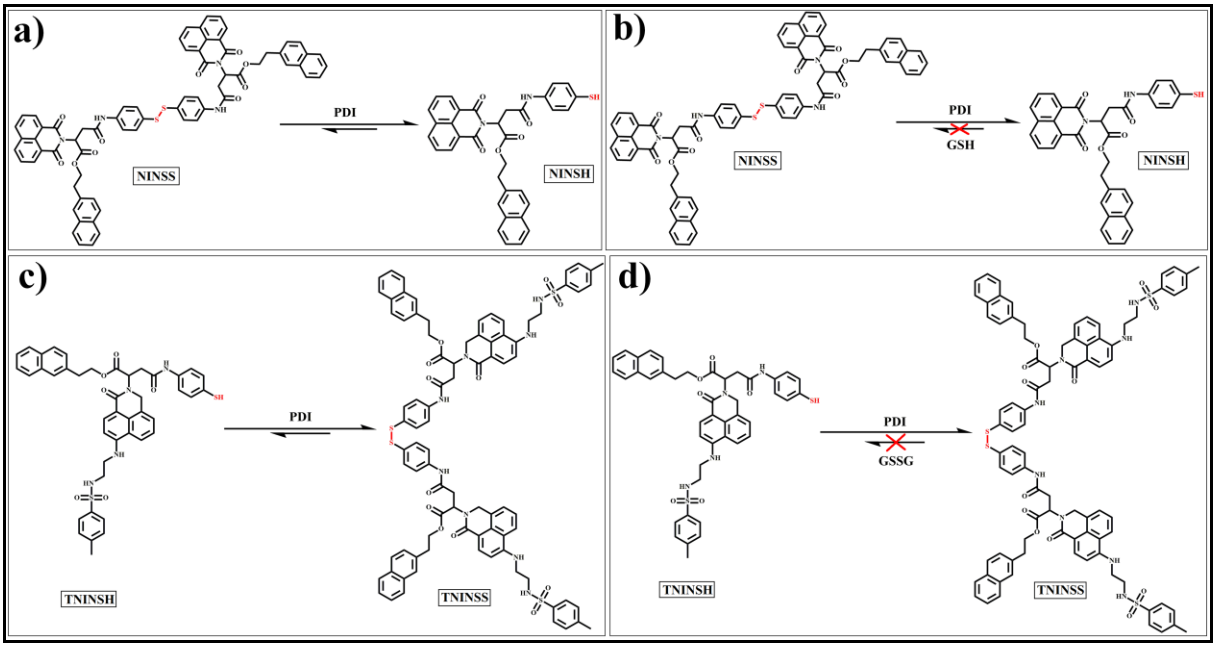

Figure 2. Possible mechanistic pathway for PDI sensing by **NINSS** FONPs (a) in absence of GSH and (b) in presence of GSH; Probable mechanistic pathway for PDI sensing by **TNINSH** FONPs (c) in absence of GSSG and (d) in presence of GSSG.

Similarly, steady decrease in emission intensity (λ_{em} = 551 nm) of **TNINSH** FONPs with simultaneous increase with red shifted fluorescence intensity at λ_{em} = 625 for **TNINSS** FONPs nm were observed upon gradual addition of 5-1000 ng/mL of PDI in presence of GSSG (Figure 3d,e). Considering the greater affinity of GSH or GSSG towards PDI, oxidative form of PDI will oxidize GSH over **NINSH** so that PDI gets back to its dithiol state and reduced form of PDI will reduce GSSG over **TNINSS** so that PDI gets back to its disulfide state. Thereby, oxidation of **NINSH** (reduced product of **NINSS**) could not take place predominantly in presence of GSH by oxidative form of PDI (Figure 2b). Consequently, steady drop in fluorescence intensity was witnessed for **NINSS** FONPs that gradually reached a plateau with further addition of PDI (1 μg/mL). Similarly, reduction of **TNINSS** by reduced form of PDI could not take place predominantly in presence of GSSG (Figure 2d). Marked decrease in emission intensity of **TNINSH** FONPs by PDI in presence of GSSG demonstrates complete oxidation of thiol bond of **TNINSH** by PDI to its dimeric disulfide state, **TNINSS** (Figure 2d, 3d). Thus, **TNINSH** AIE-gens

displayed sensitive "fluorescence-on" response towards PDI on account of "Dual AIE" characteristics of the oxidized product **TNINSS** FONPs.

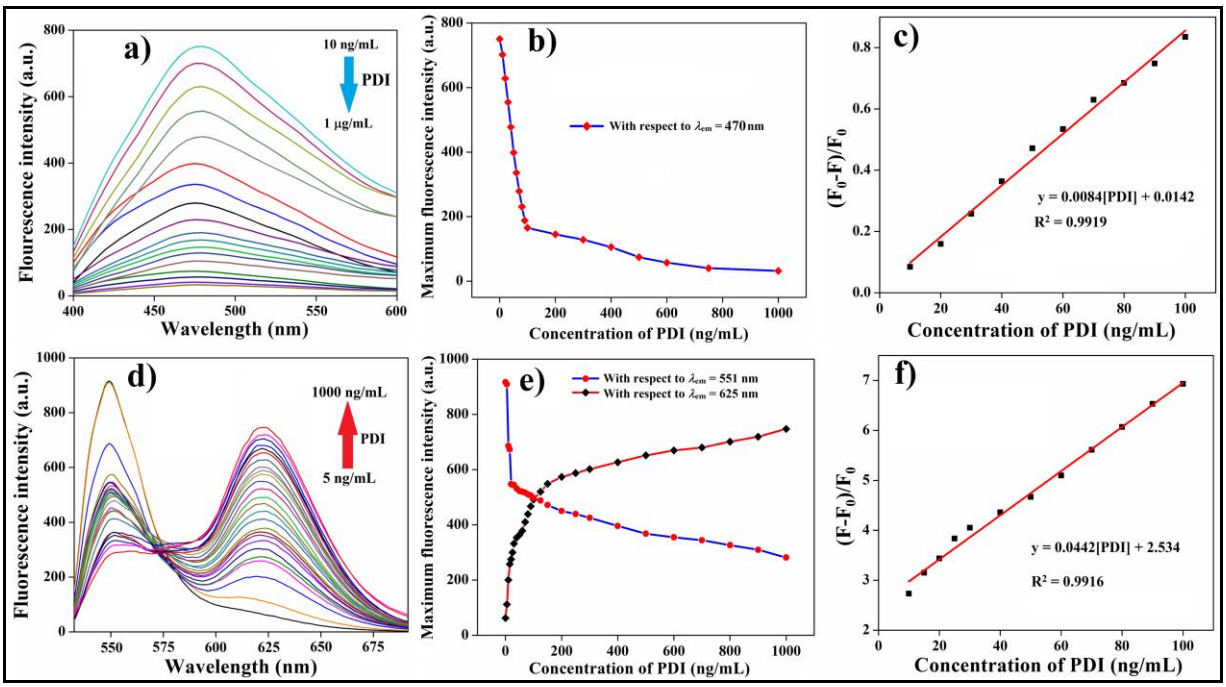

Figure 3. Fluorescence spectra of (a) **NINSS** FONPs (25 μM), (d) **TNINSH** FONPs (25 μM) in presence of PDI in (1:99, v/v) DMSO-PBS (pH = 7.4, 10 mM), [GSH] and [GSSG] = 25 μM; Plot of maximum emission intensity of (b) **NINSS** FONPs (2.5 μM), (e) **TNINSH** FONPs (5 μM) vs the PDI concentration; Fluorescence response of (c) **NINSS** FONPs (25 μM), (f) **TNINSS** (oxidized product of **TNINSH** FONPs) towards PDI sensing at f_w = 99 vol%, (l_{ex} = 350 nm).

After ensuring sensitive detection of PDI by **NINSS** and **TNINSH** FONPs, we used lower concentrations of both FONPs to minimize inner filter effects in fluorescence measurements. We performed the same PDI sensing experiment in presence of GSH (10 μM) and GSSG (10 μM), respectively using **NINSS** (2.5 μM) and **TNINSH** (5 μM) FONPs so that the optical density (OD)<0.1. Similar trend of plots was observed (Figure 4) as that was seen for 25 μM FONPs. In case of **NINSS** FONPs, quenching of fluorescence signal was noted due to formation of non-fluorescent monomer **NINSH** via reduction of **NINSS** by PDI whereas for **TNINSH** FONPs, enhancement of emission intensity (Dual-AIE) was observed due to formation of dimeric **TNINSS** via oxidation of **TNINSH** by PDI) as those witnessed in Figure 3. Thus, even at low concentrations, **NINSS** and **TNINSH** AIE-gens can serve as sensitive fluorometric probe PDI detection.

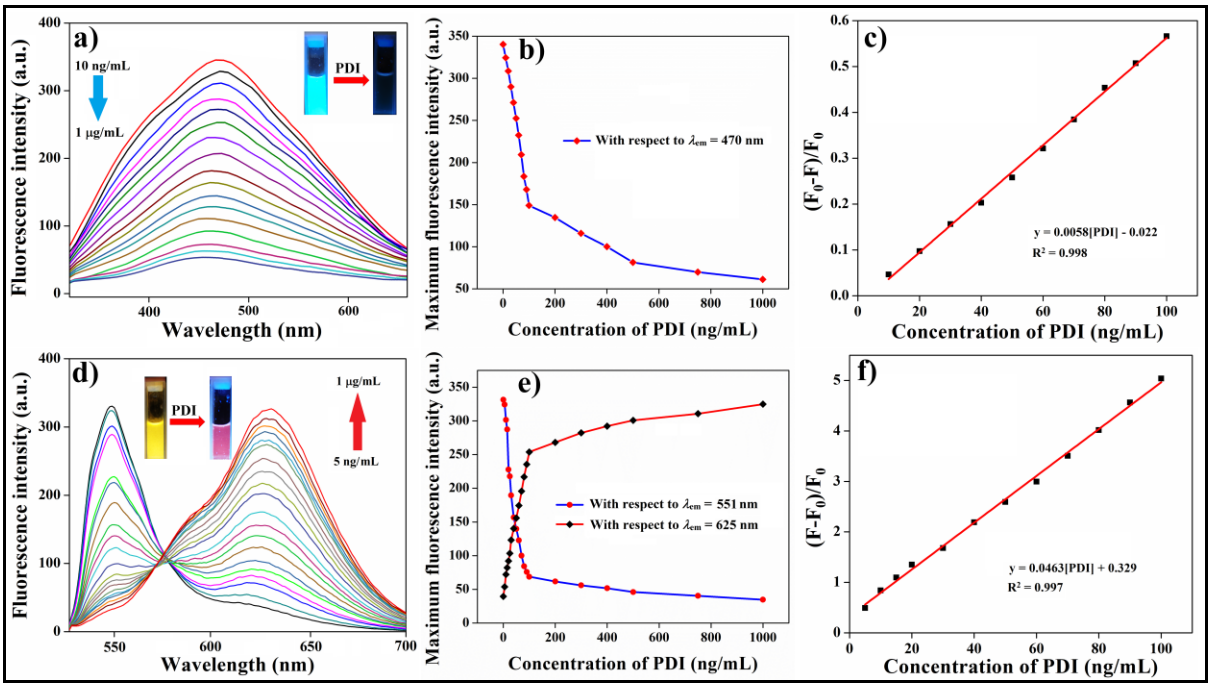

Figure 4. Fluorescence spectra of (a) **NINSS** FONPs (2.5 μM), (d) **TNINSH** FONPs (5 μM) in presence of PDI in (1:99, v/v) DMSO-PBS (pH = 7.4, 10 mM), [GSH] and [GSSG] = 10 μM; Plot of maximum emission intensity of (b) **NINSS** FONPs (2.5 μM), (e) **TNINSH** FONPs (5 μM) vs the PDI concentration; Fluorescence response of (c) **NINSS** FONPs (2.5 μM), (f) **TNINSS** (oxidized product of **TNINSH** FONPs) towards PDI sensing at f_w = 99 vol%, (l_{ex} = 350 nm).

To quantitatively determine the quenching of **NINSS** and enhancing of **TNINSS** emission with increasing PDI concentration, the Stern-Volmer equation is applied.

$$\frac{F}{F_0} = 1 + K_{SV}[Q] \qquad (1)$$

where F_o and F are fluorescence intensities of FONPs in absence and presence of PDI; K_{SV} is the Stern-Volmer constant, which denotes quenching efficiency of quencher; and [Q] is the concentration of quencher. Change in F/F_o of was plotted against PDI concentration from the respective fluorescence quenching or enhancement experiments in presence of GSH/GSSG at λ_{em} = 470 nm and 625 nm, respectively for varying concentrations (2.5 and 25 μM or 5.0 and 25 μM) of **NINSS** and **TNINSS** FONPs. The Stern-Volmer plot exhibited linear regression curve both in quenching of **NINSS** and in enhancing of **TNINSS** emissions (Figure 5). Subsequently, we quantified the limit of detection (LOD) of PDI in presence of both higher (25 μM) and lower concentration (2.5 μM for **NINSS** and 5 μM for **TNINSH**) FONPs at f_w = 99 vol%. Changes in

emission intensity were correlated to PDI concentration (0-100 ng/mL) using $(F_0-F)/F_0$, where F_0 and F were fluorescence intensities of **NINSS** FONPs at 470 nm and **TNINSS** FONPs at 625 nm in absence and presence of PDI (Figure 4c,f and 3c,f). LOD was calculated from the linear regression curve based on 3σ/S in triplicate experiment (σ = standard deviation and S = slope of the curve). The LOD values for PDI were in the range of ~12.6-17.7 ng mL^{-1} and ~11.7-16.5 ng mL^{-1} at high and low concentrations of **NINSS** and **TNINSH** FONPs, respectively suggesting superior sensitivity of both FONPs towards PDI sensing at different oxidative state.

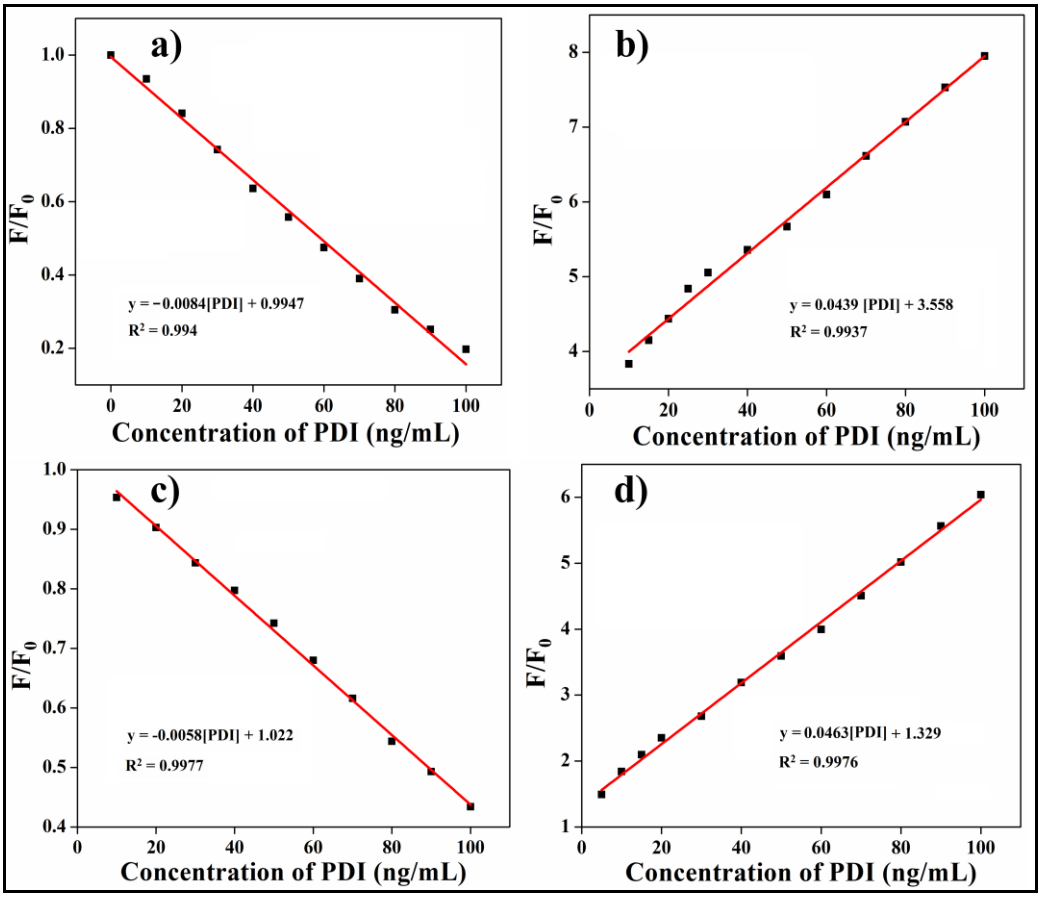

Figure 5. Stern-Volmer plots for quenching of emission intensity of **NINSS** FONPs having concentration (a) 25 μM and (c) 2.5 μM by PDI in (1:99, v/v) DMSO-PBS (pH = 7.4, 10 mM) solution; Stern-Volmer plots for enhancing of emission intensity of **TNINSS** (oxidized product of **TNINSH** FONPs) having concentration of **TNINSH** FONPs (b) 25 μM and (d) 5 μM by PDI in (1:99, v/v) DMSO-PBS (pH = 7.4, 10 mM) solution.

Enzymatic reduction of **NINSS** to **NINSH** and oxidation of **TNINSH** to **TNINSS** was also confirmed from the corresponding mass spectrometry (Figure 6).

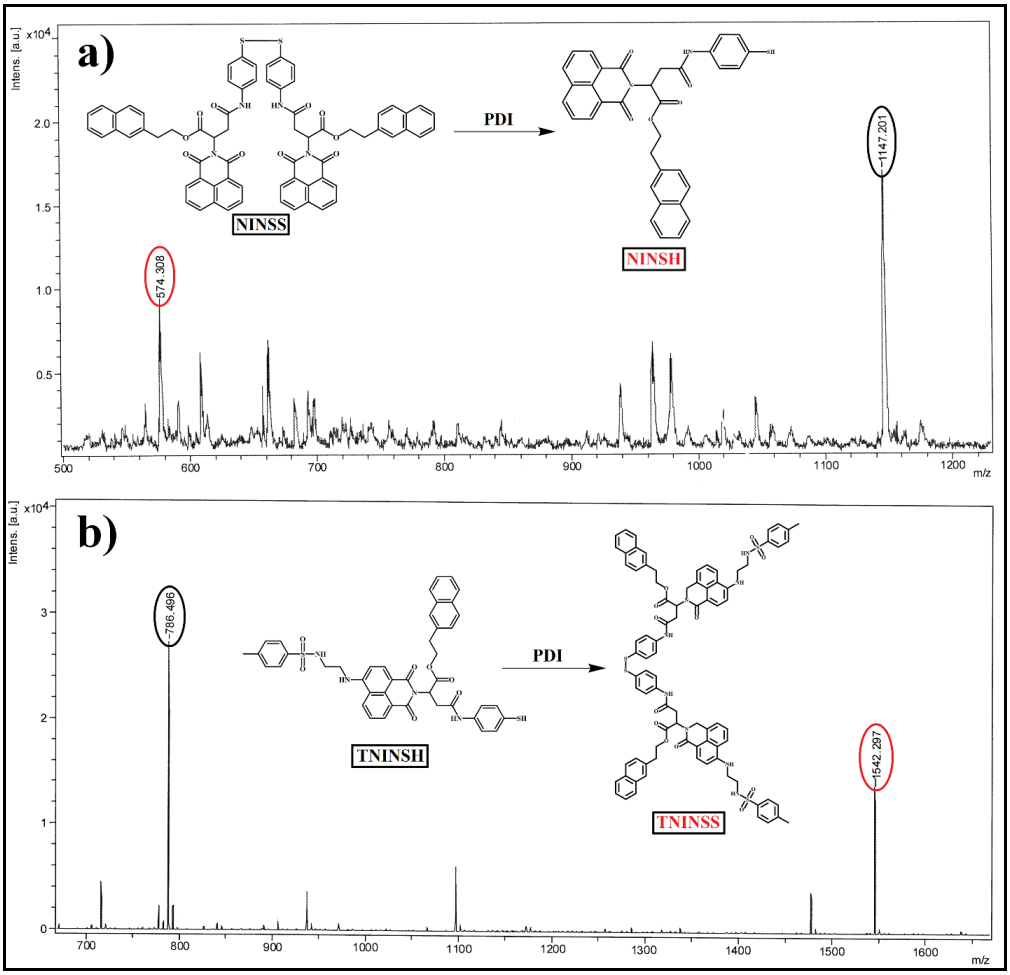

Figure 6. MALDI-TOF spectra of (a) reduction of **NINSS** into **NINSH** by PDI and (b) oxidation of **TNINSH** into **TNINSS** by PDI.

Quenching of **NINSS** emission due to formation of **NINSH** and enhancement in fluorescence intensity of red shifted excimer peak (λ_{em} = 625 nm) due to formation of **TNINSS** by PDI were in accordance with the aggregation pattern and spectroscopic behavior of separately synthesized **NINSH** and **TNINSS** (Figure 7). Quenching in blue emission of **NINSS** FONP by PDI was also evident in the respective solution (in cuvette) under UV-light exposure (λ_{ex} = 365 nm, inset Figure 4a). Similarly, "Dual AIE" effect has been reflected in the corresponding UV irradiated (λ_{ex} = 365 nm) cuvette that showed yellow to light red transition in emission color due to quenching of **TNINSH** emission with enhancement in emission for **TNINSS** (inset, Figure 4d). Hence, both reductive and oxidative form of PDI can be successfully detected with high sensitivity simply by "fluorescence off/on" technique due to noteworthy

sensitivity of **NINSS** FONPs and **TNINSH/TNINSS** FONPs through thiol-disulfide redox exchange.

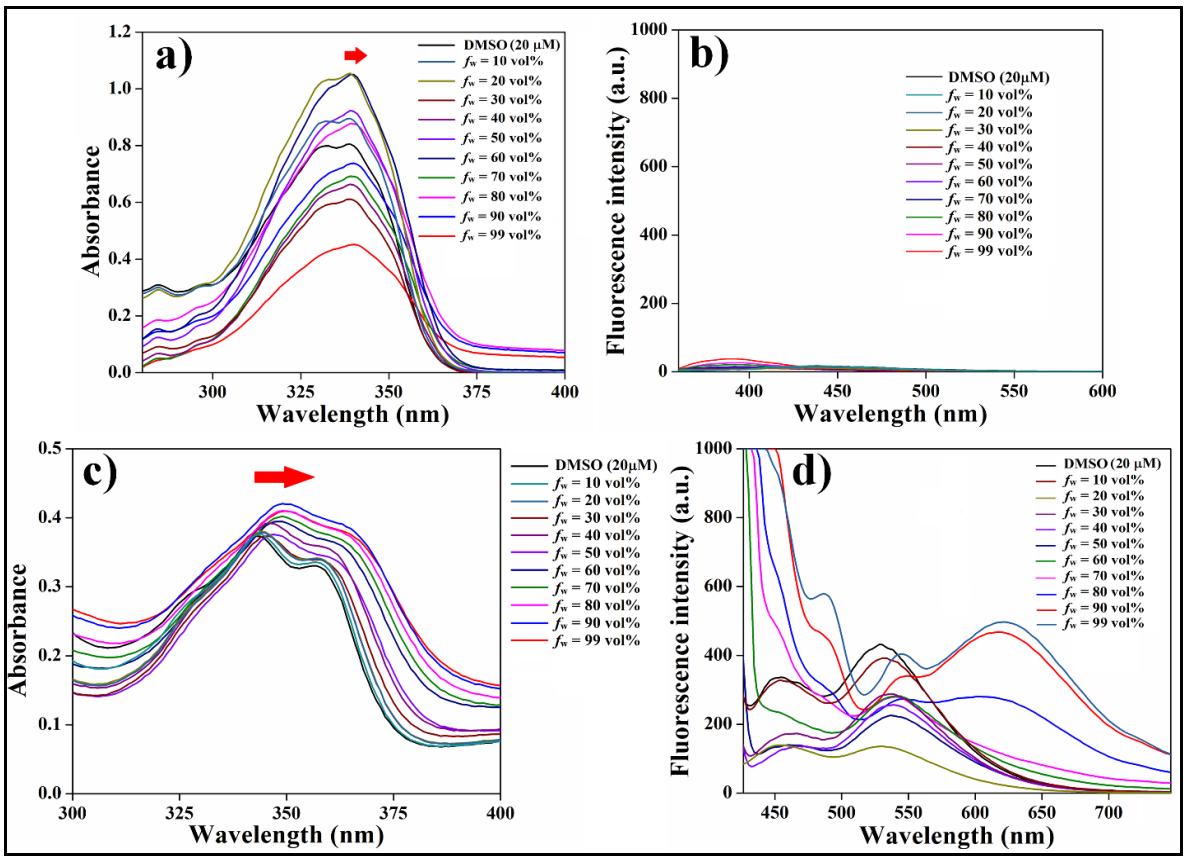

Figure 7. UV-visible spectra of (a) **NINSH** (20 μM), (b) **TNINSS** (20 μM) in varying DMSO-water solvent mixtures; Fluorescence spectra (λ_{ex} = 350 nm) of (c) **NINSH** (20 μM) and (d) **TNINSS** (20 μM) in DMSO-water solvent mixture.

Microscopic characterization of **NINSS** and **TNINSH** FONPs in presence of PDI showed that dimension of resulting mixture of FONPs and PDI (~100-130 nm) were marginally increased by ~20-30 nm which might be attributed to the generation of **NINSH** and **TNINSS** upon reduction and oxidation by PDI, respectively (Figure 8). The zeta potential values of native **NINSS** and **TNINSH** FONPs were -24.66 mV and -34.91 mV, respectively, which confirms their adequate stability (Table 1). Notably, zeta potential of the mixture containing **NINSS/TNINSH** and PDI were found to be -19.63 and -16.29 mV, respectively (Table 1), which further indicates the ample stability of the resulting mixture without any significant changes in its characteristics.

Table 1. Zeta potential values of **NINSS** and **TNINSH** FONPs in absence and presence of PDI.

Solution	Zeta-potential (ζ) (mV)
NINSS	-26.66
TNINSH	-34.91
NINSS + PDI	-19.63
TNINSH + PDI	-16.29

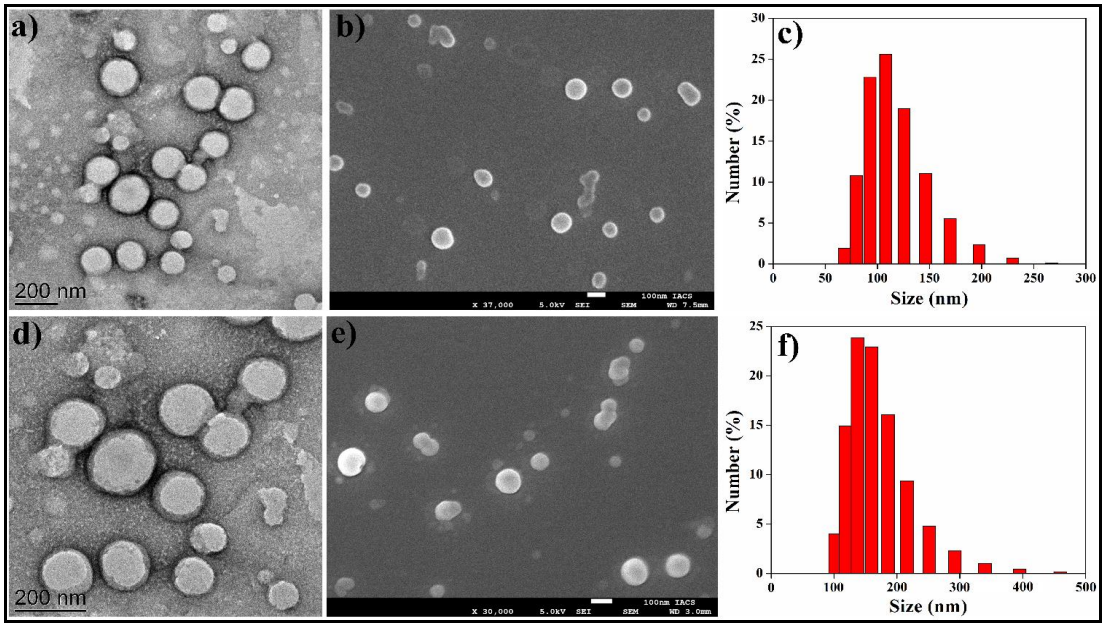

Figure 8. UV-visible spectra of (a) **NINSH** (20 μM), (b) **TNINSS** (20 μM) in varying DMSO-water solvent mixtures; Fluorescence spectra (λ_{ex} = 350 nm) of (c) **NINSH** (20 μM) and (d) **TNINSS** (20 μM) in DMSO-water solvent mixture.

To substantiate the pivotal role of glutathione (GSH) as a catalyst in harnessing the reproducibility of Protein Disulfide Isomerase's (PDI) reductive attributes, we engaged in a fluorescence-based exploration. The fluorescence intensity of synthesized **NINSH** was measured in the presence of introduced PDI, revealing an intriguing enhancement in emission. This augmentation was attributed to the formation of **NINSS** dimers via the oxidation of **NINSH** by PDI. Conversely, when GSH was introduced, the emission intensity remained relatively unchanged, indicative of GSH's swift binding with PDI, rendering it less available for oxidizing **NINSH** into **NINSS** (Figure 9a). This interaction diverted the enzymatic pathway,

preventing the reversion of **NINSS** back to its monomeric form due to GSH's heightened reactivity with PDI. A parallel investigation involving synthesized **TNINSS**, PDI, and GSSG (oxidized GSH) was conducted. Fluorescence intensity of **TNINSS** was found to diminish with the gradual addition of PDI, resulting in the emergence of a new emission peak at 551 nm (Figure 9b). This phenomenon was attributed to the formation of **TNINSH** monomers through PDI-mediated reduction of **TNINSS**. In contrast, the addition of GSSG exhibited a minor impact on the reduction of emission intensity, attributed to GSSG's robust interaction with reduced PDI, diminishing its availability for reducing **TNINSS**. Consequently, the formation of **TNINSH** was hindered due to GSSG's higher reactivity with PDI than **TNINSS**, substantiating its role in driving the oxidative pathway, promoting PDI's disulfide state. This comprehensive exploration underscores the pivotal roles of GSH and GSSG in inducing and modulating PDI's reproducible reductive and oxidative attributes, offering a refined understanding of PDI's intricate redox dynamics.

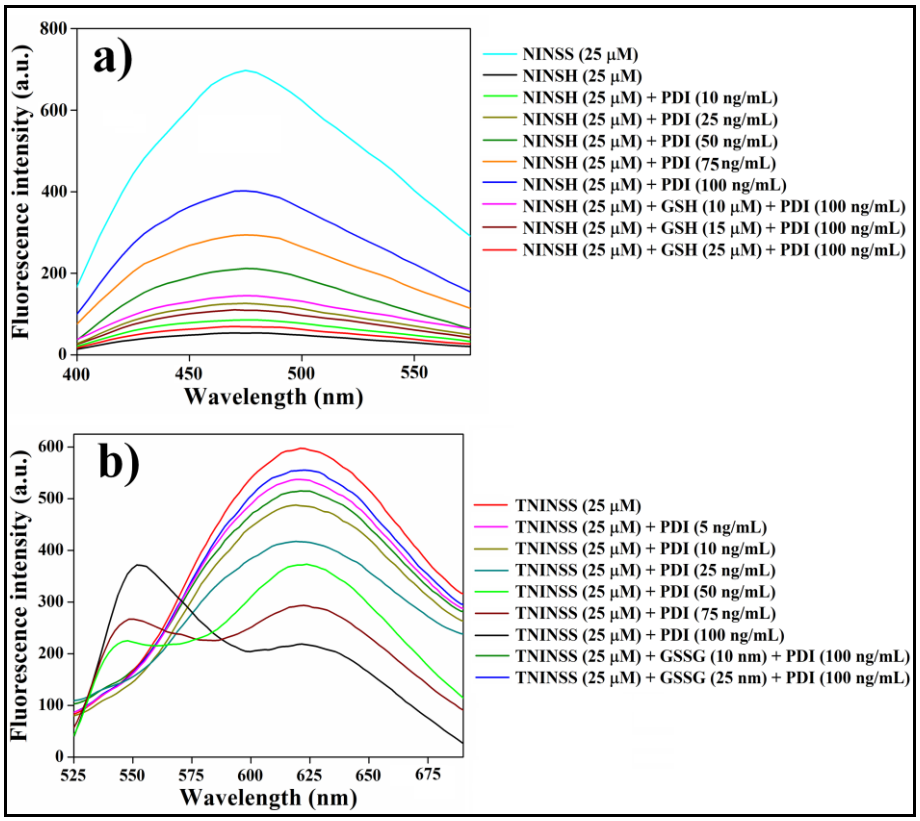

Figure 9. Fluorescence spectra of (a) **NINSH** (25 μM) in presence of different concentration of PDI and GSH and (b) **TNINSS** (25 μM) in presence of varying concentration of PDI and GSSG in (1:99, v/v) DMSO–PBS (pH = 7.4, 10 mM) solution;(excitation wavelength = 350 nm).

To affirm the reduction ability of PDI on **NINSS**, we investigated the effect of rutin on PDI activity by utilizing fluorescence property of **NINSS** and **TNINSH** FONPs. Rutin (quercetin-3-O-rutinoside or vitamin P) is a specific and reversible inhibitor of PDI with IC_{50} at micromolar range.[21-23] Emission spectra of the mixture of **NINSS** FONPs (25 μM) and 100 ng/mL PDI were recorded in presence of varying amount of rutin (Figure 10a). Emission of **NINSS** FONPs (f_w = 99 vol%) obviously got quenched in presence of PDI. Interestingly, in presence of increasing content of rutin (10-100 μM) into this mixture of **NINSS** FONPs and PDI, emission of AIE-gen got recovered almost to its native state (Figure 10a). Binding of rutin to PDI led to inhibition of its reduction ability of **NINSS** to **NINSH** that led to regaining of **NINSS** FONP's fluorescence intensity. However, emission nature of **TNINSH** FONPs remain unaltered in presence of rutin in mixture of 25 μM **TNINSH** AIE-gen (f_w = 99 vol%) and PDI (200 ng/mL) (Figure 10b). The "Dual-AIE" effect due to appearance of **TNINSS** by PDI oxidation of **TNINSH** was not affected in presence of rutin. This observation established the selective PDI reductase activity on **NINSS**.

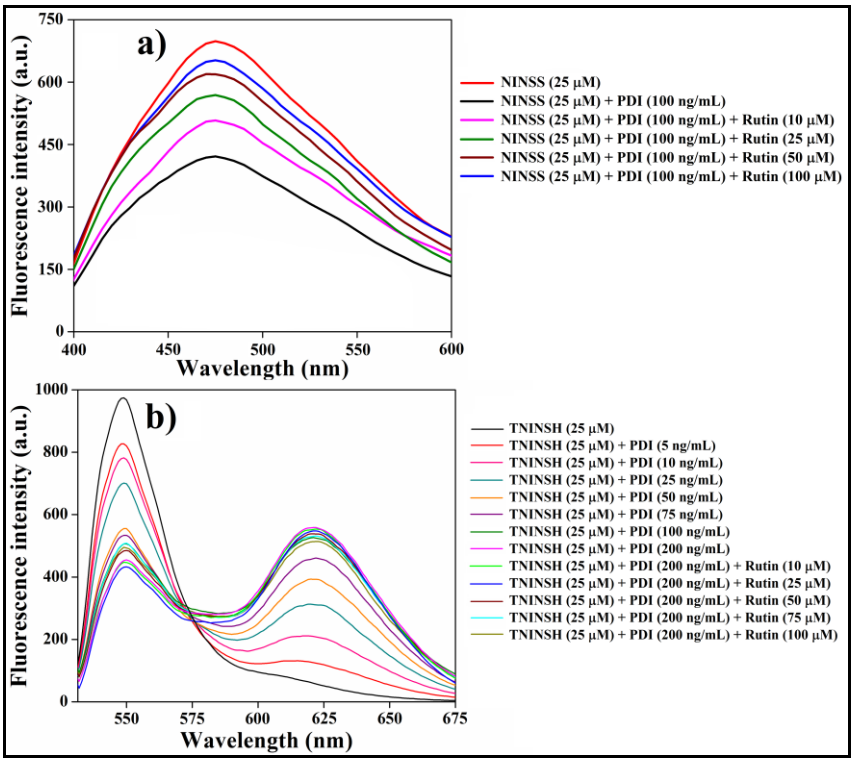

Figure 10. Fluorescence spectra of (a) **NINSS** FONPs (25 μM) and (b) **TNINSH** FONPs (25 μM) in presence of different concentration of PDI and rutin in (1:99, v/v) DMSO-PBS (pH = 7.4, 10 mM) solution; (excitation wavelength = 350 nm).

Anti-interference is one of the crucial pre-requisites for any fluorometric sensor. To ascertain the specificity of newly developed AIE-sensors towards PDI, a number of other enzymes and proteins were also examined through fluorescence sensing using **NINSS** and **TNINSH** FONPs. Solutions of several interference species including GOx, HRP, SOD, Lys, Cytc, BSA and Hb each at 1 μg/mL in presence and absence of 100 ng/mL PDI were examined for studying their interference in PDI sensing. Both **NINSS** and **TNINSH** FONPs did not give any notable fluorometric response even at 10 times higher concentration of interference species with respect to PDI (Figure 11). Importantly, the AIE-gens still displayed strong fluorescence response upon subsequent PDI addition in those interfering species containing solutions, which demonstrates the high sensitivity and selectivity of **NINSS** and **TNINSH** FONPs as PDI sensor.

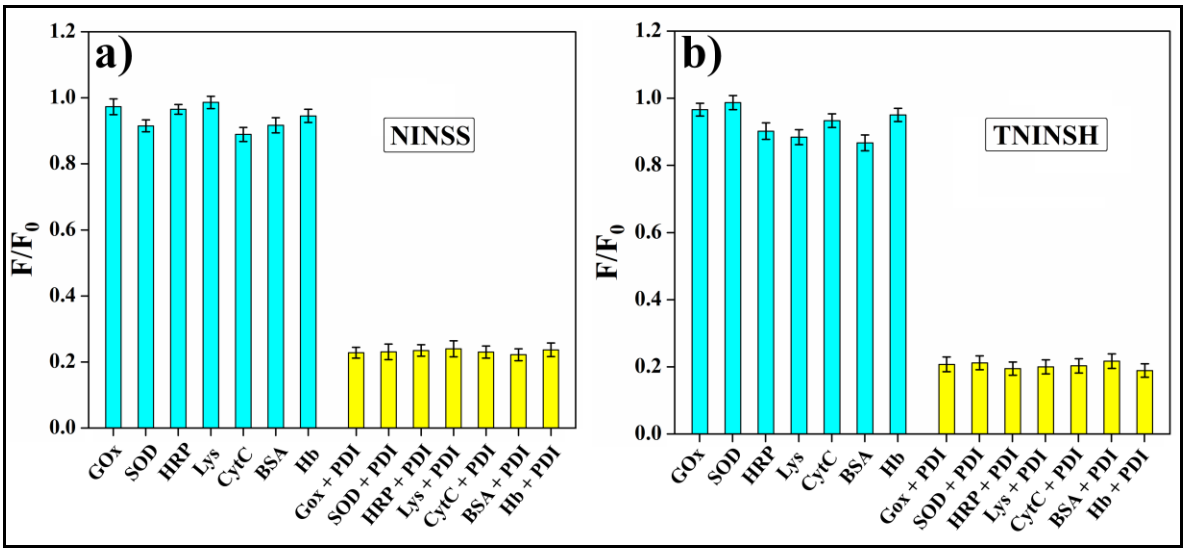

Figure 11. Anti-interference study of (a) **NINSS** FONPs and (b) **TNINSH** FONPs ([**NINSS**/**TNINSH**] = 25 μM) to PDI (100 ng/mL) over other biomolecules (1 μg/mL) in (1:99, v/v) DMSO-phosphate buffer saline (pH = 7.4, 10 mM) solution. The error bars represent the standard deviations.

3B.2.2 MEDIA STABILITY AND CYTOCOMPATIBILITY OF NINSS AND TNINSH FONPs.

After successful sensing of PDI *in-vitro*, we aimed to explore these FONPs in analyzing redox behavior of PDI inside cellular environment. Prior to that we examined (i) time dependent media stability in biological milieu and (ii) cytocompatibility of **NINSS** and **TNINSH** FONPs against eukaryotic cells. Both FONPs (25 μM) were added in FBS-DMEM

media having FBS from 0 to 75% for 48 h (Figure 12). The extended stability of FONPs was also studied by keeping mixtures of FONPs (100 μM)-FBS (10%)-DMEM media for 10 days (Figure 12a,c). In both cases, media stability of **NINSS** and **TNINSH** FONPs was ~ 80-85%, which was also in agreement with the respective visual images (Figure 12b,d).

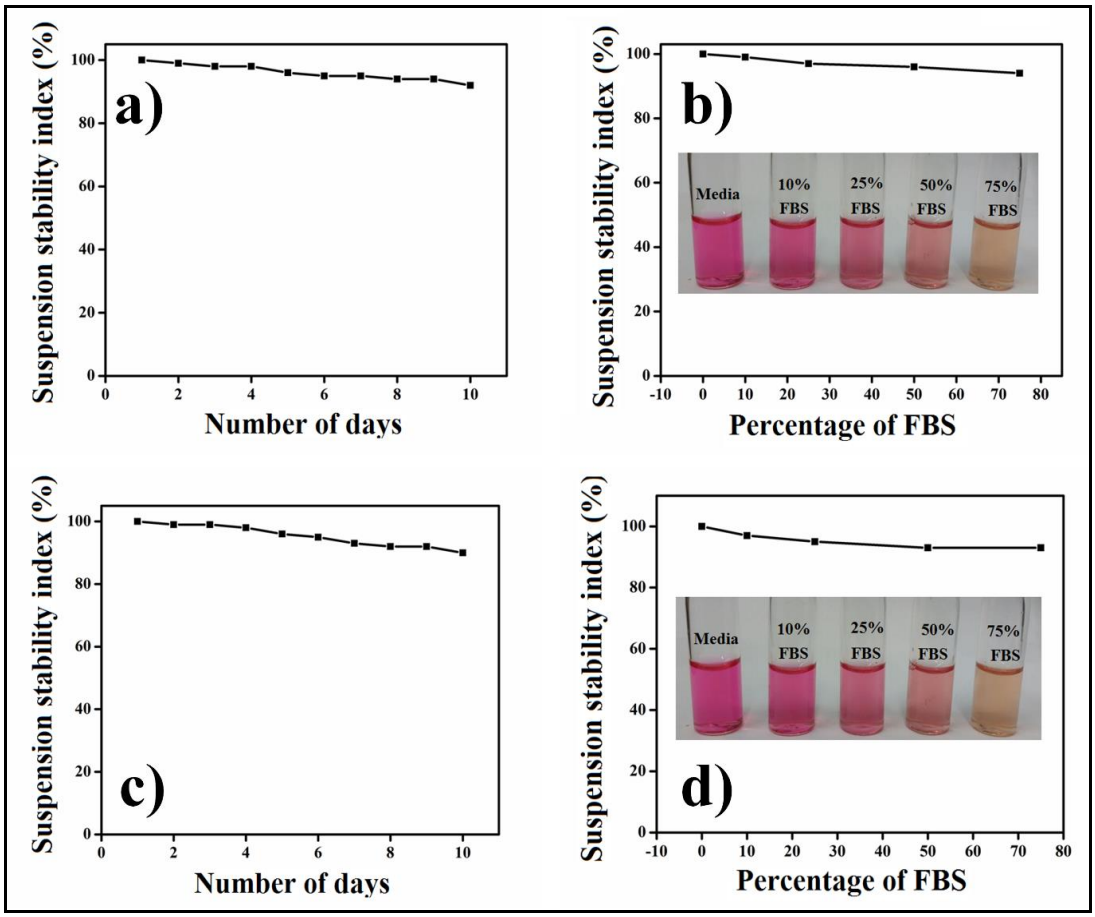

Figure 12. Suspension stability index of **NINSS** FONPs and **TNINSH** FONPs (100 μM) (prepared in 1:99 (v/v) DMSO-water) in (a), (c) DMEM media supplemented with different percentage of FBS (0-75%) and (b), (d) DMEM media supplemented with 10% of FBS over the 10 days incubation respectively.

The octanol-water partition coefficient (log P) value of **NINSS** and **TNINSH** FONPs were found to be 1.56 and 1.37, respectively (determined using calibration curve of **NINSS** and **TNINSH** FONPs) suggesting higher lipophilicity (log P>1), which can enhance their ability to permeate cell membranes (Figure 13). Cytocompatibility of both **NINSS** and **TNINSH** FONPs (f_w = 99 vol%) was investigated by MTT experiment in non-cancerous NIH3T3 and melanoma B16F10 cells. Around ~84-87% and ~80-83% cells were viable after incubation with varying

concentrations (5-100 μM) of FONPs for 24 h (Figure 14). Therefore, **NINSS** and **TNINSH** FONPs having substantial stability in biological milieu and cytocompatibility could be exploited for bioimaging and therapeutic applications.

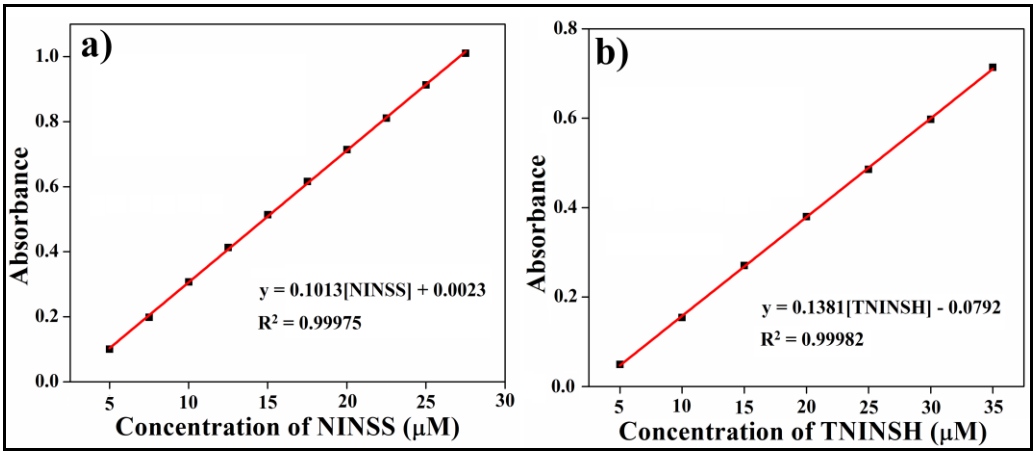

Figure 13. Calibration curve of (a) **NINSS** and (b) **TNINSH** FONPs.

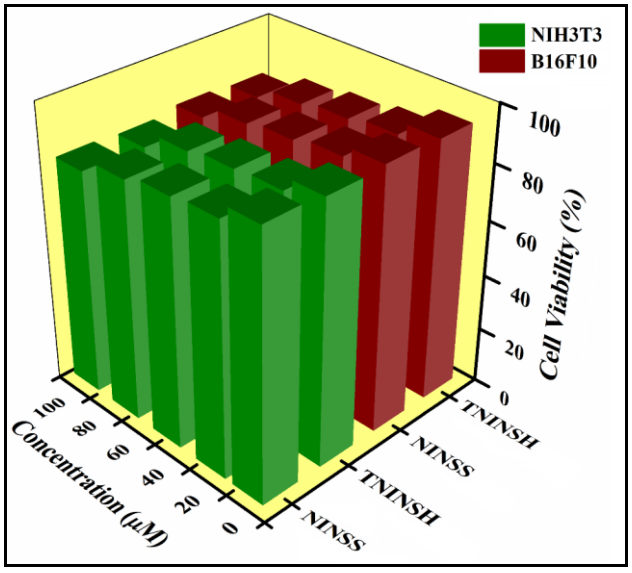

Figure 14. MTT-based % cell viability of NIH3T3 and B16F10 in presence of varying concentration of FONPs derived from **NINSS** and **TNINSH** in 1:99 v/v, DMSO-water over 24 h incubation period. Percent errors are within ± 3% in triplicate experiments.

3B.2.3 CELLULAR IMAGING

NINSS and **TNINSH** FONPs (25 μM, f_w = 99 vol%) were incubated separately with NIH3T3 and B16F10 cells for 12-24 h. Cellular uptake of FONPs was evaluated by fluorescence microscopy.

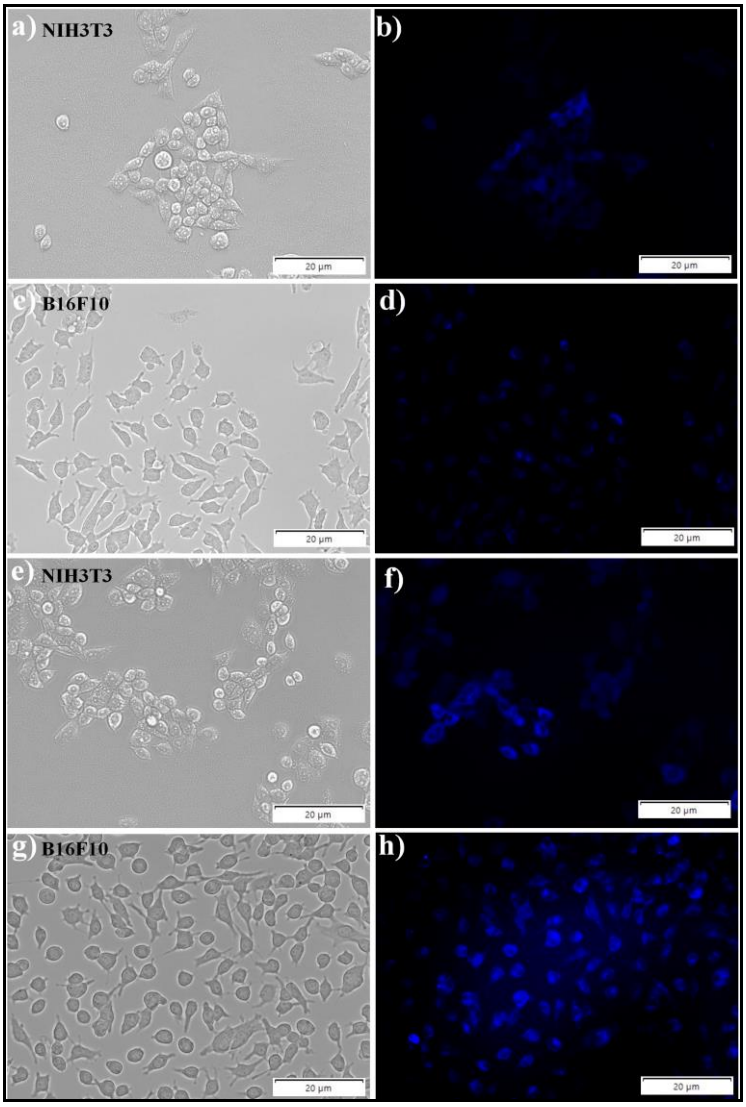

Figure 15. Bright-field and fluorescence microscopic images of (a,b) NIH3T3 cells, (c,d) B16F10 cells after 12 h incubation with **NINSS** FONPs (25 µM) in (1:99, v/v) DMSO-PBS (pH = 7.4, 10 mM); Bright-field and fluorescence microscopic images of (e,f) NIH3T3 cells, (g,h) B16F10 cells after 12 h incubation with **NINSS** FONPs (25 µM) and rutin (25 µM) in (1:99, v/v) DMSO-PBS (pH = 7.4, 10 mM). Scale bars correspond to 20 µm.

In case of **NINSS** FONPs, weak blue fluorescence was noted after 12 h incubation (Figure 15a-d), which got significantly quenched after 24 h (Figure 16a-c,d-f) inside both NIH3T3 and B16F10 cells. Quenching of weak blue emission with time confirms reduction of internalized **NINSS** FONPs by PDI as reductase in cell surface and cytoplasm to its non-fluorescent monomer (**NINSH**). This observation was in accordance with *in-vitro* studies (Figure 1a,b, 3a,b, 4a,b). Cancer cells necessitate over-expressed PDI to encounter ER stress and

surge in protein synthesis to endure rapid proliferation.[19,23,24] Considering the overexpression of PDI in melanoma cells, quenching effect was more prominent in B16F10 than that of NIH3T3 (non-cancerous) cells, which was evident from the corresponding flow cytometry data (Figure 16c,f). Mean fluorescence intensity of **NINSS** FONPs after 24 h incubation was very low, 189 and 47 for NIH3T3 and B16F10 cells, respectively (Figure 16c,f). Hence, intracellular PDI can be sensed through its reductive action from "fluorescence off" mechanism of **NINSS** FONPs (Scheme 1).

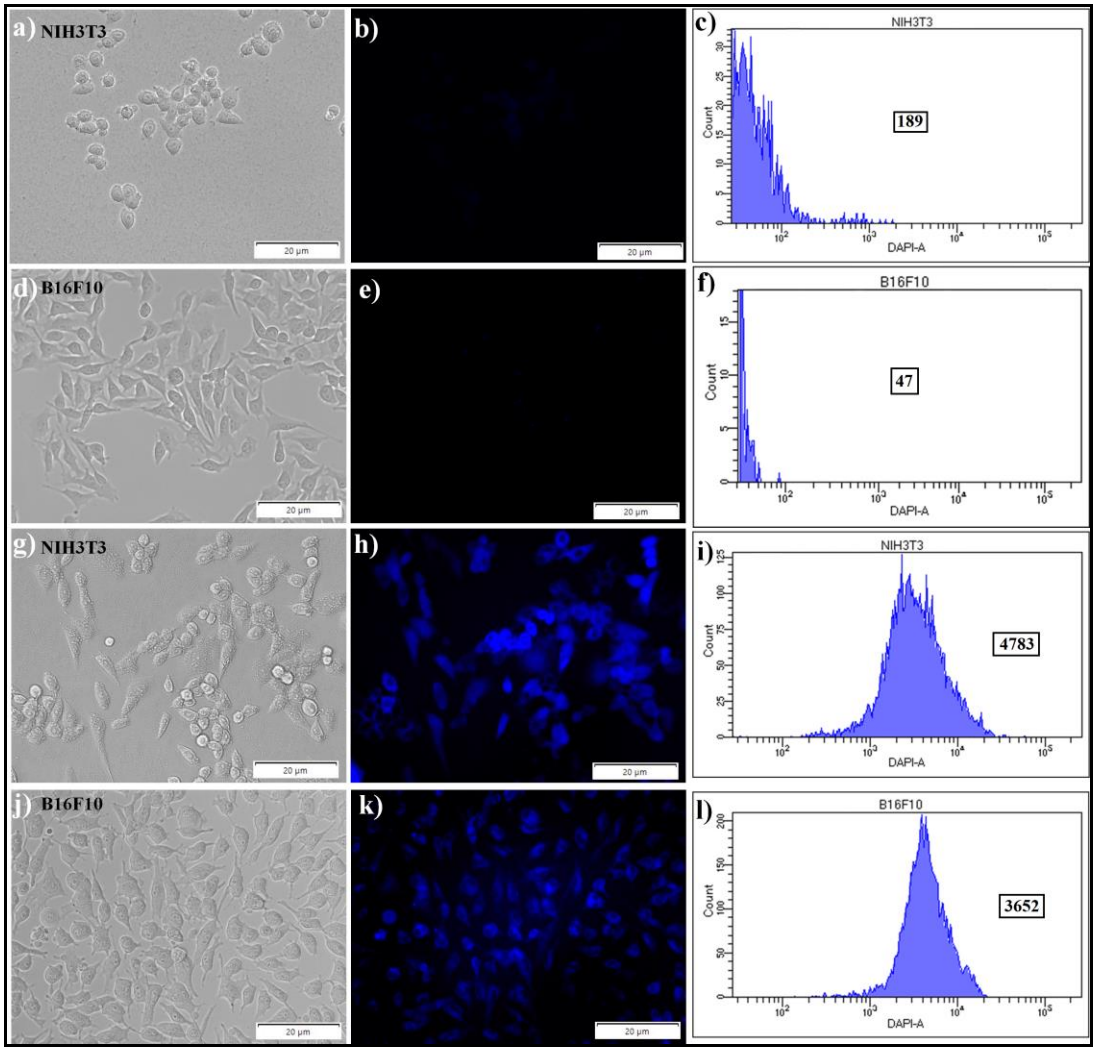

Figure 16. Bright-field, fluorescence microscopic image and flow cytometry data of (a-c) NIH3T3 cells, (d-f) B16F10 cells after 24 h incubation with **NINSS** FONPs (25 µM) in (1:99, v/v) DMSO-PBS (pH = 7.4, 10 mM); after 24 h incubation with **NINSS** FONPs (25 µM) and rutin (25 µM) for (g-i) NIH3T3 cells, (j-l) B16F10 cells in (1:99, v/v) DMSO-PBS (pH = 7.4, 10 mM). Scale bars correspond to 20 µm.

To further corroborate cellular internalization, a mixed solution of **NINSS** FONPs (25 μM, f_w = 99 vol%) and rutin (25 μM) was incubated for 12-24 h separately with NIH3T3 and B16F10 cells. Fluorescence intensity of **NINSS** FONPs was markedly high after 12 h incubation (Figure 15e-h). After 24 h incubation, this high emission of **NINSS** FONPs got remarkably intensified inside the cells with the mean fluorescence intensity of 4783 and 3652 for NIH3T3 and B16F10, respectively (Figure 16h,i,k,l). Rutin has greater specificity to bind with PDI and inhibit its reductase activity.[21-23] Subsequently, reduction of **NINSS** FONPs by PDI got substantially decreased in presence of rutin. A greater number of **NINSS** FONPs internalized within NIH3T3 and B16F10 cells exhibited significantly high fluorescence intensity (Figure 15e-h, 16g-l), which was in concurrence with *in-vitro* study (Figure 10). Reduction of disulfide bond in **NINSS** FONPs by PDI was very selective as it did not take place in presence of rutin by other thiol isomerases.[24] Thus, **NINSS** FONPs successfully emerged as a sensitive and selective PDI (reductase form) responsive cellular biomarker.

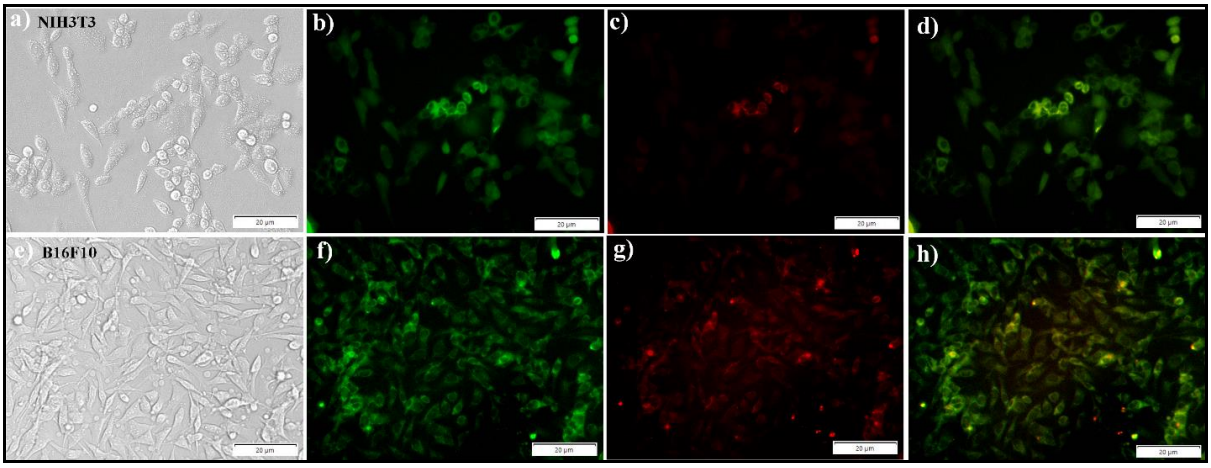

Figure 17. Bright-field, fluorescence microscopic image in green filter, red filter and corresponding overlay image for (a-d) NIH3T3 cells, (e-h) B16F10 cells after 12 h incubation with **TNINSH** FONPs in (1:99, v/v) DMSO-PBS (pH = 7.4, 10 mM) where [**TNINSH**] = 25 μM; Scale bars correspond to 20 μm.

PDI as oxidase in the ER, form disulfide bonds in nascent secretory proteins. To substantiate the role of PDI inside ER, **TNINSH** FONPs (25 μM, f_w = 99 vol%) was incubated with NIH3T3 and B16F10 cell for 12-24 h. Both green (FITC) and red (TRITC) filter were used to record fluorescence microscopic images of cells. Notable fluorescence intensity of **TNINSH** FONPs was witnessed in green filter (Figure 17b,f) inside both cells after 12 h incubation.

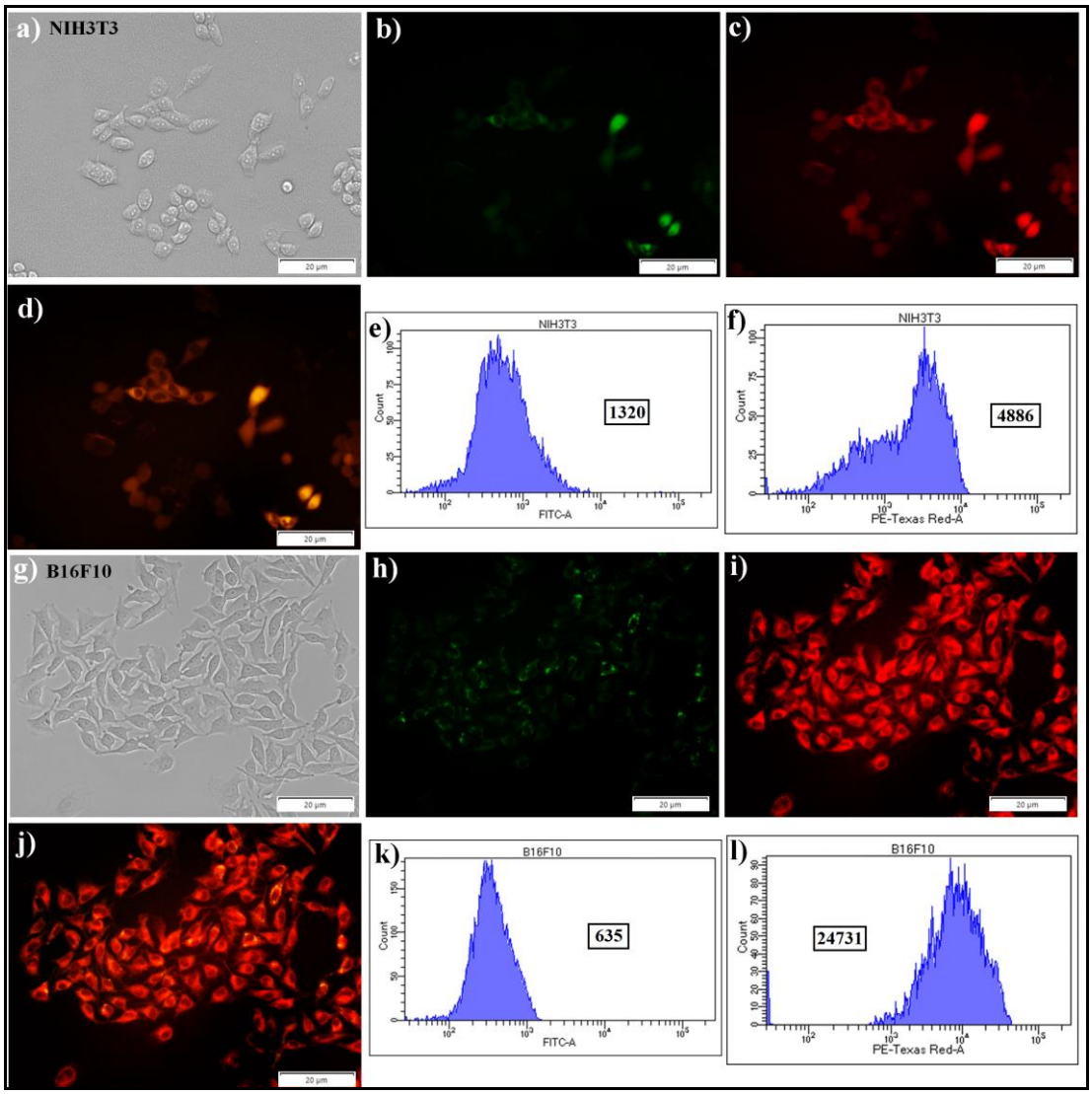

Figure 18. Bright-field, fluorescence microscopic image in green filter and red filter (a-c) NIH3T3 cells after 24 h incubation with **TNINSH** FONPs (1:99, v/v) DMSO-PBS (pH = 7.4, 10 mM), (d) corresponding overlay image of (b) and (c), and flow cytometry plot (e) of (b) and (f) of (c); [**TNINSH**] = 25 μM; after 24 h incubation with **TNINSH** FONPs (g-i) for B16F10 cells where [**TNINSH**] = 25 μM (j) corresponding overlay image of (i) and (j), and flow cytometry plot (k) of (i) and (l) of (j). Mean fluorescence intensity was mentioned in inset of (e), (f), (k) and (l); Scale bars correspond to 20 μm.

Moreover, feeble red fluorescence was observed for both cells under red filter (Figure 17c,g). After 24 h incubation, green emission of **TNINSH** FONPs got remarkably quenched (Figure 18b,h), while red emission got significantly intensified (Figure 18c,i). Enhanced red fluorescence suggests that **TNINSH** FONPs containing N-tosylethylenediamine moiety got

internalized inside ER of the cells where PDI oxidized thiol group of **TNINSH** into disulfide to form its dimer (**TNINSS**) and displayed enhanced emission. "Dual-AIE" phenomena was observed inside cells similar to that was found *in-vitro* studies (Figure 1c,d, 2d,e 4d,e). For NIH3T3 cells, mean fluorescence intensities of **TNINSH** FONPs were found to be 1320 in green filter and 4886 in red filter whereas the same for B16F10 cells were 635 and 24731, respectively. The decrease in green emission (Figure 18e,k) and enhancement in red emission (Figure 18f,l) were significant in case of B16F10 than NIH3T3 cells due to the over-expression of PDI in cancer cells. Thus, newly developed **TNINSH** FONPs comprising of ER targeting motif, successfully emerged as a selective targeted biomarker towards PDI enriched cancer cells (B16F10) through oxidative behavior of PDI in ER (Scheme 1).

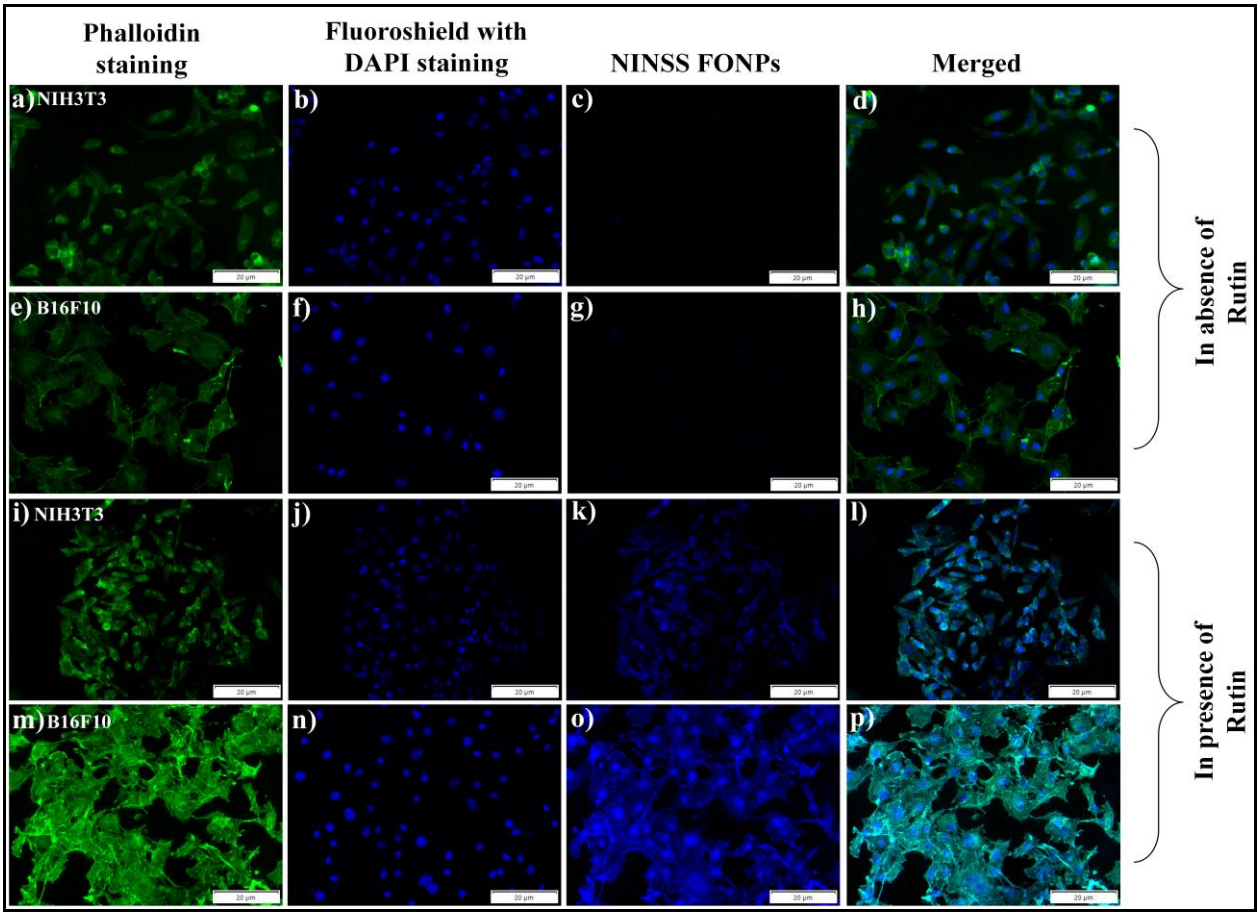

Figure 19. Fluorescence microscopic images of cells with Phalloidin cytoplasm staining along with Fluoroshield with DAPI nuclei staining. (a-d) NIH3T3 cells and (e-h) B16F10 cells incubated with [**NINSS**] FONPs = 25 μM; (i-l) NIH3T3 cells and (m-p) B16F10 cells incubated with [**NINSS**] FONPs = 25 μM and [rutin] = 25 μM; Scale bars correspond to 20 μm.

Next, colocalization study was performed through staining of cytoskeleton along with nuclei to know the distribution of the FONPs within NIH3T3 and B16F10 cells (Figure 19, 20). Emission intensity of **NINSS** FONPs got quenched in 24 h by PDI and only the color of Phalloidin-stained cytoplasm (green) and DAPI-stained nuclei (blue) were observed. Interestingly, in presence of rutin (PDI reductase inhibitor), blue fluorescence of **NINSS** FONPs inside both cells were distinct along with Phalloidin-stained cytoplasm and DAPI-stained nuclei (Figure 19i-p). Similarly, we witnessed the red fluorescence of **TNINSS** (oxidized product of **TNINSH** by intracellular PDI) in both cells accompanying with Phalloidin-stained cytoplasm and DAPI-stained nuclei (Figure 20a-h). Moreover, red fluorescence located adjacent to the nuclei and spread throughout cytoplasm indicates ER localization of **TNINSH** FONPs. Therefore, **NINSS** and **TNINSH** AIE-gens were distributed throughout cytoplasm of both cells (B16F10 and NIH3T3) as confirmed from colocalization study.

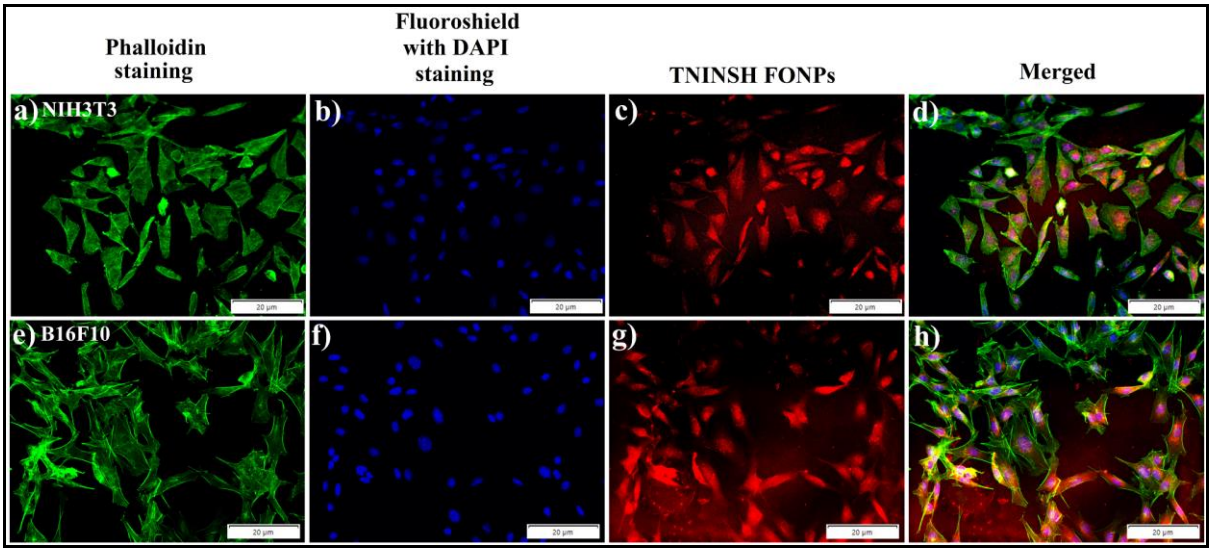

Figure 20. Fluorescence microscopic images of cells with Phalloidin cytoplasm staining along with Fluoroshield with DAPI nuclei staining. (a-d) NIH3T3 cells and (e-h) B16F10 cells incubated with [**TNINSH**] FONPs = 25 μM; Scale bars correspond to 20 μm.

3B.3 CONCLUSION

In summary, **NINSS** and **TNINSH**, two types of fluorescent organic nanoparticles (FONPs) derived from specific precursor molecules (**NINSS** and **TNINSH**), exhibit remarkable biocompatibility and stability within biological systems. These FONPs have been effectively harnessed for photodynamic imaging (PDI) through their inherent oxidoreductase activity,

capitalizing on the phenomenon of aggregation-induced emission (AIE). This utilization spans both laboratory settings (*in vitro*) and cellular environments. In the case of **NINSS** FONPs, their fluorescence intensity, observed at an emission wavelength of 470 nm (λ_{em} = 470 nm), experiences quenching upon exposure to PDI. This quenching is attributed to the reduction of disulfide bonds (-S-S-) into thiol groups (-SH) by PDI. Similarly, the emission spectrum of **TNINSH** FONPs shifts from yellow to a reddish hue upon interaction with PDI, demonstrating a "dual-AIE" effect. This shift results from the formation of dimers through disulfide linkages, prompted by thiol oxidation by PDI. Consequently, **NINSS** and **TNINSH** FONPs offer high sensitivity in probing the redox behavior of PDI through an AIE-based "fluorescence off/on" mechanism. The limit of detection (LOD) for PDI detection is estimated to be approximately 12.6-17.7 ng/mL for **NINSS** FONPs and 11.7-16.5 ng/mL for **TNINSH** FONPs. These FONPs also exhibit promising potential for differentiating between cancer (B16F10) and non-cancer (NIH3T3) cells based on their fluorescence response to PDI in the respective cell types. This distinction is particularly notable due to the heightened expression of PDI within cancer cells, rendering the cancer cell detection more sensitive than that of non-cancerous cells. Consequently, the application of **NINSS** and **TNINSH** FONPs as diagnostic probes holds immense promise for the selective and sensitive analysis of PDI. By leveraging their AIE properties to monitor the "fluorescence off/on" phenomenon, these FONPs offer a powerful tool for detecting and studying PDI in a variety of biological contexts.

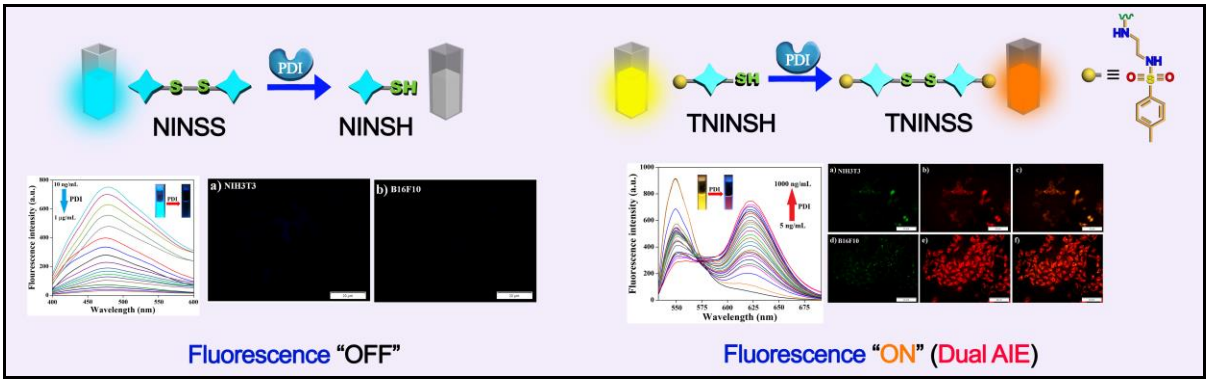

Scheme 1. Schematic representation of analyzing PDI redox state by exploitation of AIE of **NINSS** and **TNINSH** FONPs. NI: Naphthalimide, AIE: aggregation induced emission.

3B.4 EXPERIMENTAL SECTION

3B.4.1 MATERIALS.

1,8-Naphthalic anhydride, 4-benzyl N-Boc-L-aspartate, 1-naphthaleneethanol, 4-aminophenyl disulfide, N-tosylethylenediamine, Glucose oxidase (GOx), Horseradish peroxidase (HRP), Superoxide dismutase (SOD), Lysozyme, Bovine Serum Albumin (BSA), Cytochrome C, Hemoglobin (Hb), Fluoroshield with DAPI and all deuteriated solvents were bought from Sigma-Aldrich. Alexa Fluor™ 488 Phalloidin was procured from Thermo-Fisher Scientific. 4-aminothiophenol, 4-bromo-1,8-naphthalenedicarboxylic anhydride and quercetin 3-rutinoside (rutin) were purchased from TCI chemicals, India. 1-Hydroxy-2,5-pyrrolidinedione (NHS), *N*,*N*'-Dicyclohexylcarbodiimide (DCC), trifluoroacetic acid (TFA), N,N-Dimethylpyridin-4-amine (DMAP), 1,2,3-benzotriazol-1-ol (HOBt), palladium 10% on activated carbon powder, column chromatography reagents and other solvents and chemicals were acquired from SRL, India. Bruker Ultraflex MALDI mass spectrometer (2,5-dihydroxy benzoic (DHB) acid as matrix) was used to record MALDI-TOF spectra.

3B.4.2 SYNTHESIS OF NAPHTHALIMIDE DERIVATIVES (CONTROL COMPOUNDS).

In order to synthesize **NINSS**, first 1.0 equiv of 1-naphthaleneethanol and 1.2 equiv of *N*-(*tert*-butoxycarbonyl)-L-aspartic acid 4-benzyl ester were conjugated using 1.1 equiv of DCC, DMAP and HOBt in dry DCM. The reaction mixture was stirred for 12 h under N_2 atmosphere. After washing the organic part with HCl (1N) and drying over anhydrous sodium sulfate, the solvent was evaporated and the coupled product was purified by column chromatography (60-120 mesh silica gel) using 1% MeOH in $CHCl_3$ as eluent. Next, deprotection of the BOC group was carried out using TFA (~1.5 equiv) in dry DCM for 5 h. After removing the solvent, the crude mass taken in ethyl acetate was worked-up with 10% aqueous Na_2CO_3 solution and water. The organic part was evaporated to obtain a free amine. Finally, 1,8-naphthalic anhydride (1.0 equiv) and free amine derivative (1.2 equiv) were heated (75 °C, 12 h) in dry EtOH. After solvent removal, the crude mass was solubilized in DCM and washed with water. The product was collected from the DCM part. Purification of the condensed product was performed by column chromatography (100-200 mesh silica gel, 3% MeOH/$CHCl_3$ as an eluent) and washed with diethyl ether to obtain the product. The obtained product was debenzylated in methanol under

hydrogen (H_2) atmosphere in presence of Pd on activated charcoal. The mixture was filtered in a celite-545 column after overnight stirring at room temperature. The deprotected acid was subjected to NHS activation by using 2.6 equiv of DCC and 2.3 equiv of NHS in dry DMF and stirred overnight under N_2 atmosphere. 4-Aminophenol (1.0 equiv) and dry pyridine (excess) were added to this activated acid. After overnight stirring the DMF was distilled out from the reaction mixture and coupled product was purified by column chromatography (100-200 mesh silica gel, 5 % MeOH in $CHCl_3$ used as the eluent) followed by washing with diethyl ether (Scheme 2).

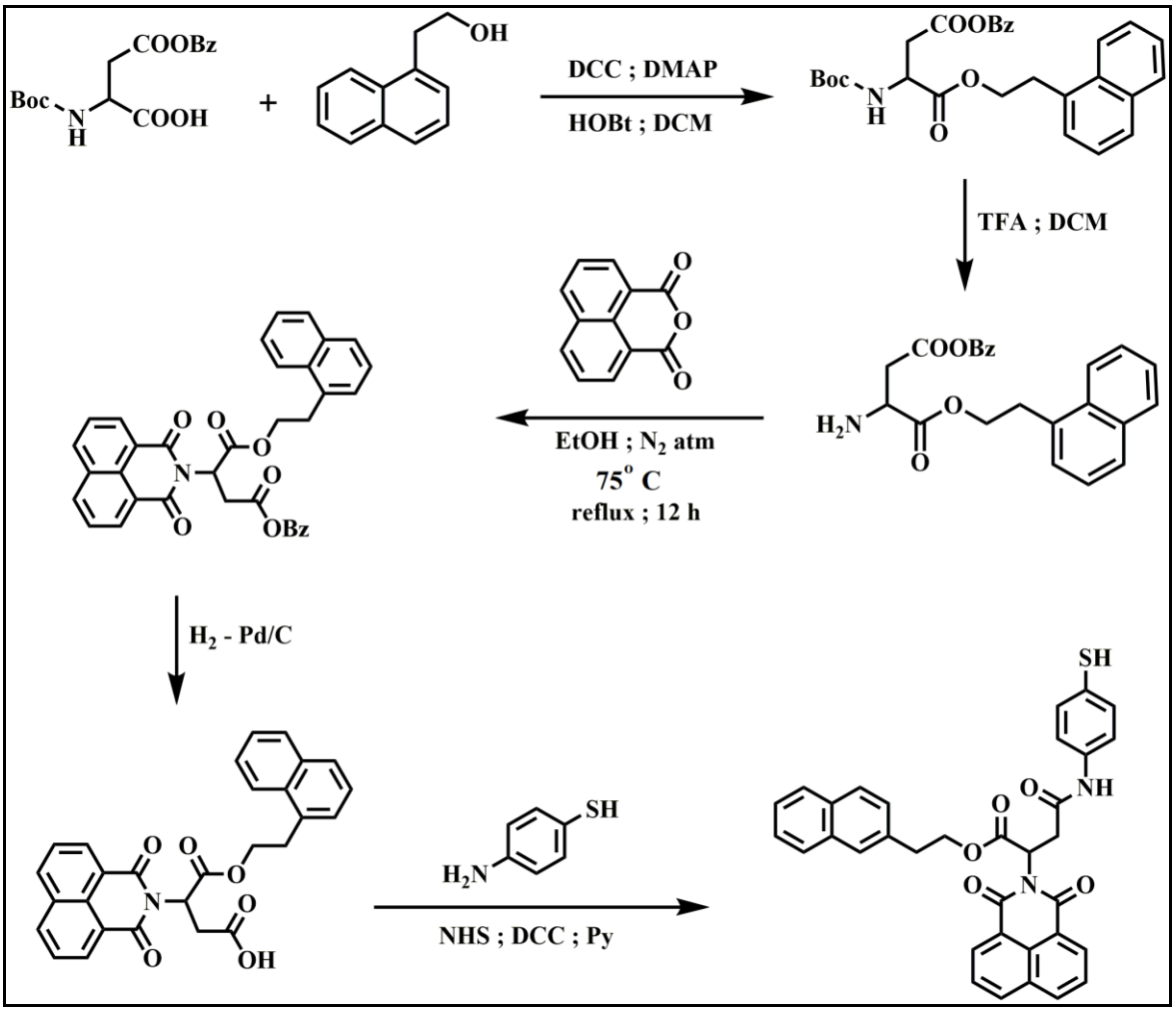

Scheme 2. Synthetic scheme for **NINSH** amphiphile.

To synthesize **TNINSH**, at first, coupling reaction between N-(*tert*-butoxycarbonyl)-L-aspartic acid 4-benzyl ester (1.2 equiv) and 1-naphthaleneethanol (1.0 equiv) was carried out using DCC (1.1 equiv), HOBt (1.1 equiv) DMAP (1.1 equiv), in dry DCM. The reaction mixture

was stirred for 12 h under nitrogen atmosphere. 1N HCl was used to wash the organic part and consequently it was dried over anhydrous Na_2SO_4. The residue obtained after evaporation was purified by column chromatography using 60-120 mesh silica gel as the stationary phase and the eluent was 1% methanol in chloroform. The BOC group was deprotected in 5 h using TFA (~1.5 equiv) in dry DCM. After solvent removal, the crude mass taken in ethyl acetate was twice washed with 10% aqueous Na_2CO_3 solution and water. Drying and evaporation of the solvent resulted in the formation of free amine.

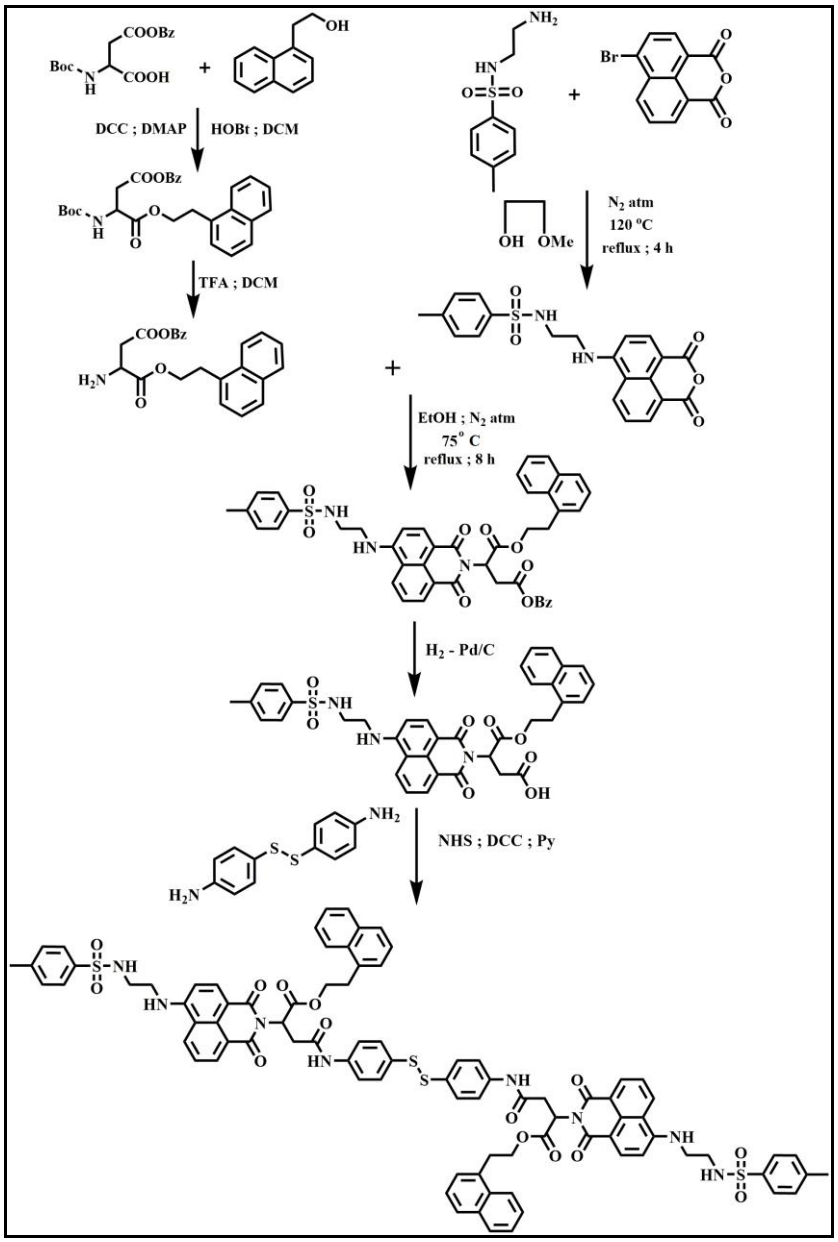

Scheme 3. Synthetic scheme for **TNINSS** amphiphile.

On the other hand, 4-bromo-1,8-naphthalene anhydride (1.0 equiv) and *N*-tosylethylenediamine (1.5 equiv) were dissolved in methoxy-ethanol and heated at 120 °C for 4 h under reflux conditions. The reaction mixture was cooled to room temperature and poured into 50 mL of ice-cold distilled water. The mixture was filtered, and the filtrate was vacuum-evaporated to get a yellow solid. This solid was purified in 100-200 mesh silica gel chromatography using 3% methanol in chloroform (v/v) as the eluent to obtain the product. After that, the free amine (1.2 equiv) and naphthalene anhydride derivative (1.0 equiv) were heated (75 °C, 12 h) in dry EtOH. The reaction mixture was cooled to room temperature and EtOH was evaporated. The crude mass was solubilized in DCM and washed with water. The expected product was collected from the DCM part. Purification of the condensed product was performed by column chromatography (100-200 mesh silica gel, 5% MeOH/$CHCl_3$ as an eluent) and washed with diethyl ether to obtain the product. The hydrogenation reaction of the obtained product (in the preceding step) was carried out in the presence of Pd on activated charcoal in dry tetrahydrofuran (THF) and the reaction mixture was stirred overnight at room temperature to deprotect the benzyl protection. The whole mixture was filtered in a $Celite_{545}$ column where hot THF was used as the eluent. The THF was then removed completely with a vacuum pump to get the acid. NHS activation of the acid was performed by using the previously formed acid, DCC (2.6 equiv), and NHS (2.3 equiv) in dry DMF and stirred overnight under N_2 atmosphere. To this activated acid, 4-aminophenyl disulfide (0.5 equiv) and dry pyridine (excess) were added. The reaction mixture was stirred overnight and the DMF was distilled out under vacuum. The residue mixture was then purified through column chromatography by using 100-200 mesh silica gel and 5% MeOH/$CHCl_3$ as the eluent to obtain pure **TNINSH** (Scheme 3).

3B.4.3 TRANSMISSION ELECTRON MICROSCOPY (TEM) STUDY.

NINSS and **TNINSH** (25 μM) in presence of PDI (100 ng/mL) in (1:99 v/v) DMSO-water (f_w = 99 vol%) was deposited on a 300-mesh carbon-coated copper grid and dried. Negative staining of the copper grid was done with freshly prepared 1 μL of uranyl acetate solution (1% w/v), and a filter paper was used to blot the excess solution. Before taking the image in transmission electron microscopic, the sample was dried for 4 h in vacuum. The TEM images were taken in JEOL JEM 2010 microscope.

3B.4.4 FIELD-EMISSION SCANNING ELECTRON MICROSCOPY (FESEM) STUDY.

To obtain FESEM images, a JEOL-6700F microscope was used. 5.0 μL of **NINSS** and **TNINSH** having concentration of 25 μM solution in presence of PDI (100 ng/mL) in f_w = 99 vol% was used to drop cast on a coverslip. After drying it for overnight, the FESEM images were taken.

3B.4.5 DYNAMIC LIGHT SCATTERING (DLS) STUDY AND ZETA POTENTIAL MEASUREMENT.

To determine the mean hydrodynamic diameter (D_h) of **NINSS** and **TNINSH** (25 μM) in presence of PDI (100 ng/mL) in f_w = 99 vol% we performed DLS study using a fixed-angle apparatus (Zen 3690 Zetasizer Nano ZS instrument (Malvern Instrument Ltd.). Measurement of the scattering intensity was done at an angle of 175°. The zeta (ζ) potential measurement was performed with solution of **NINSS** and **TNINSH** (25 μM) in (1:99 v/v) DMSO-water mixture in presence and absence of PDI.

3B.4.6 UV-VISIBLE STUDY.

Agilent Cary 60 spectrophotometer was used to record UV-vis spectra. UV-vis spectra of **NINSH** and **TNINSH** (20 μM) were performed in various solvent compositions of DMSO-water changing the water content from f_w = 0 vol% (non-self-assembled state) to f_w = 99 vol% (self-assembled state).

3B.4.7 PHOTOLUMINESCENCE STUDY.

Agilent Cary Eclipse luminescence spectrometer was used to record the fluorescence spectra of the **NINSH** and **TNINSS** (20 μM) solutions in f_w = 0-99 vol% (excitation wavelength (λ_{ex}) = 350 nm).

3B.4.8 PDI SENSING STUDY.

Photoluminescence spectra of **NINSS** (2.5 μM and 25 μM) and **TNINSH** (5.0 μM and 25 μM) FONPs were recorded in presence of different concentration of PDI (with and without GSH and GSSG) and in presence of rutin (10 mM stock in methanol). PDI sensing was carried

out using the FONPs at their lower concentrations, where optical density was <0.1. Anti-interference study was carried in presence of other enzymes and proteins.

3B.4.9 CELL CULTURE.

B16F10 (melanoma) and NIH3T3 (non-cancer) were cultured using 10% FBS, streptomycin and penicillin in DMEM media while keeping in incubator (5% CO_2, 37 °C). We performed cytocompatibility, bioimaging, MTT assay and all other biological experiments with those treated cells. **NINSS** and **TNINSH** FONPs prepared at f_w = 99 vol% was used to perform all the cellular experiments.

3B.4.10 STABILITY EXPERIMENTS AND CYTOCOMPATIBILITY OF NINSS AND TNINSH FONPs.

The stability of 50 μM of **NINSS** and **TNINSH** FONPs (in f_w = 99 vol%) was investigated in biological milieu by adding **NINSS** and **TNINSH** FONPs in the FBS-supplemented media and kept for a long-time duration. The suspension stability index (SSI) of **NINSS** and **TNINSH** FONPs was determined by recording the absorbance at 334 nm (corresponding to the λ_{max} of **NINSS** and **TNINSH** in f_w = 99 vol%) at various time intervals.

Suspension stability index (SSI) = $(A_t/A_o) \times 100$ where A_t = absorbance of the solutions at different time intervals and A_o = initial absorbance of the solutions at 381 nm **NINSS** and **TNINSH** FONPs, respectively.

MTT assay was performed to investigate cytocompatibility of **NINSS** and **TNINSH** FONPs in f_w = 99 vol%). In this assay, mitochondrial dehydrogenase excreting from viable cells reduced the soluble tetrazolium gets into insoluble formazan. Spectrophotometric method was used to estimate the amount of insoluble formazan dissolving in DMSO. The production of formazan is proportional to the quantity of alive cells. First, B16F10 and NIH3T3 cells (2×10^4 cells per well) were incubated in a 96-well plate for 24 h (5% CO_2, 37 °C). Next, all the cells were treated with 5-100 μM of **NINSS** and **TNINSH** FONPs (f_w = 99 vol%) for 24 h. Addition of 10 μL of MTT stock solution (5 mg mL^{-1}) was carried out into the cells which were incubated further for 4 h. After the incubation, Bio Tek1 Elisa Reader was used to record the absorbance of the precipitated formazan which was solubilized in DMSO (λ_{ex} = 570 nm). The number of alive cells was calculated as % viability by following the equation,

% viability = (A_{570} (treated cells) – background) / (A_{570} (untreated cells) – background) × 100 (2)

3B.4.11 OCTANOL-WATER PARTITION COEFFICIENT DETERMINATION.

We measured the octanol-water partition coefficient (log P) for **NINSS** and **TNINSH** FONPs using the shake-flask method. Approximately 5 mL of distilled, de-ionized water, pre-saturated with octanol and 5 mL of octanol-FONPs stock solution, consisting of octanol pre-saturated with water and containing a known concentration of **NINSS** and **TNINSH** FONPs (1 mM) was added to the centrifuge tube. The tube was shaken vigorously for about five minutes and then the octanol and water phases were separated by centrifugation. Samples were taken from the octanol-rich phase and the water-rich phase with a glass syringe and analyzed directly. FONPs concentration in each phase was analyzed by UV-vis spectrophotometry. A calibration curve was prepared for both **NINSS** and **TNINSH** FONPs at their absorbance maxima (334 nm). Determinations were made at least in triplicate to ensure repeatability of the tests and the mean values are reported.

3B.4.12 BIOIMAGING.

B16F10 and NIH3T3 cells were cultured in a chamber slide. After that, cells were incubated with i) **NINSS** FONPs (25 μM, f_w = 99 vol%), ii) **NINSS** FONPs (25 μM, f_w = 99 vol%) + rutin (25 μM), iii) **TNINSH** FONPs (25 μM, f_w = 99 vol%) for 12 h and 24 h. Washing of cells were done with phosphate buffer saline (PBS) (three times). After that, 4% paraformaldehyde was used for fixing. Next, glycerol (50%) was used to mount and the glass slide was covered with a cover slip for 24 h. IX83 inverted microscope at 20x magnification was used for cellular imaging.

3B.4.13 FLOW CYTOMETRY.

We incubated i) **NINSS** FONPs (25 μM, f_w = 99 vol%), ii) **NINSS** FONPs (25 μM, f_w = 99 vol%) + rutin (25 μM), iii) **TNINSH** FONPs (25 μM, f_w = 99 vol%) with NIH3T3 and B16F10 cells for 24 h. In order to remove the excess compounds from cell medium, we washed all the treated cells using DMEM media and PBS buffer after incubation. Cells were trypsinized and centrifuge for 5 min. The flow cytometric experiment was carried out with the precipitated cells

suspended in PBS (500 µL) after centrifugation. BD FACS Aria™ III flow cytometer was employed to inspect the cells at emission wavelength using 450 nm (for DAPI), 530 nm (for FITC) and 610 nm (for PE-TexasRed) bandpass filter upon excitation at 405 nm, 488 nm and 488 nm, respectively.

3B.4.14 COLOCALIZATION STUDY.

To check the distribution of **NINSS** and **TNINSH** FONPs (25 µM, f_w = 99 vol%) in B16F10 (cancer) and NIH3T3 (non-cancer) cells, both the FONPs were incubated by following the mentioned procedure in the manuscript (experimental section). The cells were consequently washed with PBS thrice, and thereafter fixed using paraformaldehyde (4%). Both the cells were treated with 0.1% Triton X-100 in PBS solution for 5 min. After washing with PBS (3 times) both the fixed cells were incubated with PBS containing 1% BSA for 30 mins to reduce nonspecific background staining. The cells were further stained with 5 ml of Alexa Fluor™ 488 Phalloidin (Thermo-Fischer Scientific), diluted in 200 mL PBS and incubated for 30 mins. Finally, the cells were washed three times with PBS and mounted on a slide using Fluoroshield with DAPI (Sigma-Aldrich), covered with a cover slip and kept for 24 h. in the chamber slide. Next, glass slides were covered with cover slips and real time bioimaging was also carried out in a IX83 inverted microscope at 20X magnification.

3B.5 REFERENCES

[1] Wilkinson, B.; Gilbert, H. F. Protein Disulfide Isomerase. *Biochimica et Biophysica Acta* **2004**, *1699*, 35-44.

[2] Hatahet, F.; Ruddock, L. W. Protein Disulfide Isomerase: A Critical Evaluation of Its Function in Disulfide Bond Formation. *Antioxid. Redox Signal.* **2009**, *11*, 2807-2850.

[3] Noiva, R. Protein Disulfide Isomerase: The Multifunctional Redox Chaperone of the Endoplasmic Reticulum. *Semin. Cell Dev. Biol.* **1999**, *10*, 481-493.

[4] Laurindo, F. R. M.; Pescatore, L. A.; Fernandes, D. de C. Protein Disulfide Isomerase in Redox Cell Signaling and Homeostasis. *Free Radic. Biol. Med.* **2012**, *52*, 1954-1969.

[5] Hillson, D. A.; Lambert, N.; Freedman, R. B. Formation and Isomerization of Disulfide Bonds in Proteins: Protein Disulfide-Isomerase. *Methods Enzymol.* **1984**, *107*, 281-294.

[6] Khan, H. A.; Mutus, B. Protein Disulfide Isomerase a Multifunctional Protein with Multiple Physiological Roles. *Front. Chem.* **2014**, *2*, 70.

[7] Moretti, A. I. S.; Laurindo, F. R. M. Protein Disulfide Isomerases: Redox Connections In and Out of the Endoplasmic Reticulum. *Arch. Biochem. Biophys.* **2017**, *617*, 106-119.

[8] Xu, S.; Sankar, S.; Neamati, N. Protein Disulfide Isomerase: A Promising Target for Cancer Therapy. *Drug Discov. Today* **2014**, *19*, 222-240.

[9] Khan, M. M. G.; Simizu, S.; Kawatani, M.; Osada, H. The Potential of Protein Disulfide Isomerase as a Therapeutic Drug Target. *Oncol. Res.* **2011**, *19*, 445-453.

[10] Wang, C. C.; Tsou, C. L. Protein Disulfide Isomerase Is Both an Enzyme and a Chaperone. *FASEB J.* **1993**, *7*, 1515-1517.

[11] Quan, H.; Fan, G.; Wang, C. Independence of the Chaperone Activity of Protein Disulfide Isomerase from Its Thioredoxin-like Active Site. *J. Biol. Chem.* **1995**, *270*, 17078-17080.

[12] Khan, R. H.; Siddiqui, M. K.; Salahuddinv, P. Protein Disulfide Isomerase: Structure, Mechanism of Oxidative Protein Folding and Multiple Functional Roles. *J. Biochem. Mol. Biol. Res.* **2016**, *2*, 173-179.

[13] Lee, E.; Lee, D. H. Emerging Roles of Protein Disulfide Isomerase in Cancer. *BMB Rep.* **2017**, *50*, 401-410.

[14] Grek, C.; Townsend, D. M. Protein Disulfide Isomerase Superfamily in Disease and the Regulation of Apoptosis. *Endoplasmic Reticulum Stress Dis.* **2014**, *1*, 4-17.

[15] Parakh, S.; Atkin, J. D. Novel Roles for Protein Disulphide Isomerase in Disease States: A Double Edged Sword? *Front. Cell Dev. Biol.* **2015**, *3*, 30.

[16] Benham, A. M. The Protein Disulfide Isomerase Family: Key Players in Health and Disease. *Antioxid. Redox Signal.* **2012**, *16*, 781-789.

[17] Powell, L. E.; Foster, P. A. Protein Disulphide Isomerase Inhibition as a Potential Cancer Therapeutic Strategy. *Cancer Med*. **2021**, *10*, 2812-2825.

[18] Khalaf, N. B.; Fathallah, M. D. Protein Disulfide Isomerase: A New Class of Drug Target. *Curr*. *Trends Biomed*. *Eng*. *Biosci*. **2018**, *12*, 555838.

[19] Yang, S.; Jackson, C.; Karapetyan, E.; Dutta, P.; Kermah, D.; Wu, Y.; Wu, Y.; Schloss, J.; Vadgama, J. V. Roles of Protein Disulfide Isomerase in Breast Cancer. *Cancers* **2022**, *14*, 745.

[20] Watanabe, M. M.; Laurindo, F. R. M.; Fernandes, D. C. Methods of Measuring Protein Disulfide Isomerase Activity: A Critical Overview. *Front*. *Chem*. **2014**, *2*, 73.

[21] Liao, X.; Zhuang, X.; Liang, C.; Li, J.; Flaumenhaft, R.; Yuan, C.; Huang, M. Flavonoids as Protein Disulfide Isomerase Inhibitors: Key Molecular and Structural Features for the Interaction. *J*. *Agric*. *Food Chem*. **2022**, *70*, 4475-4483.

[22] Wang, X.; Xue, G.; Song, M.; Xu, P.; Chen, D.; Yuan, C.; Lin, L.; Flaumenhaft, R.; Li, J.; Huang, M. Molecular Basis of Rutin Inhibition of Protein Disulfide Isomerase (PDI) by Combined In Silico and Experimental Methods. *RSC Adv*. **2018**, *8*, 18480-18491.

[23] Lin, L.; Gopal, S.; Sharda, A.; Passam, F.; Bowley, S. R.; Stopa, J.; Xue, G.; Yuan, C.; Furie, B. C.; Flaumenhaft, R.; Huang, M.; Furie, B. Quercetin-3-rutinoside Inhibits Protein Disulfide Isomerase by Binding to Its b′x Domain. *J*. *Biol*. *Chem*. **2015**, *290*, 23543-23552.

[24] Jasuja, R.; Passam, F. H.; Kennedy, D. R.; Kim, S. H.; Hessem, L. V.; Lin, L.; Joshi, S. S.; Dilks, J. R.; Furie, B.; Furie, B. C.; Flaumenhaft, R. C. Protein Disulfide Isomerase Inhibitors: A New Class of Antithrombotic Agents. *Blood* **2011**, *118*, 369.

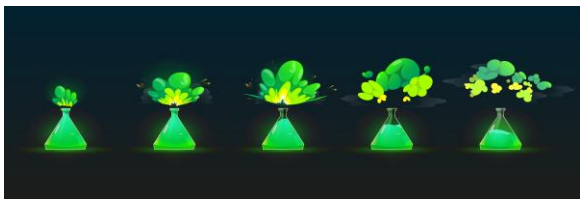

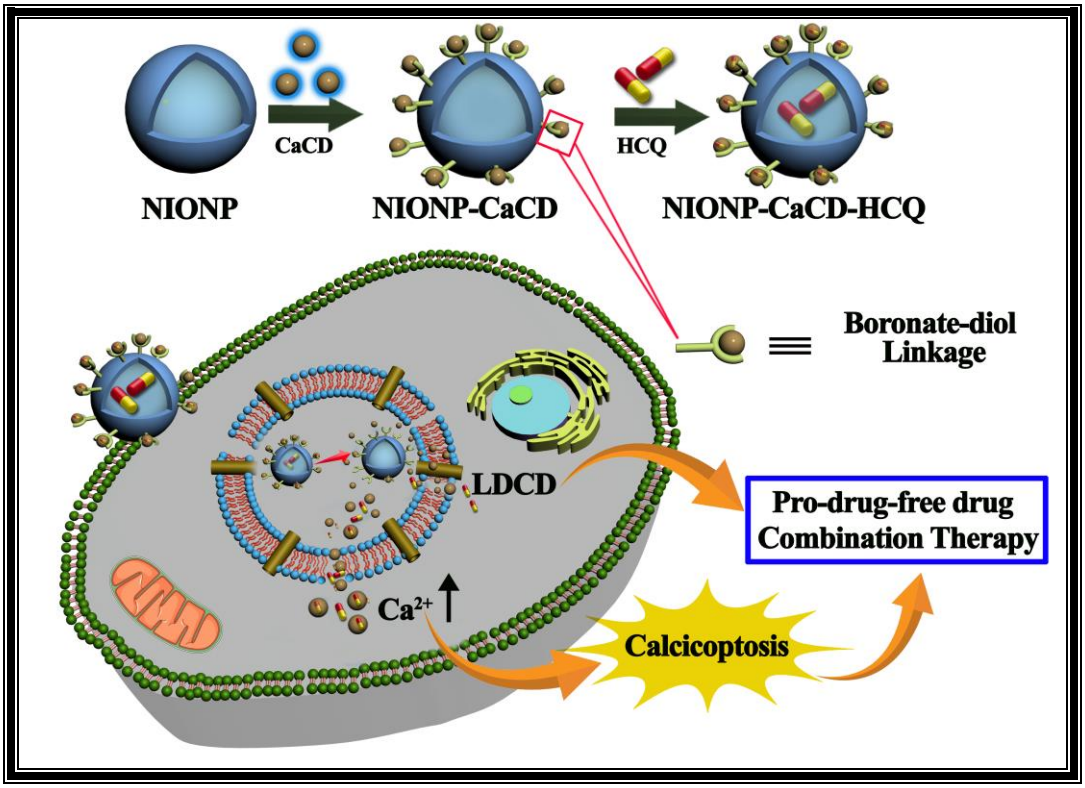

Organic Nanoparticle-Carbon Dot Conjugates in Synergistic Combination Therapy for Cancer Treatment

4.1 INTRODUCTION

Nanotechnology has had a huge impact on the development of therapeutics over the last couple of decades. To date, a large number of nanoparticles have been developed to encapsulate and deliver therapeutic and imaging agents.[1-3] Over the past few decades, organic nanoparticles (ONPs) derived from diverse precursors like amphiphiles, polymers, and lipids have gained attraction in therapeutic delivery due to considerable cargo loading ability, excellent cytocompatibility, and biodegradability.[4-6] Concurrently, in recent years carbon dots (CDs), a zero-dimensional nanomaterial, could be a good choice as cellular transporter as well as diagnostic probe due to its ease of surface passivation, superior cytocompatibility, and high-water solubility.[7,8] Both ONPs and CDs have their individual prominence in supramolecular self-assembly and nanomedicine. Despite having such extraordinary credentials, the major limitations of using CDs as a drug delivery vehicle are variable biocompatibility, limited drug loading capacity, challenges in controlled drug release, and the need for additional targeting modifications.[9] Moreover, they face issues with short circulation time, stability, and degradation, while their clinical translation is hindered by regulatory and manufacturing challenges.[10] On the contrary, Organic nanoparticles in drug delivery have limitations including potential biocompatibility issues, and complex manufacturing processes.[11] Achieving precise targeting, regulatory compliance, and ensuring long-term safety also remain key concerns. To overcome these hurdles, the necessity of developing a new soft-nanoconjugate has emerged with low cytotoxicity and improved drug loading ability. To this end, amalgamation of self-assembled organic nanoparticles with carbon dots may lead to the development of a ONP-CD conjugate with the desired features i.e., improved drug encapsulation efficacy with fluorometric diagnosis. To date, very few attempts were made to develop various nanoconjugates. Regev and co-workers reported the formation of a CNT-liposome conjugate through a covalent amide linkage between carboxylated multiwalled CNT and the primary amine containing liposome and this conjugate was utilized as a molecular-transporter by utilizing the ligand-receptor interaction between liposome and CNT.[12] Electrostatic interaction had also been used to form a single-walled carbon nanotube-liposome complex.[13] Also, there are several reports on hybrid nanomaterials, composed of

both inorganic and organic components, that can serve as promising platforms for imaging and therapeutic applications.[14,15] However, reports on ONP-CD conjugates are rare and the befitting role of the ONP-CD conjugate over the individual cargo carrier (ONP or CD) is yet to be emphasized.

Cancer poses a complex and enduring challenge that has spanned decades, necessitating a range of treatments beyond surgery, immunotherapy, and chemotherapy.[16] Despite these efforts, effectively conquering this lethal disease remains a formidable task. The drawbacks of lacking selectivity against cancer cells, grappling with toxic side effects, and having limited options for single-drug treatment are critical impediments in the field of cancer therapy.[17-19] In chemotherapy, individual anticancer drugs often operate via distinct mechanisms, potentially harming both cancerous and healthy cells. Consequently, new approaches are imperative to enhance treatment efficacy. Recent advances have led to the emergence of combination therapy, a strategy aimed at optimizing therapeutic outcomes while minimizing adverse effects.[20] This involves amalgamation of various therapeutic modalities, such as radiotherapy and chemotherapy, or the simultaneous administration of diverse therapeutic agents (pro-drug-free drug combinations or free drug-free drug combinations) with varying mechanisms of action, all working synergistically.[21] In this context, the present chapter focuses on investigating the potential of the "prodrug-free drug" combination, a promising avenue within chemotherapy that holds the promise of improved treatment outcomes.

Pro-drugs are inert biomolecules that get activated in vivo by enzymatic or chemical reactions in the presence of an activator.[22] Pro-drugs are often used to (i) improve solubility in water or lipid membrane, (ii) decrease side effects, and (iii) increase cellular uptake.[23,24] It is widely known that Ca^{2+} overload has been an efficient, yet safe theranostic model for cancer therapy, by activating mitochondrial apoptosis pathways to achieve cancer suppression.[25-28] So, we aim to use Ca^{2+} overload as a prodrug and Ca^{2+} doped carbon dot as a pro-drug activator as one of the components in combination therapy. Importantly, the chosen components (free drug or pro-drug) should act through different mechanisms so that multidrug resistance as well as anticancer drug-induced toxicity can be minimized. In this regard, we plan to use anticancer drug Hydroxychloroquine (HCQ) as a free drug as HCQ is a lysosomotropic autophagy inhibitor and also responsible for lysosomal cell death.[29,30]

As we envisage pro-drug-free drug combination chemotherapy, we aim to develop HCQ loaded nanoconjugate between carbon dot and organic nanoparticles through boronate diol linkage. Herein, we report development of naphthalimide based organic nanoparticle (**NIONP**) comprising of lysosome targeting moiety and boronic acid residue at terminal. Furthermore, these **NIONP**s were utilized to fabricate **NIONP-CaCD** conjugate with hydroxyl (-OH) functionalized Ca^{2+} doped carbon dot (**CaCD**) via boronic acid-diol interaction. To the best of our knowledge, this is the first ever approach in which the ONPs has been decorated with CDs. Microscopic and spectroscopic techniques were utilized to characterize this newly developed **NIONP-CaCD** conjugate as well as its individual components. The **NIONP-CaCD** conjugate was found to be stable in biological milieu. HCQ was encapsulated within this **NIONP-CaCD** conjugate with improved loading capacity compared to its individual constituents. Importantly, the **NIONP-CaCD** conjugate delivered the drug with greater efficiency inside the A549 and HepG2 cells compared to the drug-loaded individual **NIONP** or **CaCD** resulting in greater killing of the cancer cells by the conjugate. Hence, the combination of Ca^{2+} overload-mediated calcicoptosis and lysosomal cell death induced by HCQ, facilitated through the **NIONP-CaCD** conjugate, established a potent theranostic contender within the realm of cancer treatment's combination therapy.

4.2 RESULTS AND DISCUSSION

The landscape of cancer therapy is witnessing the ascendancy of combination therapy as a pivotal strategy. Multiple therapeutic agents are concurrently administered to attain a synergistic anti-proliferative impact on cancer cells. By amalgamating diverse treatment modalities (e.g., chemotherapy, radiotherapy, immunotherapy), effectiveness is bolstered through additive targeting of critical pathways.[20,21] This approach has become the gold standard for many cancer types, achieving heightened therapeutic benefits, improved specificity, and diminished metastatic potential by halting actively dividing cells. Our study delves into exploring the potential of pro-drug-free drug combinations for precision-oriented cancer therapy.

As a potent second messenger, calcium (Ca^{2+}) is involved in multitudinous physiological behaviors, such as neuronal excitation, protease expression, and bone morphogenesis as well as

various cancer diagnostic and therapeutic events. This includes calcium overload-induced calcium homeostasis disorder, calcium channels dysregulation, mitochondrial dysfunction, calcium-associated immunoregulation, cell/vascular/tumor calcifcation, and calcifcation-mediated CT imaging.[25,26,31,32] Entry of excess calcium through voltage-dependent calcium channels (VDCCs), released by the endoplasmic reticulum (ER) or from the mitochondria can cause calcium overload that leads to several intracellular processes like oxidative stress, mitochondrial depolarization, release of cytochrome C, and activation of caspase-3, to cause cell death (calcicoptosis).[26,32] Accordingly, we decided to develop a nanoplatform (carbon dot) for Ca^{2+} overload (pro-drug) with novel structures and prominent functions instigating the need for comprehensive exploration toward practical implementation. Given calcium's efficient potential against diverse cancers, free from drug resistance, oxygen dependence, and phototoxicity, the fusion of Ca^{2+} overload and other therapeutic methods within nanoplatforms presents an appealing avenue in the landscape of anti-tumor nanomedicine.[27,28,33] With this objective, the judicious design and development of a calcium-doped carbon dot can serve a dual purpose, functioning both as a prodrug activator and a diagnostic probe. Notably, for tumor cells in which catalase (CAT) is downregulated, the constant challenge from oxidative stress would alter protein functions, resulting in the desensitization of calcium-related channels followed by an uncontrollable cellular accumulation of Ca^{2+}. This biological effect could hinder the accurate transmission of calcium signals and induce cell death. By comparison, healthy cells are more tolerant of the adverse influence of nanoparticles. This could be attributed to the presence of a sufficient amount of CATs that prevent oxidative activation of the cells and thus allow the exogenous Ca^{2+} to be more efficiently pumped out or stored through calcium channels.[34] This underscores the interconnectedness of calcium and oxidative stress in cellular dynamics. Considering the limitations of monotherapies in complete tumor eradication, nanoplatform-facilitated combination therapies emerge as more potent strategies with diminished toxic effects. Hitherto, an approach of combination therapeutic strategy has been demonstrated in this work.

Up until now, extensive research has focused on lysosomes' role in tumor chemo-resistance.[35,36] A common strategy to sensitize tumors to chemotherapy involves targeting lysosomes within tumor cells. Originally seen as organelles responsible for breaking down large molecules and various cellular functions, recent findings highlight lysosomes' capacity to trap

drugs due to the overexpression of P-gp (P-glycoprotein 1). Subsequently, the acidic environment of lysosomes contributes to breaking down these drugs. This accumulation in lysosomes diminishes the drugs' effectiveness, making lysosomes an attractive target for boosting sensitivity. Beyond direct cancer cell targeting, using specific agents to trigger the host's immune defenses for suppressing tumor growth holds promise for refining treatments. Lysosome-associated agents like hydroxychloroquine (HCQ) have emerged as potential chemo-sensitizers. Clinical trials have explored HCQ's potential to enhance chemotherapy's efficacy across various cancers. Additionally, HCQ's immunomodulatory role in macrophages has been investigated. HCQ induces signs of lysosomal membrane permeabilization (LMP), such as the decrease in the lysosomal pH gradient and the release of cathepsin B from the lysosomal lumen, followed by signs of apoptosis including caspase activation, phosphatidylserine exposure, and chromatin condensation with DNA loss.[37] Additionally, hydroxychloroquine induces oxidative DNA damage and mutation in mammalian cells.[38] Despite its chemo-sensitization benefits, HCQ has been linked to significant side effects. Therefore, there is a pressing need to identify new lysosome-targeting agents that avoid organ damage.

To this end, we synthesize organic nanoparticles formed by self-assembly of naphthalimide based amphiphile comprising of a lysosome targeting unit i.e., 4-(2-aminoethyl)morpholine and boronic acid moiety (**NIONP**) (Figure 1a). Boronic acid residue present in molecular framework of ONPs may engendered boronate-diol interaction with hydroxyl (-OH) functionalized Ca^{2+} doped carbon dots (**CaCD**) (Figure 1b) in order to fabricate the **NIONP-CaCD** conjugate. As we conceptualize the strategy of pro-drug-free drug combination chemotherapy, we employed hydroxychloroquine (HCQ) as the free drug. Now, to achieve its benefit as an anticancer agent via LMP induced cell death, we introduce the lysosome targeting unit in the **NIONP** part of the **NIONP-CaCD** conjugate system. Notably, the breakdown of the **NIONP-CaCD** conjugate into its separate constituents could have occurred through the cleavage of the boronate-diol bond at the lysosomal pH range (4.5-5.0).[39] This would result in the liberation of HCQ and **CaCD**. Subsequently, this release could lead to cell death initiated by lysosomal membrane permeabilization (LMP), possibly intertwined with a phenomenon known as calcific apoptosis or calcicoptosis. Therefore, in this work, we introduce **NIONP-CaCD** conjugate for Ca^{2+} overload-based oncotherapy in synergism with HCQ induced lysosomal cell death.

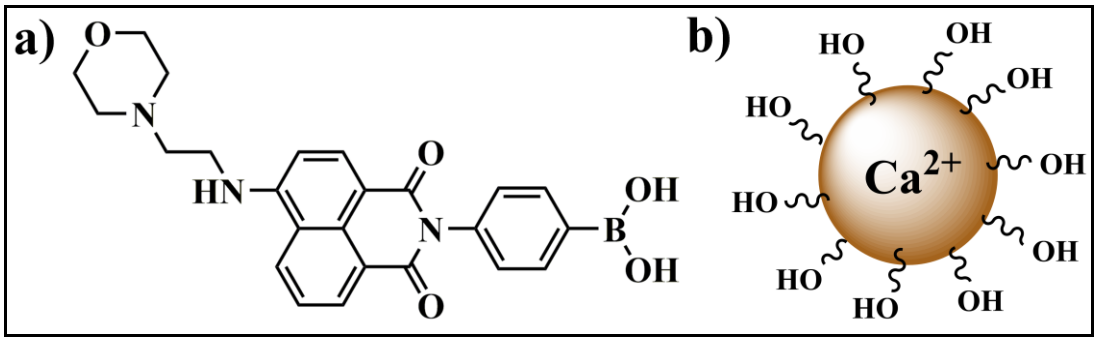

Figure 1. (a) Molecular structure of **NIONP**, (b) structure of **CaCD**.

4.2.1 MICROSCOPIC AND DLS STUDY FOR SELF-ASSEMBLY OF NIONP.

The self-assembly behavior of the designed NI-derivatives (**NIONP**) as well as their aggregation pattern were investigated by both spectroscopic and microscopic methods. The newly synthesized naphthalimide (NI)-based amphiphilic compound was completely soluble in DMSO. Addition of small amount of water into the solution of **NIONP** in DMSO showed macroscopic translucency in the solution signifying the formation of self-aggregated structures by the NI-based amphiphile in DMSO-H_2O binary solvent mixture (Figure 2a). For **NIONP**, the transparent solutions converted into translucent solution without precipitation at and above 40 % water (f_w = 40 vol%) inclusion (Figure 2a). The macroscopic translucent solution was unswerving up to 99% water content (f_w = 99 vol%) by virtue of self-assembly of the amphiphile. Motivated by these preliminary observations, the morphology of the self-aggregated structure was investigated.

Microscopic study i.e., TEM was employed to examine the self-assembled structure of the NI-derivative, **NIONP** in 99% water content (f_w = 99 vol%). Negatively stained TEM image suggested formation of the spherical aggregates of **NIONP** (50 μM) in 1:99 (v/v) DMSO-water (f_w = 99 vol%) solution having diameters in the range of ~50-70 nm (Figure 2b). No clear contrast of the spherical particles indicates the solid physical appearance of the aggregated organic nanoparticles. Concurrently, the mean hydrodynamic diameter (D_h) of **NIONP** in its self-assembled state (f_w = 99 vol% water in DMSO) was observed to be around 50-70 nm in dynamic light scattering (DLS) spectroscopy (Figure 2c). The corresponding correlogram of the DLS study was also provided (Figure 2d).

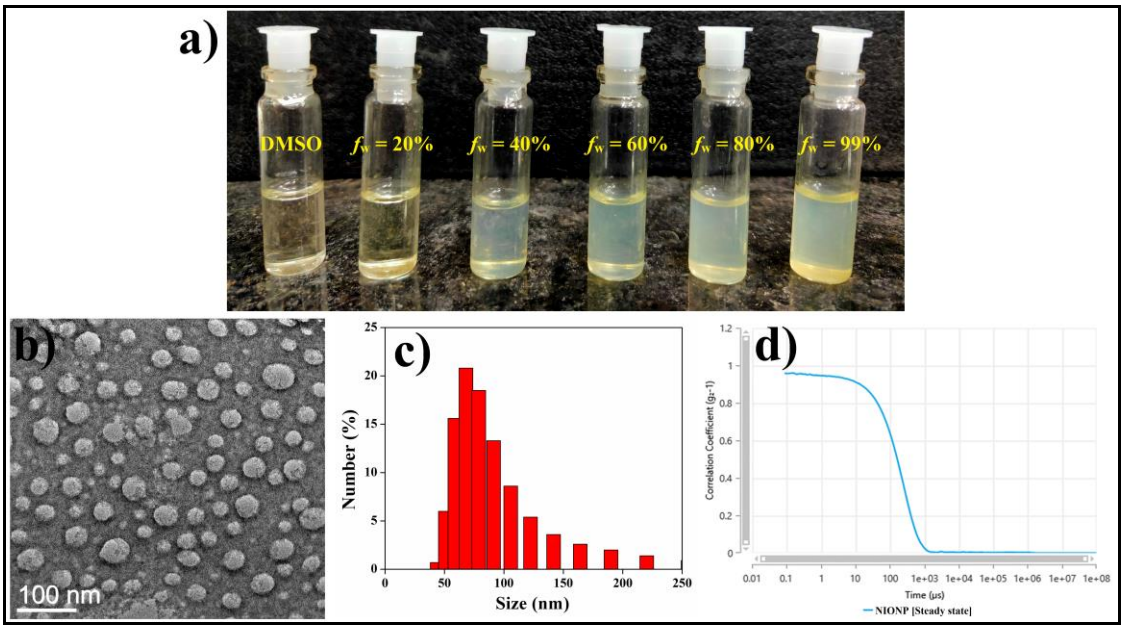

Figure 2. (a) Photograph of formation of translucent solutions for **NIONP** with increase in water content in DMSO, (b) Negatively stained TEM image, (c) DLS plot and (d) corresponding correlograms of particles size distribution of **NIONP** in (1:99, v/v) DMSO-water ([**NIONP** = 50 µM).

4.2.2 SPECTROSCOPIC STUDIES FOR SELF-AGGREGATION BY NIONP.

Driven by the microscopic findings, the mechanistic pathway for self-aggregation was investigated by spectroscopic investigations of the NI-based amphiphile, **NIONP**. To this account, UV-vis spectroscopic study was performed with 50 µM of **NIONP** in various solvent system of DMSO-H_2O by altering the water composition from 0% to 99% (i.e., f_w = 0 to 99 vol%). UV-vis spectra of **NIONP** (50 µM) in pure DMSO (non-self-aggregated solvent) exhibited a characteristics absorbance peak in the range of 300-370 nm with absorption maxima (λ_{max}) at 342 nm (Figure 3a). This may be attributed to the π-π* transition polarized along the long axis of naphthalimide (NI) chromophoric unit.[40] Subsequently, in DMSO-water binary solvent systems (self-assembled state) of different composition, UV-vis spectra were recorded to comprehend the deviation of the absorbance peaks to that of non-self-aggregated state. With gradual increment in water content in the DMSO solutions, steady bathochromic shifting of the absorption maxima was observed for **NIONP** and the λ_{max} was noticed at 348 nm at highest water composition (f_w = 99 vol%) (Figure 3a). These red shifting of absorbance maxima (λ_{max}) upon gradual inclusion of water illustrated the self-assembly driven construction

of organic nanoparticles possibly via *J*-aggregation (head-to-tail arrangement) by stair like stacking for **NIONP**.

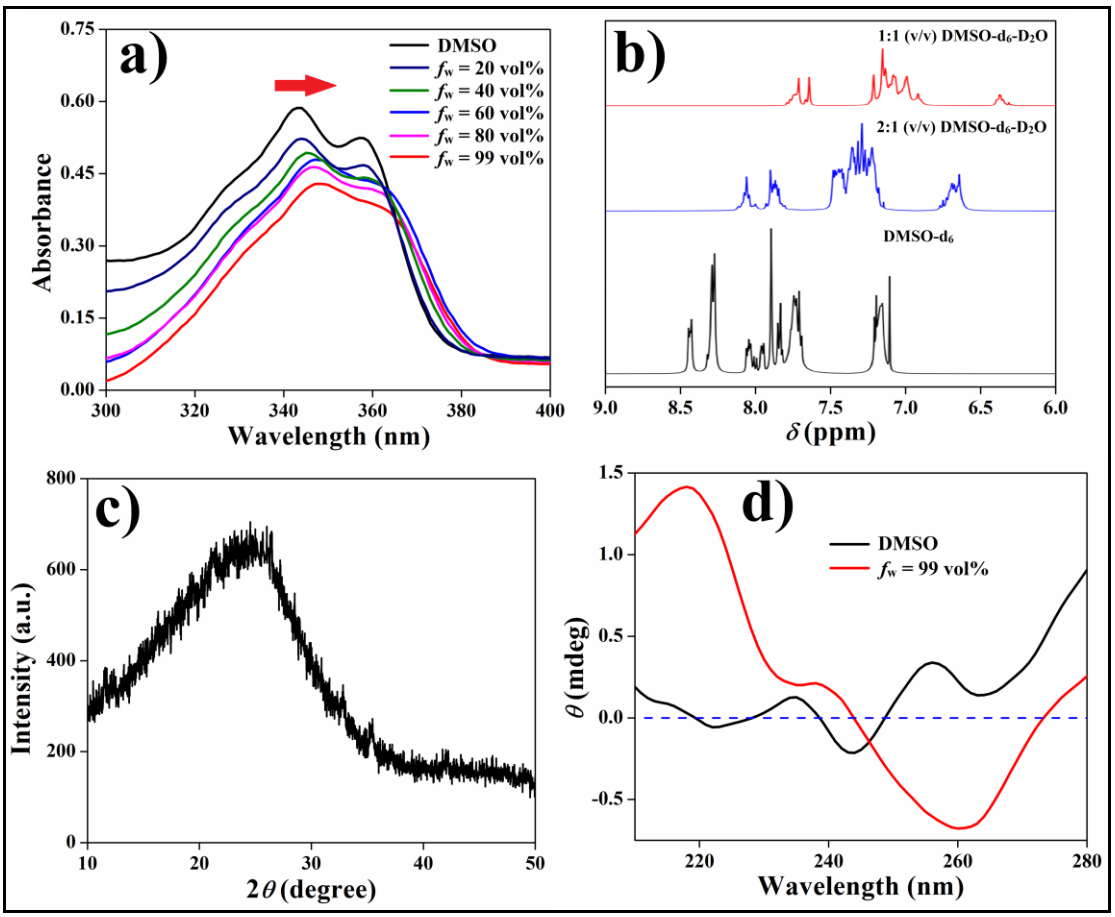

Figure 3. (a) UV-vis study of **NIONP** varying DMSO-water solvent mixtures, (b) solvent dependent ^{1}H-NMR spectra, (c) XRD plot and (d) CD spectra of **NIONP** ([**NIONP**] = 50 μM).

The influence of non-covalent interactions, including π-π interactions, in driving the formation of aggregated nanoparticles through self-assembly was assessed using solvent-dependent ^{1}H-NMR spectroscopy and XRD analysis. In the solvent-dependent ^{1}H-NMR investigation, **NIONP**'s aromatic protons exhibited distinct and sharp signals in the δ = 8.38-8.45 (NI core), 8.24-8.32 (NI core), 7.70-8.11 (NI core and phenyl ring), and 7.16-7.24 (NI core) range in DMSO-d_6, indicating its non-aggregated state (Figure 3b). As the proportion of D_2O increased gradually, the characteristic NMR signals experienced upfield shifts along with reduced peak intensity (Figure 3b). In a (1:1, v/v) mixture of DMSO-d_6 and D_2O, the ^{1}H-NMR signals from the NI aromatic core and the phenyl ring exhibited broadening and shifted to δ = 7.71-7.75 (NI core), 7.67-7.69 (NI core), 6.85-7.23 (NI core and phenyl ring), and 6.31-6.45 (NI

core) for the corresponding protons (Figure 3b). In the non-self-assembled state (DMSO-d_6), there was no significant π-π stacking or hydrophobic interaction. However, as D_2O content increased, the initiation of self-assembly facilitated non-covalent interactions, such as π-π stacking and hydrophobic interactions, among the aromatic components of the molecular framework. These spectroscopic findings unequivocally verified the involvement of non-covalent interactions during the process of forming self-assembled organic nanoparticles. Moreover, XRD spectra of **NIONP** (50 μM) in self-assembled state at 1:99 v/v DMSO-water solvent system exhibited peak at $2\theta \sim 24.7^{o}$ (d spacing 3.601 Å) (Figure 3c). This finding also confirmed distinct and compact π-π stacking between aromatic rings of the **NIONP** in its self-aggregated state. These findings were consistent with the outcomes of a solvent-dependent ^{1}H-NMR investigation conducted on **NIONP**.

Subsequently, circular dichroism (CD) spectroscopy was employed to analyze the supramolecular characteristics of **NIONP** aggregates. When NIONP was in a DMSO solution (non-self-assembled state), it did not display any distinct CD signals (Figure 3d). In contrast, in the self-aggregated state with a water fraction (f_w) of 99%, the CD spectra exhibited a notable positive signal at 217 nm and a prominent negative signal at 260 nm for **NIONP**. This demonstrated that **NIONP** exhibited a negative cotton effect, indicative of its aggregated state, whereas the individual monomers lacked this response.

Furthermore, steady-state fluorescence anisotropy study was carried out for **NIONP** to investigate microenvironment of aggregated structures using 1,6-diphenyl-1,3,5-hexatriene (DPH) probe, which is known to intercalate between the hydrophobic interior of the aggregates. A higher steady-state anisotropy (r) value indicated that the movement of DPH was restricted, signifying the presence of less polar and more hydrophobic conditions within the aggregates. Throughout the investigation, the 'r' values were observed to increase for **NIONP**. This phenomenon was particularly noticeable when the water content within the DMSO was gradually raised from 50% to 99%. Additionally, an increase in the concentration of **NIONP** from 50 to 200 μM also led to a rise in the 'r' values (Table 1). The collective observations strongly supported the notion that **NIONP** formed stable organic nanoparticles within a DMSO-water environment with higher water content.

Table 1. Steady-state fluorescence anisotropy (r) of DPH with varying concentrations of **NIONP** in different ratios of DMSO-water solvent mixture.

Concentration (μM)	f_w = 50 %	f_w = 75 %	f_w = 99 %
50	0.061	0.104	0.161
100	0.067	0.117	0.173
150	0.074	0.125	0.226
200	0.089	0.154	0.267

4.2.3 SYNTHESIS AND CHARACTERIZATION OF Ca^{2+}-DOPED CARBON DOT (CaCD).

Ca^{2+}-doped carbon dot (**CaCD**) was prepared via the hydrothermal method using equivalent amounts of citric acid, tris(hydroxymethyl)aminomethane, and $Ca(CH_3COO)_2$. Citric acid was used as the source of carbon core, Ca^{2+} as the doping element, and tris(hydroxymethyl)aminomethane was utilized for surface functionalization by hydroxyl (-OH) groups. The synthesized **CaCD** was soluble in water, and the corresponding ζ-potential values were -24.7 mV, indicating their stability in aqueous medium. The microscopic characterization of **CaCD** was investigated by TEM. The data from TEM image confirmed that the size of **CaCD** was around 4-6 nm (Figures 4a). The XPS analysis of **CaCD** showed peaks at 285, 400, and 531 eV, which correspond to C (1s), N (1s), and O (1s) orbitals (Figure 4b).[41] Two more peaks at 346 and 350 eV, corresponding to the orbital Ca $2p_{3/2}$ and Ca $2p_{1/2}$, were observed indicating the presence of calcium in the divalent (Ca^{2+}) state in **CaCD** (Figure 4c).[42] Further characterization of **CaCD** was carried out by XRD analysis. The peak ranges from 20 to 25° established the amorphous nature of prepared **CaCD** (Figure 4d). We observed excitation-dependent blue emission with emission maxima for **CaCD** at 451 nm, upon excitation at 280 nm (Figure 4e). We also observed the emission maximum of **CaCD** (25 μg/mL) at 420 nm (blue-shifted) upon excitation at 340 nm (Figure 4e). Aqueous solution of **CaCD** displayed blue fluorescence (inset, Figure 4e), under UV light irradiation (295 nm), which is in accordance with the emission behavior of **CaCD**. Furthermore, **CaCD** showed the blue emitting dots in the fluorescence microscopic images affirmed the blue emissive property of **CaCD** (Figure 4f). The relative quantum yield of **CaCD** was found to be 7.41% (with respect to quinine hydrogen sulfate).

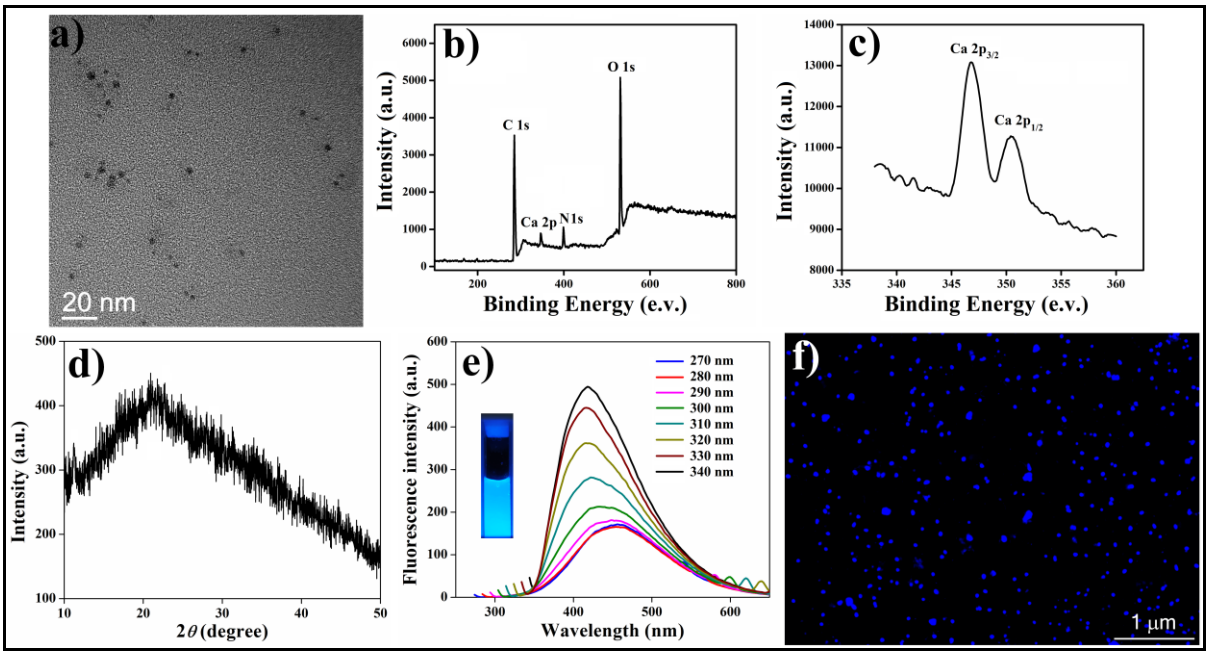

Figure 4. (a) TEM image, (b) XPS spectra, (c) deconvoluted XPS spectra for Ca^{2+}, (d) XRD spectra, (e) excitation dependent fluorescence spectra ([**CaCD**] = 25 μg/mL), (f) fluorescence microscopic image of **CaCD**.

4.2.4 FABRICATION OF NIONP-CaCD CONJUGATE AND ITS CHARACTERIZATION.

At this point, we intend to amalgamate the newly developed organic nanoparticles (**NIONP**) with Ca^{2+} doped carbon dot (**CaCD**) to fabricate the **NIONP-CaCD** conjugate. **CaCD** was surface functionalized by hydroxyl (-OH) groups, which would be appropriate for linking with the boronic acid tethered **NIONP** by a boronate-diol covalent interaction (Lewis acid-base chemistry) in order to construct **NIONP-CaCD** conjugate. The formation of **NIONP-CaCD** conjugate from **NIONP** and **CaCD** was investigated by UV-visible spectroscopy. Different weight ratios (w/w) of **CaCD** and **NIONP** were mixed (1:1, 1:2, 1:3, 1:4, 1:5, 1:6, 1:7), and the UV-visible spectra of these different solutions of varying weight ratios were recorded (Figure 5). The absorbance spectra of **NIONP** showed λ_{max} at 343 nm, which got red-shifted up to 351 nm with increasing concentration of **CaCD** in the mixture of **NIONP** and **CaCD** (from 1:1 to 1:5, w/w) indicating the change in surface property of **NIONP** (Figure 5). Covalent surface modification of the **NIONP** with **CaCD** was reflected by the red shifting of λ_{max} in UV-vis spectra possibly due to the formation of **NIONP-CaCD** conjugate having new λ_{max} (Figure 5). The absorption maxima did not change further upon increasing the concentration of **NIONP**

in the mixture of **NIONP** and **CaCD** mixtures at 1:7, w/w, which possibly indicates the saturation of **NIONP** nanoparticle surface by **CaCD** through boronate-diol bond formation (Figure 5). Thus, for all further experiments and investigations, we prepared **NIONP-CaCD** conjugate using 1:5 w/w **CaCD** and **NIONP**.

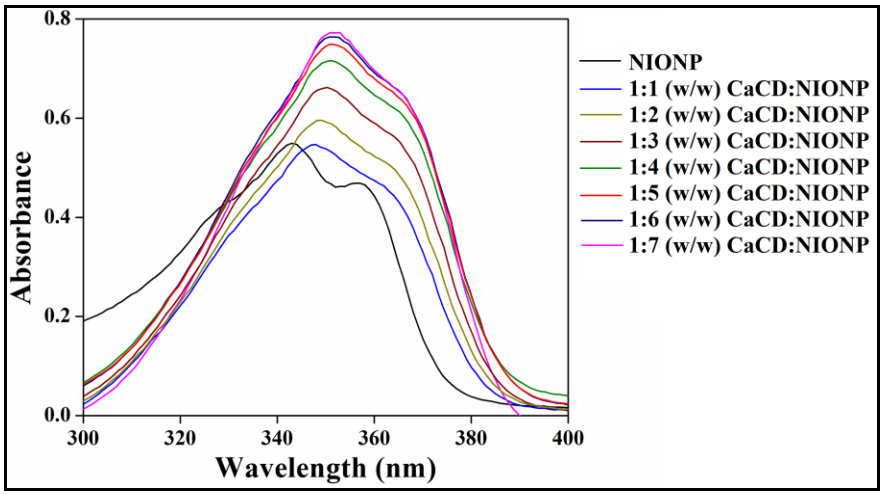

Figure 5. UV-visible spectra of **NIONP** and **CaCD** adducts at different weight ratio to form **NIONP-CaCD** conjugate.

NIONP-CaCD conjugate was also characterized by TEM, XPS, and fluorescence microscopy. The size of **NIONP-CaCD** conjugate was found to be ~100-120 nm according to the TEM image and DLS plot (Figure 6). Moreover, the TEM image (without staining) suggested the presence of carbon dots on the surface of spherical shaped organic nanoparticles confirming the formation of the conjugate between **NIONP** and **CaCD** (Figure 6a,b).

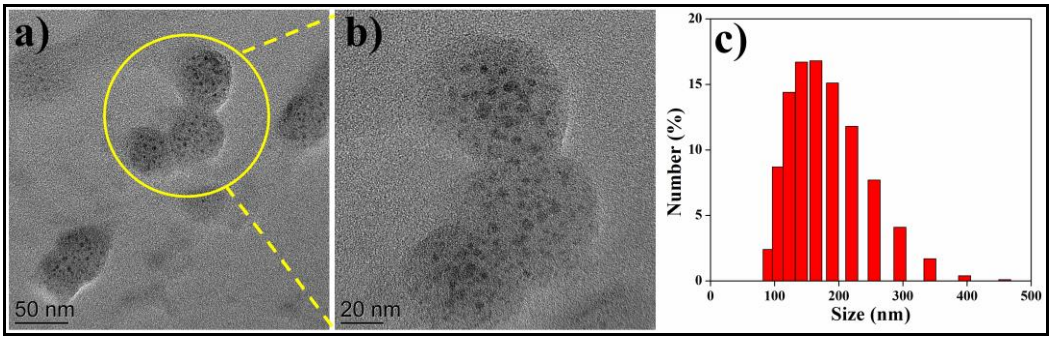

Figure 6. (a) TEM image of **NIONP-CaCD** conjugate, (b) zoomed TEM image and (c) DLS plot of **NIONP-CaCD** conjugate ([**NIONP-CaCD**] = 25 μg/mL)

The zeta potential value of **NIONP-CaCD** conjugate was –17.5 mV, indicating its ample aqueous stability. Elemental analysis (XPS) also confirmed that **NIONP-CaCD** conjugate

contains B along with other elements C, N, O and Ca (Figure 7a). Furthermore, the deconvoluted spectra of B 1s orbital of **NIONP-CaCD** conjugate exhibited peaks corresponding to B-C bond and B-OH bond at 190.47 and 192.37 eV (Figure 7b).[43] Along with these, a new peak at 191.44 eV was observed corresponding to the B-O linkage due to formation of boronate-diol adduct (Figure 7b).[43] **NIONP-CaCD** conjugate formation was further characterized by TGA. To this end, the TGA plot of the **NIONP-CaCD** conjugate exhibited a sharp decrease in weight between 200 and 300 °C corresponding to the decomposition of newly formed boronate-diol linkage conjugate (Figure 7c).

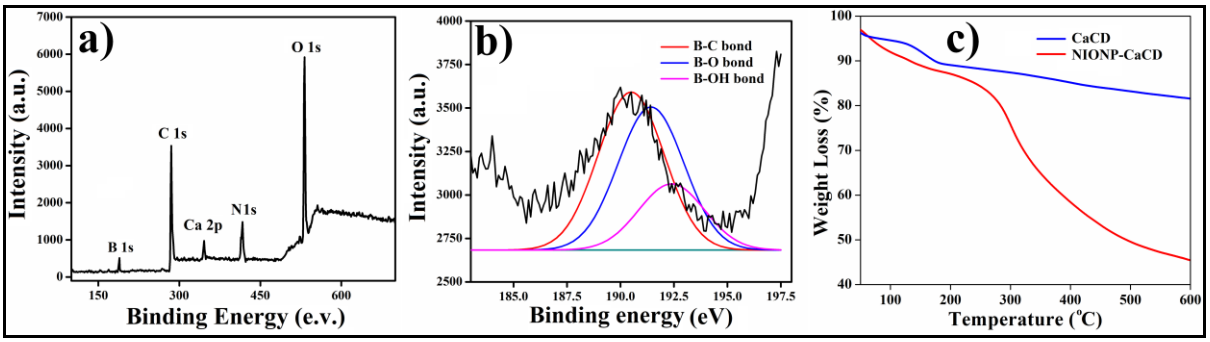

Figure 7. (a) XPS spectra, (b) deconvoluted B 1s orbital XPS spectra and (c) TGA plot of **NIONP-CaCD** conjugate.

The conjugation of **NIONP** with **CaCD** was also investigated by photoluminescence spectroscopy. Notably, the fluorescent intensity at λ_{em} = 440 nm of **CaCD** gets quenched in the **NIONP-CaCD** conjugate (Figure 8a), which further validates the conjugate formation by the attachment of **CaCD** on the surface of **NIONP**, which is in concurrence with microscopic evidence. Additionally, fluorescence microscopic image demonstrated the abundance of blue emitting **CaCD** around the surface of **NIONP** (Figure 8b). In the FTIR spectra, **CaCD** exhibited characteristic broad transmittance peak at ν_{N-H} (amide A, stretching) and ν_{O-H} (hydroxyl, stretching) = 3209-3565 cm^{-1}, and $\nu_{C=O}$ (amide, stretching) = 1601 cm^{-1} whereas, **NIONP** showed distinct transmittance peak at ν_{B-OH} (stretching) = 1039 cm^{-1} and 771 cm^{-1} and $\nu_{C=O}$ (imide, stretching) = 1657 cm^{-1} (Figure 8c). Moreover, for morpholine ring peaks at ν_{C-H} (stretching and bending) = 2985, 2816 and 1438 cm^{-1} and δ_{O-H} (bending) = 1395 cm^{-1} and ν_{C-O-C} (stretching) = 1239 cm^{-1} were also observed for **NIONP** (Figure 8c). After **NIONP-CaCD** conjugate formation, the FTIR spectra displayed peaks at ν_{N-H} (amide A, stretching) and ν_{O-H} (hydroxyl, stretching) = 3172-3590 cm^{-1}, $\nu_{C=O}$ (amide, stretching) = 1588 cm^{-1}, ν_{B-OH} (stretching) = 1027 cm^{-1} and 783 cm^{-1},

$\nu_{C=O}$ (imide, stretching) = 1663 cm^{-1}, ν_{C-H} (stretching and bending) = 2979, 2810 and 1395 cm^{-1} and δ_{O-H} (bending) = 1401 cm^{-1} and ν_{C-O-C} (stretching) = 1233 cm^{-1} which were correspond to the peak observed for **CaCD** and **NIONP** (Figure 8c). Furthermore, a characteristic transmittance peak at ν_{B-O} (stretching) = 1350 cm^{-1} suggesting the formation of **NIONP-CaCD** conjugate by virtue of boronate-diol linkage between **NIONP** and **CaCD** (Figure 8c). The **NIONP-CaCD** conjugate's relative quantum yield was determined to be 5.63% (with respect to quinine hydrogen sulfate).

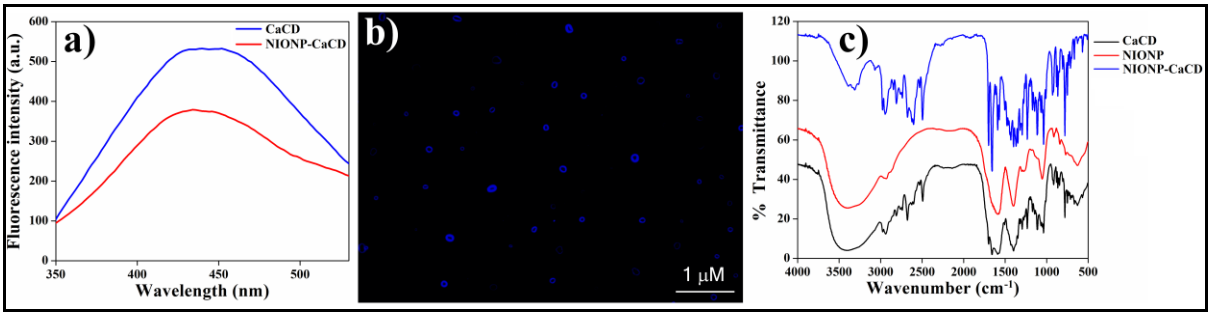

Figure 8. (a) Fluorescence spectra, (b) fluorescence microscopic image and (c) FTIR spectra of **NIONP-CaCD** conjugate.

To establish our proposed objective about the disintegration of **NIONP-CaCD** conjugate in lysosomal pH (4.5-5.0) through boronate-diol bond cleavage in acidic medium,[39] we performed fluorescence study of **NIONP-CaCD** conjugate in varying pH medium. In the pH-dependent photoluminescence study, we have seen that there is no significant change in intensity or in λ_{em} of the characteristic emission band (Figure 9a) of **NIONP-CaCD** conjugate at pH range from 6.0 to 7.4. Interestingly, at more acidic pH i.e., at pH 5.0 and 4.0, the fluorescence intensity of the peak got enhanced and similar to that witnessed in **CaCD**. This finding might be attributed to the generation of native **CaCD** from **NIONP-CaCD** conjugate through acidic pH induced decomposition of the boronate-diol bond of **NIONP-CaCD** conjugate into its primary constituents. Furthermore, this fragmentation was also evidenced by the fluorescence microscopic image of **NIONP-CaCD** conjugate in presence of acidic pH (5.0) (Figure 9b). This observation further suggests that the boronate-diol linkage, present in **NIONP-CaCD** conjugate could act as a stimuli-responsive (pH responsive) junction.

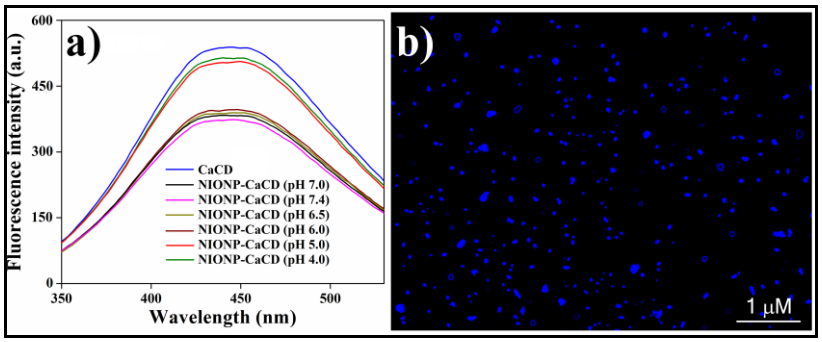

Figure 9. (a) Fluorescence spectra of **NIONP-CaCD** conjugate at different pH medium, (b) fluorescence microscopic image of **NIONP-CaCD** conjugate at pH 5.0.

4.2.5 HYDROXYCHOLOROQUINE (HCQ) LOADING ON NIONP-CaCD CONJUGATE.

After confirming the **NIONP-CaCD** conjugate's formation, we aim to assess its cargo loading and cellular transport efficiency. We separately loaded hydroxychloroquine (HCQ) into **NIONP**, **CaCD**, and **NIONP-CaCD** conjugate for this purpose. Hydroxychloroquine (HCQ) is a 4-aminoquinoline compound that has a history of over 50 years in usage, primarily for the prevention and treatment of malaria infections.[44] However, in recent times, there has been emerging evidence suggesting that HCQ may possess noteworthy anticancer properties through the inhibition of the autophagy pathway.[29,30] This effect has been observed in several types of cancer, including breast cancer, glioblastoma, lung cancer, multiple myeloma, pancreatic cancer, melanoma, hepatocellular carcinoma, and bladder cancer.[45] Although these findings underscore the potential of HCQ as a therapeutic option in the realm of cancer treatment, the primary drawback posed by HCQ is its dose-dependent adverse reaction and drug-drug Interactions. To mitigate these side effects and enhance drug delivery, our objective was to employ the **NIONP-CaCD** conjugate as a means of cellular transporter.

The HCQ-loading efficiency of the **NIONP-CaCD** conjugate was found to be 88% whereas in case of the individual **NIONP** and **CaCD**, it was 69 and 57 %, respectively (measured by comparing the absorbance of released HCQ with a standard calibration curve, Figure 10). The **NIONP** is capable of accommodating a considerable amount of HCQ in its inner core, whereas **CaCD** can upload HCQ to its surface adsorption. In the **NIONP-CaCD** conjugate, the combined presence of the aqueous core of the organic nanoparticle and the **CaCD** surface resulted in a synergistic contribution towards the notable improvement in the drug-loading efficiency compared to the individual constituents.

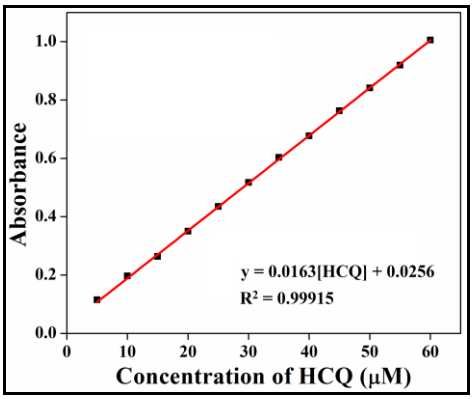

Figure 10. Calibration curve of HCQ in water.

Additionally, successful encapsulation of HCQ into **NIONP**, **CaCD**, and **NIONP-CaCD** conjugate was evidenced UV-vis and FTIR spectroscopy. In the FTIR spectra, the characteristic peaks of HCQ appeared at ν_{O-H} (stretching) = 3290 cm^{-1}, $\nu_{C=N}$ (stretching) = 1706 and 1525 cm^{-1}, $\nu_{C=C}$ (stretching) = 1626 and 1432 cm^{-1}, ν_{C-N} (bending) = 1133 cm^{-1} and $\nu_{C=Cl}$ = 1014 cm^{-1}. For **CaCD-HCQ**, the peaks were observed at approximately 3371-3615 cm^{-1} (O–H stretching), 1688 and 1519 cm^{-1} (C=N stretching), 1632 and 1444 cm^{-1} (C=C stretching), 1120 cm^{-1} (C–N bending), 1033 cm^{-1} (C–Cl stretching) (Figure 11a). Similarly, in the case of **NIONP-HCQ**, peaks at 3240-3478 cm^{-1} (O–H stretching), 1694 and 1544 cm^{-1} (C=N stretching), 1632 and 1438 cm^{-1} (C=C stretching), 1151 cm^{-1} (C–N bending), 1080 cm^{-1} (C–Cl stretching) were observed (Figure 11a). Furthermore, for **NIONP-CaCD-HCQ** we witnessed transmittance peaks at 3190-3490 cm^{-1} (O–H stretching), 1719 and 1520 cm^{-1} (C=N stretching), 1619 and 1445 cm^{-1} (C=C stretching), 1126 cm^{-1} (C–N bending) and 1052 cm^{-1} (C–Cl stretching) (Figure 11a) which correspond to the peaks of native HCQ, **NIONP** and **CaCD**. In the UV-vis study the characteristics peaks of native HCQ (λ_{max} at 329 and 342 nm) were present in all the drug loaded materials i.e., **CaCD-HCQ**, **NIONP-HCQ** and **NIONP-CaCD-HCQ** (Figure 11b). Moreover, a shoulder peak at 356-361 nm correspond to the distinct UV-vis peak of **NIONP** (Figure 11b). Therefore, FTIR and UV-vis investigations delineated the successful loading of HCQ on **NIONP-CaCD** conjugate. HCQ being a cationic amphiphilic molecule can be accumulated inside self-assembled **NIONP** and the noncovalent grafting of the sp^2-carbon network of **CaCD** with the aromatic moieties of HCQ via π–π interactions facilitated drug loading on the surface of carbon dots. Therefore, the HCQ loading efficiency of the **NIONP-CaCD** conjugate exhibited significant enhancement compared to the individual components.

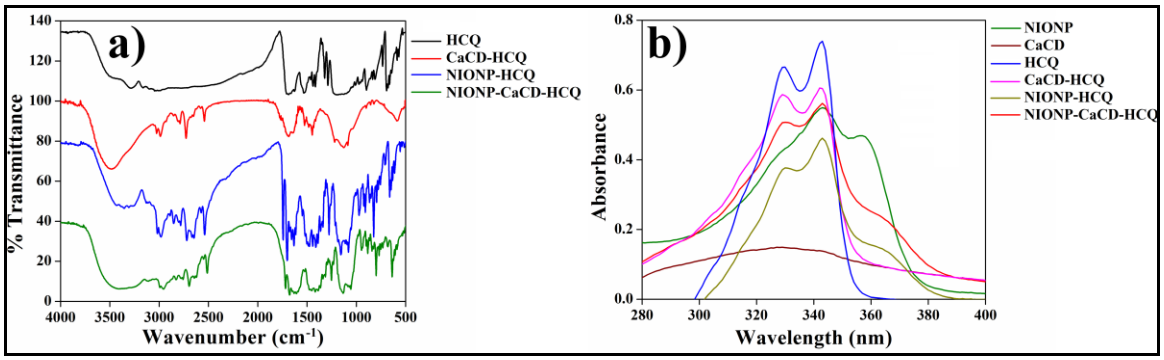

Figure 11. (a) FTIR spectra and (b) UV-vis spectra of HCQ loaded **NIONP**, **CaCD** and **NIONP-CaCD** conjugate.

4.2.6 MEDIA STABILITY AND CELL VIABILITY STUDY.

Prior to the utilization of the newly synthesized NI-based organic nanoparticle (**NIONP**), Ca^{2+}-doped carbon dot (**CaCD**) and **NIONP-CaCD** conjugate as theranostic bioprobe, we investigated their stability in biological media in a time dependent manner. In FBS-DMEM media, **NIONP** (200 µg/mL), **CaCD** (200 µg/mL) and **NIONP-CaCD** (200 µg/mL) were added separately having FBS of different concentrations (up to 75%) and kept for 48 h (Figure 11a-c). The prolonged stabilities all the components were also investigated by keeping the mixtures of **NIONP** (200 µg/mL)-DMEM (10% FBS), **CaCD** (200 µg/mL)-DMEM (10% FBS) and **NIONP-CaCD** (200 µg/mL)-DMEM (10% FBS) for 10 days (Figure 11d-f). In all cases the suspension stability index (SSI) in media was ~90 ± 2% for different concentrations of FBS (0–75%, Figure 11a-c). The stability of all the solutions in biological media was also in accordance with the respective visual images (Figure 11a-c). Ensuring a high media stability of all the samples, the cytocompatibility of **NIONP**, **CaCD** and **NIONP-CaCD** conjugate was investigated against the A549 and HepG2 mammalian cell line by MTT assay (Figure 13a,b). The **NIONP** nanoparticle (10-200 µg/mL) showed a superior cytocompatibility with 85–90% viable cells after 24 h of incubation. On the contrary, in the case of **CaCD** (10-200 µg/mL), moderate cell viability (43–80%) i.e, substantial cell killing ability was noted presumably due to the inherent toxicity and killing effect due to calcium overload mediated cell death (calcicoptosis) by **CaCD** (Figure 13a,b). Notably, **NIONP-CaCD** conjugate with similar concentration range (10-200 µg/mL), exhibited similar cell killing efficacy for which ~53–85% of cells were found to be alive after 24 h incubation (Figure 13a,b). On the contrary, substantial cell viability (70-95%) was observed for NIH3T3 (noncancer) cells upon exposure of all the components (Figure 13c).

This might be attributed due to sufficient levels of CAT (Catalase) in normal cells, which can effectively combat oxidative damage and facilitate the passage of exogenous Ca^{2+} ions through the channels associated with calcium (Ca^{2+}). Therefore, the inclusion of cytotoxic **CaCD** on the surface of **NIONP** significantly enhanced the toxic effect i.e., cell killing potency of the **NIONP-CaCD** conjugate and satisfied its suitability as a superior theranostic agent as well as cellular transporter in the combination therapy.

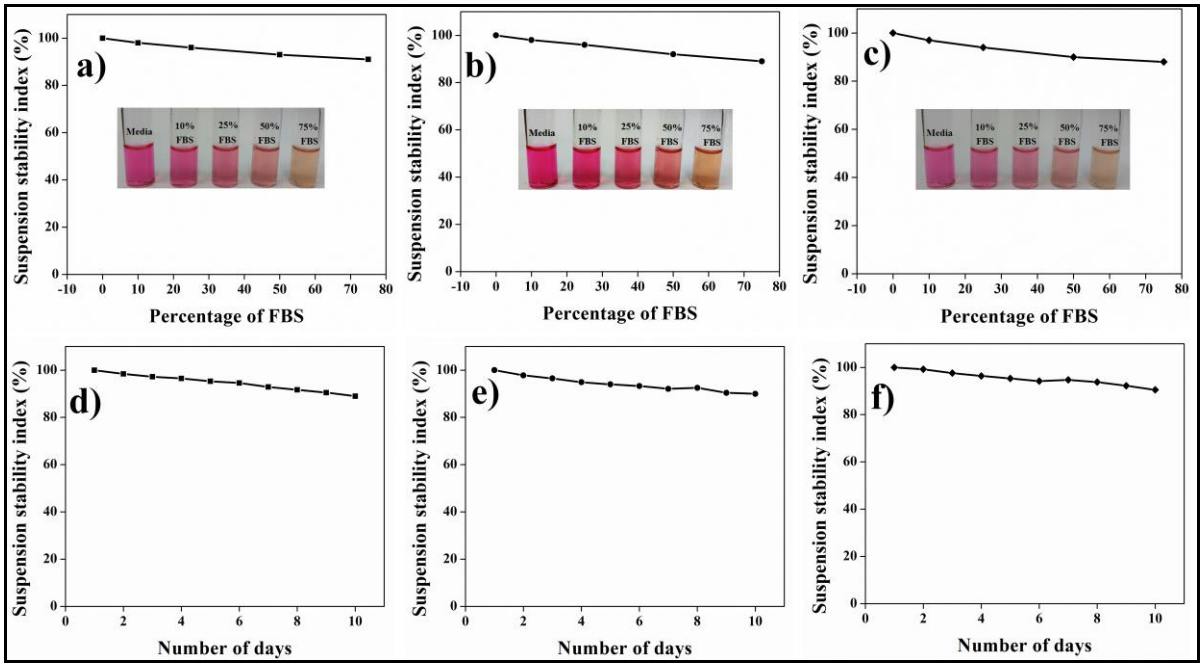

Figure 12. Suspension stability index of **NIONP**, **CaCD** and **NIONP-CaCD** conjugate (200 µg/mL) in (a-c) DMEM media supplemented with different percentage of FBS (0-75%) and (d-e) DMEM media supplemented with 10% of FBS over the 10 days incubation respectively.

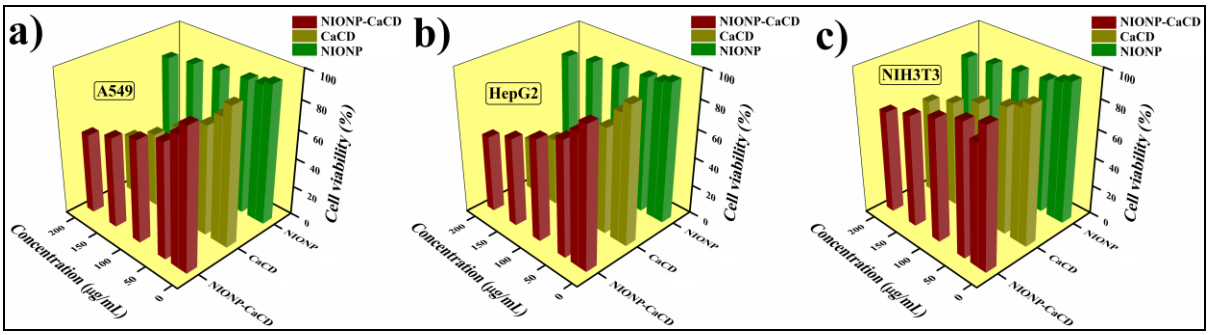

Figure 13. MTT-based % cell viability of (a) A549 and (b) HepG2 cells in presence of varying concentration of **NIONP**, **CaCD** and **NIONP-CaCD** conjugate over 24 h incubation period. Percent errors are within ± 3% in triplicate experiments.

4.2.7 INTERNALIZATION OF CaCD AND NIONP-CaCD CONJUGATE WITHIN CANCER CELLS.

The potential application of **CaCD** and its conjugate with **NIONP** (**NIONP-CaCD** conjugate) as a theranostic probe relies heavily on their intrinsic fluorescence characteristics. Due to their impressive emissive properties, we initially explored their uses in cellular imaging and biolabeling. The process involved introducing **CaCD** and the **NIONP-CaCD** conjugate to mammalian cells and observing the outcomes using fluorescence microscopy. Specifically, we conducted experiments on A549 (lung carcinoma) and HepG2 (hepatocellular carcinoma) cells. These cells were individually incubated with 50 µg/mL of both **CaCD** and **NIONP-CaCD** conjugate for a duration of 6 h. Subsequently, the images captured using fluorescence microscopy exhibited a blue fluorescence within the both types of cells (Figure 14,15). This phenomenon signified a substantial intracellular uptake of both **CaCD** and **NIONP-CaCD** conjugate by the mammalian cells. Notably, the fluorescence intensity observed in cells treated with the **NIONP-CaCD** conjugate showed a slight reduction compared to cells treated with native **CaCD**. This finding correlated with the results obtained from in vitro studies, as depicted in the corresponding figures (Figure 8a). Consequently, the luminous behavior of both **CaCD** and **NIONP-CaCD** conjugate validated their capacity to stain cells, thereby potentially serving as bioprobes for diagnostic purposes (Figure 14,15).

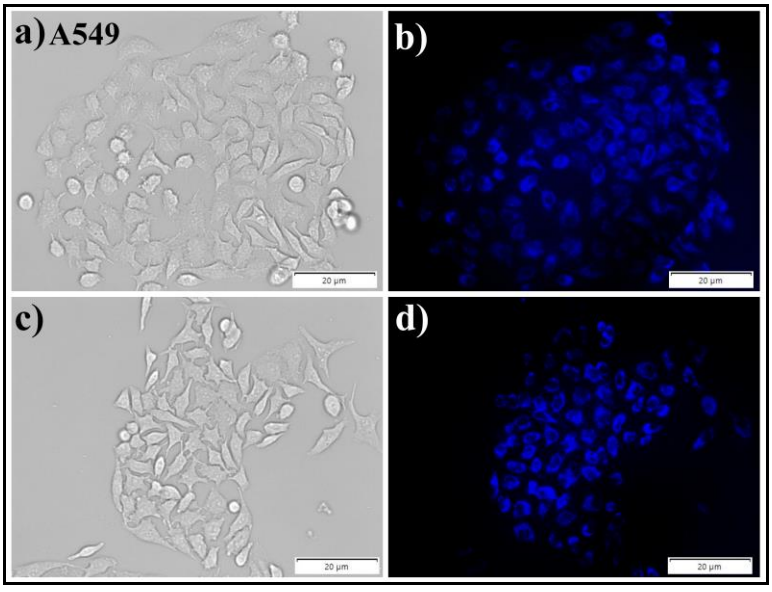

Figure 14. Bright-field and fluorescence microscopic images of A549 cells of after 6 h incubation with (a,b) **CaCD** and (c,d) **NIONP-CaCD** conjugate (50 µg/mL), respectively.

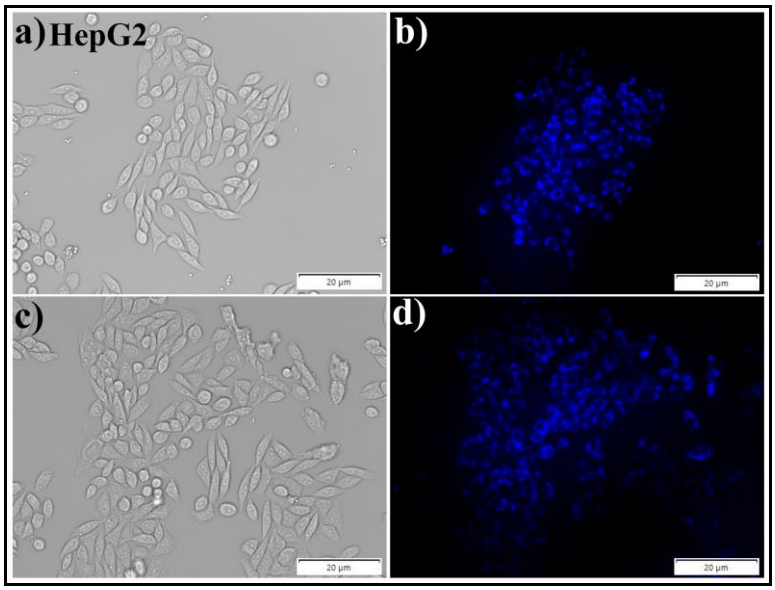

Figure 15. Bright-field and fluorescence microscopic images of HepG2 cells of after 6 h incubation with (a,b) **CaCD** and (c,d) **NIONP-CaCD** conjugate (50 μg/mL), respectively.

4.2.8 KILLING OF CANCER CELLS THROUGH COMBINATION THERAPY.

As we have seen in the preceding experiments, the newly developed **NIONP-CaCD** conjugate have shown the potential to kill cancer cell via calcium (Ca^{2+}) overload mediated apoptosis as well as considerable cellular internalization capacity. Therefore, after successful loading of hydroxychloroquine (HCQ), we were curious to investigate the cell killing efficiencies in HepG2 and A549 cells following exposure to the **NIONP-CaCD-HCQ** by exploiting the synergistic action of both Ca^{2+} overload (as pro-drug) and HCQ (drug) in prodrug-free drug combination therapy. To this end, **NIONP-HCQ**, **CaCD-HCQ** and **NIONP-CaCD-HCQ** were separately incubated with both A549 and HepG2 cancer cells for 24 h. **NIONP-HCQ** exhibited a comparable killing efficacy against both cancer cells, A549 (5 ± 3 to 64 ± 1%), and HepG2 (6 ± 2 to 65 ± 1%), with varying concentration from 10 to 200 μg/mL (Figure 16a,b). Expectedly, cytocompatible **NIONP** showed cancer cell killing ability owing to the HCQ mediated lysosomal membrane permeabilization (LMP) resulting in the translocation to the cytoplasm of intralysosomal components, such as cathepsins, inducing lysosomal-dependent cell death (LDCD). To enhance the therapeutic efficiency, next we utilized combination of pro-drug and free drug by means of HCQ loaded **CaCD** (**CaCD-HCQ**) and **NIONP-CaCD** (**NIONP-CaCD-HCQ**). According to the MTT assay, in the case of **CaCD-HCQ**,

with its increasing concentration (10-200 μg/mL), 6 ± 1 to 75 ± 2% and 4 ± 1 to 77 ± 2% killing was observed for A549 and HepG2 cells, respectively (Figure 16a,b) due to synergistic effect of calcicoptosis by **CaCD** and lysosomal cell death by HCQ (Scheme 1). Although the **CaCD-HCQ** formulation showed synergistic action in killing the cells in comparison to that of only **CaCD**, the killing was not that much substantial for **CaCD-HCQ** due to poor drug loading efficacy (57%) by **CaCD** and also absence of any lysosome targeting moiety in **CaCD** in order to maximize the effect of HCQ. Conversely, in the case of **NIONP-CaCD-HCQ**, A549 and HepG2 cell killing steadily increased from 7 ± 2 to 89 ± 1% and 5 ± 1 to 92 ± 2%, respectively with increasing concentration of the drug formulation (Figure 16a,b).

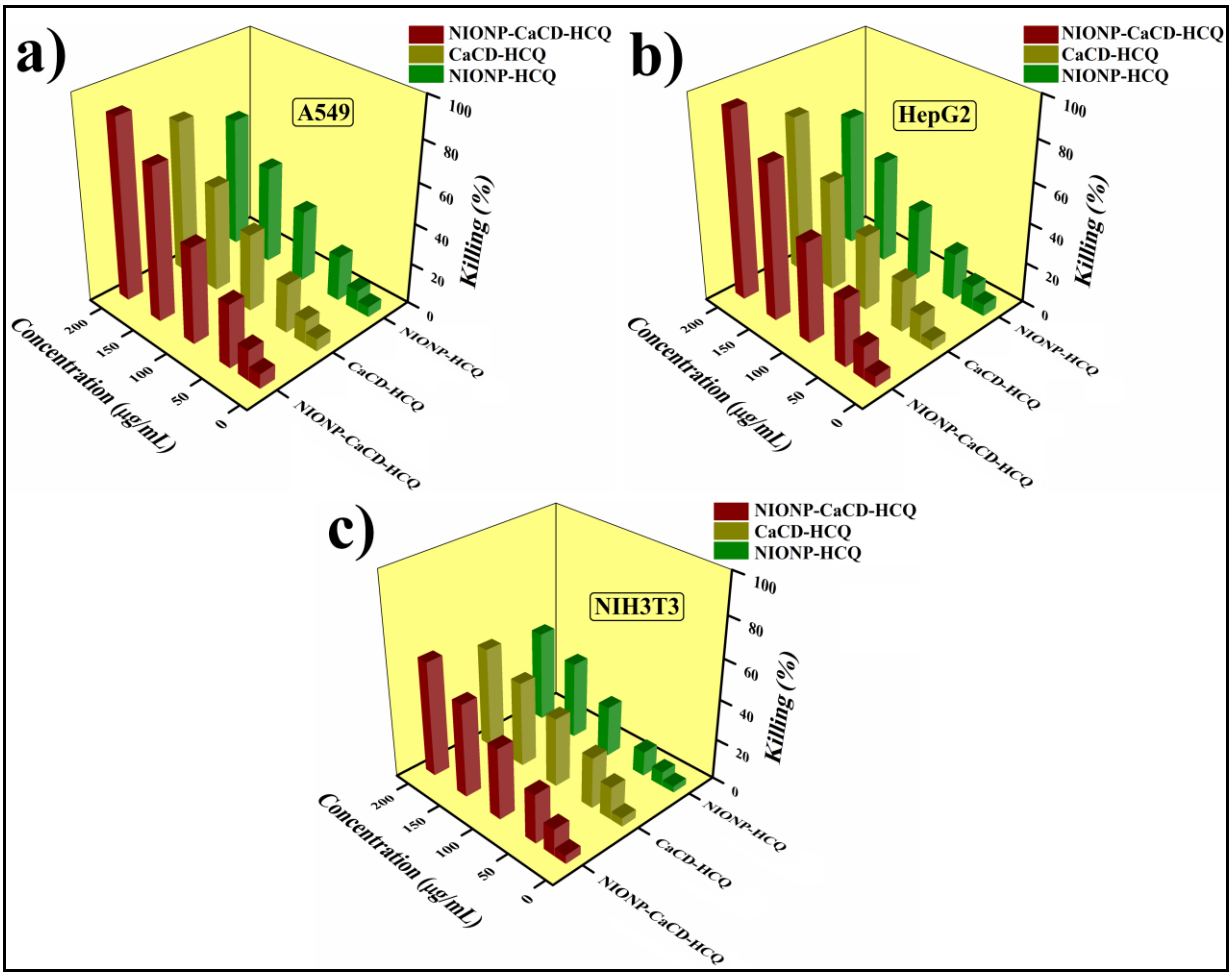

Figure 16. Killing efficiency (determined by MTT assay) of hydroxychloroquine (HCQ)-loaded **NIONP** (**NIONP-HCQ**), **CaCD** (**CaCD-HCQ**) and **NIONP-CaCD** conjugate (**NIONP-CaCD-HCQ**) toward NIH3T3, (a) A549, (b) HepG2, (c) NIH3T3 cells for 24 h. Percent experimental errors are within approximately ±3% in triplicate experiments.

Here, the **NIONP-CaCD-HCQ** formulation successfully exhibited synergistic action toward efficient killing (~ 1.5-fold) compared to that of **NIONP-HCQ** and **CaCD-HCQ** as a result of combination therapy, and at the same time, it was more effective to kill cancer cells due to better drug loading capacity of **NIONP-CaCD** conjugate (88%) and presence of lysosome targeting unit to achieve the maximum killing effect by HCQ. Notably, the combination of two modes of cancer therapy (calcium overload induced calcicoptosis by **CaCD** and lysosomal cell death by HCQ) led to higher killing of cancer cells even with a lower dose of HCQ, which is expected to minimize the HCQ-induced systemic side effects (Scheme 1). Furthermore, we also checked the killing efficiency of **NIONP-HCQ**, **CaCD-HCQ** and **NIONP-CaCD-HCQ** formulation for NIH3T3 (non-cancerous) cells. For normal cell NIH3T3, killing ability of **NIONP-CaCD-HCQ** varied from 4 ± 1 to 57 ± 2% under the similar experimental concentration range (Figure 16c). **NIONP-CaCD-HCQ** exhibited ~1.7-fold higher killing of A549 and HepG2 malignant cells than NIH3T3 normal cells at different concentrations of pro-drug-free drug formulation. Due to the down-regulation of catalase (CAT) in cancer cells, the constant HCQ-mediated oxidative stress could destroy protein functions, thus leading to the desensitization of the Ca^{2+}-related channels and impeding the Ca^{2+} signal transmission. Conversely, adequate amounts of CAT in normal cells could resist oxidative damage and enable the exogenous Ca^{2+} to transfer through the Ca^{2+}-associated channels. Hence, **NIONP-CaCD-HCQ** may emerge as a selective theranostic agent in the field of combination therapy for treating cancer.

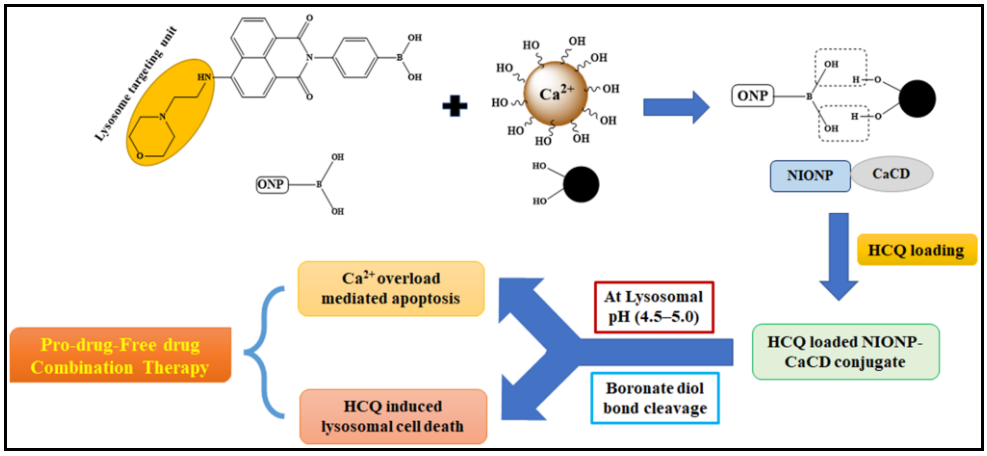

Scheme 1. Schematic representation of fabrication of **NIONP-CaCD** conjugate through boronate-diol linkage and its application in cancer theranostic by exploiting pro-drug-free drug combination therapy.

4.3 CONCLUSION

In summary, we have developed a naphthalimide based amphiphile (**NIONP**) consisting of boronic acid moiety and lysosome targeting unit. In addition, we also synthesized hydroxyl (-OH) functionalized Ca^{2+}-doped carbon dot (**CaCD**) having intrinsic fluorescence (blue emitting). **NIONP** formed self-assembly directed spherical shaped organic nanoparticles in DMSO-water solvent system via *J*-type aggregation. Next, we fabricated the **NIONP-CaCD** conjugate through boronate-diol interaction between boronic acid moiety in **NIONP** and -OH group in **CaCD**. This newly construct **NIONP-CaCD** conjugate was then employed in bioimaging by exploiting the intrinsic fluorescence of **CaCD** as well as in pro-drug-free drug combination therapy for cancer treatment. **NIONP-CaCD** conjugate also showed the excellent ability of uploading the drug hydroxychloroquine (HCQ) (**NIONP-CaCD-HCQ**). Notably, the disintegration of the **NIONP-CaCD** conjugate into its separate constituents took place through the cleavage of the boronate-diol bond at the lysosomal pH range (4.5-5.0) resulting in the liberation of HCQ and **CaCD**. Subsequently, this release could lead to cell death initiated by HCQ induced lysosomal membrane permeabilization (LMP), possibly intertwined with a phenomenon known as calcific apoptosis or calcicoptosis. This cytocompatible pro-drug-free drug formulation, **NIONP-CaCD-HCQ**, led to approximately a 1.5-fold increase in cancer cell death compared to standalone therapy with individually loaded cargo using the native compounds. The majority of advancements in this research domain are at early stages due to the existing obstacles linked to clinical application. Our strategy, which investigates the combined **NIONP-CaCD** conjugate mediated synergistic impact of Ca^{2+} overload-based oncotherapy and HCQ-induced chemotherapy, could be contemplated as a potential combined treatment approach for cancer in the future, provided its effectiveness is substantiated.

4.4 EXPERIMENTAL SECTION

4.4.1 MATERIALS.

MTT dye (3-(4,5-dimethylthiazol-2-yl)-2,5-diphenyltetrazolium bromide), 4-(2-aminoethyl) morpholine, Tris(hydroxymethyl)aminomethane, 4-aminophenylboronic acid, and all deuteriated solvents were bought from Sigma-Aldrich. 4-bromo-1,8-naphthalenedicarboxylic anhydride were purchased from TCI chemicals, India. Citric acid,

calcium acetate, methyl cellosolve, column chromatography reagents and other solvents and chemicals were acquired from SRL, India. Dialysis tubing was procured from Thermo Scientific SnakeSkin (3.5K MWCO). All the studies were done using Milli-Q water. All type of cells and cell culture ingredients were procured from NCCS, Pune India and Invitrogen, respectively. 300 MHz and 400 MHz AVANCE (Bruker) spectrometer was used for NMR spectroscopy and Bruker Ultraflex MALDI mass spectrometer (2,5-dihydroxy benzoic (DHB) acid as matrix) was used to record MALDI-TOF spectra.

4.4.2 SYNTHESIS OF NAPHTHALIMIDE BASED AMPHIPHILE, NIONP.

1,8-Naphthalimide-based amphiphile (**NIONP**) was synthesized following the pathway, as depicted in Scheme 2. At first, 4-bromo-1,8-naphthalene anhydride (1 equiv) and 4-(2-aminoethyl)morpholine (1 equiv) were refluxed (80 °C) in methoxy ethanol for 4 h under an inert atmosphere. The reaction mixture was cooled to room temperature and poured into 50 mL of ice-cold distilled water. The precipitate was filtered, and washed with ethanol, and dried under vacuum at 60 °C overnight to afford a light-yellow solid. This yellow intermediate product (1 equiv) and 4-aminomethylphenylboronic acid (1 equiv) were dissolved in dry EtOH and refluxed at 75-80 °C for 8 h under N_2 atmosphere. After cooling to room temperature, the filtrate was vacuum-evaporated to get a brown solid. This solid was purified in 100-200 mesh silica gel chromatography using 5% methanol in chloroform (v/v) as the eluent to obtain the **NIONP** (Scheme 2).

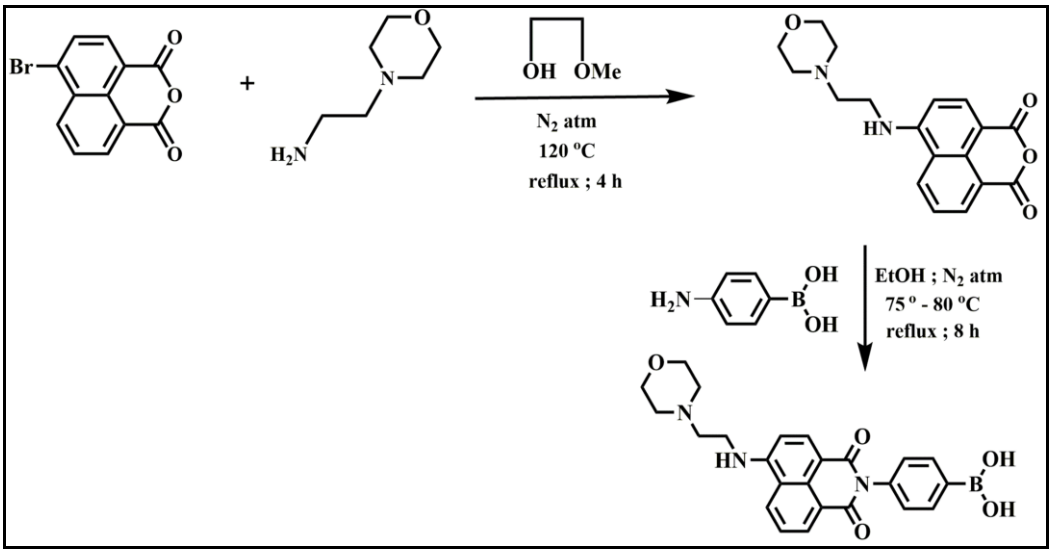

Scheme 2. Synthetic scheme of **NIONP**.

4.4.3 SYNTHESIS OF Ca^{2+}-DOPED CARBON DOT (CaCD).

A Ca^{2+}-doped carbon dot (**CaCD**) was synthesized by the hydrothermal route (Scheme 3). Mono-hydrated citric acid, tris(hydroxymethyl)aminomethane, and calcium acetate were dissolved in Milli-Q water maintaining a 2:2:1 molar ratio. The solution was mixed and sonicated to obtain a transparent solution. The solution was heated at 180 °C for 6 h in a heating platform. The color of the solution gradually turned brown. Next, dialysis with the solution was carried out (MWCO, 3.5 K) in Milli-Q water and the compound in dialysis tube was lyophilized to obtain Ca^{2+}-doped carbon dot (**CaCD**) with an ~67% yield (Scheme 3).

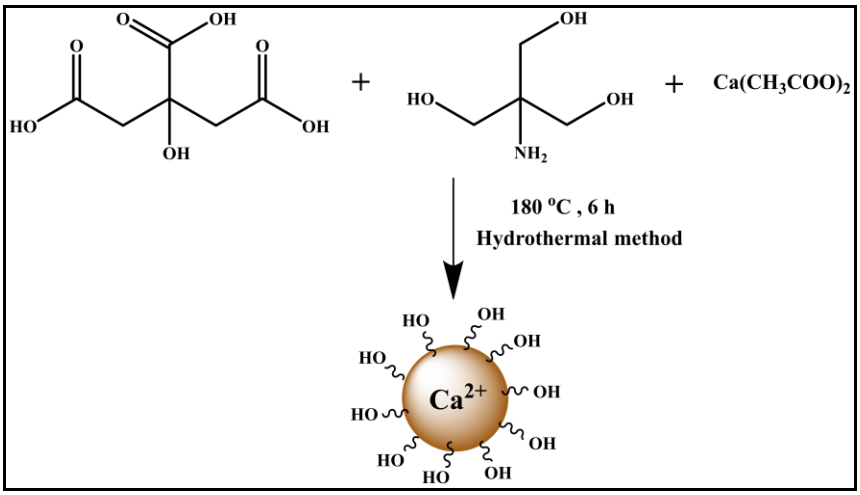

Scheme 3. Synthetic scheme of **CaCD**.

4.4.4 PREPARATION OF NIONP-CaCD CONJUGATE.

1 mg of **NIONP** was dissolved in 10 ml of DMSO-water (f_w = 99 vol%) to form the translucent self-aggregated organic nanoparticle solution. Aqueous solution of **CaCD** (200 µg/mL) was added with this preformed **NIONP** solution by mixing with the weight ratio of 1:5 w/w for **NIONP** and **CaCD**. The resulting mixture was stirred for overnight to form the **NIONP-CaCD** conjugate through boronate-diol linkage between **NIONP** and **CaCD**. Next, the solution was centrifuged at 3000 g for 20 min. Under such conditions all free **NIONP** were in the supernatant, which was discarded and the pellet was dispersed in Milli-Q water. The resulting suspension (**NIONP-CaCD** conjugate) was found to be stable and stored at 4 °C for further examination. Furthermore, the above **NIONP-CaCD** conjugate suspension was centrifuged at 24000 g for 30 min and the supernatant was stored. The obtained pellet was dispersed in Milli-Q water and again centrifuged at 24000 g for 30 min. This process was

repeated for three times to ensure the removal of excess **CaCD** from the boronate-diol adduct. Consequently, all free **CaCD** got precipitated out from the solution. All the supernatant containing the boronate-diol adduct was collected and lyophilized in Virtis4KBTXL-75 freeze drier under vacuum to get solid boronate-diol adduct i.e., **NIONP-CaCD** conjugate.

4.4.5 SAMPLE PREPARATION FOR SELF-ASSEMBLY OF NIONP.

The naphthalimide derivative (**NIONP**) was dissolved in DMSO to prepare the stock solution of 10 mM concentration. To achieve different composition needed for subsequent experiments, required amount aliquot was added to the varying compositions of DMSO-water binary solvent mixture in various ratio from this stock solutions in DMSO. Detailed characterization and application experimental procedure of the self-aggregated **NIONP** in varying compositions of DMSO-H_2O by different microscopic and spectroscopic studies have been provided.

4.4.6 TRANSMISSION ELECTRON MICROSCOPY (TEM) STUDY.

NIONP (50 μM) solution in (1:99 v/v) DMSO-water (f_w = 99 vol%) was deposited on a 300-mesh carbon-coated copper grid and dried. Negative staining of the copper grid was done with freshly prepared 1 μL of uranyl acetate solution (1% w/v), and a filter paper was used to blot the excess solution. Before taking the image in transmission electron microscopic, the sample was dried for 4 h in vacuum. The TEM images were taken in JEOL JEM 2010 microscope. Similarly, we also performed TEM study for the solution of **CaCD** and **NIONP-CaCD** conjugate without any staining.

4.4.7 DYNAMIC LIGHT SCATTERING (DLS) STUDY AND ZETA (ζ) POTENTIAL MEASUREMENT.

To determine the mean hydrodynamic diameter (D_h) of **NIONP** (50 μM) in f_w = 99 vol% we performed DLS study using a fixed-angle apparatus (Zen 3690 Zetasizer Nano ZS instrument (Malvern Instrument Ltd.). Measurement of the scattering intensity was done at an angle of 175°. We also carried out DLS experiments for **NIONP-CaCD** conjugate solution. The zeta (ζ) potential measurement was performed with solution of **CaCD** and **NIONP-CaCD** conjugate.

4.4.8 UV-VISIBLE STUDY.

Agilent Cary 60 spectrophotometer was used to record UV-vis spectra. UV-vis spectra of **NIONP** (50 μM) were performed in various solvent compositions of DMSO-water changing the water content from f_w = 0 vol% (non-self-assembled state) to f_w = 99 vol% (self-assembled state). Formation of **NIONP-CaCD** conjugate in different weight ratios of **NIONP** and **CaCD** was followed by recording UV-vis spectra in a quartz cell (path length 10 mm). Sample temperature was fixed at 25 °C by a Peltier thermostat.

4.4.9 FTIR STUDY.

PerkinElmer Spectrum 100 FTIR spectrometer was used for FTIR measurements. FTIR spectra of **NIONP** was performed in the amphiphilic state i.e., in $CHCl_3$ (in non-self-assembled state) at room temperature. 1 mm CaF_2 cell was used to perform the experiment of FTIR study. Similarly, FTIR spectra of **CaCD** and **NIONP-CaCD** conjugate were also recorded.

4.4.10 SOLVENT-DEPENDENT ^{1}H-NMR STUDY.

Solvent dependent ^{1}H-NMR study was performed with a Avance 300 MHz (Bruker) spectrometer. The spectra **NIONP** (1 mM) in DMSO-d_6 and in several solvent systems (2:1 (v/v) and 1:1 (v/v) of DMSO-d_6-D_2O) were recorded.

4.4.11 CIRCULAR DICHROISM (CD) STUDY.

CD spectra of **NIONP** (50 μM) in DMSO (non-self-assembled state) and 1:99 v/v DMSO-water system (self-aggregated state) was recorded by using a quartz cuvette of 1 mm path length in a JASCO J-815 CD spectropolarimeter.

4.4.12 STEADY-STATE FLUORESCENCE ANISOTROPY STUDY.

Fluorescence spectra were recorded using the hydrophobic fluorescent probe 1,6-diphenyl-1,3,5-hexatriene (DPH) in a Varian Cary Eclipse fluorescence spectrophotometer. The steady-state anisotropy (r) of DPH was measured in individual solution of **NIONP** in different solvent compositions of DMSO-water and with different concentration of **NIONP** (50-200 μM). A stock solution of DPH (0.2 mM) was prepared in tetrahydrofuran (THF), and in each investigating solution (1 mL) the final concentration of DPH was maintained at 1 μM. The DPH

included **NIONP** solution was excited at 325 nm. The emission intensity was measured at 450 nm using an emission cutoff filter at 430 nm to avoid any scattering due to turbidity of the solution. The excitation and emission slit widths were kept at 5 nm. The fluorescence anisotropy (r) was calculated by the instrument software using following equation,

$$r = \frac{(I_{VV} - G I_{VH})}{(I_{VV} + 2G I_{VH})} \quad (1)$$

where I_{VV} and I_{VH} are the intensities of the emission spectra obtained with vertical and horizontal polarization (for vertically polarized light), respectively, and G = I_{HV}/I_{HH} is the instrumental correction factor, where I_{HV} and I_{HH} are the emission intensities obtained with vertical and horizontal polarization (for horizontally polarized light), respectively. The fluorescence measurements were performed at least five times for each sample at 25 °C.

4.4.13 X-RAY PHOTOELECTRON SPECTROSCOPY (XPS) STUDY.

For X-ray photoelectron spectroscopy (XPS), two drops of **CaCD** and **NIONP-CaCD** conjugate solutions were cast on rectangular Cu plates and dried overnight before investigation in a X-ray photoelectron spectrometer (Omicron series 0571). The spectra were processed with Casa XPS v.2.3.12 software using a peak-plotting routine with symmetrical Gaussian-Lorentzian functions.

4.4.14 X-RAY DIFFRACTION (XRD) STUDY.

X-ray diffraction (XRD) spectra of dried **CaCD** and **NIONP** (in f_w = 99 vol%) were obtained on a diffractometer (Bruker D8 Advance) having CuK_α radiation (α = 0.15406 nm) as the source (voltage and current was 40 kV and 30 mA, respectively).

4.4.15 FLUORESCENCE MICROSCOPIC STUDY.

Drop casting of 10 µL solution of **CaCD** and **NIONP-CaCD** conjugate (in pH 7.0 and 4.0) was performed on a glass slide. After that, images were taken under fluorescence microscope (Olympus IX83 inverted) at 40x magnification.

4.4.16 PHOTOLUMINESCENCE STUDY.

Excitation dependent emission spectra of **CaCD** (25 µg/mL) were recorded with varying λ_{ex} from 280 to 340 nm using excitation and emission slits at 5 nm. In case of **NIONP-CaCD**

conjugate ([**NIONP-CaCD**] = 25 μg/mL), the fluorescence spectra were recorded at λ_{ex} = 340 nm using excitation and emission slits at 5 nm. Moreover, pH dependent fluorescence spectra of **NIONP-CaCD** conjugate were recorded.

4.4.17 QUANTUM YIELD (QY) MEASUREMENT.

Quantum yields are usually calculated with respect to an optical dilute standard fluorophore solution having a well-known QY (ϕ_s). The Parker-Rees method was used to determine the QYs (ϕ_u) of the unknown fluorophore.

$$\emptyset_u = \left(\frac{A_s F_u n_u^2}{A_u F_s n_s^2}\right)\emptyset_s \qquad (2)$$

Here, A_u and A_s were the absorbance of unknown sample and reference sample at the excitation wavelength respectively. Exciting at the same excitation wavelength, the area of the integrated fluorescence intensity for the unknown sample and known sample were F_u and F_s respectively. A solution having similar absorbance (<0.01) was used to measure the QY. n_u = the refractive indices of the solvents in which the unknown was prepared and n_s = the refractive indices of the solvents in which the standard samples were prepared. Here, we have chosen quinine sulfate dissolved in 0.1 M sulfuric acid (H_2SO_4) as the standard and its QY (ϕ_s) = 54.0%.

4.4.18 CELL CULTURE.

10% FBS, antibiotic (streptomycin and penicillin) added DMEM were used to culture A549, HepG2 and NIH3T3 cells in an incubator (5% CO_2 and 37 °C). Both types of cells were cultured, and trypsinization was performed after every 3 days when the cells were 80% confluent. We performed cytocompatibility, bioimaging, MTT assay and all other biological experiments with those treated cells.

4.4.19 MEDIA STABILITY AND CYTOCOMPATIBILITY CHECK.

The stability of 50 μM of **NIONP** (in f_w = 99 vol%) and 50 μg/mL of **CaCD** and **NIONP-CaCD** conjugate was investigated in biological milieu by adding **NIONP**, **CaCD** and **NIONP-CaCD** conjugate in the FBS-supplemented media and kept for a long-time duration. The suspension stability index (SSI) of **NIONP**, **CaCD** and **NIONP-CaCD** conjugate was determined by recording the absorbance at 348 nm (corresponding to the λ_{max} of **NIONP** in f_w = 99 vol%) at various time intervals.

Suspension stability index (SSI) = $(A_t/A_o) \times 100$ where A_t = absorbance of the solutions at different time intervals and A_o = initial absorbance of the solutions at 348 nm, respectively.

MTT assay was performed to investigate cytocompatibility of **NIONP**, **CaCD** and **NIONP-CaCD** conjugate. In this assay, mitochondrial dehydrogenase excreting from viable cells reduced the soluble tetrazolium gets into insoluble formazan. Spectrophotometric method was used to estimate the amount of insoluble formazan dissolving in DMSO. The production of formazan is proportional to the quantity of alive cells. First, HepG2 and A549 cells (2×10^4 cells per well) were incubated in a 96-well plate for 24 h (5% CO_2, 37 °C). Next, all the cells were treated with 10-200 µM of **NIONP** (f_w = 99 vol%) and 10-200 mg/mL of **CaCD** and **NIONP-CaCD** conjugate for 24 h. Addition of 10 µL of MTT stock solution (5 mg mL^{-1}) was carried out into the cells which were incubated further for 4 h. After the incubation, Bio Tek1 Elisa Reader was used to record the absorbance of the precipitated formazan which was solubilized in DMSO (λ_{ex} = 570 nm). The number of alive cells was calculated as % viability by following the equation,

% viability = (A_{570} (treated cells) – background) / (A_{570} (untreated cells) – background) × 100 (3)

4.4.20 CELLULAR IMAGING.

A549 and HepG2 cells were cultured in a chamber slide. After that, cells were incubated with i) **CaCD** (50 µg/mL), and ii) **NIONP-CaCD** conjugate (50 µg/mL) for 6 h. Washing of cells were done with phosphate buffer saline (PBS) (three times). After that, 4% paraformaldehyde was used for fixing. Next, glycerol (50%) was used to mount and the glass slide was covered with a cover slip for 24 h. IX83 inverted microscope at 20x magnification was used for cellular imaging.

4.4.21 HCQ LOADING AND MTT ASSAY.

To the 1:99 v/v DMSO-water solution of **NIONP**, aqueous **CaCD** and **NIONP-CaCD** conjugate solutions (1 mg/mL), aqueous solution of hydroxychoroquine (2 mg/mL) was added. The mixture was taken in a 10 mL volumetric flask containing 1 mg of all the components and 2 mg of hydroxychoroquine (HCQ) and stirred for 24 h. For **NIONP**, separation of the drug-encapsulated ONPs was carried out by centrifugation (10000 rpm, 1 h). After dispersing the pellet in 1:99 v/v DMSO-water, 100 µL of aliquot was diluted to 1 mL of water to estimate the

quantity of loaded HCQ. Measurement of the absorbance of the solution was calculated by using standard calibration curve of HCQ. For, **CaCD** and **NIONP-CaCD** conjugate the standard Thermo Scientific SnakeSkin 3.5 K MWCO dialysis tubing was used for dialysis. The **NIONP-CaCD-HCQ** complex was dialyzed in Milli-Q water for 48 h. Possible loading of HCQ on **NIONP-CaCD** conjugate was further investigated by UV-vis and FTIR study. The drug loading efficiency was calculated by recording the UV-vis absorbance (329 nm) and calibration curve (y = 0.0163[HCQ] + 0.0256).

drug loading efficiency (DLE) = [(amount of drug taken - free drug)/amount of drug taken] x 100 (4)

In an another MTT assay, HepG2, A549 and NIH3T3 cells were incubated separately with HCQ-loaded **NIONP**, **CaCD** and **NIONP-CaCD** (10-200 μg/mL) for 24 h in 96-well plates. Equation 3 was used to determine the % of cell killing efficiency by **NIONP-HCQ**, **CaCD-HCQ** and **NIONP-CaCD-HCQ**.

4.5 CHARACTERIZATION DATA

NIONP: ^{1}H-NMR (400 MHz, $CDCl_3$, 25°C) δ/ppm: 8.46-8.51 (m, 1H, C-7 proton of naphthalimide (NI) core), 8.26-8.40 (m, 2H, C-2 and C-5 proton of NI core), 7.67-8.12 (m, 5H, C-6 proton of NI core and C-2, C-3, C-4, C-5 proton of phenyl ring), 6.87-7.18 (m, 1H, C-3 proton of NI core), 3.63-3.84 (m, 6H, $C\underline{H}_2$-O-$C\underline{H}_2$ protons of morpholine ring and NH-$C\underline{H}_2$-CH_2-C_4H_8NO), 2.32-2.73 (m, 6H, NH-CH_2-$C\underline{H}_2$-C_4H_8NO and $C\underline{H}_2$-N-$C\underline{H}_2$ proton of morpholine ring). ^{13}C-NMR (100 MHz, $CDCl_3$, 25°C) δ/ppm: 164.56, 157.15, 142.63, 137.07, 134.22, 132.29, 129.17, 128.34, 127.09, 126.82, 122.45, 117.24, 108.93, 108.04, 104.76, 63.11, 56.62, 52.83. MALDI-TOF MS: *m*/*z*: 445.282 $[M]^+$ (calculated); 445.949 $[M]^+$, 467.987 $[M+Na]^+$ (found).

4.6 SPECTRA

4.6.1 ^{1}H-NMR SPECTRUM

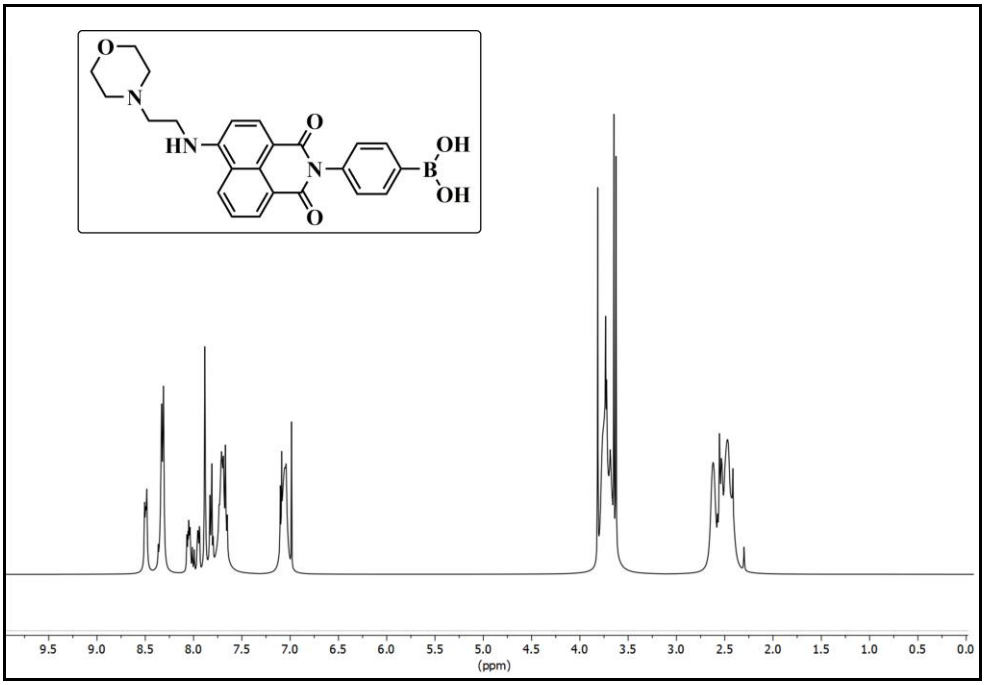

4.6.2 ^{13}C-NMR SPECTRUM.

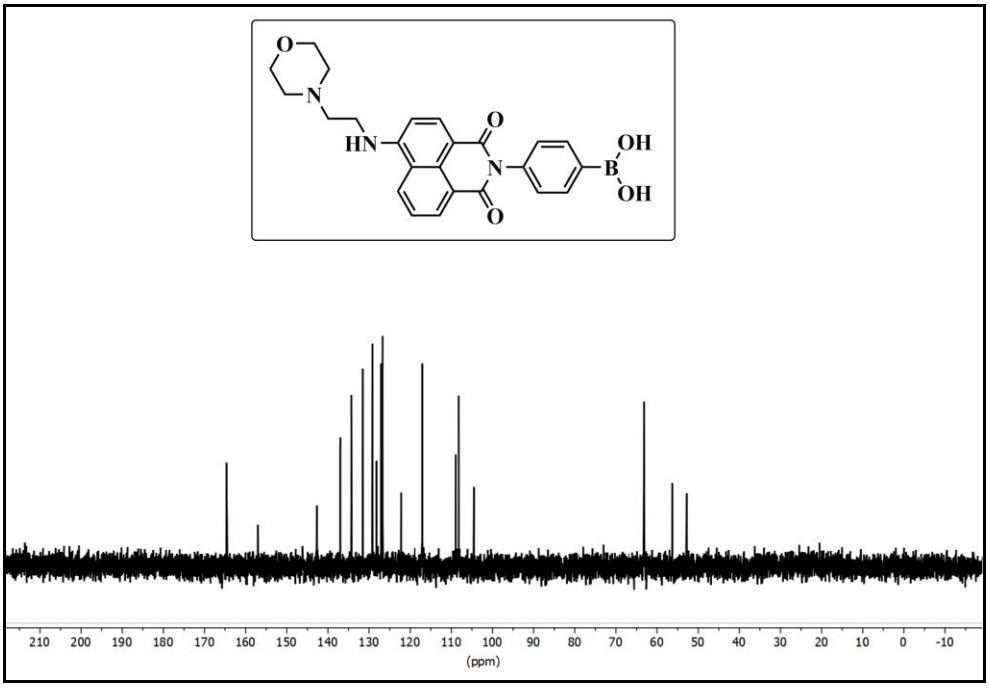

4.6.3 MALDI-TOF MASS SPECTRUM.

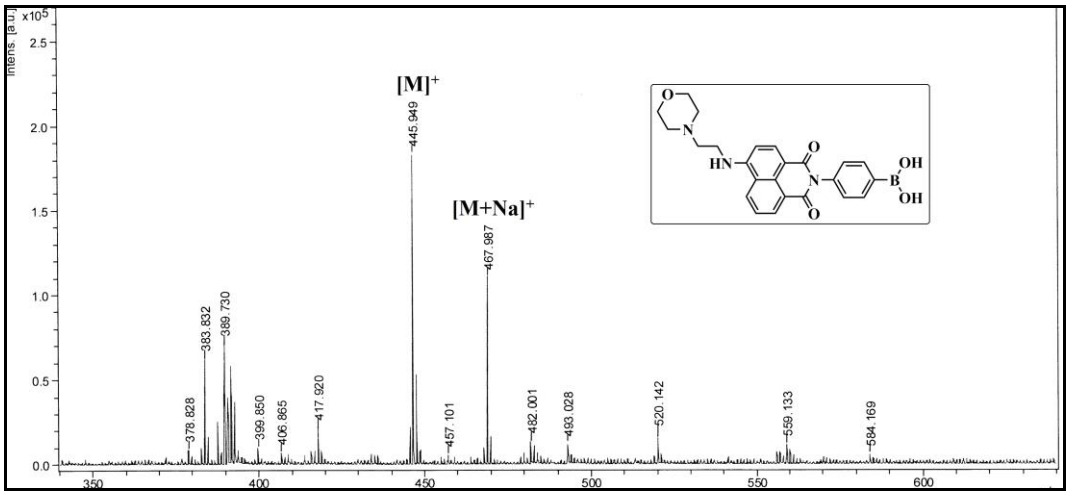

4.7 REFERENCES

[1] Bogart, L. K.; Pourroy, G.; Murphy, C. J.; Puntes, V.; Pellegrino, T.; Rosenblum, D.; Peer, D.; Lévy, R. Nanoparticles for Imaging, Sensing, and Therapeutic Intervention. *ACS Nano* **2014**, *8*, 3107-3122.

[2] Mir, M.; Ishtiaq, S.; Rabia, S.; Khatoon, M.; Zeb, A.; Khan, G. M.; Rehman, A.; Din, F. Nanotechnology: from In Vivo Imaging System to Controlled Drug Delivery. *Nanoscale Res. Lett.* **2017**, *12*, 500.

[3] Sim, S.; Wong, N. K. Nanotechnology and its use in imaging and drug delivery (Review). *Biomed Rep.* **2021**, *14*, 42.

[4] Li, K.; Liu, B. Polymer-encapsulated organic nanoparticles for fluorescence and photoacoustic imaging. *Chem. Soc. Rev.* **2014**, *43*, 6570-6597.

[5] Mitragotri, S.; Patrick, S. Organic nanoparticles for drug delivery and imaging. *MRS Bulletin* **2014**, *39*, 219-223.

[6] Ng, K. K.; Zheng, G. Molecular Interactions in Organic Nanoparticles for Phototheranostic Applications. *Chem. Rev.* **2015**, *115*, 11012-11042.

[7] Liu, J.; Li, R.; Yang, B. Carbon Dots: A New Type of Carbon-Based Nanomaterial with Wide Applications. *ACS Cent. Sci.* **2020**, *6*, 2179-2195.

[8] Wang, B.; Cai, H.; Waterhouse, G. I. N.; Qu, X.; Yang, B.; Lu, S. Carbon Dots in Bioimaging, Biosensing and Therapeutics: A Comprehensive Review. *Small* **2022**, *2*, 2200012.

[9] Truskewycz, A.; Yin, H.; Halberg, N.; Lai, D. T. H.; Ball, A. S.; Truong, V. K.; Rybicka, A. M.; Cole, I. Carbon Dot Therapeutic Platforms: Administration, Distribution, Metabolism, Excretion, Toxicity, and Therapeutic Potential. *Small* **2022**, *18*, 2106342.

[10] Bhattacharya, T.; Shin, G. H.; Kim, J. T. Carbon Dots: Opportunities and Challenges in Cancer Therapy. *Pharmaceutics* **2023**, *15*, 1019.

[11] Desai, N. Challenges in Development of Nanoparticle-Based Therapeutics. *AAPS J.* **2012**, *14*, 282-295.

[12] Karchemski, F.; Zucker, D.; Barenholz, Y.; Regev, O. Carbon nanotubes-liposomes conjugate as a platform for drug delivery into cells. *J. Control. Release* **2012**, *160*, 339-345.

[13] Kim, T.; Do, C.; Kang, S.; Lee, M.; Lim, S.; Choi, S. Highly ordered superstructures of single wall carbon nanotube–liposome complexes. *Soft Matter* **2012**, *8*, 9073-9078.

[14] Mehdi, A.; Reye, C.; Corriu, R. From molecular chemistry to hybrid nanomaterials. Design and functionalization. *Chem. Soc. Rev.* **2011**, *40*, 563-574.

[15] Park, W.; Shin, H.; Choi, B.; Rhim, W. K.; Na, K.; Han, D. K. Advanced hybrid nanomaterials for biomedical applications. *Prog. Mater. Sci.* **2020**, *114*, 100686.

[16] Urruticoechea, A.; Alemany, R.; Balart, J.; Villanueva, A.; Vinals, F.; Capella, G. Recent Advances in Cancer Therapy: An Overview. *Curr. Pharm. Des.* **2010**, *16*, 3-10.

[17] Schaue, D.; McBride, W. H. Opportunities and challenges of radiotherapy for treating cancer. *Nat. Rev. Clin. Oncol.* **2015**, *12*, 527-540.

[18] Tan, S.; Li, D.; Zhu, X. Cancer immunotherapy: Pros, cons and beyond. *Biomed. Pharmacother.* **2020**, *124*, 109821.

[19] Zugazagoitia, J.; Guedes, C.; Ponce, S.; Ferrer, I.; Pinelo, S. M.; Ares, L. P. Current Challenges in Cancer Treatment. *Clin. Ther.* **2016**, *38*, 1551-1566.

[20] Mokhtari, R. B.; Homayouni, T. S.; Baluch, N.; Morgatskaya, E.; Kumar, S.; Das, B.; Yeger, H. Combination therapy in combating cancer. *Oncotarget*. **2017**, *8*, 38022-38043.

[21] Hu, C. M. J.; Zhang, L. Nanoparticle-Based Combination Therapy toward Overcoming Drug Resistance in Cancer. *Biochem. Pharmacol.* **2012**, *83*, 1104-1111.

[22] Denny, W. A. Prodrug strategies in cancer therapy. *Eur. J. Med. Chem.* **2001**, *36*, 577-595.

[23] Ge, Y.; Ma, Y.; Li, L. The Application of Prodrug-Based Nano-Drug Delivery Strategy in Cancer Combination Therapy. *Colloids Surf. B* **2016**, *146*, 482-489.

[24] Bildstein, L.; Dubernet, C.; Couvreur, P. Prodrug-Based Intracellular Delivery of Anticancer Agents. *Adv. Drug Deliv. Rev.* **2011**, *63*, 3-23.

[25] Monteith, G. R.; McAndrew, D.; Faddy, H. M.; Thomson, S. J. R. Calcium and cancer: targeting Ca^{2+} transport. *Nat. Rev. Cancer* **2007**, *7*, 519-530.

[26] Zhivotovsky, B.; Orrenius, S. Calcium and cell death mechanisms: A perspective from the cell death community. *Cell Calcium* **2011**, *50*, 211-221.

[27] Yao, J.; Peng, H.; Qiu, Y.; Li, S.; Xu, X.; Wu, A.; Yang, F. Nanoplatform-mediated calcium overload for cancer therapy. *J. Mater. Chem. B* **2022**, *10*, 1508-1519.

[28] Xiao, Y.; Li, Z.; Bianco, A.; Ma, B. Recent Advances in Calcium-Based Anticancer Nanomaterials Exploiting Calcium Overload to Trigger Cell Apoptosis. *Adv. Funct. Mater.* **2023**, *33*, 2209291.

[29] Manic, G.; Obrist, F.; Kroemer, G.; Vitale, I.; Galluzzi, L. Chloroquine and hydroxychloroquine for cancer therapy. *Mol. Cell. Oncol.* **2014**, *1*, e29911.

[30] Shi, T. T.; Yu, X. X.; Yan, L. J.; Xiao, H. T. Research progress of hydroxychloroquine and autophagy inhibitors on cancer. *Cancer Chemother. Pharmacol.* **2017**, *79*, 287-294.

[31] Marchi, S.; Pinton, P. Alterations of calcium homeostasis in cancer cells. *Curr. Opin. Pharmacol.* **2016**, *29*, 1-6.

[32] Orrenius, S.; Jr., M. J. M.; Nicotera, P. Ca^{2+}-dependent mechanisms of cytotoxicity and programmed cell death. *Toxicol. Lett.* **1992**, *64-65*, 357-364.

[33] Bai, S.; Lan, Y.; Fu, S.; Cheng, H.; Lu, Z.; Liu, G. Connecting Calcium-Based Nanomaterials and Cancer: From Diagnosis to Therapy. *Nanomicro Lett.* **2022,** *14*, 145.

[34] Zhang, M.; Song, R.; Liu, Y.; Yi, Z.; Meng, X.; Zhang, J.; Tang, Z.; Yao, Z.; Liu, Y.; Liu, X.; Bu, W. Calcium-Overload-Mediated Tumor Therapy by Calcium Peroxide Nanoparticles. *Chem* **2019**, *5*, 2171-2182.

[35] Geisslinger, F.; Müller, M.; Vollmar, A. M.; Bartel, K. Targeting Lysosomes in Cancer as Promising Strategy to Overcome Chemoresistance-A Mini Review. *Front. Oncol.* **2020**, *10*, 1156.

[36] Towers, C. G.; Thorburn, A. Targeting the lysosome for cancer therapy. *Cancer Discov.* **2017**, *7*, 1218-1220.

[37] Boya, P.; Polo, R. A. G.; Poncet, D.; Andreau, K.; Vieira, H. L. A.; Roumier, T.; Perfettini, J. L.; Kroemer, G. Mitochondrial membrane permeabilization is a critical step of lysosome-initiated apoptosis induced by hydroxychloroquine. *Oncogene* **2003**, *22*, 3927-3936.

[38] Besaratinia, A.; Caliri, A. W.; Tommasi, S. Hydroxychloroquine induces oxidative DNA damage and mutation in mammalian cells. *DNA Repair (Amst.)* **2021**, *106*, 103180.

[39] Yang, B.; Lv, Y.; Zhu, J. Y.; Han, Y. T.; Jia, H. Z.; Chen, W. H.; Feng, J.; Zhang, X. Z.; Zhuo, R. X. A pH-responsive drug nanovehicle constructed by reversible attachment of cholesterol to PEGylated poly(L-lysine) via catechol-boronic acid ester formation. *Acta Biomater.* **2014**, *10*, 3686-3695.

[40] Ghosh, A. K.; Choudhury, P.; Das, P. K. Fabrication of Orange-Emitting Organic Nanoparticle-Protamine Conjugate: Fluorimetric Sensor of Heparin. *Langmuir* **2019**, 35, 15180-15191.

[41] Chowdhury, M.; Das, P. K. Paclitaxel-Loaded Biotinylated Fe^{2+}-Doped Carbon Dot: Combination Therapy in Cancer Treatment. *ACS Appl. Bio Mater.* **2021**, *4*, 7563–7577.

[42] Demri, B.; Muster, D. XPS study of some calcium compounds. *J. Mater. Process. Technol.* **1995**, 55, 311-314.

[43] Zhu, X.; Gu, J.; Zhu, J.; Li, Y.; Zhao, L.; Shi, J. Metal-Organic Frameworks with Boronic Acid Suspended and Their Implication for cis-Diol Moieties Binding. *Adv. Funct. Mater.* **2015**, *25*, 3847-3854.

[44] Tanenbaum, L.; Tuffanelli, D. L. Antimalarial agents: chloroquine, hydroxychloroquine, and quinacrine. *Arch Dermatol*. **1980**,*116*, 587-591.

[45] Verbaanderd, C.; Maes, H.; Schaaf, M. B.; Sukhatme, V. P.; Pantziarka, P.; Sukhatme, V.; Agostinis, P.; Bouche, G. Repurposing Drugs in Oncology (ReDO)-chloroquine and hydroxychloroquine as anti-cancer agents. *Ecancermedicalscience* **2017**, *11*, 781.

POSTLUDE

Molecular chemistry has pioneered a diverse set of potent techniques to craft increasingly intricate molecules and materials, achieved through the linkage of atoms via covalent bonds. In contrast, supramolecular chemistry surpasses this molecular level, crafting complex, functional systems from amphiphiles. These systems are united through intermolecular non-covalent interactions, enabling the emergence of sophisticated structures with advanced properties.

For the past four decades, the "bottom-up" approach to constructing nano-architectures through supramolecular self-assembly has garnered significant attention. This strategy revolves around the spontaneous arrangement of molecular building blocks, known as tectons, leading to organized structures or patterns at various scales. The interactions at play are influenced by the structural and electronic attributes of individual molecules, dictating factors such as their shape, charge, and polarizability. Recently, the self-organization of small amphiphilic molecules through supramolecular processes has emerged as a pivotal avenue of exploration, characterized by its artistic nano-scale methodology. This approach has rapidly opened up new avenues in physics, chemistry, and biology. Notably, the capacity of supramolecular self-assembly to replicate intricate biological systems using simple components has facilitated insights into the nature of "life" and the resolution of practical challenges. Furthermore, this technique has expanded the realm of molecular chemistry by enabling the development of eco-friendly micro/nano-reactors for synthetic processes. Globally, an extensive community of researchers tirelessly engages in unraveling the potential benefits of supramolecular self-assemblies across diverse interdisciplinary domains.

The central research focus of our team at IACS revolves around the innovative design of multimodal, functionally enhanced amphiphiles, which in turn yield a rich spectrum of supramolecular aggregates. These self-assembled soft materials find applications spanning biochemical and bio-medicinal realms. The present thesis elaborates on our investigation into the fabrication of AIE-based FONPs and their utilization in sensing, bioimaging and drug delivery. This pursuit extends to the incorporation of carbon dots into soft-nanoconjugates. The scientific exploration chronicled in this thesis is the culmination of our steadfast dedication to the advancement of functional nanomaterials. As we conclude, we hold the aspiration that this work resonates with and provides insights for those keenly interested in the field.

LIST OF PUBLICATIONS

[1] **Anup Kumar Ghosh**, Aftab Hossain Khan, and Prasanta Kumar Das. Naphthalimide based AIEgens for Sensing Protein Disulfide Isomerase through Thiol-Disulfide Redox Exchange. ***Anal. Chem.*** **2023**, *95*, https://doi.org/10.1021/acs.analchem.3c02442.

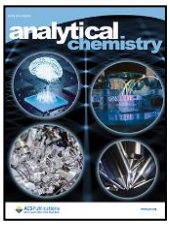

[2] **Anup Kumar Ghosh**, Monalisa Chowdhury and Prasanta Kumar Das. Nipecotic Acid Tethered Naphthalene Diimide based Orange Emitting Organic Nanoparticles as Targeted Delivery Vehicle and Diagnostic Probe towards $GABA_A$ Receptor Enriched Cancer Cells. ***ACS Appl. Bio Mater.*** **2021**, *4*, 7563–7577.

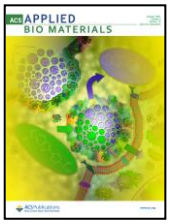

[3] **Anup Kumar Ghosh**, Pritam Choudhury and Prasanta Kumar Das. Fabrication of Orange Emitting Organic Nanoparticle-Protamine Conjugate: Fluorimetric Sensor of Heparin. ***Langmuir***, **2019**, *35*, 15180-15191.

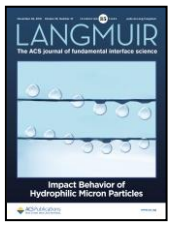

[4] **Anup Kumar Ghosh**, Kathakoli Roy, and Prasanta Kumar Das. Organic Nanoparticle-Carbon Dot Conjugates in Synergistic Combination Therapy for Cancer Treatment. *(Manuscript Communicated)*

[5] Aftab Hossain Khan, Sudeshna Pal, **Anup Kumar Ghosh** and Prasanta Kumar Das. Amino Acid and Dipeptide Amphiphile Based Supramolecular Eutectogels: Soft Materials for Drug Entrapment-Release and Waste-Water Treatment. ***ACS Appl. Eng. Mater.*** **2023**, *1*, 1809-1821.

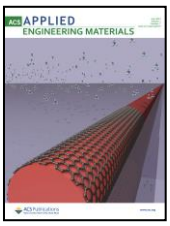

[6] Deblina Sarkar, **Anup Kumar Ghosh**, Aftab Hossain Khan and Prasanta Kumar Das. Organic nanoparticles with tuneable AIE derived from amino acids appended naphthalenediimide based amphiphiles. ***J. Mol. Liq.*** **2023,** 382, 121824.

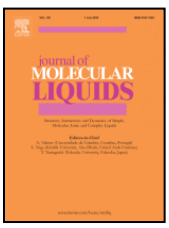

[7] Aparajita Ghosh, **Anup Kumar Ghosh**, Monalisa Chowdhury and Prasanta Kumar Das. Folic Acid Functionalized Carbon Dot Enabled Starvation Therapy in Synergism with Paclitaxel Against Breast Cancer. ***ACS Appl. Bio Mater.*** **2022**, 5, 2389-2402.

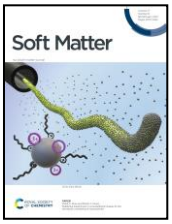

[8] Debayan Chakraborty, Deblina Sarkar, **Anup Kumar Ghosh** and Prasanta Kumar Das. Lipase sensing by naphthalene diimide based fluorescent organic nanoparticles: a solvent induced manifestation of self-assembly. ***Soft Matter* 2021**, *17*, 2170-2180.

[9] Kathakoli Roy, **Anup Kumar Ghosh** and Prasanta Kumar Das. Naphthalene Diimide based Orange Emitting AIE-gen: A Fluorometric Probe for Thiol Sensing through Click Reaction. *(Manuscript Communicated)*

[10] Aparajita Ghosh, **Anup Kumar Ghosh**, Afreen Zaman and Prasanta Kumar Das. Metformin Loaded Hyaluronic Acid Derived Carbon Dots for Targeted Therapy against Hepatocellular Carcinoma by Glutamine Metabolic Reprogramming. *(Manuscript Communicated)*

[11] Aparajita Ghosh, **Anup Kumar Ghosh** and Prasanta Kumar Das. Nanotechnology Meets Stem Cell Therapy: A Cutting-Edge Approach for Glioblastoma Treatment. *(Manuscript under Preparation)*